INFORMATION TO USERS

This manuscript has been reproduced from the microfilm master. UMI films the text directly from the original or copy submitted. Thus, some thesis and dissertation copies are in typewriter face, while others may be from any type of computer printer.

The quality of this reproduction is dependent upon the quality of the copy submitted. Broken or indistinct print, colored or poor quality illustrations and photographs, print bleedthrough, substandard margins, and improper alignment can adversely affect reproduction.

In the unlikely event that the author did not send UMI a complete manuscript and there are missing pages, these will be noted. Also, if unauthorized copyright material had to be removed, a note will indicate the deletion.

Oversize materials (e.g., maps, drawings, charts) are reproduced by sectioning the original, beginning at the upper left-hand corner and continuing from left to right in equal sections with small overlaps.

Photographs included in the original manuscript have been reproduced xerographically in this copy. Higher quality 6" x 9" black and white photographic prints are available for any photographs or illustrations appearing in this copy for an additional charge. Contact UMI directly to order.

Bell & Howell Information and Learning
300 North Zeeb Road, Ann Arbor, MI 48106-1346 USA
800-521-0600

THE STUDY OF A NOVEL THERMAL PLASMA PROCESS FOR THE PRODUCTION OF FUMED SILICA

A Thesis by Tony Addona, M. Eng.

Department of Chemical Engineering
McGill University
Under the Supervision of Dr. R. J. Munz and Dr. P. Proulx

A thesis submitted to the Faculty of Graduate Studies and Research
of McGill University in partial fulfillment of the requirements
of the degree of Ph. D. of Engineering

McGill University
Montreal, Canada

January 1998

ABSTRACT

A novel thermal plasma process for fumed silica production was investigated. The novelty was the result of the method used for silica decomposition which consisted of transferring an arc (Ar or Ar/H_2) to a silica anode. The primary objective was to examine the effect of current (150 - 250 A), plasma gas flow rate (10 - 20 lpm Ar) and plasma gas composition (0 - 2.8 % H_2) on the rate of silica decomposition. The decomposition rate (0.09 - 1.8 g/min) was determined to be a heat transfer limited process which occurred below the arc root where the surface had attained its boiling point. The decomposition rate was not affected by plasma gas flow rate since convective heat transfer was reduced by the counter flow of decomposition products ($SiO_{(g)}$ and O_2) from the anode surface. Increasing current increased the decomposition rate because the heat input to the anode due to electron flow and arc radiation was increased. Adding H_2 to the plasma gas increased the decomposition rate because of an increase in radiative heat transfer to the anode, a reduction in the theoretical energy requirement for decomposition and a consumption of O_2 which lowered the boiling point. A mathematical model was developed to simulate the behavior of the silica anode. The predicted decomposition rates were of the same order of magnitude as those observed experimentally. A secondary objective was to examine the effect of oxidation zone parameters including $SiO_{(g)}$ concentration (0.09 - 3.24 %) and temperature (1414 - 1801 K) of the reactor exit gas and steam flow rate (46 - 71 g/min) on powder properties. The oxidation zone was where $SiO_{(g)}$ was quenched with steam to generate fumed silica. The specific surface area of the powders (104 - 257 m^2/g) increased with increasing steam flow rate due to the higher quench rates. The high $H_2O_{(g)}$ concentration in the oxidation zone produced surface hydroxyl densities which approached saturation (7.85 Si-OH/nm^2). The powders had typical characteristics associated with commercial fumed silica except for a low thickening and thixotropic ability which was suspected to be due to a difference in agglomerate structure.

RÉSUMÉ

Un procédé inédit de production de silice ultrafine a été étudié. L'originalité du procédé résulte d'une méthode de décomposition de la silice par transfert d'un arc (Ar ou Ar/H_2) vers une anode de silice. L'objectif premier était d'examiner les effets du courant (150-200 A) ainsi que du débit (10-20 lpm Ar) et de la composition (0-2.8 % H_2) du gaz plasmagène sur le taux de décomposition de la silice. Ce taux de décomposition (0.09-1.8 g/min) s'avère limité par le transfert de chaleur sous la racine de l'arc où la surface atteint son point d'ébullition. Le taux de décomposition n'est pas affecté par le débit de gaz car le transfert de chaleur par convection est atténué par le flux à contre-courant des produits de décomposition ($SiO_{(g)}$ et O_2) provenant de la surface anodique. Une augmentation du courant accélère le taux de décomposition en augmentant l'apport de chaleur vers l'anode par le flux d'électrons et par radiation. L'ajout d'hydrogène au gaz plasmagène accélère la décomposition en augmentant le chauffage anodique par radiation, en réduisant l'énergie théoriquement requise pour la décomposition, et en consommant O_2, ce qui abaisse le point d'ébullition. Un modèle mathématique a été développé pour simuler le comportement de l'anode de silice. Les taux de décomposition prédits sont du même ordre de grandeur que ceux observés expérimentalement. Un objectif second était d'examiner l'effet de certains paramètres de la zone d'oxydation, incluant la concentration de $SiO_{(g)}$ (0.09-3.24 %), la température du gaz s'échappant du réacteur (1414-1801 K) et le débit de vapeur (46-71 g/min), sur les propriétés de la poudre produite. La zone d'oxydation est située là où $SiO_{(g)}$ refroidit au contact de la vapeur pour former la silice ultrafine. L'aire de surface spécifique des poudres (104-257 m^2/g) augmente avec le débit de vapeur dû à une trempe plus rapide. La concentration élevée de $H_2O_{(g)}$ dans la zone d'oxydation produit une densité de surface de groupes hydroxy approchant la saturation (7.85 Si-OH/nm^2). Les poudres présentent les caractéristiques typiquement associées aux silices ultrafines commerciales, à l'exception de faibles propriétés épaississantes et thixotropiques attribuées à une différence de structure des agglomérats.

ACKNOWLEDGMENTS

To Professor R. J. Munz for his guidance, patience and moral support without which the completion of this thesis would not have been possible.

To Professor P. Proulx for his advice and helpful insight on the mathematical modeling work done during this project.

To Ian Turner for the many helpful discussions we had on the problems encountered during the course of this study. I would also like to thank him for his help in the preparation of the quartz raw material and the purity analysis.

To the present members of the plasma group: S. Coulombe, H. Seon, A. C. DaCruz, J. Filion, P. Nadeau, J. Obereste Berghaus, K. Sum, Prof . J. L. Meunier and Prof. D. Berk, and to past members: G. Kim, J. E. Kwak, M. El-Naas, M. Kandah, J. F. Bilodeau and F. Moura.

To the members of the Chemical Engineering non-academic staff: J. Terrasi, B. Hanley, A. Prihoda, P. Fong, L. Cusmich, A. Gagnon, W. Greenland, C. Dolan, J. Dumont, E. Siliauskaus, B. Habib and M. Harrigan.

To summer students V. Tong, for his help in setting up the particle feeder, and A. Hanstead, for her help in the characterization of the fumed silica powders.

To Baskatong Quartz Inc., NSERC and FCAR for their financial support.

TABLE OF CONTENTS

page

NOMENCLATURE

Roman Letters

A	Constant
a	Subscript referring to the anode surface
B	Constant
B_θ	Self-induced azimuthal magnetic field
C	Constant
C_p	Heat capacity
D_{SiO2}	Local silica decomposition flux at the anode surface
d^*	Critical diameter for a stable particle
E_{cond}	Rate of heat loss by conduction through the thermocouples wires
E_{rad}	Rate of heat input to the thermocouple junction by radiation
E_{conv}	Rate of heat input to the thermocouple junction by convection
e	Subscript referring to the edge of the thermal boundary layer
e_o	Elementary charge
F_i	Molar flow rate of species i
F_{SiO2}	Molar decomposition rate of silica
f	Friction factor
H	Enthalpy
ΔH_{decomp}	Heat of silica decomposition
h_m	Mass transfer coefficient
h_T	Heat transfer coefficient
I	Current
j_H	Chilton-Colburn j-factor for heat transfer

j_r	Radial current density
j_z	Axial current density
$j_{z,surf}$	Axial current density at arc/anode interface
k	Thermal conductivity
k_B	Boltzmann constant
Nu	Nusselt number
n_o	Initial monomer concentration of the condensable species
P	Pressure
Pr	Prandtl number
Q_{plasma}	Plasma gas flow rate
q_{conv}	Anode surface heat flux input due to convection
q_{decomp}	Anode surface heat flux absorbed due to silica decomposition
q_{elec}	Anode surface heat flux input due to electron flow
$q_{rad,in}$	Anode surface heat flux input due to arc radiation
q_{rad,in_j}	Anode surface heat flux input due to arc radiation from plasma volume V_j
$q_{rad,out}$	Radiation heat flux emitted by the anode surface
q_{surf}	Net anode surface heat flux
R	Molar gas constant
Re	Reynolds number
r	Radial direction
r_j	Distance from anode surface element to plasma volume element j
S	Monomer supersaturation ratio
S_{absorb}	Generation term in anode energy equation which accounts for internal heat generation due to absorption of arc radiation
S_r	Volumetric radiation density which accounts for the net radiation emitted by a plasma volume which is not re-absorbed
S_T	Generation term in anode energy equation
S_t	Degree of shear thinning

S_u	Generation term in anode axial momentum equation
S_v	Generation term in anode radial momentum equation
T	Temperature
T_a	Anode surface temperature
T_{boil}	Silica boiling point
T_{chamb}	Chamber wall temperature
T_{cruc}	Crucible temperature
T_e	Electron temperature
T_{exit}	Reactor exit gas temperature
T_h	Degree of thickening
T_{surr}	Temperature of surroundings or enclosure
$T_{\Delta z}$	Anode temperature at an axial distance Δz below the surface
U	Activation energy
u	Axial velocity
$\bar{u}$	Velocity vector composed of u and v
V	Voltage due to arc and anode
V_{anode}	Anode fall potential
V_j	Plasma volume j
v	Radial velocity
v_1	Monomer volume
$x_{SiO,a}$	Mass fraction of $SiO_{(g)}$ at the anode surface
$x_{SiO,\infty}$	Characteristic mass fraction of $SiO_{(g)}$ in the bulk gas above the anode surface
y_i	Mole fraction of species i
z	Axial direction
z_{cruc}	Depth of silica anode at the radial position where $q_{rad,in}$ is evaluated
Δz	Small axial distance below the anode surface

Greek Letters

$\beta_0, \beta_1, \beta_2$	Regression parameters in equation 3.4
β_o	Initial collision frequency function for collisions between two monomers
δ_T	Thermal boundary layer thickness
δ_v	Velocity boundary layer thickness
ε	Emissivity
ϕ	Electric potential
ϕ_w	Work function
γ	Surface tension
η_{oil}	Viscosity of the calibration oil (1000 cp)
η_{rpm}	Apparent viscosity of suspension at specified spindle speed
μ	Viscosity
μ_o	Permeability of vacuum
ρ	Mass density
ρ_e	Electrical resistivity
ρ_p	Particle mass density
σ	Stefan-Boltzmann constant
τ_{arc}	Anode surface shear stress due to arc impingement
τ_c	Characteristic response time for aerosol dynamics
τ_{surf}	Net anode surface shear stress
ψ	Angle that r_j makes with the normal to the anode surface element
ζ_{max}	Maximum value of ζ
$\Delta\zeta_{max}$	Maximum change for variable ζ in a given calculation domain from one iteration to the next

Chapter 1 - INTRODUCTION

Fumed silica is an amorphous, ultrafine SiO_2 powder considered unique in industry because of its unusual particle properties. Common applications of the powder include its use as a reinforcing filler in rubbers, a thickening and thixotropic agent in paints, thermosetting resins and printing inks, and a free-flow and anti-caking agent in the processing of dry materials. Commercial production of fumed silica is primarily done using the flame hydrolysis process which consists of burning $SiCl_{4(g)}$ in an oxygen/hydrogen flame. As a result, large quantities of by-product $HCl_{(g)}$ are also generated. An alternative route to fumed silica production is via the thermal plasma process which consists of rapidly quenching $SiO_{(g)}$ with an oxidizing agent such as air or steam. Silicon monoxide vapor generation is accomplished by decomposing silica in a thermal plasma reactor with the aid of a reducing agent. The process can be described by the following overall reactions:

$$SiO_2 + \{\text{reducing agent}\} \rightarrow SiO_{(g)} + \{\text{products}\} \quad (1.1)$$

$$SiO_{(g)} + \{\text{oxidizing agent}\} \rightarrow SiO_2 + \{\text{products}\} \quad (1.2)$$

Common reducing agents include C, Si, H_2, CH_4 and NH_3. Because of the elimination of $SiCl_4$ and HCl, the thermal plasma process is seen as having potential economic advantages over flame hydrolysis.

During the past few decades, various studies have demonstrated the use of this alternative technique for fumed silica production. The majority of these studies have involved the use of dc rather than inductively coupled plasma torches because of their higher energy efficiency and greater potential for scale-up (Schnell et al., 1978). DC arc torches are classified as transferred when one of the electrodes is a material being processed and non-transferred when both electrodes are non-consumable. In the studies which employed non-transferred arc torches, the plasma flame was used to heat and

decompose the silica feed with the aid of a gaseous reducing agent such as H_2 and CH_4 (Everest et al., 1973 and Schnell et al., 1978). Gaseous reducing agents were also used by Gans and Gauvin (1988), Addona (1993) and Chang (1994); however, plasma generation in these studies was accomplished by striking an arc to a graphite anode. Other transferred arc processes have involved mixing the silica raw material with electrically conducting reducing agents such as C or Si (Biegler et al., 1963, Illigen and Neugebauer, 1969, Bakken et al., 1989 and Mishra et al., 1995). Although the results of the works mentioned above have been promising, presently, fumed silica generation by the thermal plasma route is of little or no economic significance (Ullmann's Encyclopedia of Industrial Chemistry, 1993).

1.1 Statement of the Problem

As with any alternative process, the thermal plasma production of fumed silica must be shown to be economically feasible if it is to have any commercial success. The lack of success of this process on an industrial scale is evidence that, while previous studies have shown technical feasibility, the economics must still be improved. The main goal of the current study was to investigate a novel thermal plasma process which could potentially produce fumed silica more economically. The novelty of the process is the result of the proposed method for silica decomposition which was to be accomplished by transferring a thermal arc directly to a silica anode. Although the possible use of silica as an anode material in a transferred arc configuration has been mentioned previously (Gans and Gauvin, 1988), to the knowledge of this author, the use of this technique for silica decomposition has not been demonstrated. Due to the inherent advantages of transferred arc operation in terms of energy transfer efficiency to the anode material (MacRae, 1989), it is believed that the use of this technique can greatly increase the efficiency with which silica is decomposed. Since silica decomposition is the most energy intensive step of the process, use of a transferred arc configuration will lead to an overall improvement of the

process economics.

An additional concern which must be addressed before the successful industrial application of this process is product quality. Even with improvements in process economics, the production of fumed silica powders having properties which are not equivalent to current commercial products will result in the failure of this process as a viable alternative to flame hydrolysis. The properties of fumed silica generated using the thermal plasma route are determined by conditions in the oxidation zone. This zone is located at the exit of the reactor and is the region where $SiO_{(g)}$ is rapidly quenched with an oxidizing agent to induce aerosol formation. A better understanding of the phenomena occurring in this region will lead to improvements in product quality and will aid any future scale-up of the oxidation zone.

1.2 Objectives

The primary objective of this study was to examine silica decomposition using a transferred arc system in which silica served as the anode. This was to include an experimental investigation of the effect of important operating parameters on the rate of silica decomposition. The parameters selected for study were current, plasma gas flow rate and plasma gas composition. A theoretical investigation of the silica anode was also to be undertaken using mathematical modeling. A model was to be developed which could predict the rate of silica decomposition from a knowledge of the plasma chamber operating parameters. The accuracy of the model was to be verified by a comparison with experimental observations.

A secondary objective was to investigate the effect of oxidation zone parameters on the properties of the fumed silica generated. The parameters of interest were the $SiO_{(g)}$ concentration and temperature of the gas entering the oxidation zone and the oxidizing agent flow rate. Based on promising results obtained in a previous study (Addona, 1993), steam was selected as the oxidizing agent. The powder properties to be examined

included specific surface area, surface hydroxyl density and morphology. A final verification of the quality of the powder product would be made by determining its thickening and thixotropic ability.

1.3 Thesis Organization

The thesis is organized into the following six chapters:

Chapter 1

INTRODUCTION - An introduction into the subject of the study is provided along with a statement of the problem and the objectives of the work.

Chapter 2

BACKGROUND - A review of relevant literature is given.

Chapter 3

AN EXPERIMENTAL INVESTIGATION OF SILICA DECOMPOSITION USING A TRANSFERRED ARC PROCESS - Following a brief introduction, a description of the apparatus and procedure used for this work is given. Results including the effect of plasma gas flow rate and current on the rate of silica decomposition are then presented and discussed.

Chapter 4

MATHEMATICAL MODELING OF SILICA ANODE DECOMPOSITION - The mathematical model developed to simulate silica anode decomposition is described here along with a brief description of the arc model (Ming, 1994) used to estimate the boundary conditions at the anode surface. The results of a base case simulation are presented and compared with experimental observations. The sensitivity of the model

predictions to variations in the base case assumptions is examined.

Chapter 5

THE EFFECT OF OXIDATION ZONE PARAMETERS ON POWDER PROPERTIES - The effect of oxidation zone parameters on powder properties such as specific surface area, surface hydroxyl density and morphology are discussed and the thickening and thixotropic ability of the powders is evaluated.

Chapter 6

CONCLUSION - The final chapter of the thesis summarizes the conclusions, recommendations for future work and contributions to knowledge.

Chapter 2 - BACKGROUND

2.1 Fumed Silica

The term fumed silica is used to describe an amorphous, ultrafine silica powder of unique characteristics. Also known as pyrogenic silica, this powder has been mentioned in literature as far back as 1887 (Ferch, 1981). Significant industrial production began in Germany in 1941 with the development of the flame hydrolysis process by Degussa. Today, most of the commercially available powder is produced via this process. In 1991 production capacities for fumed silica amounted to approximately 100,000 tonnes worldwide with the main producers being Degussa (Aerosil®), Cabot (Cab-O-Sil®), Wacker (HDK®), and Tokuyama (Reolosil®) (Ullmann's Encyclopedia of Industrial Chemistry, 1993).

2.1.1 Manufacture

Since its introduction, commercial fumed silica has been primarily produced using the flame hydrolysis process (see Figure 2.1). Also known as the Aerosil® process, this technique involves the burning of $SiCl_{4(g)}$ in an oxygen/hydrogen flame (Liu and Kleinschmit, 1986):

$$2H_2 + O_2 \rightarrow 2H_2O \qquad (2.1)$$

$$SiCl_{4(g)} + 2H_2O \rightarrow SiO_2 + 4HCl_{(g)} \qquad (2.2)$$

The above reactions take place in a furnace maintained at 2100 K (Cabot Corp., 1983) by burning appropriate amounts of H_2 in a large excess of air. Fumed silica generation

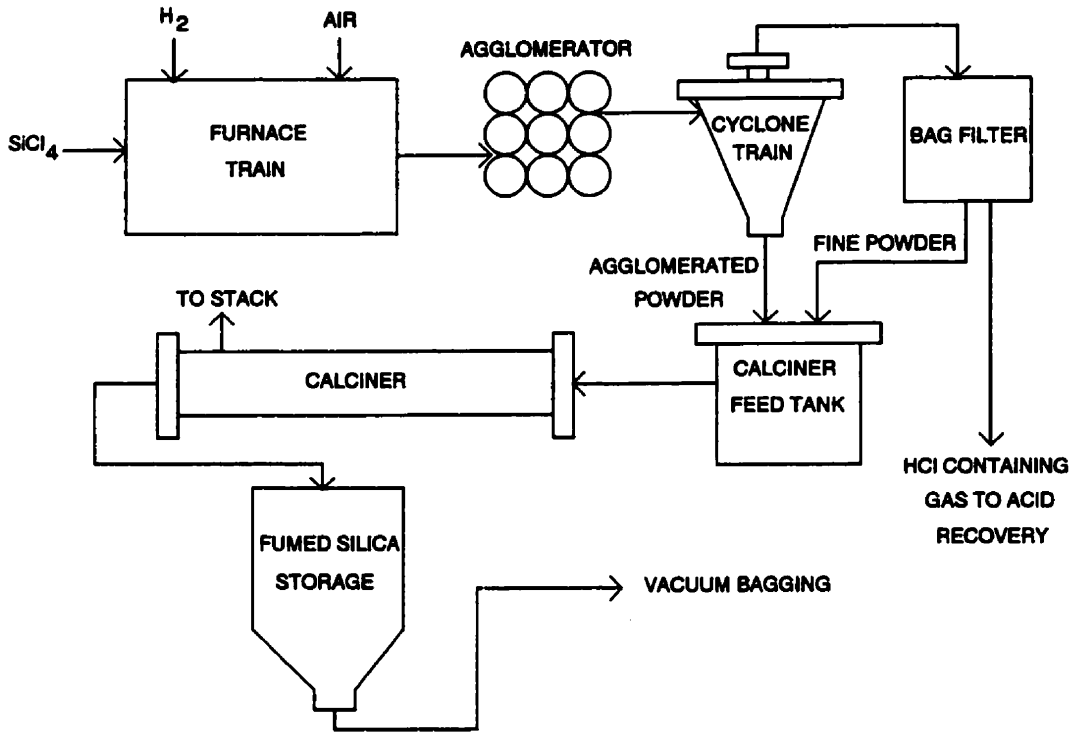

Figure 2.1 Flame hydrolysis process for fumed silica production (adapted from White and Duffy, 1959).

begins within the flame as $SiO_{2(g)}$ condenses to form liquid droplets having diameters of a few nanometer. As these particles grow and exit the flame they collide and partially fuse to form chain-like structures known as aggregates. These aggregates can have a maximum length of a few tenths of a micron (Cabot Corp., 1983). Once solidified, further collisions between aggregates lead to reversible mechanical entanglement (i.e. agglomeration). Unless extremely well dispersed, aggregates and agglomerates are difficult to distinguish in fumed silica. During the powder formation process, hydroxyl groups attach themselves to exposed Si atoms. The aerosol exiting the furnace is sent to an agglomerator which is described by White and Duffy (1959) as consisting of 16 aluminum pipes connected in series. Each pipe has a diameter of 30 cm and is approximately 5 m long. The role of the agglomerator is to generate large agglomerates which can be easily removed from the gas stream by the cyclone train and baghouse filter. The collected powder is further processed in a calciner using heat and steam to remove physically absorbed $HCl_{(g)}$. The calciner operating temperature is approximately 611 K (White and Duffy, 1959). Steam is used to minimize de-hydroxylation of the fumed silica surface which occurs above 383 K. De-hydroxylation results in the release of H_2O and can be reversed by exposure of the powder to air at 100 % relative humidity or by immersion in water (Cabot Corp., 1983). Following neutralization, the powder is sent to storage where it is ready for bagging.

Of much less commercial significance is the electric-arc process which involves the reduction of quartz sand (or other silica containing material) in an electric-arc furnace using C or Si (Biegler et al., 1963 and Illigen and Neugebauer, 1969). Mixtures of the silica raw material and C (usually coal or coke) or Si are introduced into a refractory lined furnace where $SiO_{(g)}$ generation occurs via either of the following reactions:

$$SiO_2 + C \rightarrow SiO_{(g)} + CO \qquad (2.3)$$

$$SiO_2 + Si \rightarrow 2SiO_{(g)} \qquad (2.4)$$

Heat is supplied to the furnace by an arc struck between graphite electrodes. Reducing

gas mixtures (Ar/H_2, N_2/H_2 or CO/H_2) are also added to the chamber. Quenching the hot gas exiting the furnace with a mixture of steam and air produces the desired fumed silica product. In order to increase thickening and thixotropic effectiveness, the powder is treated in a fluidized bed with air and steam. This process is currently used by Degussa to produce the fumed silica matting agent known as TK 900 (Ullmann's Encyclopedia of Industrial Chemistry, 1993).

2.1.2 Properties

Typical characteristics of fumed silica powders produced using the flame hydrolysis process are given in Table 2.1. Among their many interesting properties is the presence of hydroxyl groups in the form of Si-OH on the surface of the particles. Most of the powder's usefulness can be attributed to this property. Other unique characteristics include a large specific surface area, a lack of crystallinity and a chain-like aggregate structure. The general appearance of the powder is described as "light, fluffy and pure white" (Cabot Corp., 1983).

TABLE 2.1 Properties of fumed silica produced via flame hydrolysis (Ferch, 1981).

Property	***Value***
specific surface area (BET) [m^2/g]	50 - 600
primary particle size [nm]	5 - 50
true density [kg/m^3]	2200
average pore diameter [Å]	non-porous
structure of aggregates [-]	chain-like
thickening and thixotropic effect [-]	very strongly pronounced
surface chemistry [-]	hydroxylated surface
X-ray form [-]	amorphous

2.1.3 Use as a Thickening and Thixotropic Agent

Fumed silica's thickening and thixotropic ability is due to the presence of Si-OH groups on the surface of the particles. When added to liquids, the surface hydroxyls allow hydrogen bonding networks to form between groups of fumed silica particles (see Figure 2.2). The creation of these networks results in an increase in the apparent viscosity of the liquid at rest. When a shearing force is applied, the viscosity decreases because of a partial destruction of the networks. The decrease in viscosity is proportional to the magnitude of the shear rate and the length of time over which it is applied. Once the shearing action is stopped, the networks reform and the viscosity is restored. In addition to the properties of the fumed silica powder, the degree of network formation is also dependent on liquid type, degree of dispersion, temperature and, when dealing with aqueous systems, pH.

The nature of the liquid must be considered when using fumed silica as a thickening and thixotropic agent. Hydrogen bonding between liquid molecules and the surface hydroxyls reduces the degree of network formation. Liquids are classified according to their hydrogen bonding ability. Acids, low molecular weight alcohols and water are some examples of highly hydrogen bonding liquids. Non-hydrogen bonding liquids include aliphatic and aromatic hydrocarbons. There are also liquids which fall into an intermediate range including high molecular weight alcohols and silicone oils (Cabot Corp., 1983). Fumed silica is therefore most effective in non-hydrogen bonding systems.

Another important factor which determines thickening and thixotropic ability is the degree of dispersion. In order to maximize effectiveness, an optimum dispersion must be attained. During the initial mixing of the powder in the liquid, an increase in viscosity with time is observed. This continues until the viscosity reaches a maximum signifying the achievement of an optimum fumed silica network. In the case of non-hydrogen bonding liquids, mixing the suspension beyond this point results in little change in the apparent viscosity. For liquids with some hydrogen bonding ability, a decrease in viscosity is observed when mixed beyond this optimum time. The decrease is a result of

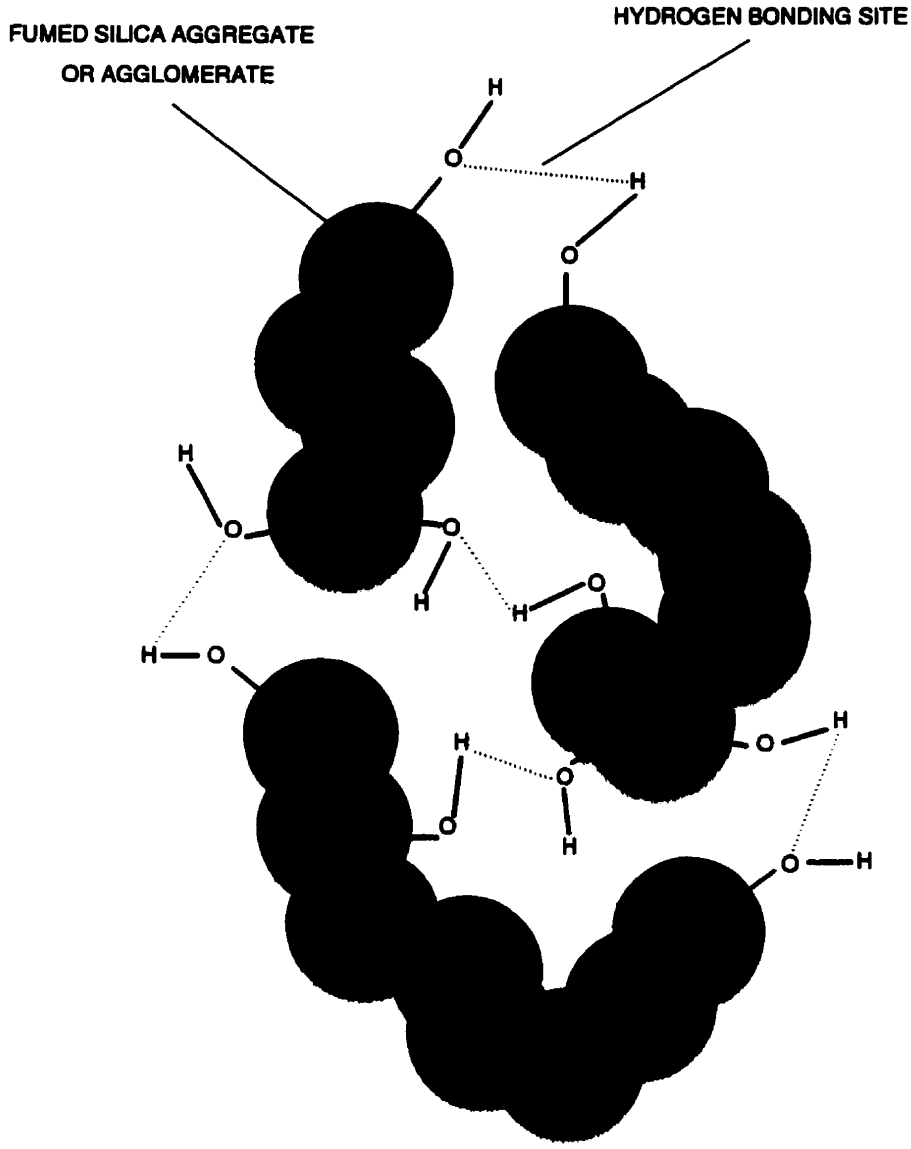

Figure 2.2 Hydrogen bonding between fumed silica aggregates or agglomerates.

the fragmentation of the fumed silica network into smaller sections which may or may not be able to recombine into the optimum structure. This depends on the nature of the liquid and the degree of fragmentation. For liquids of high hydrogen bonding ability, fragmentation of the network is irreversible since hydrogen bonding of the surface hydroxyls with available sites on the liquid molecules isolate the fumed silica fragments.

2.1.4 Use in Dry Systems

Fumed silica also finds many applications in the processing of dry materials. Its large surface area and hydrophilic character makes it an effective free-flow and anti-caking agent. As an additive to coating materials, partially exposed fumed silica particles embedded in the matrix act as frictionizing agents because of the increased surface roughness. This gives the coating a non-slip and non-stick quality.

2.1.5 Use as a Food Additive

Fumed silica is also safe for human consumption because of its nanometer size and amorphous form. In the United States, the use of Cab-O-Sil® (99.80 %) as a filler in food and pharmaceutical products has been approved by the Food and Drug Administration (Cabot Corp., 1983).

2.2 Thermal Plasma Production of Ultrafine Powders

Ultrafine powders (1 - 100 nm) are becoming a very valuable resource for today's high-tech industries. The high surface to volume ratio give ultrafine particles an advantage over conventional powders in a wide variety of applications. An example of this is in the production of ceramic structural components which are commonly produced

by sintering. Frequently, these components are of higher quality and less expensive when made from ultrafine powders (Young and Pfender, 1985). One reason for this is the low sintering temperature compared to conventional materials. Other promising areas of application are in the production of powder catalysts and electronic devices. Conventional methods for producing ultrafine powders include metallurgical reduction, fuming, atomization, electrolysis, grinding, sol-gel technique and spray drying. Common problems associated with these processes are the formation of non-spherical particles, high degrees of powder contamination, wide size distributions and high degrees of agglomeration. During the last decade, the use of thermal plasmas for ultrafine powder production has attracted increasing attention because of its potential to eliminate many of the above problems (Joshi et al., 1990). Today, with plasma spraying firmly entrenched in industry, ultrafine powder production represents the future of industrial thermal plasma technology.

2.2.1 General Process Description

Shown schematically in Figure 2.3, the thermal plasma production of ultrafine powder consists of thermal plasma generation, reaction and aerosol formation. Early systems lacked proper control of the powder forming process. This was the result of combining thermal plasma generation, reaction and aerosol formation all in the same vessel (i.e. the plasma chamber). A recent desire to improve powder quality has resulted in a more complete separation of these operations. This has caused the reaction and aerosol formation steps to be conducted outside the plasma chamber where temperature, species concentration and cooling rate can be better controlled.

The first step shown in Figure 2.3 is thermal plasma generation. Thermal (or "hot") plasmas are partially ionized gases made up of electrons and heavy particles (ions and neutrals) having approximately equivalent temperatures. They occur at pressures above 10 kPa and are commonly generated using a high intensity ac or dc arc, or by using a high frequency discharge. High intensity (> 50 A) dc arc generation techniques are of

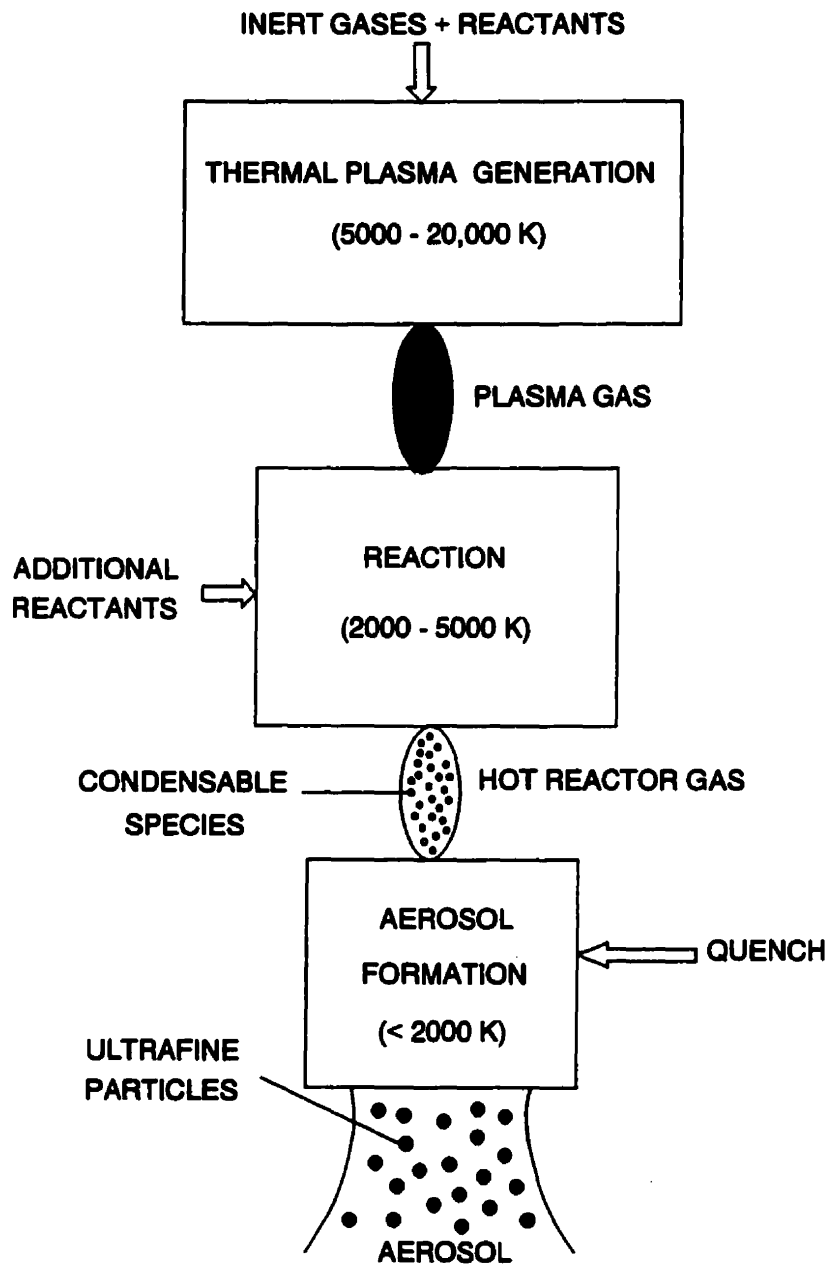

Figure 2.3 General thermal plasma process for the production of ultrafine powder (adapted from Girshick and Chiu, 1989).

particular interest to this work and are summarized in Figure 2.4. The thermal plasma exiting the generator is usually composed of a mixture of inert gases (such as Ar) and the decomposed reactants required for powder generation. One or more reactant feed streams may be used depending on whether the process involves a simple physical vaporization (i.e. metal powder production) or synthesis of a chemical compound (i.e. SiC, AlN etc.). Reactant feed streams may consist of gases, powders, particles or droplets. Temperatures within the plasma typically range from 5000 - 20,000 K. As the plasma cools (2000 - 5000 K), additional reactants (usually gases) may be added. The condensable species produced are then rapidly cooled to induce aerosol formation. In most cases, reaction and aerosol formation occur simultaneously in a region just after the plasma chamber exit. This occurs when the additional reactants added also serve as quenching agents. Rapid quenching is often the most vital step in the process because it ensures the production of nanosized particles and, in some cases, also preserves metastable products. Different methods used for quenching include cold gas mixing, injection into a fluidized bed, contact with a cold surface and evaporation of a liquid spray.

2.2.2 Aerosol Generation

The general particle formation process is summarized in Figure 2.5. This process can be divided into a reaction region and an aerosol region. Ideally, the hot gas within the reaction region contains only gaseous reactants and products. This may not always be the case especially when dealing with condensable species having low vapor pressures. If temperatures in the reaction region are too low, some condensation may occur within the gas stream prior to reaching the aerosol region. Assuming this is avoided, the desired product molecules or atoms combine with each other to form small groups known as clusters as they exit the reaction region. Since reaction is rarely complete, the gas phase still contains some reactants as well as free molecules or atoms. At this point, even though significant cluster sizes exist, particle formation is not considered to have taken place yet. Kotake and Glass (1981) estimate the point when a cluster becomes a particle

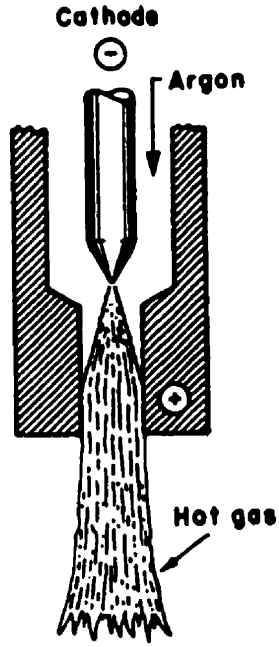

a) Non-transferred arc.

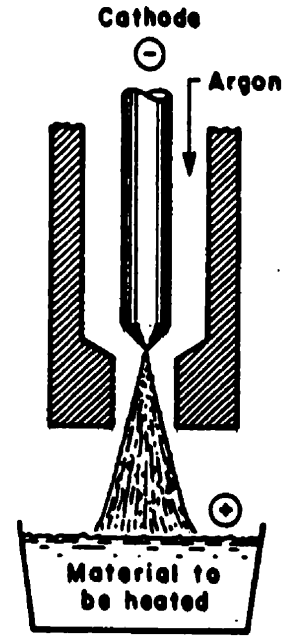

b) Transferred arc.

Figure 2.4 High intensity dc arc generation techniques (MacRae, 1989).

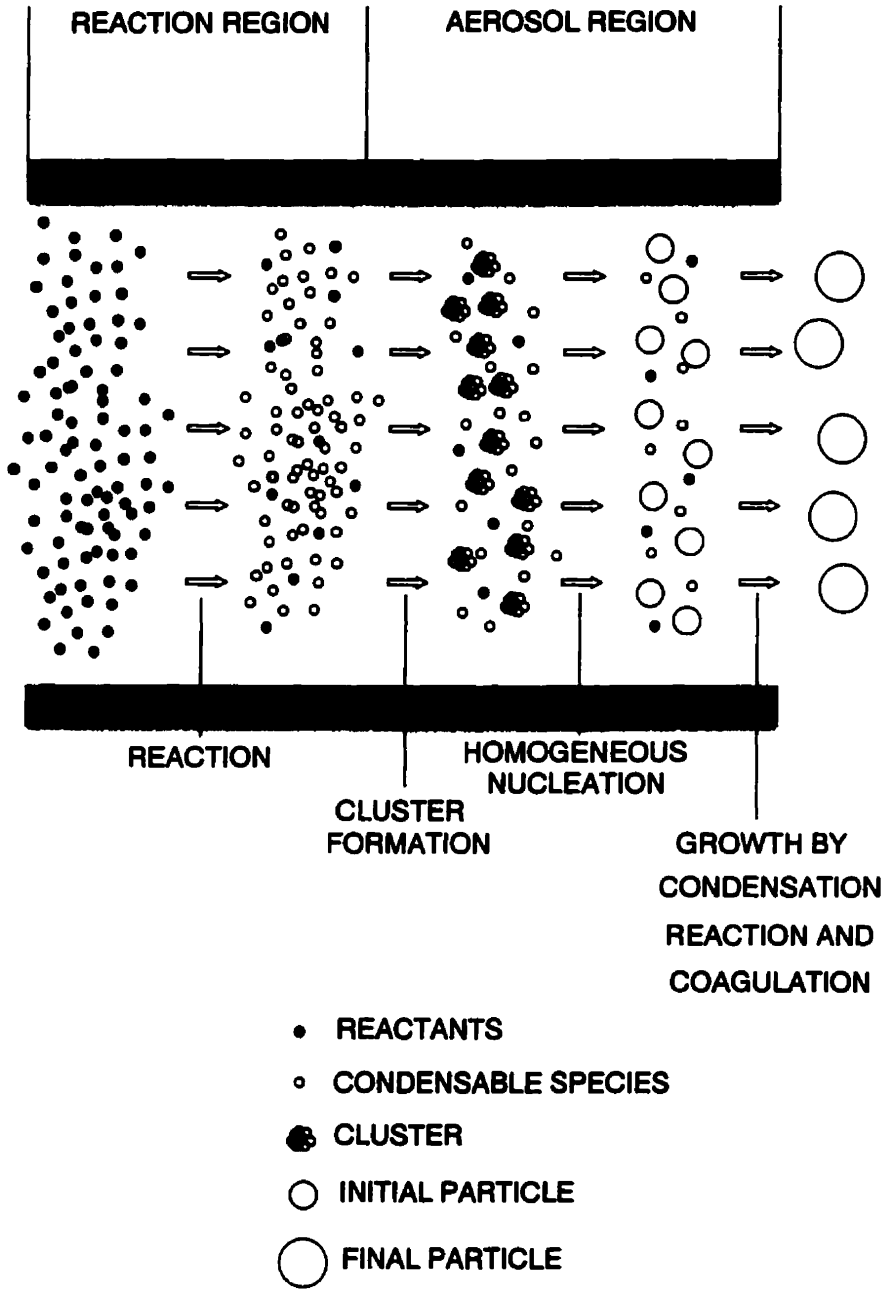

Figure 2.5 Particle formation process.

using the capillarity approximation where the transition is treated as the formation of a liquid drop. This is done by equating the free energy of formation of a droplet consisting of i monomers of the condensable species to the sum of the free energies required for the condensation of i monomers and the generation of a surface around the particle. The diameter required for a stable particle using this approach is given by:

$$d^* = \frac{4\gamma\, v_1}{k_B\, T \ln S} \tag{2.5}$$

where d^* is the critical diameter for a stable particle, S is the monomer supersaturation ratio, γ is the surface tension, T is the temperature, v_1 is the monomer volume and k_B is the Boltzmann constant. Clusters attaining a diameter of d^* are stable and tend to grow thus becoming nucleation sites for particle formation. The transition from cluster to particle is termed homogeneous nucleation. Exiting the reaction region, S is low due to the high temperature of the gas. Rapid quenching in the aerosol region quickly increases the monomer supersaturation ratio. From equation 2.5 we see that this leads to a reduction in d^*. Many subcritical clusters, which were previously unstable, now become available sites for homogeneous nucleation. The result is a "nucleation burst" in the aerosol region as most of the monomer population condenses onto these stable particles. The size distribution of particles at the point of homogeneous nucleation depends on material properties, initial monomer concentration and quench rate (Girshick et al., 1988 and Girshick and Chiu, 1989).

Fast kinetics in the reaction zone prevent continued product generation both in the vapor phase and on the particle surface after the initial nucleation event. In real processes, finite-rate kinetics and equilibrium thermodynamics may cause the continued production of condensable product long after homogeneous nucleation. The result is a significant increase in particle size due to condensation and reaction at the surface. Further growth may also occur through the coagulation of molten particles. In the production of materials which form solid phase nuclei directly, such as SiC, particle growth via coagulation does

not occur. Instead, collisions between these particles are believed to produce loose agglomerates which undergo inflight sintering if residence times and temperatures are sufficient (Kong et al., 1986). In other cases, such as in the production of fumed silica, collision and partial fusion of molten particles create chain-like structures known as aggregates. Growth through complete or partial coagulation continues until all the particles in the aerosol have solidified. High quench rates minimize coagulation because liquid phase intermediates are short-lived.

2.2.3 Examples of Powders Produced using Thermal Plasma Processes

Powders produced by this method can be classified into two major groups: ceramic and metallic. Ceramic powders consisting of carbides (SiC, TiC, TaC, etc.), oxides (Al_2O_3, SiO_2, TiO_2, etc.), nitrides (Si_3N_4, AlN, TiN, etc.) and borides (TiB_2) are seen as having great potential in a wide variety of applications including the production of advanced structural ceramics, powder catalysts and electronic devices (Kong and Lau, 1990). Common metallic powders produced by thermal plasma processes include Si, Ag, Ta, Mo and W. Ultrafine Si is a useful raw material for the production of ultrafine SiC and Si_3N_4 powders (Tanaka et al., 1987). Other ultrafine metallic powders such as Ta, Mo and W are desired because of their improved sinterability compared to conventional metallic powders. Although the feasibility of the thermal plasma production of ultrafine powders has been established for a number of years (Young and Pfender, 1985), most of the processes involved in the production of the above materials are still in the development stage.

2.3 Thermal Plasma Production of Fumed Silica

As has already been mentioned, commercial fumed silica is almost exclusively produced using flame hydrolysis. Interest in the use of the thermal plasma process as an alternative began because of the possibility of producing fumed silica more economically. This is mainly due to the use of cheaper raw materials and the elimination of $SiCl_4$ and HCl handling. The steps involved in the thermal plasma production of fumed silica are summarized in Figure 2.6. The first step involves the generation of $SiO_{(g)}$ through the decomposition of a silica source in a thermal plasma reactor with the aid of a reducing agent. Typical reducing agents include C, Si and H_2. When a gaseous reducing agent such as H_2 is used, it may be added to the reactor as part of the plasma feed gas. The $SiO_{(g)}$ generated in the reactor is then transported into the oxidation zone where air, steam or O_2 is added to induce fumed silica formation.

2.3.1 Review of Previous Studies

Because the thermal plasma production of fumed silica offers many advantages, it has been the subject of a number of studies over the years. One of the first studies demonstrating the feasibility of this technique was conducted by Everest et al. (1973). The apparatus used in this work, shown in Figure 2.7, consisted of a dc non-transferred arc torch mounted at the entrance of a centrifugal liquid-wall furnace. Experiments were of the batch type with silica introduced into the reactor as a cylindrical lining. The cylinder was constructed of ground fused quartz or natural silica sand (99.8 % SiO_2). A summary of the silica decomposition experiments conducted during this study can be found in Table 2.2. From the results of this study, we can clearly see the importance of the reducing agent. Increasing the H_2 flow rate to the torch dramatically decreased the specific energy requirement for silica decomposition which resulted in increased decomposition rates. The lowest specific energy requirement was found when a pure NH_3

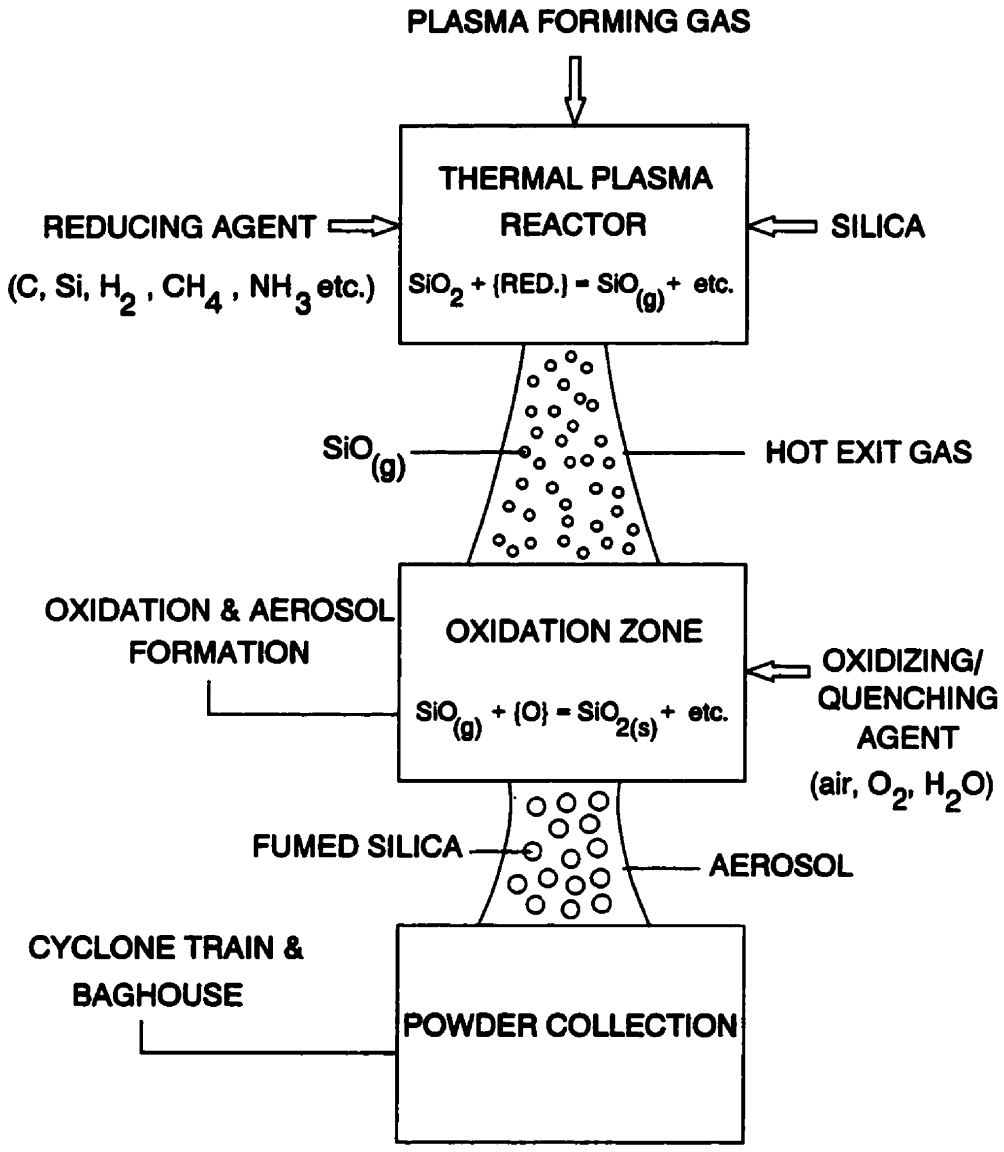

Figure 2.6 Block diagram of the thermal plasma production of fumed silica.

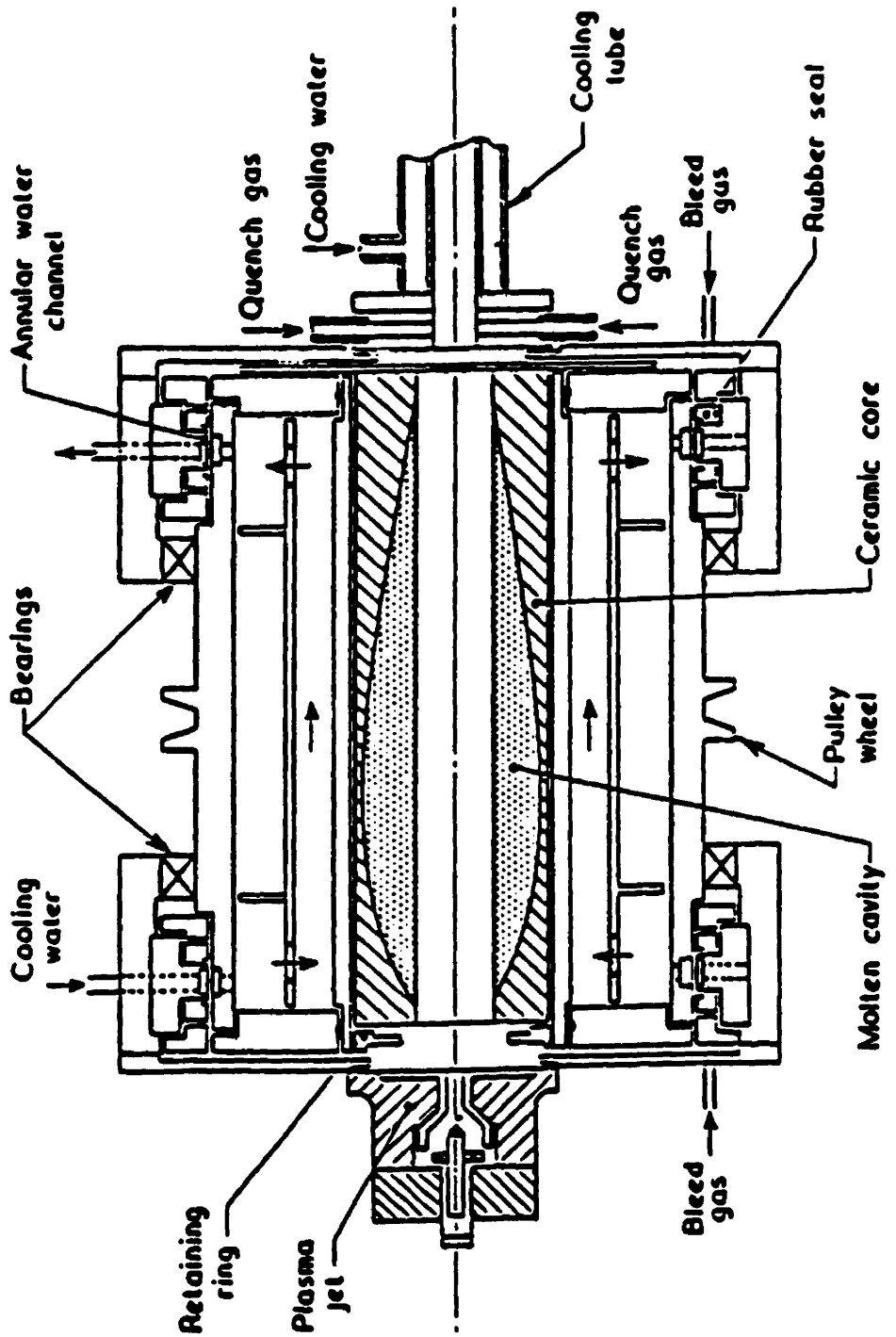

Figure 2.7 Centrifugal liquid-wall furnace used for fumed silica production by Everest et al. (1973).

TABLE 2.2 Silica decomposition experiments conducted by Everest et al. (1973).

Exp.	*Duration [min]*	*Plasma Gas Flow Rate [lpm]*	*Torch Power [kW]*	*Silica Decomposition*	
				Rate [g /min]	*Specific Energy [kWh/kg]*
1	90	Ar = 54 H_2 = 5.8	15.7	0.4	654
2	20	Ar = 40 H_2 = 40	27.3	15.0	30.3
3	22	Ar = 9 H_2 = 60	26.6	14.3	31.0
4	16	Ar = 40 H_2 = 40	27.1	24.1	18.7
5	14	H_2 = 54 N_2 = 70	30.4	25.1	20.2
6	20	Ar = 40 N_2 = 69	30.1	4.6	109.1
7	14	NH_3 = 60	29.9	29.6	16.8

plasma gas was used. A similar result would have been expected using a plasma gas flow rate of 30 lpm N_2 and 90 lpm H_2 since NH_3 injected into the arc is completely decomposed.

Everest et al. (1973) also studied the oxidation zone of this process. This mainly consisted of varying the type of oxidizing agent used (air or O_2). The results showed that rapid quenching favored the production of amorphous and high specific surface area powders (92 - 162 m^2/g). Rheological tests used to measure the thickening and thixotropic ability showed some of the powders produced to be equivalent to a commercial fumed silica product. Powders with low thickening and thixotropic ability were found to be composed of individual spheres whereas the highly effective powders

were composed of chains of particles which were difficult to distinguish individually. This morphology, described as "ribbon-like", was also observed in Aerosil® 200 (a Degussa fumed silica product).

In a later work, Schnell et al. (1978) examined a pilot plant developed at Lonza Ltd. for the production of fumed silica using a 200 kW liquid-stabilized plasma torch (see Figure 2.8). This torch was selected because of its high energy efficiency (90 - 95 %) which was comparable to that of a transferred arc torch (~ 95 %). Its operation consisted of striking an arc between a consumable graphite cathode and a rotating, water-cooled copper anode. A small portion of the liquid (ethanol/water or methanol) evaporated from the vortex surrounding the arc served as the plasma gas. The torch was mounted at the entrance of a rotating reactor where silica sand (20 kg/h) and CH_4 (5 kg/h) were introduced into the plasma tail flame. In this case, both CH_4 and the evaporated liquid served as reducing agents. Methane was chosen because it was cheap and of high purity. The hot gas (> 1500 K) exiting the reactor was quenched with steam to induce fumed silica generation. The aerosol was then sent to an agglomerator whose role was to facilitate powder collection by agglomerating the fumed silica particles to sizes of approximately 1 μm. Powder collection was accomplished using a series of cyclones and a baghouse filter. A summary of the properties of the product produced during this work can be found in Table 2.3 along with those of a commercial fumed silica powder whose identity was not mentioned. In general, the powder properties compared well with the commercial product; however, there were some problems with carbon contamination which was obviously due to the use of CH_4 and a consumable graphite cathode.

Gans and Gauvin (1988) studied the production of fumed silica using the transferred arc system shown in Figure 2.9. Silica sand (99.5 % SiO_2) was introduced tangentially along the falling film reactor sleeve at a rate of 1.3 kg/h using an Ar carrier gas (20 lpm). Plasma generation consisted of striking a 12 cm thermal arc from a thoriated-tungsten tip cathode to a water-cooled graphite anode. The torch operated at 30 kW (300 A and 100 V) and an Ar flow rate of 14 lpm. An appropriate amount of H_2

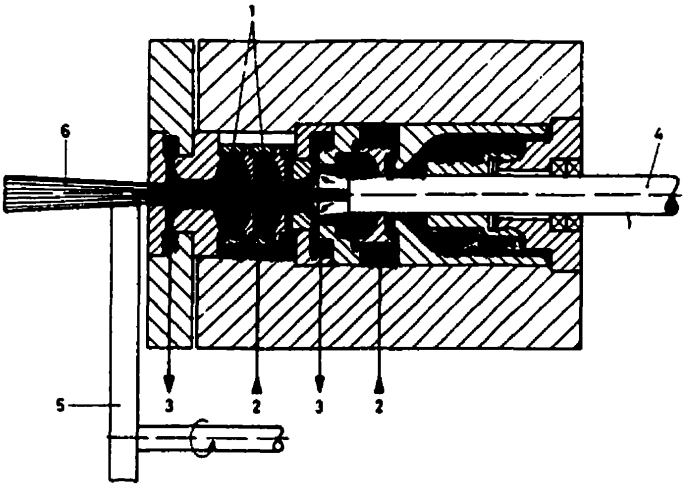

a) Liquid-stabilized plasma torch: 1. liquid vortices, 2. liquid feed, 3. liquid suction, 4. graphite cathode, 5. rotating anode, 6. plasma jet.

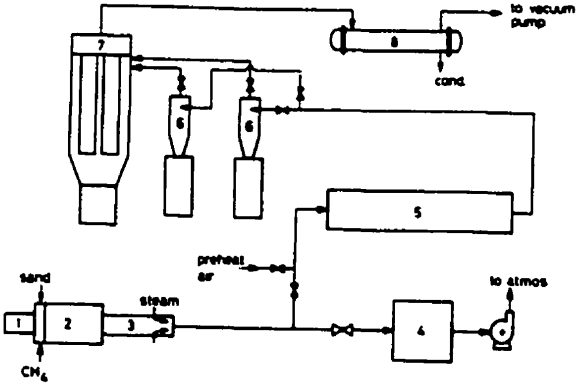

b) Fumed silica pilot plant: 1. torch, 2. rotating reactor, 3. quencher, 4. baffle separator, 5. agglomerator, 6. cyclones, 7. bag filter, 8. steam condenser.

Figure 2.8 Lonza Ltd. fumed silica production process (Schnell et al., 1978).

TABLE 2.3 Comparison of Lonza and commercial fumed silica (Schnell et al., 1978).

Property	*Commercial Fumed Silica*	*Lonza Fumed Silica*
bulk density [kg/m^3]	60	20
surface area [m^2/g]	170	190
SiO content [%]	-	0.1
carbon content [%]	-	0.1
Si-H content [/nm^2]	-	0.09
Si-OH content [/nm^2]	3.5	7.5
viscosity [cp] (3 % dispersion in DOP[1])	156	162
thixotropy effect [-]	distinct	appreciable

1. Dioctyl phthalate.

(5 lpm), steam (28.9 lpm) or NH_3 (7.5 lpm) was added to the carrier gas in order to raise the voltage to 100 V. Oxidation of the $SiO_{(g)}$ was done in the reactor itself by injecting steam or O_2 in a region adjacent to the exhaust labeled "quench zone" in Figure 2.9. The results of this study were somewhat less promising than those of the two previous works. White powders were produced when a steam or O_2 quench was used. When no oxidizing agent was introduced into the reactor, the product had a yellowish-brown color characteristic of $SiO_{(s)}$ (Tombs and Welch, 1952). Powder purity was found to range from 98.54 - 99.36 % SiO_2 with the major impurities being Fe_2O_3, Al_2O_3, CaO and C. The oxide impurities were attributed to the silica feed while the source of C contamination was the anode which had been partially eroded by the arc. The powders had a relatively low specific surface area (79 - 95 m^2/g) which could explain their lack of thickening and thixotropic ability. X-ray diffraction analysis also showed some of the powders to have crystalline impurities. These were thought to be due to inadequate quenching or entrainment of the silica sand feed.

Bakken et al. (1989) reported the production of fumed silica using the PRESS

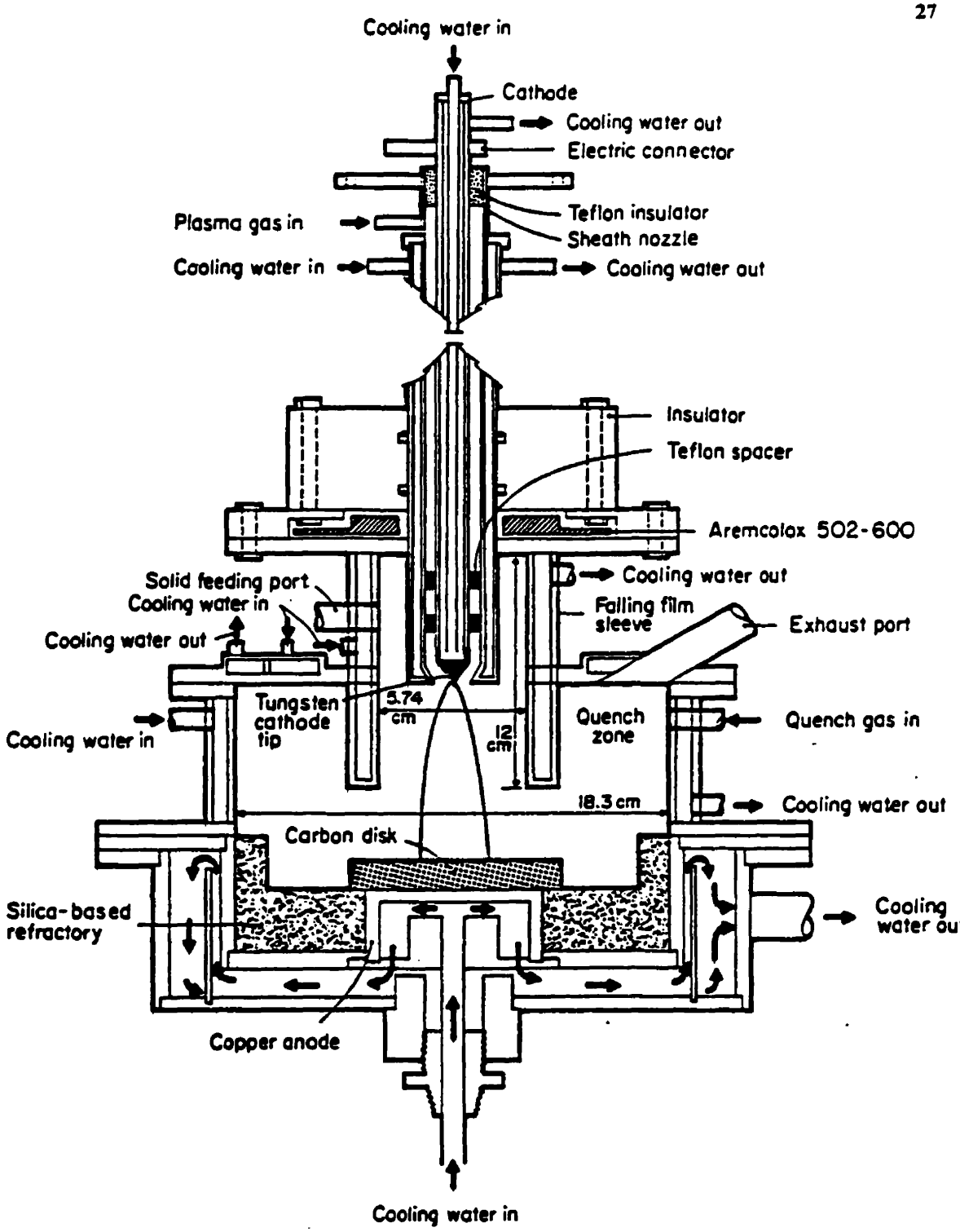

Figure 2.9 Transferred arc reactor used for fumed silica production by Gans and Gauvin (1988).

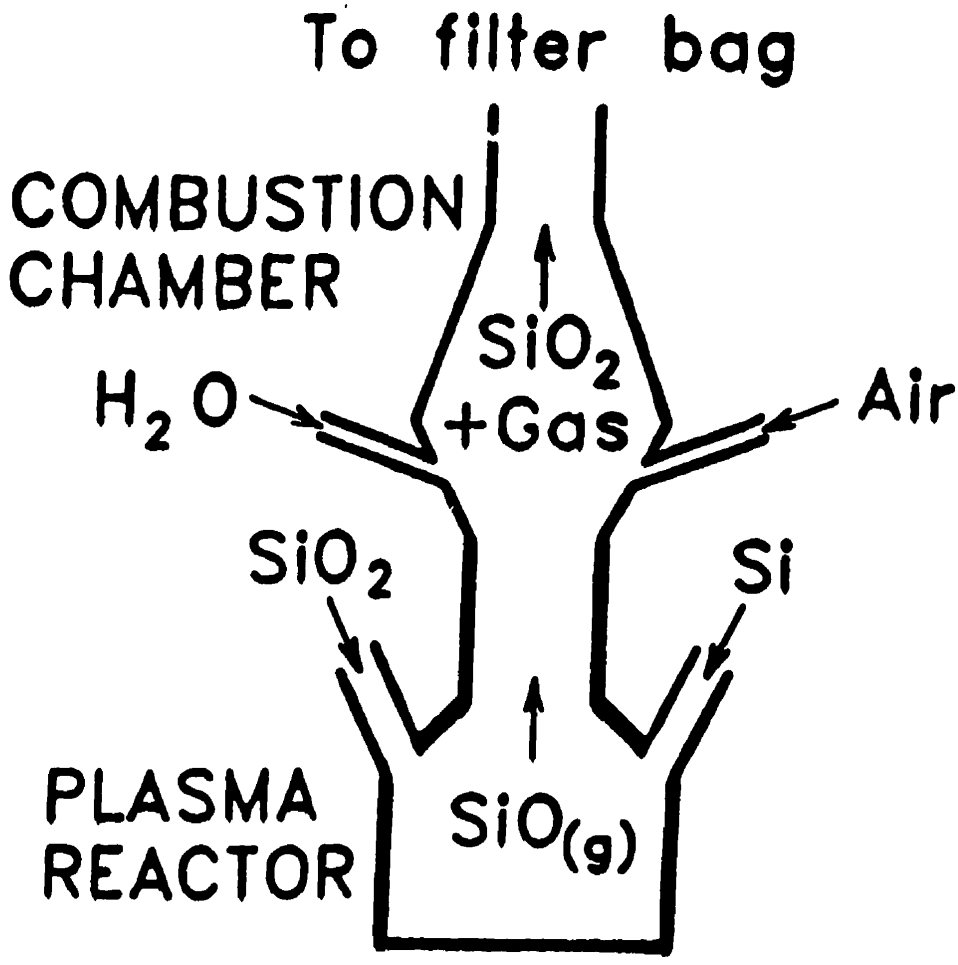

Figure 2.10 Process for fumed silica production using PRESS reactor (Bakken, 1994).

(Plasma Reactor for Smelting at SINTEF) reactor. A schematic diagram of the process is shown in Figure 2.10. The general purpose, graphite-lined reactor could be equipped with up to three plasma torches capable of transferred or non-transferred arc operation. Characterization of the reactor found the thermal efficiency to be 85 - 90 % for transferred arc operation at flow rates of 10 - 25 lpm Ar and only 30 - 50 % in the non-transferred arc mode using flow rates of 10 -100 lpm Ar. Transferred arc operation was therefore preferred. The feed to the reactor consisted of Si (98.9 %) and silica sand (99.8 % SiO_2). Silicon monoxide vapor was formed via reaction 2.4 within the molten SiO_2/Si mixture which served as the anode:

$$SiO_2 + Si \rightarrow 2SiO_{(g)} \qquad (2.4)$$

The oxidation zone for this process consisted of a combustion chamber located at the exit of the reactor where air or an air/steam mixture was injected. Production of a fumed silica powder having a purity of 99.6 % SiO_2 and a specific surface area of 250 m^2/g was reported using this process (Bakken, 1994). TEM (Transmission Electron Microscopy) analysis showed the particles to be spherical. The appearance of the characteristic chain-like aggregates observed by Everest et al. (1973) in high activity fumed silica was not mentioned here and the thickening and thixotropic ability of the powder was not reported.

In a more recent study, Chang (1994) also examined fumed silica production using a transferred arc process. Unlike previous studies, however, the goal of this work was to produce spherical particles with a specific surface area of 20 m^2/g to be used in specialized concrete production. The process used was similar to that of Gans and Gauvin (1988) with silica sand particles (98.5 - 99.0 % SiO_2) vaporized in a transferred arc reactor by injecting them directly into the plasma column. The transferred arc system consisted of a thoriated-tungsten tip cathode and a graphite anode. Both a rod and crucible geometry were used as anodes during this work. The crucible geometry was used to collect silica particles which had not been completely decomposed in the plasma column. The eventual aim of using the crucible was to operate in true transferred arc

mode once a sufficient amount of silica had been collected. However, true transferred arc operation was never reported to be observed throughout the course of this study. In a further attempt to establish an arc to a molten anode, the silica sand feed was added directly to the crucible before the start of an experiment. This attempt also failed to initiate true transferred arc operation as the arc was observed to strike the outside edge of the crucible.

Different plasma forming gases were studied during this work including Ar/H_2, Ar/CO, Ar/CO_2 and Ar/O_2. Operating conditions varied depending on the type of plasma gas, arc length (10 - 18 cm) and silica feed rate used (30 - 60 g/min.). Typically, current and voltage ranged from 300 - 800 A and 70 -160 V respectively. Oxidation of the $SiO_{(g)}$ generated in the plasma chamber was accomplished in a quench tube attached to the exit of the reactor using 100 lpm of air or O_2. When an Ar/O_2 plasma gas was used, partial oxidation of $SiO_{(g)}$ took place directly in the reactor. The powders produced were found to be amorphous with a maximum purity of 98.5 % SiO_2. TEM analysis also showed the majority of the powders to be comprised of spherical particles. Specific surface areas were found to range from 17 - 330 m^2/g.

2.4 Silica Decomposition

2.4.1 Importance of Reducing Agent

The decomposition of silica is a highly endothermic process. The theoretical energy requirement can be reduced significantly by using a reducing agent such as C, Si or H_2. This effect can be seen in Figure 2.11 where the heat of silica decomposition is plotted versus temperature for both inert and reducing conditions. Of the reducing agents listed, H_2 provides the greatest decrease in the heat of decomposition, however, the use of Si allows the production of two moles of $SiO_{(g)}$ for every mole of SiO_2 decomposed. In addition to thermodynamic considerations, the choice of reducing agent may also depend

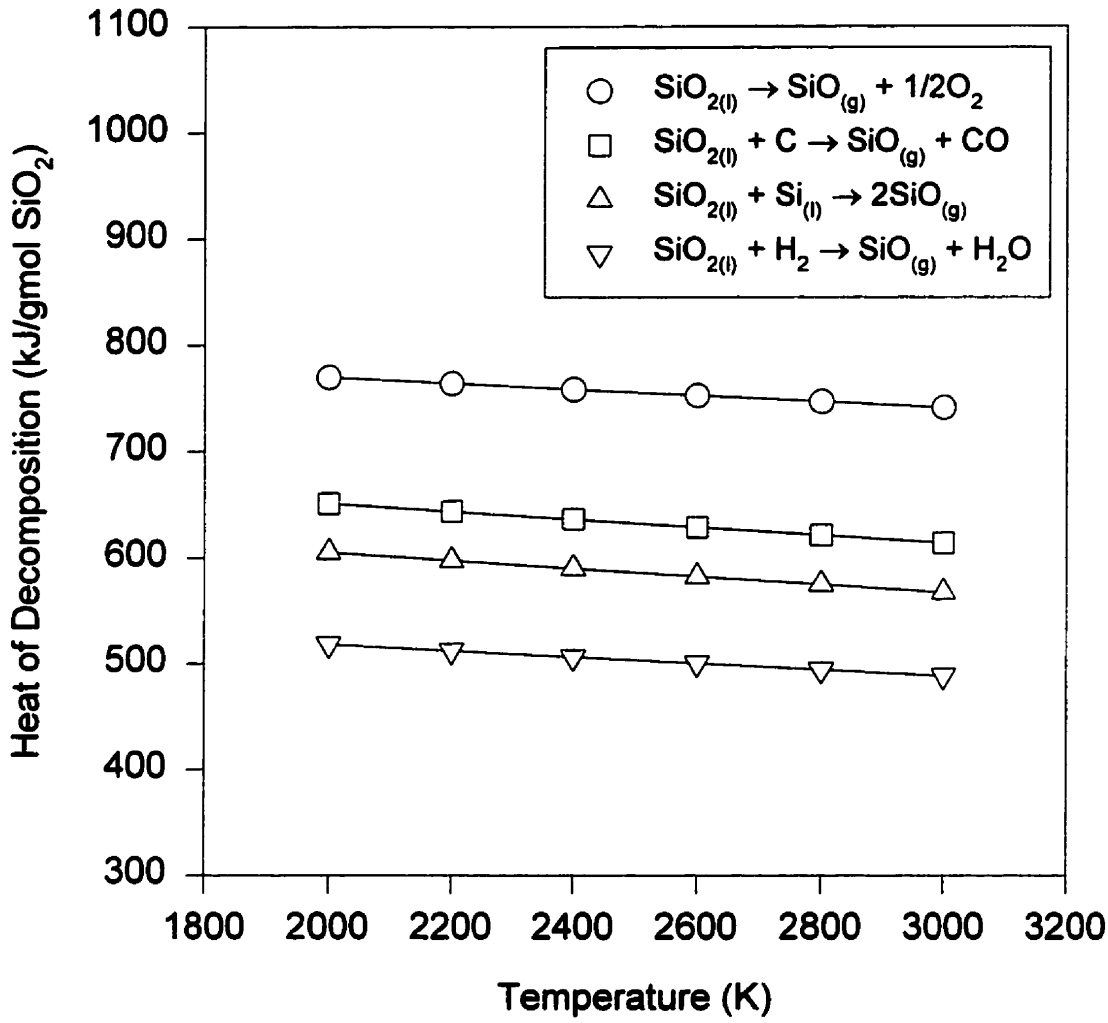

*Figure 2.11 Heat of silica decomposition for inert and reducing conditions (computed using F*A*C*T).*

on cost, purity, availability and ease of use. An ideal reducing agent for the decomposition process being considered for this study is H_2 since it can be added directly to the plasma gas.

2.4.2 Decomposition in an Inert Atmosphere

According to Schick (1960), the equilibrium reached by silica and its decomposition products under inert conditions can be described by the following set of reactions:

$$SiO_2 \leftrightarrow SiO_{(g)} + \tfrac{1}{2}O_2 \quad (2.6)$$

$$O_2 \leftrightarrow 2O \quad (2.7)$$

$$SiO_2 \leftrightarrow SiO_{2(g)} \quad (2.8)$$

$$2SiO_{(g)} \leftrightarrow Si_2O_{2(g)} \quad (2.9)$$

The total vapor pressure of the above system was found to equal 102.5 kPa at approximately 3070 K which was estimated to be the normal boiling point of silica. The partial pressures of the species at the boiling point are listed in Table 2.4. The major species predicted to be present were $SiO_{(g)}$ and O_2. Dissociation of O_2 and production of $SiO_{2(g)}$ was predicted to occur only to a minor extent and the amount of $Si_2O_{2(g)}$ was found to be negligible. Reaction 2.6 was therefore determined to be the predominant reaction describing the equilibrium of silica decomposition under inert conditions. When only reaction 2.6 was considered, a normal boiling point of 3085 K was estimated.

A similar analysis was conducted using the thermodynamic computer package known as F*A*C*T (Thompson et al., 1996). From Table 2.5 we can see that the results predicted by F*A*C*T at atmospheric pressure closely resemble those of Schick (1960). In both cases, $SiO_{(g)}$ and O_2 are predicted to be the major products of silica decomposition. Discrepancies were found with the predicted normal boiling point and the species present at equilibrium. While Schick (1960) predicted the presence of small

TABLE 2.4 Equilibrium gas phase composition at 3070 K for silica decomposition under inert conditions according to Schick (1960).

Species	*Partial Pressure [kPa]*
SiO	62.8
O_2	26.3
O	7.5
SiO_2	5.9
Si_2O_2	0.01
Total	**102.51**

TABLE 2.5 Silica decomposition equilibrium under inert conditions predicted by F*A*C*T.

Pressure	*Boiling Point*	*Gas Phase Composition*	
[kPa]	*[K]*	*Species*	y_i *[-]*
101.3	3151	SiO	0.63477
		O_2	0.26955
		O	0.09568
107	3159	SiO	0.63474
		O_2	0.26949
		O	0.09577
112	3167	SiO	0.63471
		O_2	0.26943
		O	0.09586

quantities of $SiO_{2(g)}$ and $Si_2O_{2(g)}$, these species are absent in the F*A*C*T simulation. The discrepancies are probably due to differences in thermodynamic property estimation.

2.4.3 Reaction With Carbon

Since the silica anode was to be contained in a graphite crucible, silica might be reduced by C. The possible reactions occurring at the silica/anode interface were determined by examining the species present at equilibrium from the reaction of a gmole of SiO_2 and C. Figure 2.12 shows that below 1800 K the reaction between SiO_2 and C is negligible. Above this temperature, the following reactions must be considered:

$$SiO_2 + C \rightarrow SiO_{(g)} + CO \qquad (2.3)$$

$$SiO_2 + 3C \rightarrow SiC + 2CO \qquad (2.10)$$

$$SiO_2 + 2C \rightarrow Si_{(l)} + 2CO \qquad (2.11)$$

Of these, reaction 2.10 would probably result in the least decomposition of silica at the crucible surface due to the formation of a SiC product layer. Reaction 2.11 would generate $Si_{(l)}$ which would likely dissolve within the silica anode and undergo further reaction producing $SiO_{(g)}$ via:

$$SiO_2 + Si \rightarrow 2SiO_{(g)} \qquad (2.4)$$

The net result of this process would be reaction 2.3.

2.5 Use of Silica as an Anode Material

The proposed decomposition technique requires the operation of a transferred arc to a silica anode. For this to be possible, silica must be electrically conductive. This is not the

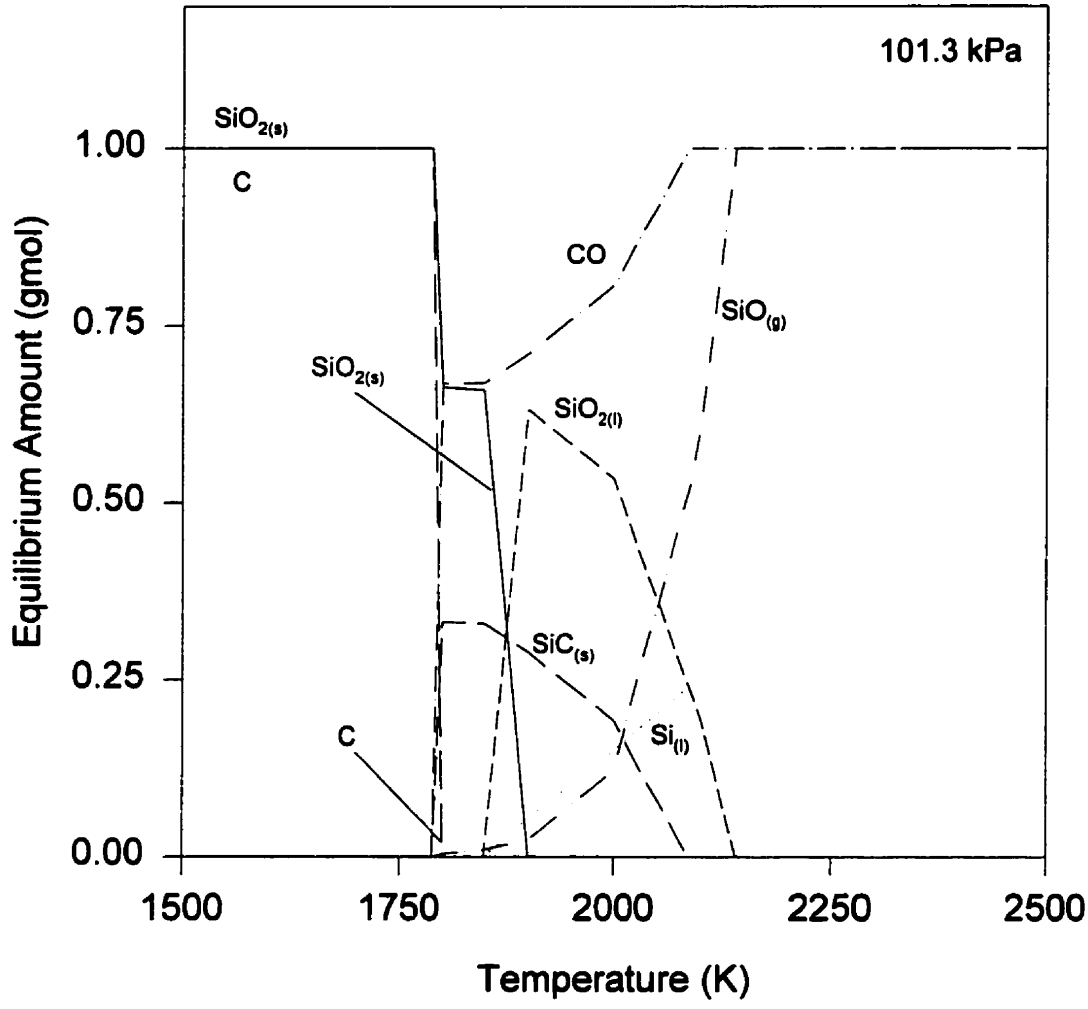

*Figure 2.12 Species generated at equilibrium from the reaction of 1 gmole of SiO_2 and 1 gmole of C (computed using F*A*C*T).*

case at low temperatures where silica is an effective insulator. As with all insulating materials, electrical resistivity is reduced with increasing temperature. Conduction is the result of electronic and ionic contributions both of which increase with increasing temperature. The dominant contribution depends on the material, its purity and temperature (Callister, 1991).

Two studies which provided some insight into the electric conduction behavior of silica were those of Cohen (1957) and Veltri (1963). The results of these works are presented in Figure 2.13. Both studies showed that the electrical resistivity of silica decreases dramatically when heated to high temperatures. Cohen (1957) reported a resistivity of 34 ohm m at 1685 K while Veltri (1963) found a value of 950 ohm m at approximately the same temperature. This is compared to a resistivity of $> 10^{18}$ ohm m at 298 K (Callister, 1991). The lower resistivity measured by Cohen (1957) may have been due to the higher impurity content of the sample analyzed. The silica sample used by Veltri (1963) had the following impurities in ppm: < 1 Fe, < 1 Cu, < 0.1 B, 2 Al. That used by Cohen (1957) had a total impurity content of 0.2 % with the major impurities being Fe_2O_3 and B_2O_3. Donor or acceptor type semiconduction has been associated with impurities in oxides (Hove and Riley, 1965). In both of the above works, electronic conduction was the likely mechanism of charge transport within the silica. Veltri (1963) suggested that electrolysis of the silica may have been the conduction mechanism although this was unlikely because the Si-O bond has significant covalent character and is relatively strong (Callister, 1991).

From the review of the above works, the electrical resistivity of silica was believed to decrease dramatically with increasing temperature and to be enhanced by the presence of impurities. Use of silica as an anode material was therefore thought possible if maintained at a sufficiently high temperature.

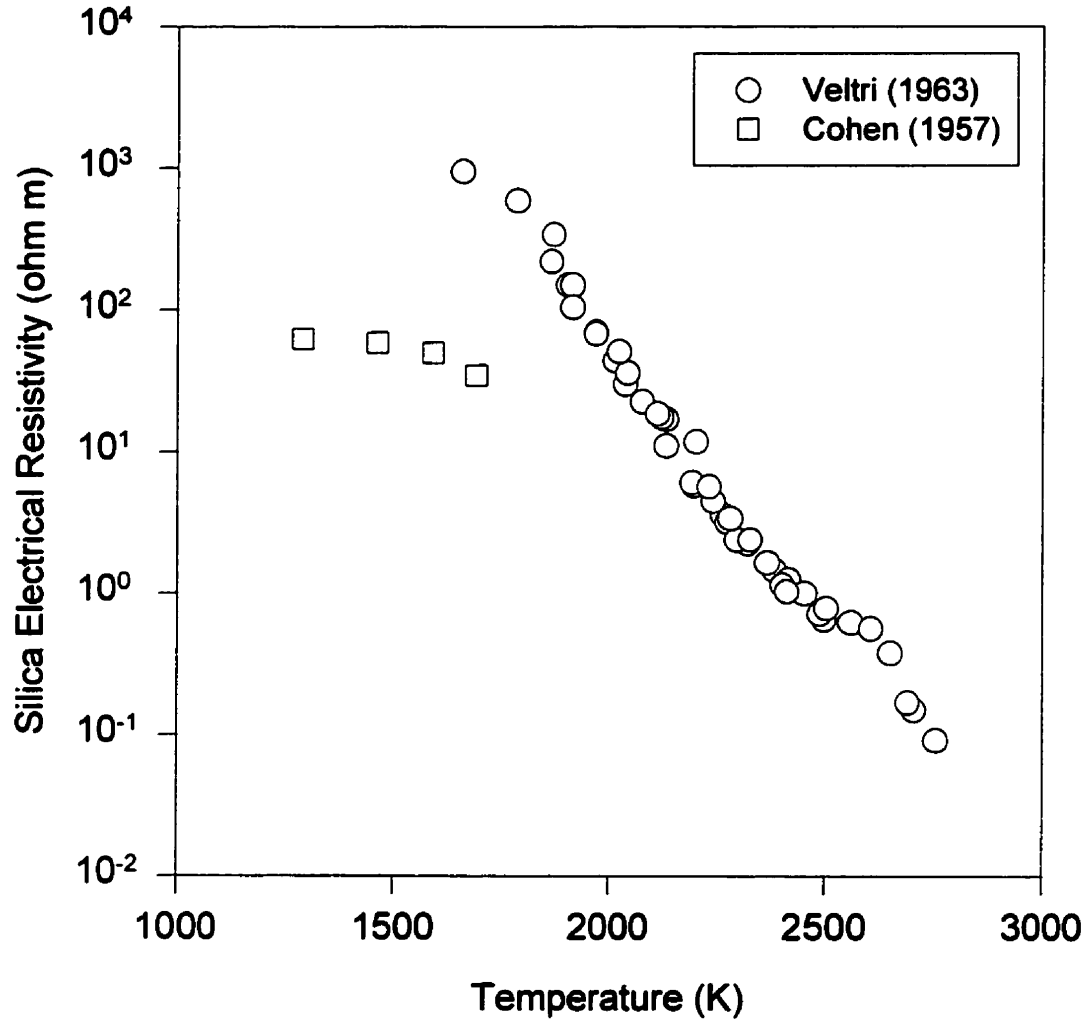

Figure 2.13 Electrical resistivity of silica as a function of temperature according to Cohen (1957) and Veltri (1963).

Chapter 3 - AN EXPERIMENTAL INVESTIGATION OF SILICA DECOMPOSITION USING A TRANSFERRED ARC PROCESS

3.1 Introduction

Silica decomposition is the first and most energy intensive step in the thermal plasma production of fumed silica. The aim of decomposition is the generation of $SiO_{(g)}$ which can then be quenched rapidly to produce fumed silica. Silica decomposition occurs in a thermal plasma reactor using a reducing agent. Some examples of reducing agents commonly used include C, Si and H_2:

$$SiO_2 + C \rightarrow SiO_{(g)} + CO \quad (3.1)$$

$$SiO_2 + Si \rightarrow 2SiO_{(g)} \quad (3.2)$$

$$SiO_2 + H_2 \rightarrow SiO_{(g)} + H_2O \quad (3.3)$$

The energy required for decomposition is supplied to the reactor by a thermal plasma heat source. Because of their high energy efficiency and potential for scale-up, dc arc torches have received the most attention as thermal plasma generators for this process. The energy required by the reactor to process the silica feed is a function of both its heat transfer efficiency and the type of reducing agent used. Silica decomposition using various reducing agents has been studied previously by various authors (Tombs and Welch, 1952, Schick, 1960, and Huczko and Meubus, 1989). Since the thermodynamic effects are well known, the type of reducing agent chosen usually depends on cost, purity, availability and ease of use. An additional method of improving the process economics is to increase the reactor's heat transfer efficiency to the silica raw material.

The efficiency with which energy is transferred to the silica feed depends on the processing method used. Previous systems have relied on convective and radiative heat transfer. For example, the technique used by Everest et al. (1973) and Schnell et al. (1978) consisted of using the plasma flame generated by a dc non-transferred arc torch to heat the silica feed. The heat transfer in these works was mainly convective. Radiative heat transfer was more significant in the studies using transferred arc torches (Gans and Gauvin, 1988, and Chang, 1994). However, since silica was not used as the anode material, these systems failed to utilize important heat transfer mechanisms associated with transferred arcs. These include heat transfer to the anode as a result of arc impingement and resistance heating. Both are important features of the transferred arc process and the main reason why it is preferred when treating condensed phases (MacRae, 1989). In other works where transferred arc configurations have been used, the anode has consisted of a mixture of silica and an electrically conductive reducing agent such as Si or C (Biegler et al., 1963, Illigen and Neugebauer, 1969, Bakken et al., 1989 and Mishra et al., 1995). Although taking advantage of true transferred arc operation, these processes suffered from the use of relatively expensive (Si) and possibly contaminating reducing agents (C).

A novel technique for silica decomposition was examined in this work to overcome these deficiencies. This novel technique consisted of using a transferred arc system in which silica alone served as the anode material. Silica decomposition using this technique would potentially be more energy efficient than previous processes. The maximum energy efficiency for a non-transferred arc torch is typically 80 % while true transferred arc operation can result in efficiencies up to 95 % (MacRae, 1989). The need to mix Si or C with the silica raw material would also be avoided thus further improving process economics since cheaper gaseous reducing agents, such as H_2, could be used instead. These gaseous reducing agents could be added to the reactor separately or as part of the plasma gas.

This chapter summarizes the experimental investigation of silica decomposition using a true transferred arc process. This study was limited to the effect of current and

plasma gas flow rate which were believed to be the most important scale-up variables for the process. The experimental procedure consisted of measuring the net mass of silica decomposed in the transferred arc reactor for a given plasma gas flow rate and current. To obtain appropriate estimates of the decomposition rates, steady-state operation was required. The small size of the reactor and the continuous feeding of quartz particles allowed steady-state to be achieved rapidly. Since the effect of reducing agents on silica decomposition is well known, a pure Ar plasma gas was used to further simplify the experiments. No reducing agent was added to the reactor to limit the decomposition rates to reasonable values. Because of this, intense feeding of quartz particles was not required and steady-state operation was more easily maintained. In order to facilitate transfer of the arc to the silica anode, a small amount (~ 4 g) of NaOH was placed in the crucible along with the quartz before the start of an experiment. The effect of adding H_2 to the plasma gas was also investigated.

3.2 Experimental Apparatus

A schematic of the experimental apparatus is shown in Figure 3.1. The main components are described in the following sections. All equipment was electrically grounded except for the cathode which was operated at an elevated negative potential. Argon and H_2 flow rates are reported in liters per minute (lpm) at 293 K and 101.3 kPa.

3.2.1 Transferred Arc Reactor

The transferred arc reactor, shown in Figure 3.2, consisted of a water-cooled, cylindrical, stainless steel vessel with a side exit and view port. The view port (not seen in Figure 3.2) was located 90° from the exit and was equipped with a 2.9 cm window which allowed a clear view of the arc and its impingement on the silica bath surface. Argon at a flow rate of 3.6 lpm was introduced into the view port to prevent condensation

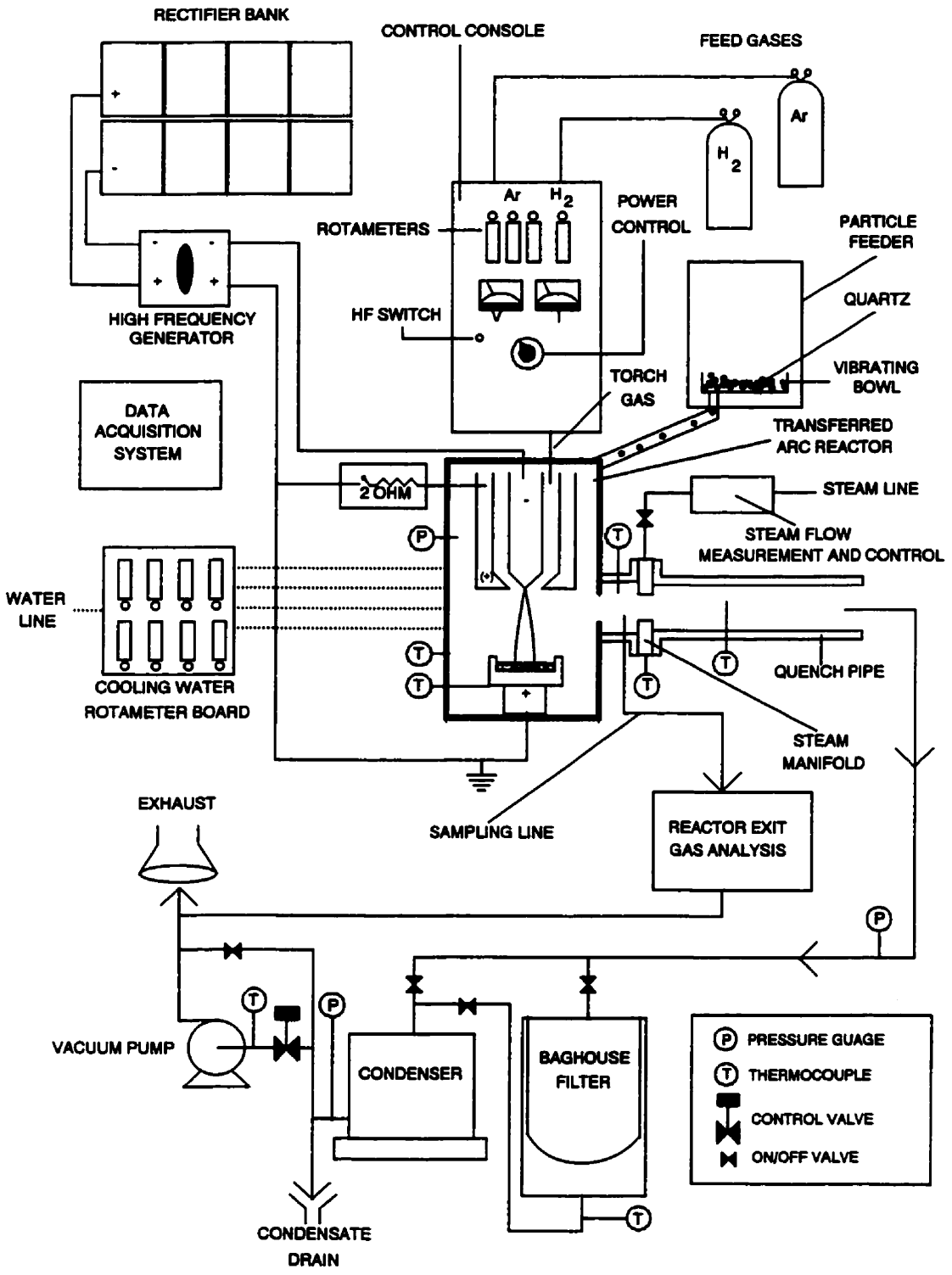

Figure 3.1 Experimental apparatus.

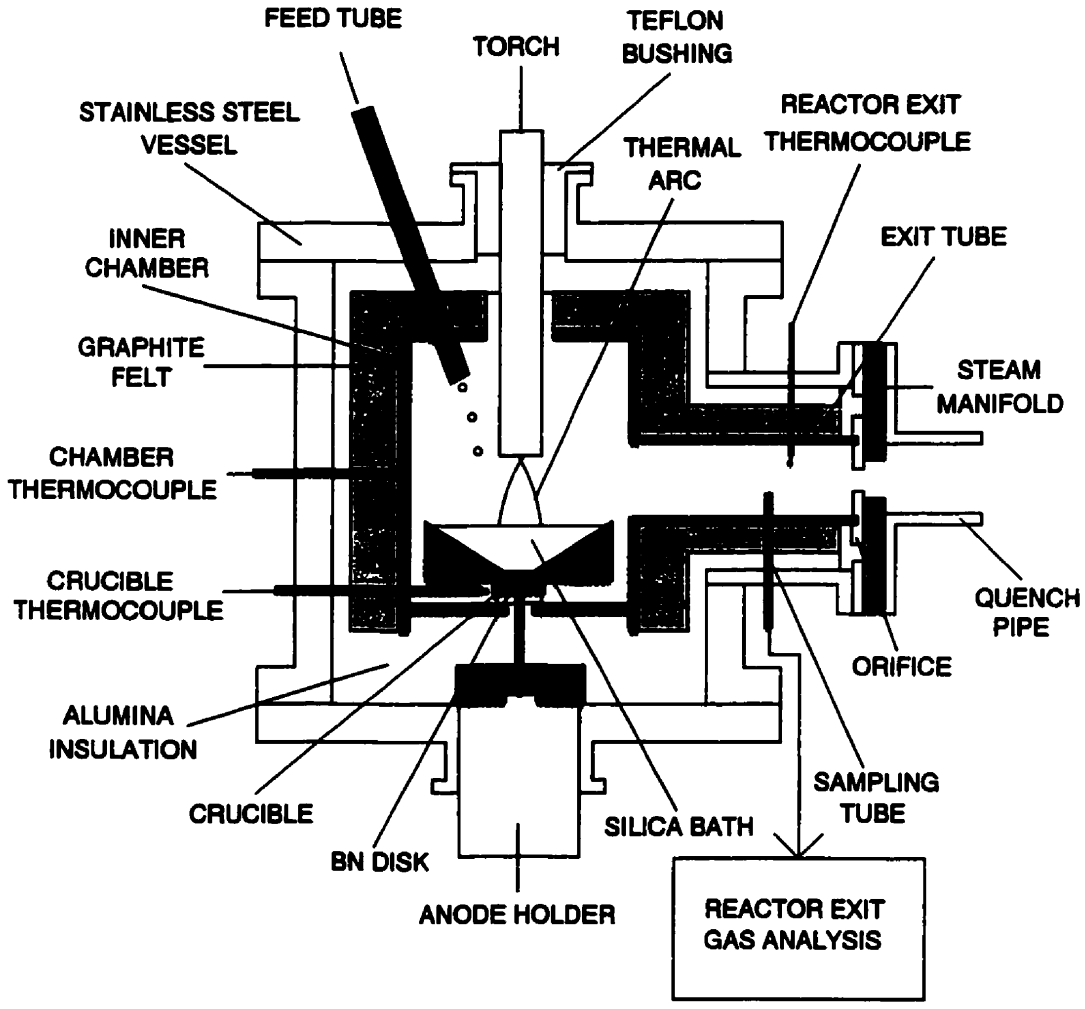

Figure 3.2 Transferred arc reactor.

of the decomposed silica onto the window. Quartz particles were fed into the crucible using an alumina tube (grade Omegatite 450, Omega Canada Inc., Laval, Quebec, Canada) connected to a particle feeder. The feed tube had an inner diameter of 0.95 cm and was inserted through an opening in the roof located opposite to the reactor exit. The stainless steel vessel was heavily insulated with graphite felt (grade GH, Materials International, Acton, Massachusetts, USA) surrounded by alumina insulation (blanket type AB, Zircar Fibrous Ceramics, Florida, New York, USA).

The actual reactor consisted of an inner graphite chamber which had an internal diameter of 12.7 cm (grade 3499, SGL Carbon Group, St. Laurent, Quebec, Canada). The chamber bottom allowed the insertion of the crucible stem and the roof had openings for the torch and feed tube. To prevent arcing to the chamber, it was electrically isolated from the stainless steel vessel by layer of alumina insulation. Contact of the chamber bottom with the crucible was avoided using a boron nitride disk (grade AX05, The Carborundum Co., Boron Nitride Division, Niagara Falls, New York, USA). The water-cooled plasma torch entered the reactor vessel concentrically through a sealed teflon bushing. The torch (see Figure 3.3) consisted of a conical (60°), thoriated-tungsten tip cathode inserted in a copper nozzle which also served as an auxiliary anode during arc ignition. The cathode tip was positioned so that it was flush with the bottom of the nozzle. This torch design was based on one already used successfully by Parisi (1984).

The crucible (see Figure 3.4) used to contain the molten silica anode was located 2 cm below the torch. Connection of the crucible to the anode was done using a stem inserted into a base which sat on a water-cooled holder. The stem consisted of a hollow cylinder 16.2 cm in length (O. D. = 1.3 cm, I. D. = 0.95 cm). The crucible, stem and base were all constructed from graphite (grade 890S for the crucible and base, and grade 580 for the stem, SGL Carbon Group). The walls of the crucible were inclined to allow the molten silica to be directed towards the center where arc attachment was most likely. The diameter of the conical crucible cavity decreased from 10.2 cm at the top edge to 2.5 cm at the bottom. The depth of the cavity was 2.5 cm. A small diameter (0.64 cm) graphite rod was inserted into the center of the crucible to allow initial arc ignition.

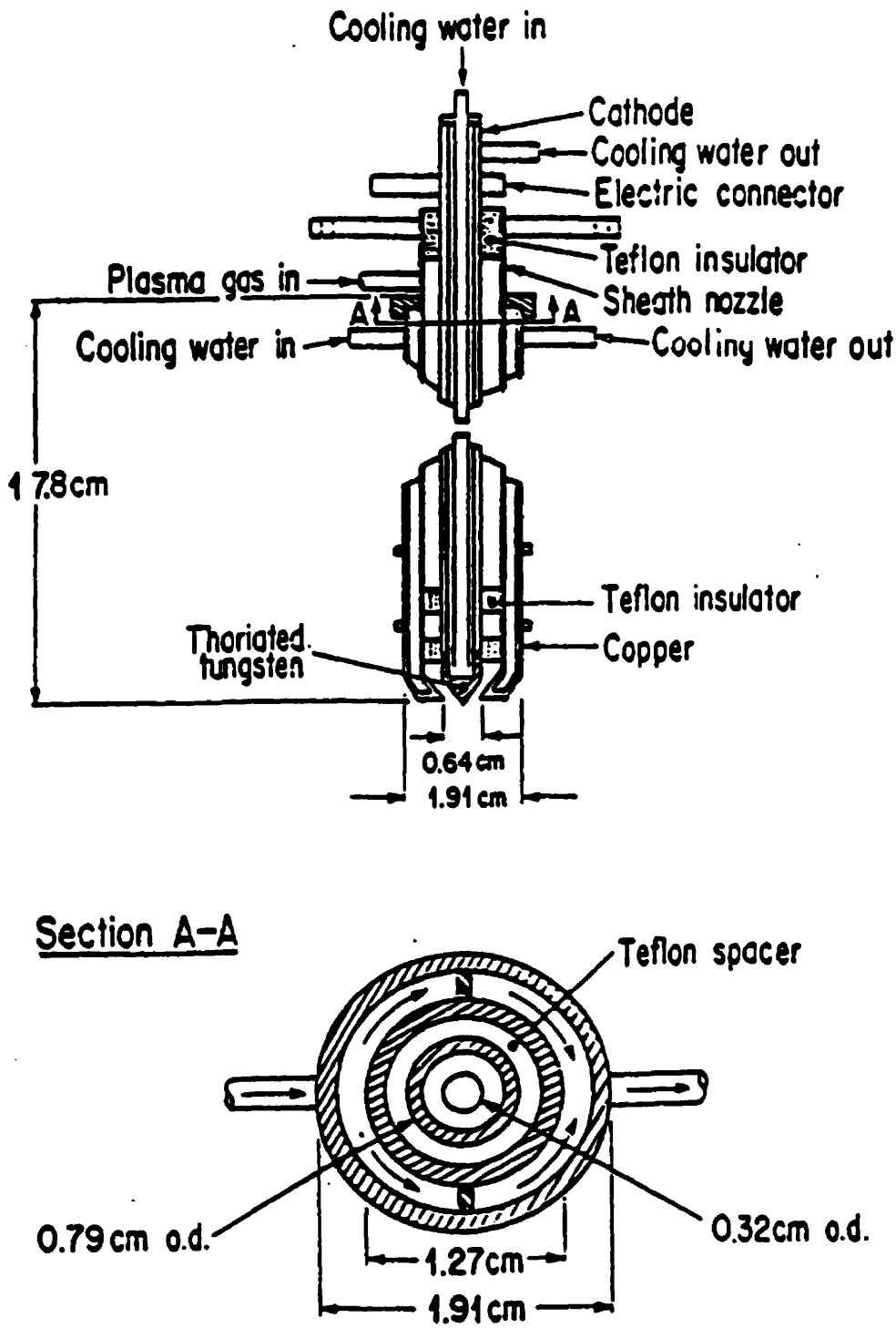

Figure 3.3 Torch assembly (Parisi, 1984).

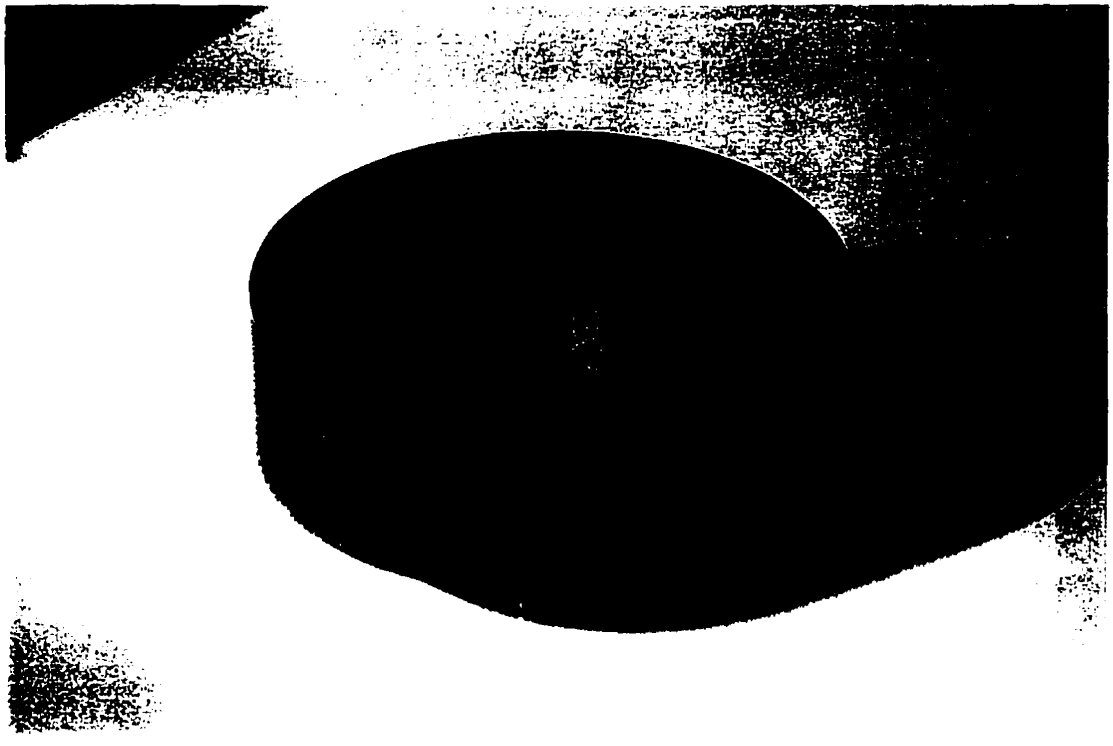

Figure 3.4 Graphite crucible.

When placed in the reactor, the top of the crucible was flush with the bottom of the graphite exit tube (grade 3499, SGL Carbon Group). The exit tube had a length of 11.4 cm and a diameter of 3.5 cm. An alumina tube with an opening of 0.64 cm (grade Omegatite 450, Omega Canada Inc.) was inserted radially into the exit for gas sampling. The end of the sampling tube was positioned close to the center of the exit tube, approximately 3 cm from the boron nitride orifice (grade AX05, The Carborundum Co., Boron Nitride Division). The orifice (1.9 cm) was used to minimize steam backflow from the oxidation zone located at the exit of the reactor. Boron nitride was selected because of its chemical inertness, high electrical resistivity and good thermal shock resistance.

3.2.2 Data Acquisition System

The data acquisition system consisted of a DAS-1401 data acquisition board and an EXP-16 expansion multiplexer amplifier system (Keithley Data Acquisition, Taunton, Massachusetts, USA). The expansion multiplexer was connected to the data acquisition board which was installed in a standard personal computer. The multiplexer allowed 16 differential inputs and was ideal for thermocouple measurements because of a built-in cold conjunction compensation unit. Control of the data acquisition system was done using a computer program written in BASIC. The rate of data acquisition was set at 0.105 1/s (~ 6 samples/min). The system was mainly used to record temperature, voltage, and current. Outputs from the O_2 meter and thermohygrometer were also connected to the acquisition system. The data acquired were saved to an ASCII text file for later processing.

3.2.3 Pressure and Temperature Measurement

Bourdon-tube gauges were used for pressure measurement. Except for the transferred arc reactor, temperature was measured using standard type K thermocouples

having an exposed junction and a stainless steel sheath (Omega Canada Inc.). The transferred arc reactor was equipped with three type C (tungsten/rhenium) thermocouples (Omega Canada Inc.). The thermocouple assembly consisted of isolated bare thermocouple wires in alumina insulators. Two configurations were used. For the crucible and chamber wall, the thermocouple wires were first inserted into a small diameter (0.16 cm) double-holed insulator and then placed in larger (0.64 cm diameter) single-holed insulator. The thermocouple junction for the above configuration was slightly retracted from the end of the large insulator which was placed in contact with the desired measurement point. This technique avoided direct contact of the junction which would lead to reaction with the graphite surface. The position of the crucible and chamber wall thermocouples can be seen in Figure 3.2. The crucible temperature was measured approximately 0.64 cm below the bottom center of the silica anode. The temperature of the chamber wall was measured 2 cm above the top of the crucible. Only the smaller double-holed alumina insulator was used for the reactor exit gas thermocouple to minimize perturbation of the exit flow. This thermocouple was placed in the center of the exit tube approximately 2.5 cm away from the orifice.

An estimate of the difference between the actual temperature and that predicted by the crucible, chamber wall and reactor exit thermocouples is shown in Table 3.1 (see Appendix 1 for details). The results show that the thermocouples became more accurate as the temperature being measured increased. Due to electrical noise problems, the outputs of these thermocouples could not be recorded using the data acquisition system during arc operation. Their outputs were instead recorded with multimeters and re-connected to the data acquisition system prior to shutdown.

3.2.4 Power Supplies, High Frequency Generator and Control Console

Power to the transferred arc torch was supplied by eight Miller SRH-444 rectifiers (Miller Electric Mfg. Co., Appleton, Wisconsin, USA) connected in series. Each rectifier had an open circuit voltage of 75 V and a power rating of 19.6 kW. The input voltage was

TABLE 3.1 Estimate of difference between actual and thermocouple temperature for the crucible, chamber wall and reactor exit gas.

Actual Temperature [K]	*Crucible and Chamber Wall Thermocouple Temperature [K]*	*Reactor Exit Gas Thermocouple Temperature [K]*
1000	924	992
1500	1481	1495
1750	1741	1746
2000	1993	1997

3-phase, 575 V at 60 Hz and the total open circuit voltage was 600 V (8 × 75 V). The output rectifier cables were connected to the cathode and anode via a high frequency generator (HF 2000 High Frequency Arc Starter, Miller Electric Mfg. Co.) used for arc ignition. Power from the rectifier bank was regulated using a remote controller mounted on a control console. The console was also equipped with Ar and H_2 gas rotameters, a switch to activate the high frequency generator and an analog ammeter and voltmeter.

3.2.5 Voltage and Current Measurement

Voltage was measured using a divider circuit. The divider was connected across the cathode and anode at the output of the high frequency generator. Current was measured using a shunt which was placed in series with the anode. The outputs of both devices were connected to the data acquisition system. Because electrical noise from the arc sometimes caused problems with the voltage acquisition, a multimeter connected in parallel with the divider was also used to acquire voltage data.

3.2.6 Feed Gases

The gases used in this study were high purity Ar (Matheson Gas Products, Calgary, Alberta, Canada) and H_2 (Air Products Canada Ltd., Brampton, Ontario, Canada). Both gases were supplied from regulated high pressure cylinders. The gas flows were measured and regulated using standard calibrated rotameters operating at room temperature and 308 kPa.

3.2.7 Quartz Raw Material and Particle Feeder

The silica raw material for this work consisted of quartz particles (99.94 % SiO_2) supplied by Baskatong Quartz Inc. (Montreal, Quebec, Canada). The particles were irregular in shape and had a nominal size of 1 - 3 mm. The particles were fed with a TAFA vibrating bowl powder feeder (model 104B, TAFA Metallisation Inc., New Hampshire, USA). The exit of the particle feeder was connected to an alumina feed tube inserted through the top of the reactor. Argon was introduced into the particle feeder at a rate of 4.1 lpm to cool the feed tube which helped prevent blocking due to partial melting of the quartz particles.

3.2.8 Steam Flow Measurement and Control

The steam flow measurement and control system is shown in Figure 3.5. To avoid condensation, the entire system was heavily insulated. Steam was available at a pressure of 928 kPa from an existing line in the laboratory. Measurement of the steam mass flow rate was accomplished by calibrating a needle valve at a constant opening. The flow rate was varied by varying the inlet valve pressure using a regulator. The exit of the valve was connected to the steam manifold.

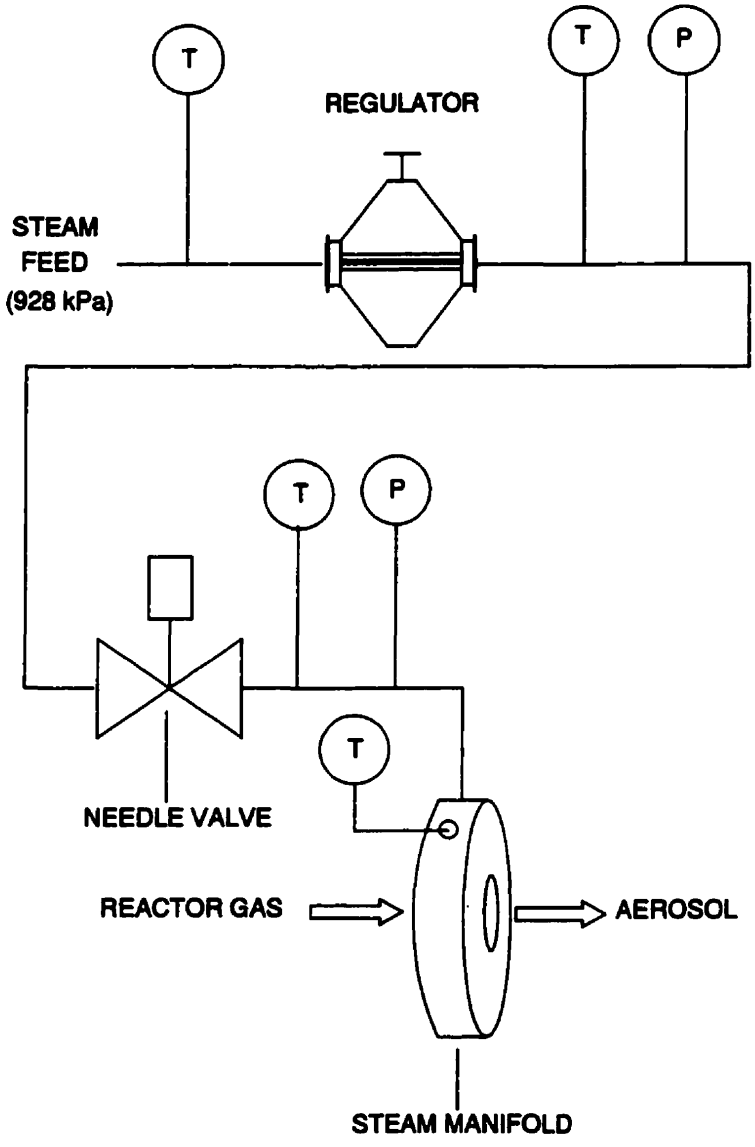

Figure 3.5 Steam flow measurement and control system.

3.2.9 Steam Manifold and Quench Pipe

The steam manifold (see Figure 3.6) was attached directly to the reactor exit. Radial steam injection into the hot reactor exit gas occurred via 18 equally spaced orifices (0.079 cm), angled 20° downstream to minimize backflow. A double-walled, stainless-steel quench pipe with an internal diameter of 3.5 cm connected the transferred arc reactor to the baghouse filter. The quench pipe was either water-cooled or insulated depending on the type of experiment (decomposition or powder production) being conducted.

3.2.10 Reactor Exit Gas Analysis

Analysis of the reactor exit gas consisted of determining the concentrations of H_2O, O_2 and CO. The system, shown in Figure 3.7, was composed of a thermohygrometer (Cole-Parmer, Illinois, USA), an O_2 meter (model GC 502, G. C. Industries, Fremont, California, USA) and a CO meter (model MEXA-201GE, Horiba Instruments Inc., Irvine, California, USA). The range of the thermohygrometer was 0 - 100 % RH with an error of ± 2 % of the reading. Calibration was done using standards of 33 and 75 % RH purchased from the supplier. The O_2 meter had a range of 0 - 25 % and an error of ± 0.5 %. Calibration was done using a 2 % O_2 in Ar mixture (Air Products Ltd.). The CO meter had a range of 0 - 10 % CO and an error of ± 0.04 % for concentrations < 2 %. Calibration of the CO meter was done using a 1.89 % CO gas mixture (Horiba Calibration Gas, Horiba Instruments Inc.).

A vacuum pump located in the CO meter provided the required suction for sampling. A control valve allowed adjustment of the sampling flow rate to approximately 120 ml/min. The volume of the sampling line was approximately 400 ml. The pressure in the line was slightly below that of the reactor up to the control valve inlet and approximately 85 kPa at the entrance of the CO meter. The analysis system was vacuum

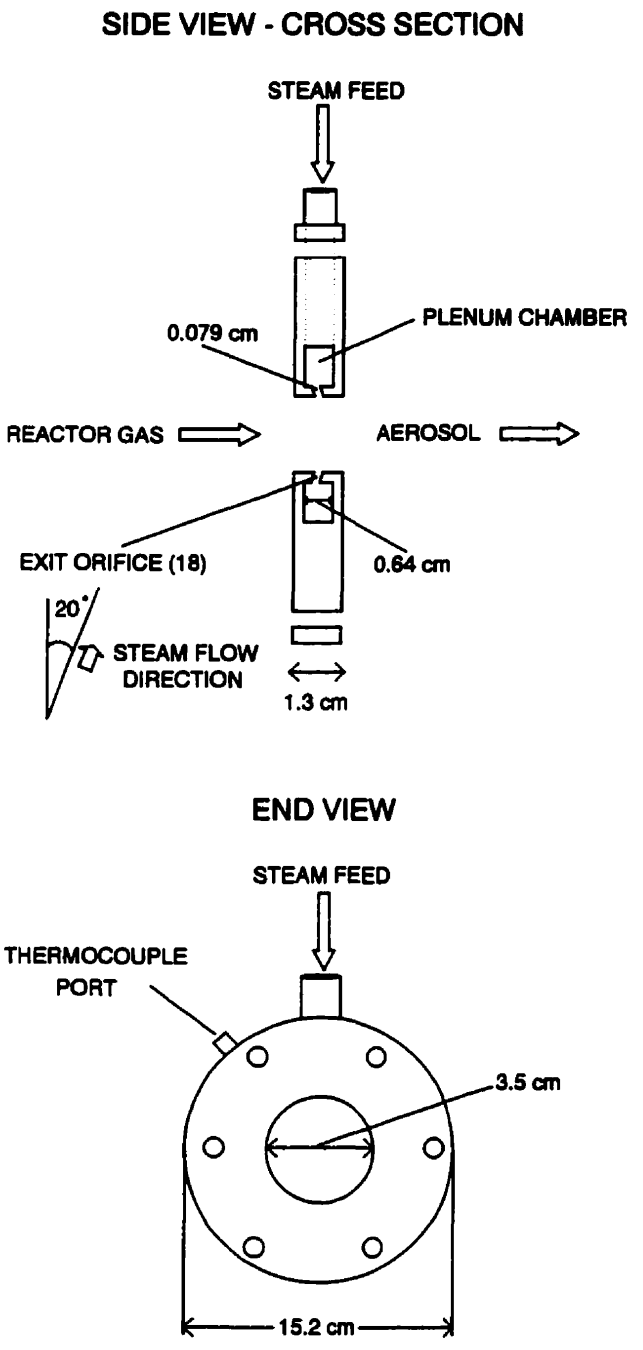

Figure 3.6 Steam manifold.

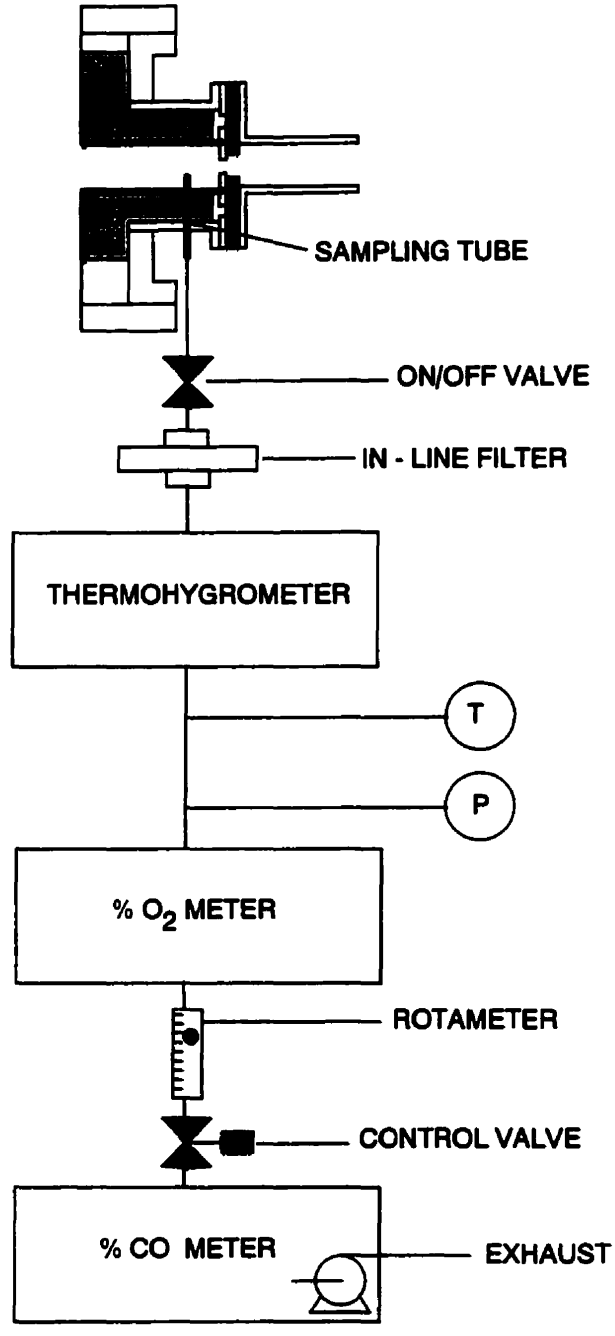

Figure 3.7 Reactor exit gas analysis system.

tested (66 kPa) prior to each experiment to ensure that air leaks were not present. An in-line filter was used after the on/off valve to remove any powders generated through the cooling of the gas being sampled. The thermohygrometer and O_2 meter outputs were connected to the data acquisition system. The output of the CO meter was recorded manually.

3.2.11 Baghouse Filter and Vacuum Pump

The baghouse filter used during this study can be seen in Figure 3.8. Powder was collected in a Nomex® filter bag (P & S Filtration, Point Claire, Quebec, Canada). The baghouse was wrapped with heating tapes and heavily insulated to prevent steam condensation during powder collection. The exhaust gas was evacuated using a diaphragm vacuum pump (Gast, Benton Harbour, Michigan, USA). A control valve at the pump entrance was used to regulate the reactor pressure.

3.3 Experimental Procedure

3.3.1 Pre-Experimental Preparation

1. The inside of the reactor was cleaned with a vacuum cleaner to remove any debris left from the previous experiment. Damaged insulation and other internals were replaced. The torch was cleaned and inspected. Electrical isolation of the cathode and nozzle was verified. The remainder of the apparatus components were cleaned and assembled.

2. The crucible was weighed and its mass recorded. A new crucible was used for each experiment.

3. The crucible was charged with approximately 4 g of NaOH pellets (lab grade,

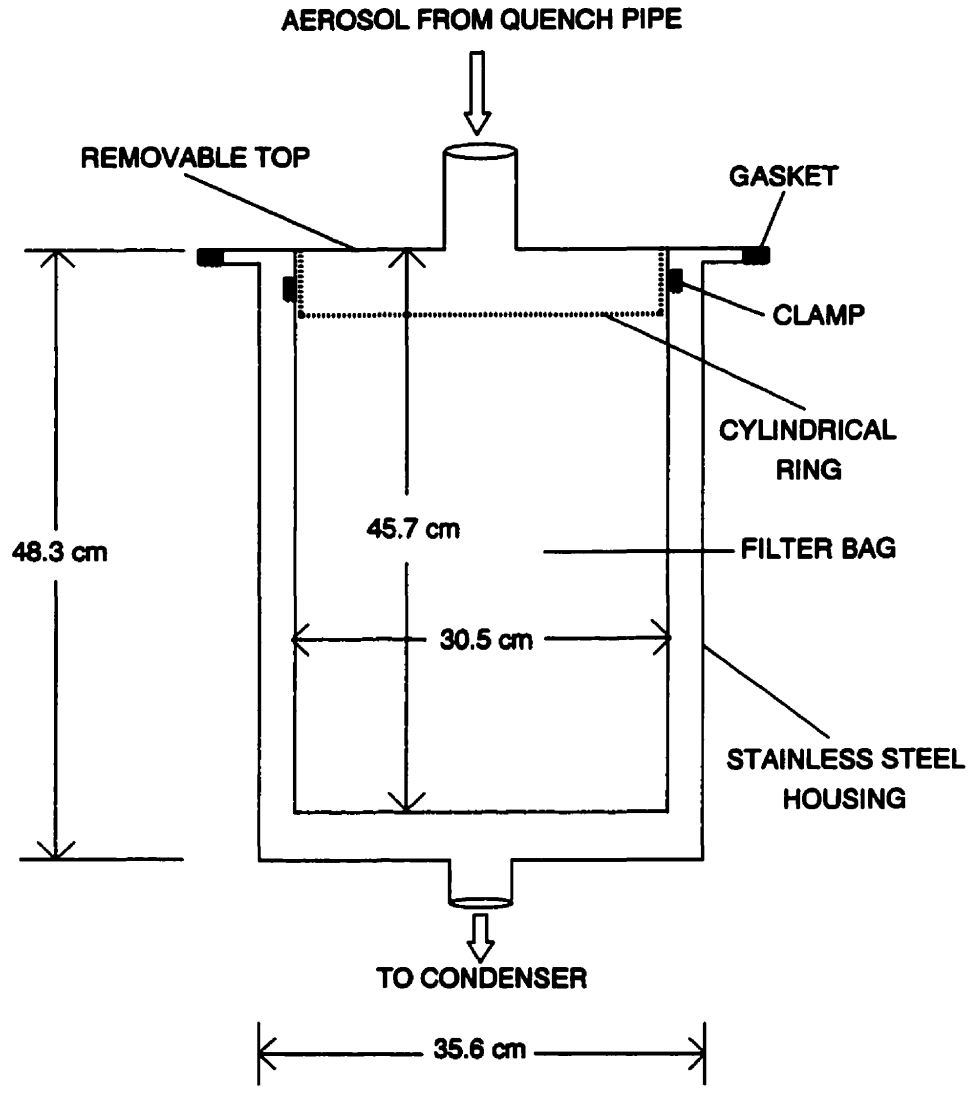

Figure 3.8 Baghouse filter used for powder collection.

Anachemia Canada Inc., Ville St. Pierre, Quebec, Canada) and 140 g of quartz feed particles. The NaOH pellets were placed in the center of the crucible surrounding the graphite rod. The quartz particles covered the NaOH and filled the remainder of the crucible. The top of the rod was exposed to allow arc ignition. The charged crucible was placed into the reactor. Electrical isolation of the crucible and chamber was verified.

4. A known mass of quartz was placed into the particle feeder.

5. The reactor was sealed and the torch was lowered to within 2 cm of the top of the crucible. The entire apparatus was purged at 66 kPa with 5 lpm Ar for 1 hour.

3.3.2 Arc Ignition

1. Gas, water and electrical connections were inspected. Argon and cooling water flows were started and operation of the exhaust vent was verified. The plasma gas flow rate used during ignition was 15 lpm.

2. All secondary electrical appliances were disconnected. The rectifier bank and high frequency generator were turned on. A relay switch connecting the torch nozzle to the anode through a 2 ohm resistor was closed (see Figure 3.1). The high frequency generator was activated. The spark created resulted in the generation of an arc between the cathode and nozzle which then transferred to the graphite rod in the center of the crucible. Once this occurred, the nozzle relay was opened.

3.3.3 Execution of an Experiment

1. The plasma gas flow rate and current were adjusted to their desired levels. Cooling of the reactor exit gas was accomplished by water-cooling the quench pipe. Steam was not

used during the decomposition experiments.

2. Data acquisition was begun. The time delay from arc ignition to the start of data acquisition was approximately 1 minute.

3. Particle feeding was started.

4. Once steady-state was achieved (15 - 30 min), gas sampling from the reactor exit was begun.

5. Just prior to terminating an experiment, particle feeding and gas sampling were stopped and the outputs of the reactor thermocouples were re-connected to the data acquisition system.

6. An experiment was terminated by shutting down the rectifier bank. Argon and cooling water flows were continued until the apparatus had cooled.

3.3.4 Post Experimental Procedure

1. A silica mass balance was performed by weighing the following items:

   a) The silica left in the crucible.
   b) The quartz left in the particle feeder.
   c) The quartz fed during the experiment which landed on the chamber floor.
   d) The condensation on the chamber walls, orifice, exit tube, torch nozzle and crucible.

2. The crucible was weighed to determine its mass loss during the experiment.

3.4 Results and Discussion

3.4.1 Silica Decomposition Using an Argon Plasma Gas

3.4.1.1 Summary of Experiments

The experiments performed during this study are summarized in Table 3.2. A three level factorial design was used to investigate the effect of plasma gas flow rate and current and a minimum of one replicate was performed at each condition. Argon served as the plasma gas and was also introduced into the reactor at a rate of 4.1 lpm through the feed tube and 3.6 lpm through the view port. The plasma gas flow rates and currents investigated were 10, 15 and 20 lpm, and 150, 200 and 250 A respectively. Using the remote power controller of the rectifier bank, current could be consistently regulated to within ± 5 A of the desired value. The arc length, defined as the distance from the cathode tip to the top of the crucible, was 2 cm for all experiments. The mass of silica required to maintain the anode surface approximately flush with the top of the crucible was 140 g. Reactor pressure was maintained between 101.3 - 112 kPa throughout the experiment. The duration of experiments varied between 1 - 3 hours depending on the current level being studied.

3.4.1.2 Use of NaOH to Initiate Arc Transfer to a Silica Anode

Attempts to transfer the arc to a silica anode failed when only quartz feed particles were added to the crucible initially. After igniting the arc to the graphite rod, a liquid silica anode failed to develop even after prolonged operation. Examination of the crucible after shutdown revealed that the arc had consumed the graphite rod and was impinging on the bottom of the crucible. The particles surrounding the rod had been decomposed but very little of the remaining quartz had melted. This difficulty was caused by the high

TABLE 3.2 Summary of decomposition experiments using an Ar plasma gas.

Experiment	*Plasma Gas Flow Rate [lpm]*	*Current [A]*	*Duration [min]*
54	10	150	180
60	10	150	180
119	10	150	180
50	15	150	180
59	15	150	180
120	15	150	190
52	20	150	180
61	20	150	190
87	10	200	130
89	10	200	120
90	10	200	120
81	15	200	120
88	15	200	120
85	20	200	120
86	20	200	120
76	10	250	65
78	10	250	60
82	15	250	60
84	15	250	60
77	20	250	60
83	20	250	60
91	20	250	60

electrical resistivity of silica at low temperature. For silica to be electrically conductive, it must be heated to a sufficiently high temperature (see section 2.5). The only way this could be done in the present reactor was using the transferred arc since the heat input to the silica would greatly increase once it was established as the anode. To accomplish this, it was decided to temporarily decrease the electrical resistivity of the silica anode by adding a conductive, volatile impurity. A good candidate was Na because of its relatively low boiling point (1153 K at 101.3 kPa) and the high mobility of Na^+. The source of Na selected for this work was NaOH because it was safe to handle and easily available. The amount of NaOH and quartz initially added to the crucible is shown in Table 3.3.

Using NaOH, arc transfer to a silica anode was easily achieved. The probable arc transfer mechanism is shown schematically in Figure 3.9. Once the arc had been ignited, energy from the plasma gas melted the NaOH pellets. This probably occurred within a few seconds after start-up because of the low melting point of NaOH (591 K). Given the close proximity of the arc, the surrounding quartz particles would also have melted during this period and reacted with the liquid NaOH. The result was the formation of a Na^+ rich silicate liquid on the bottom of the crucible. To verify this, the initial heat-up step was simulated using the F*A*C*T thermodynamic package (Thompson et al., 1996) to determine the equilibrium products generated from the reaction of the initial contents of the crucible (140 g SiO_2, 4 g NaOH and 1.28 g C). The results are shown in Table 3.4. The mass of C assumed was proportional to the exposed length of the graphite rod (2.5 cm). This simulation was only an estimate of the actual heat-up process since it did not consider the removal of gaseous products. From Table 3.4 we can see that even at a relatively low temperature (1200 K), the formation of a liquid solution composed of SiO_2, $(Na_2O)(SiO_2)_2$ and $(Na_2O)(SiO_2)$ is predicted. This was an additional benefit of NaOH addition since it allowed the rapid formation of a liquid which would flow to the center of the crucible. As this occurred, the graphite rod was being eroded by the impinging arc and consumed through reaction with the surrounding liquid mainly resulting in the formation of CO. When the graphite rod had been eroded sufficiently, the liquid flowed

TABLE 3.3 Initial mass of NaOH and quartz added to crucible.

Experiment	*NaOH Pellets [g]*	*Quartz Feed Particles [g]*	*Initial SiO_2 Content [mass %]*
54	4.02	140.38	97.16
60	4.08	141.66	97.14
119	3.76	140.89	97.34
50	3.75	143.56	97.40
59	3.94	142.83	97.26
120	3.72	140.54	97.36
52	4.00	140.16	97.17
61	3.90	139.55	97.22
87	3.94	140.53	97.21
89	3.91	140.63	97.24
90	3.98	140.19	97.18
81	3.98	141.45	97.20
88	3.97	140.85	97.20
85	3.98	140.32	97.18
86	3.96	140.26	97.20
76	3.96	140.29	97.20
78	3.97	140.62	97.20
82	4.00	140.20	97.17
84	3.99	140.20	97.17
77	3.96	140.24	97.20
83	3.92	140.11	97.22
91	3.93	140.36	97.22

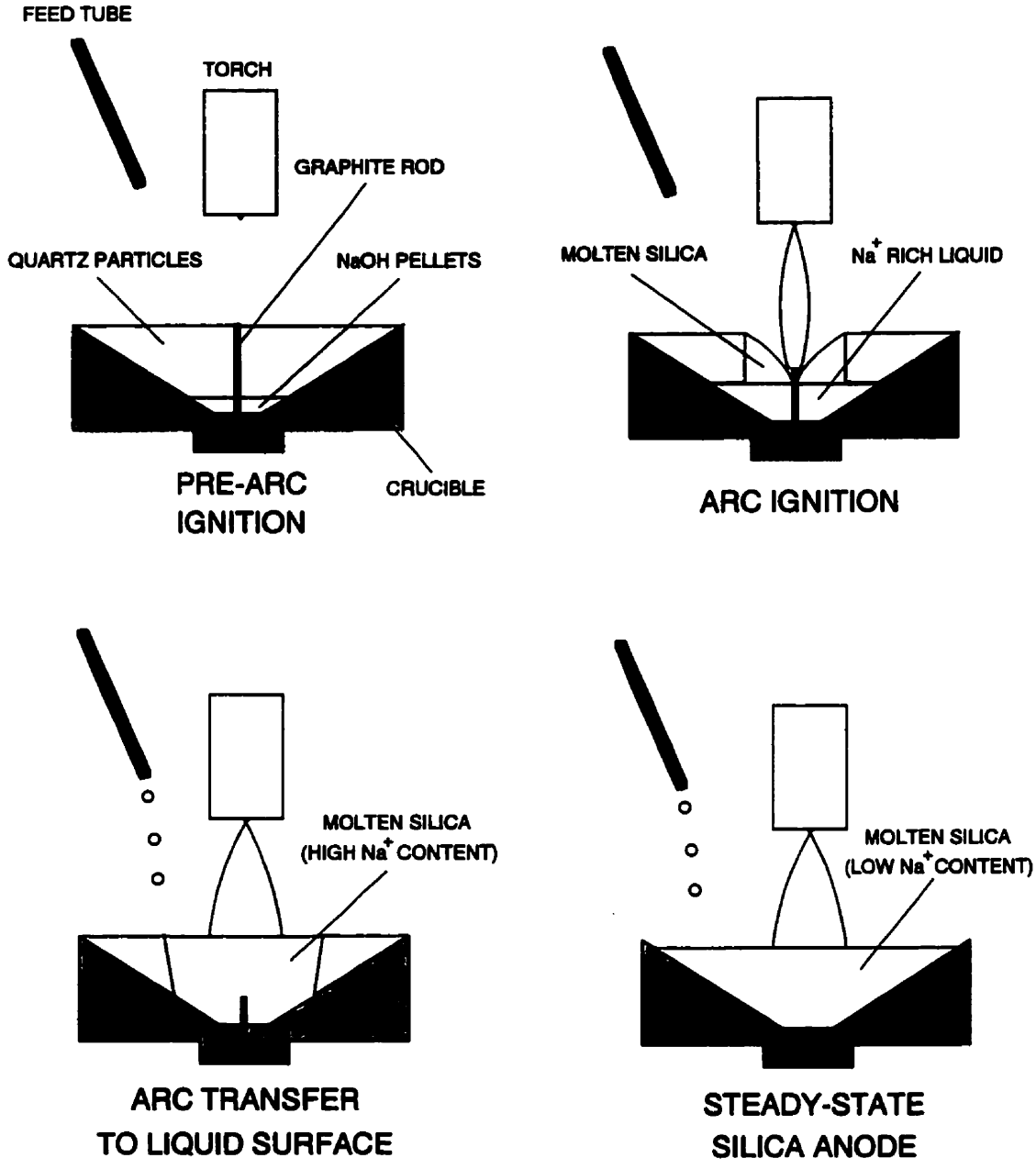

Figure 3.9 Probable arc transfer mechanism to a silica anode.

TABLE 3.4 Equilibrium amounts generated from the reaction of 2.33 gmole (140 g) SiO_2, 0.1 gmole (4 g) NaOH and 0.1067 gmole (1.28 g) C at 101.3 kPa.

Component	*Equilibrium Amounts [gmol]*					
	1200 K	*1400 K*	*1600 K*	*1800 K*	*2000 K*	*2200 K*
Pure Solids						
SiO_2	2.1278	2.0560	1.9101	1.0294	---	---
C	0.05742	0.05673	0.05673	---	---	---
Liquid Solution						
SiO_2	0.10561	0.17785	0.32410	1.1791	1.1791	2.2042
Si	---[1]	---	1.2×10^{-4}	0.02724	0.02463	0.01424
Na	---	---	---	5.4×10^{-4}	8.7×10^{-4}	1.0×10^{-3}
$(Na_2O)(SiO_2)_2$[2]	0.04663	0.04618	0.04578	0.04460	0.04358	0.04137
$(Na_2O)(SiO_2)$[3]	3.4×10^{-3}	3.8×10^{-3}	4.1×10^{-3}	4.1×10^{-3}	4.2×10^{-3}	4.3×10^{-3}
Gas Phase						
H_2	0.04861	0.04969	0.04990	0.04994	0.04981	0.04925
CO	0.04844	0.04982	0.05035	0.10668	0.10665	0.10652
H_2O	6.3×10^{-4}	---	---	---	1.0×10^{-4}	4.4×10^{-4}
CO_2	4.6×10^{-4}	---	---	---	---	1.8×10^{-4}
CH_4	3.8×10^{-4}	1.0×10^{-4}	---	---	---	---
SiO	---	---	---	9.6×10^{-4}	5.4×10^{-3}	0.02453
Na	---	---	2.4×10^{-4}	2.0×10^{-3}	3.5×10^{-3}	7.7×10^{-3}
H	---	---	---	---	1.5×10^{-4}	5.4×10^{-4}

1. Less than 1.0×10^{-4} gmole. 2. Sodium disilicate. 3. Sodium metasilicate.

over it causing arc transfer which was facilitated by the presence of high levels of Na^+ in the liquid.

3.4.1.3 Silica Anode Purity

The use of NaOH to facilitate arc transfer created a problem of Na contamination. This was not serious because Na would be removed through vaporization eventually leading to the formation of a silica anode with a purity approaching that of the quartz feed. The sodium ion (Na^+) was transported under the influence of the applied electric field and the concentration gradient to the anode surface where it was neutralized and vaporized due to its low boiling point. The presence of Na in the condensate collected in the quench pipe was verified by its explosive reaction with moisture. The degree to which the anode had been purified during an experiment was examined using ICP (Inductively Coupled Plasma) emission spectroscopy (SKW, Becancour, Quebec, Canada). Table 3.5 lists the silica anode elemental impurities in the form of their common oxides. The same oxides typically used to characterize the quartz raw material were used for this analysis. The samples were taken from the bottom center of the crucible where Na contamination was believed to be highest. The overall purity of the anode was expected to be higher than what is reported in Table 3.5. The mass of the samples was approximately 35 g which represented 20 - 25 % of the final silica anode mass.

The final purity of the silica anodes listed in Table 3.5 ranged from 97.92 - 99.77 % SiO_2 compared to 99.94 % for the quartz feed. As expected, Na was the greatest impurity. The increased Al_2O_3 content may have been due to insulation fibers falling into the crucible during reactor assembly. Other impurity levels were comparable to what was present in the quartz feed. The final purity of the anode approached that of the quartz raw material for experiments conducted at 200 and 250 A and was lower at 150 A despite a longer experimental duration. The increase in the rate of sodium vaporization with increasing current was due to the higher temperatures within the anode which increased

TABLE 3.5 Final silica anode composition compared to quartz raw material.

Oxide[1]	*Final Silica Anode Composition [mass %]*					
	Exp. 50 (15/150)	***Exp. 59 (15/150)***	***Exp. 85 (20/200)***	***Exp. 86 (20/200)***	***Exp. 78 (10/250)***	***quartz***
Al_2O_3	0.0240	0.0232	0.0136	0.0340	0.0297	0.0060
As_2O_3	0.0013	0.0008	0.0009	0.0012	0.0009	0.0015
BaO_2	0.0001	0.0001	---	0.0001	---	0.0005
Bi_2O_3	0.0006	0.0006	0.0007	0.0010	0.0010	0.0004
CaO	0.0165	0.0169	0.0077	0.0245	0.0105	0.0040
CdO	---[2]	---	---	---	---	---
CoO	0.0353	0.0098	0.0104	0.0136	0.0117	0.0296
Cr_2O_3	0.0009	0.0010	0.0006	0.0007	0.0007	---
CuO	0.0004	0.0004	0.0001	0.0003	0.0005	0.0001
Fe_2O_3	0.0126	0.0116	0.0081	0.0102	0.0127	0.0050
La_2O_3	---	---	---	0.0001	0.0001	---
MgO	0.0103	0.0106	0.0086	0.0113	0.0103	0.0030
MnO	0.0001	0.0003	---	---	0.0001	0.0001
MoO_3	---	---	---	---	---	0.0002
Na_2O	1.1792	1.9958	0.5719	0.1783	0.1462	0.0067
NiO	0.0003	0.0011	0.0003	0.0003	0.0008	---
P_2O_5	0.0016	0.0002	0.0009	0.0011	0.0009	0.0016
Pb_3O_4	---	---	---	0.0004	0.0003	0.0001
Sb_2O_3	0.0011	0.0006	0.0008	0.0008	0.0008	0.0012
Sc_2O_3	---	---	---	---	---	0.0002
SnO_2	---	0.0001	---	---	---	---
SrO	0.0001	0.0001	0.0001	0.0002	0.0001	---
TiO_2	0.0008	0.0005	0.0005	0.0007	0.0005	0.0010
V_2O_5	0.0004	0.0004	0.0004	0.0004	0.0004	0.0002
ZnO	0.0016	0.0019	0.0019	0.0011	0.0025	0.0001
ZrO_2	0.0001	0.0004	0.0001	0.0001	0.0001	0.0001
SiO_2[3]	***98.713***	***97.924***	***99.372***	***99.720***	***99.769***	***99.938***

1. Impurity is assumed to be in its common oxide form. 2. Less than 0.0001 %. 3. Silica content by difference.

the mobility of Na^+ (Choudhary, 1997) and therefore increased its rate of transport to the surface.

3.4.1.4 Electric Conduction Mechanism in the Silica Anode

The possible charge carriers in the silica anode were free electrons and holes, Na^+, Si^{4+} and O^{2-}. The electrolysis of silica would produce Si^{4+} and O^{2-}; however, the low crucible mass loss suggested that this was not significant (see section 3.4.1.10). The contribution of Na^+ to conduction was limited by its initial amount. Its biggest contribution was at 250 A since most of the sodium was vaporized during the short experimental duration (60 min). The average contribution of Na^+ conduction at this condition was estimated to be 2.68 A which represented approximately 1 % of the total current. The main charge carriers within the anode were therefore free electrons and holes.

3.4.1.5 Silica Decomposition due to Reaction with the Graphite Rod and NaOH

The use of a graphite rod and NaOH to initiate arc transfer to a silica anode resulted in the introduction of reducing agents (C and H) into the crucible at the start of an experiment. If all of the carbon and hydrogen initially added was consumed according to the following overall reactions:

$$SiO_2 + C \rightarrow SiO_{(g)} + CO \qquad (3.1)$$

$$SiO_2 + H_2 \rightarrow SiO_{(g)} + H_2O \qquad (3.3)$$

this would have resulted in the decomposition of 9.4 g of silica (assuming 4 g NaOH and 1.28 g C). However, as is shown in Table 3.4, the initial heat up of the crucible contents up to 1600 K likely produced various product gases such as H_2 and CO without any significant silica decomposition. Since these gases would be removed by the gas flowing

over the anode, the amount of carbon and hydrogen available for silica reduction was reduced as the crucible contents were heated. In addition, the mass of C assumed for this analysis (1.28 g) was proportional to the exposed length of the graphite rod (2.5 cm). The actual mass of C available for silica reduction was significantly lower because of partial vaporization of the rod due to arc impingement.

3.4.1.6 Crucible, Chamber Wall and Reactor Exit Gas Temperature

The crucible, chamber wall and reactor exit gas temperatures were measured using type C thermocouples (described in section 3.2.3) having an error of ± 1 % of the reading. From Table 3.1 we see that the thermocouples underestimated the actual temperature due to heat losses. Considering the range of temperatures measured during this study, the discrepancy was expected to be less than 10 K for the crucible and reactor exit gas and less than 20 K for the chamber wall. Steady-state was assumed to have been achieved when the crucible temperature had reached 90 % of its value prior to shutdown. The time required to achieve steady-state was found to be 30, 20 and 15 minutes for current levels of 150, 200 and 250 A respectively. These times did not vary with plasma gas flow rate. The decrease with increasing current can be explained by the increase in power which resulted in a more rapid heating of the plasma chamber components. For experiments at 150 and 200 A, approximately 83 % of the experimental duration was spent at steady-state compared to 75 % for experiments at 250 A.

Typical temperature profiles of the crucible, chamber wall and reactor exit gas are shown in Figures 3.10 - 3.12. The three temperatures approached steady-state at approximately the same rate. Once steady-state was reached, the crucible and chamber wall temperatures were quite stable. Some problems were encountered with the measurement of the reactor exit gas temperature. Wide variations were observed during steady-state (see Figure 3.11) and the measured temperature was higher than expected. This was suspected to be caused by arc radiation. Figure 3.2 shows that the thermocouple junction in the reactor exit was directly exposed to the arc radiation. A better measure of

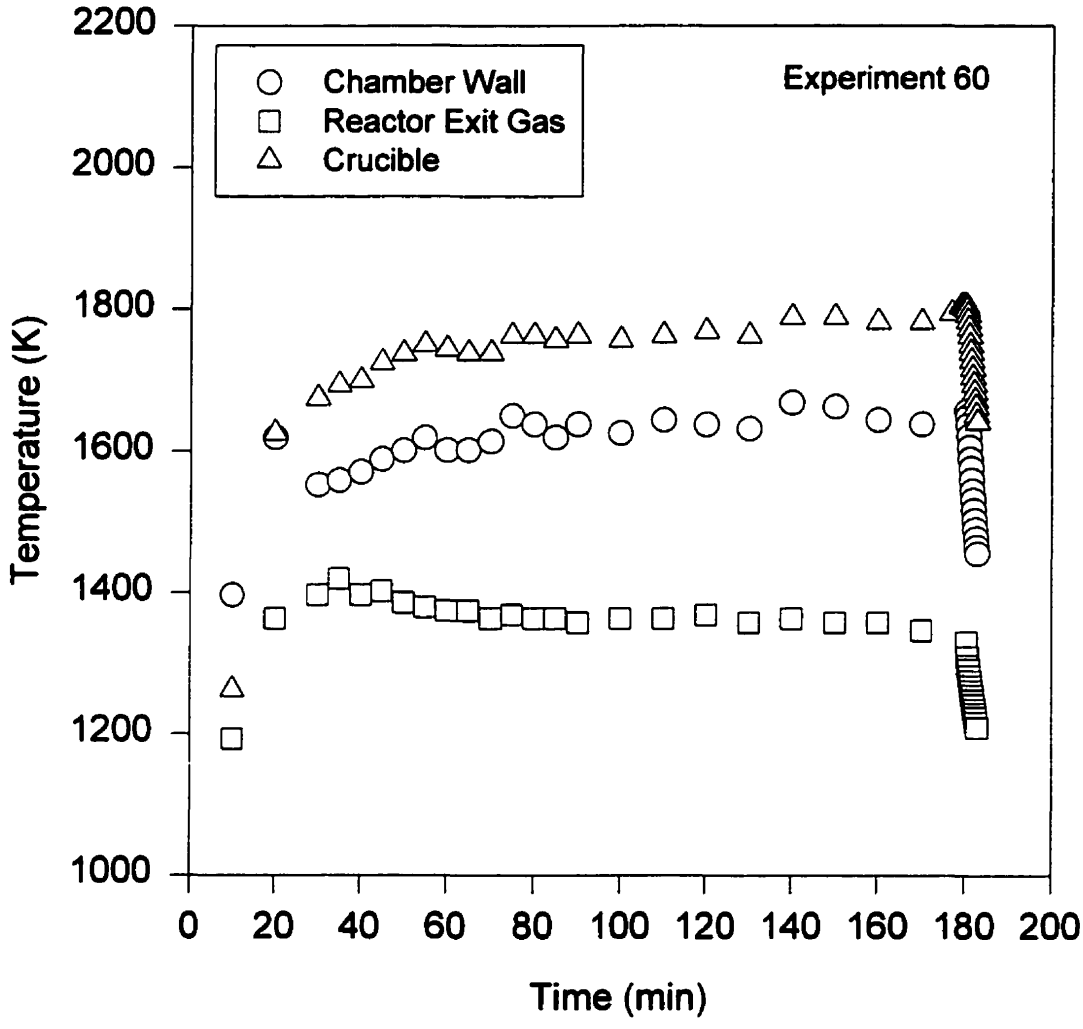

Figure 3.10 Temperature profile of crucible, chamber wall and reactor exit gas during experiment 60 (10 lpm/150 A).

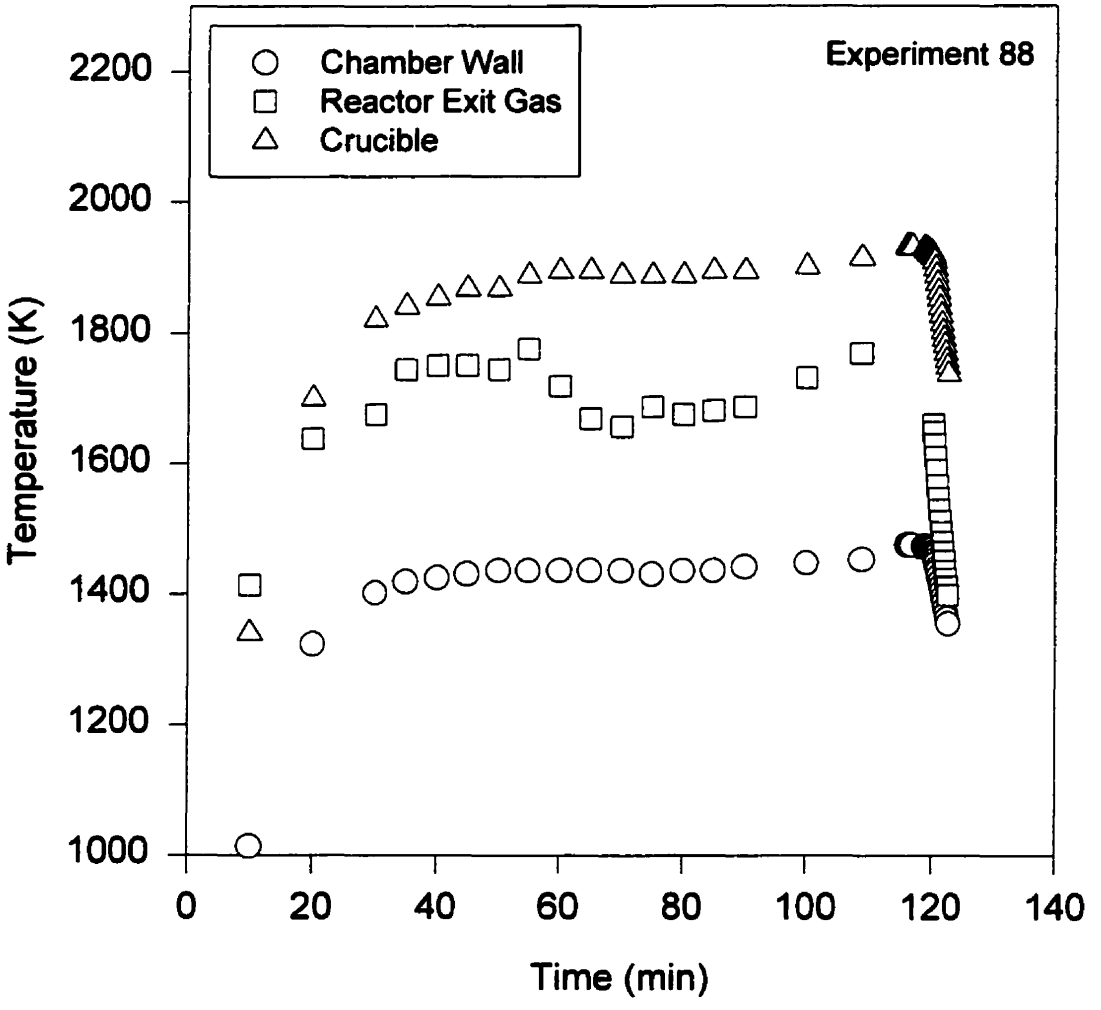

Figure 3.11 Temperature profile of crucible, chamber wall and reactor exit gas during experiment 88 (15 lpm/200 A).

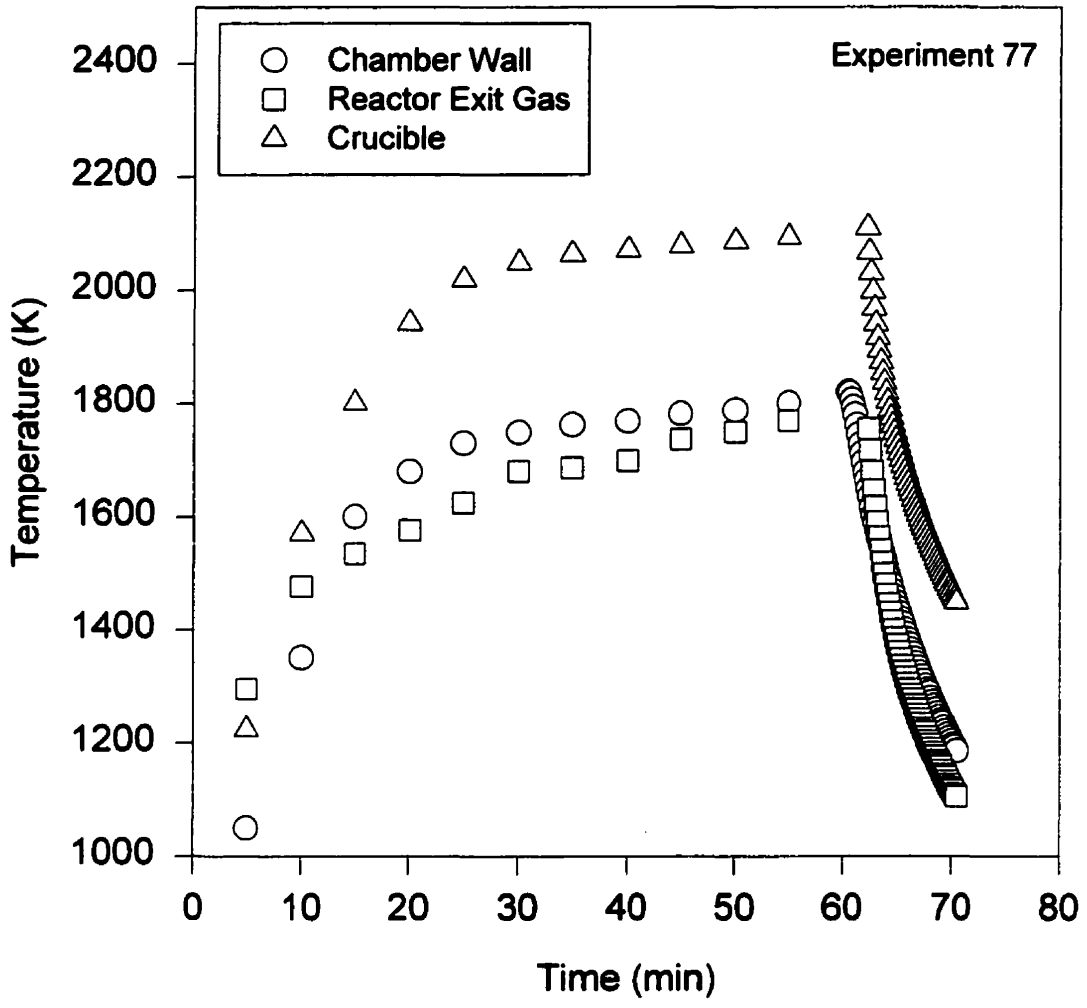

Figure 3.12 Temperature profile of crucible, chamber wall and reactor exit gas during experiment 77 (20 lpm/250 A).

the steady-state reactor exit gas temperature was determined to be the value obtained immediately following arc shutdown.

The steady-state crucible and chamber wall temperatures are plotted in Figures 3.13 and 3.14. The reactor exit gas temperatures after arc shutdown are plotted in Figure 3.15. In each case the mean and standard deviation was plotted for a given condition. For more detail on the data, the reader is referred to Appendix 2. Increasing current resulted in higher crucible temperatures while increasing the plasma gas flow rate had essentially no effect. The trend with current was due to an increase in the heat input to the silica anode. The independence of crucible temperature to variations in the plasma gas flow rate demonstrated that convective heat transfer was a minor component of the overall heat input to the anode surface. The effect of current on the reactor exit gas temperature was similar to that seen for the crucible. Increasing current increased power to the gas and therefore resulted in higher temperatures. As will be shown in the following section, the slight increase in reactor exit gas temperature with increasing plasma gas flow rate was the result of an increase in power due to higher arc voltages. Similar trends were observed with the chamber wall temperature. The only anomaly was that increasing current from 150 to 200 A seemed to have resulted in a slight cooling of the chamber. Given the wide data scatter, this effect was believed to be due to experimental error. Increasing current should have resulted in higher chamber wall temperatures due to an increase in arc radiation and gas temperature.

3.4.1.7 Appearance of the Silica Anode

Figures 3.16 - 3.18 show the top and bottom view of the silica anode at the end of selected experiments. In all cases, the appearance of the top surface was transparent and glass-like suggesting its temperature was well above 2000 K during transferred arc operation. This was expected because of the high heat load to the surface. This glass-like appearance was also noticed at the bottom of the silica anode for experiments conducted at 250 A although it was much less transparent. This was due to the lower temperatures

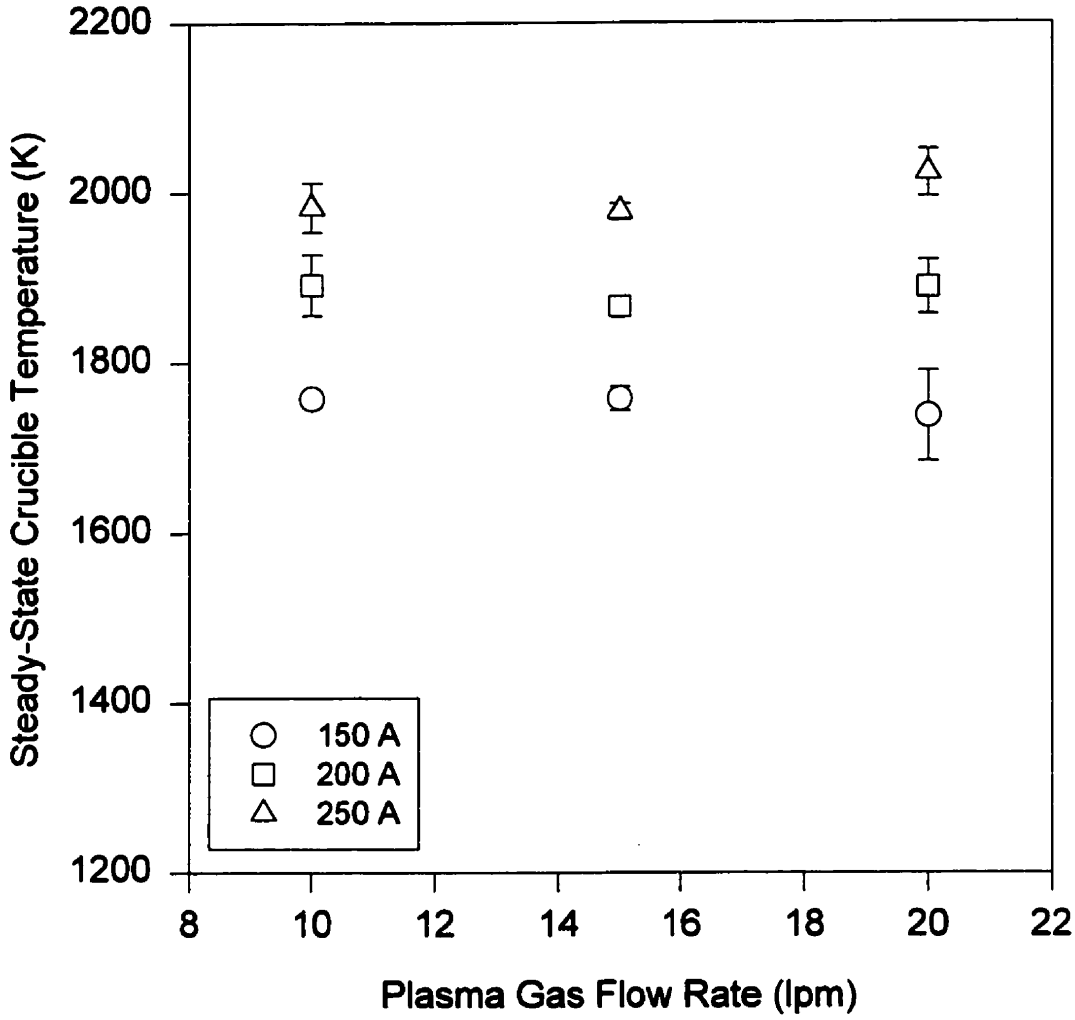

Figure 3.13 Steady-state crucible temperature for Ar plasma gas experiments.

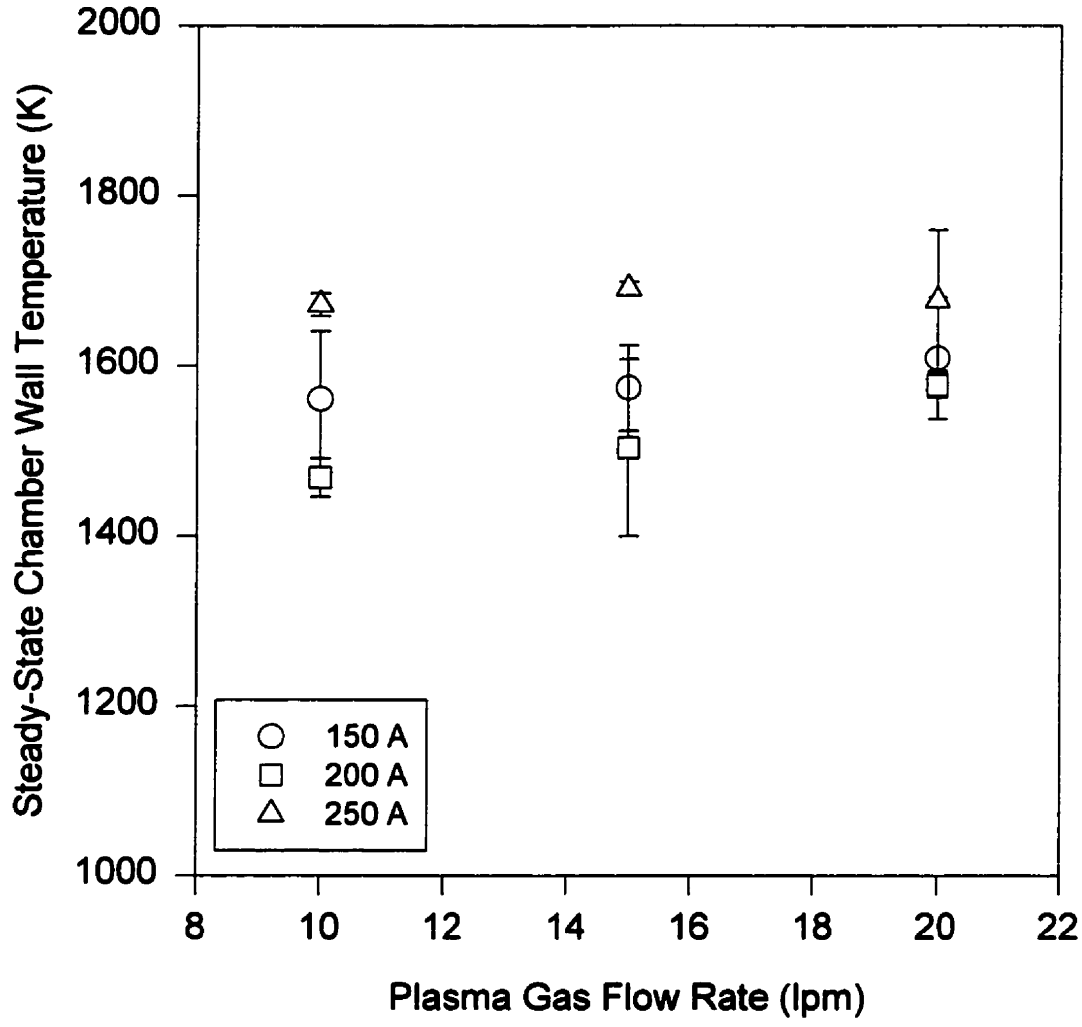

Figure 3.14 Steady-state chamber wall temperature for Ar plasma gas experiments.

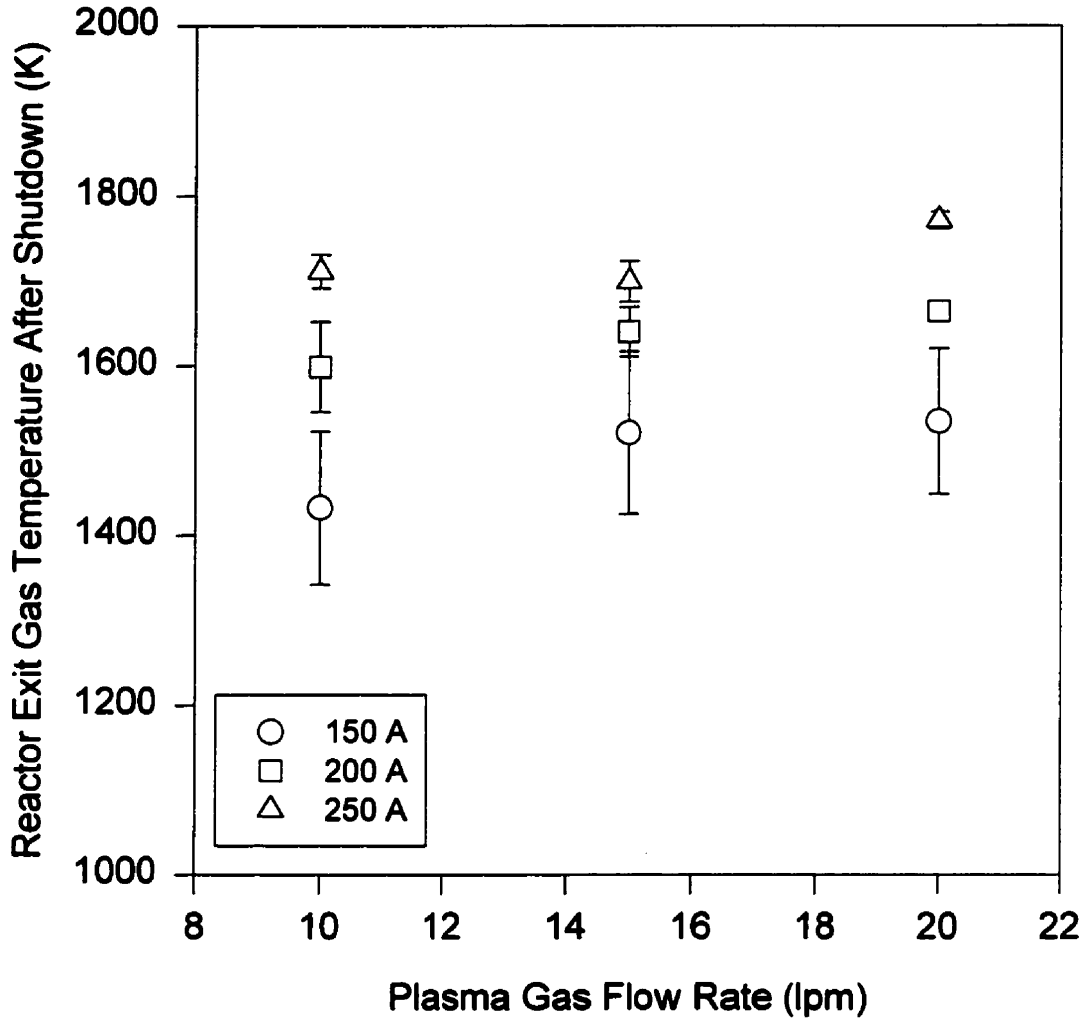

Figure 3.15 Reactor exit gas temperature after arc shutdown for Ar plasma gas experiments.

a) Top of silica anode.

b) Bottom of silica anode.

Figure 3.16 Silica anode appearance at end of experiment 60 (10 lpm/150 A).

a) Top of silica anode.

b) Bottom of silica anode.

Figure 3.17 Silica anode appearance at end of experiment 81 (15 lpm/200 A).

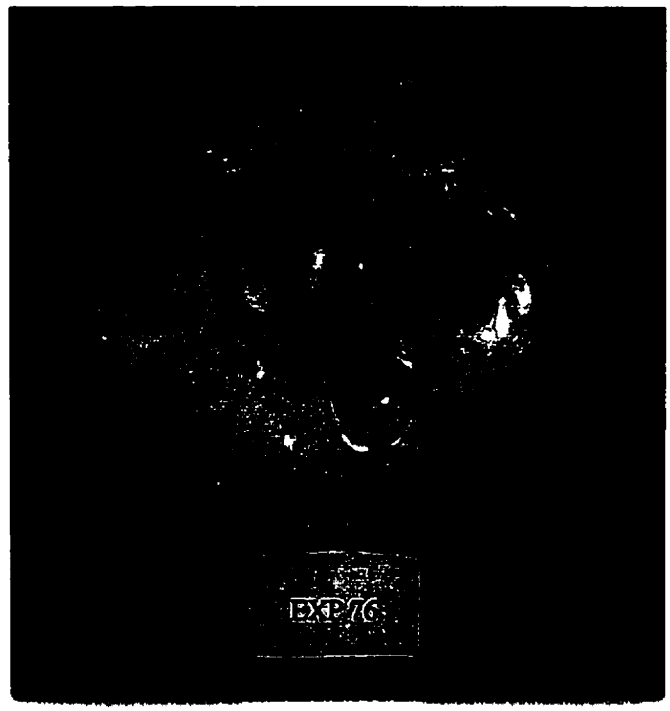

a) Top of silica anode.

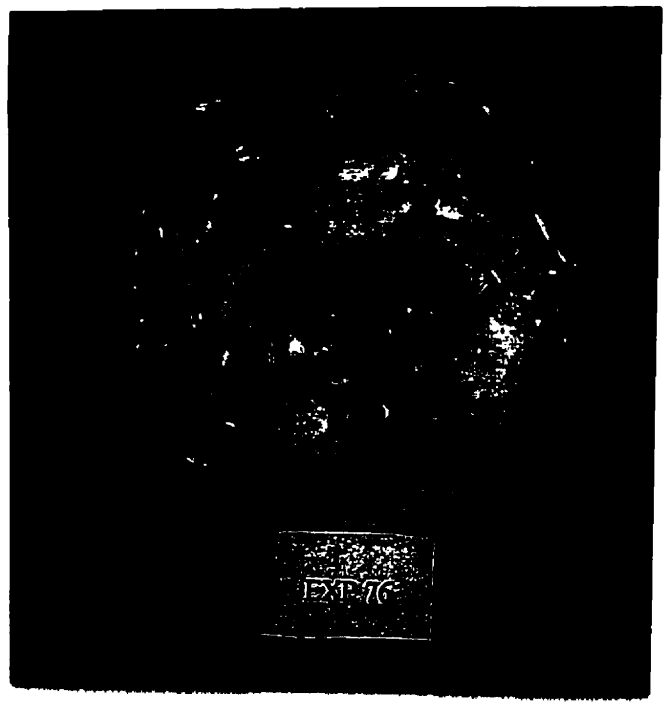

b) Bottom of silica anode.

Figure 3.18 Silica anode appearance at end of experiment 76 (10 lpm/250 A).

within the anode as it approached the crucible (1962 - 2048 K). The silica anode bottom at 150 and 200 A was composed of fused particles and was completely opaque. The crucible temperature for these experiments ranged from 1700 -1930 K. Transition to the vitreous state occurs at approximately 2000 K. The melting point of quartz has, however, been reported to be as low as 1883 K (Schick, 1960). The melting point would have been further reduced by the high Na impurity in this region.

3.4.1.8 Arc and Anode Voltage

The voltage measured during an experiment included the voltage drops across the arc, silica anode, crucible, crucible stem and other electrical connections. Calculations and measurements showed that all except those due to the arc, silica anode and crucible stem were negligible. Since the resistivity of graphite is a weak function of temperature, the voltage drop in the stem could be computed as a function of current. As will be explained later, the arc voltage could be approximated by measurements of the voltage in which the silica anode was replaced by a graphite disk. This allowed the voltage drop of the silica anode to be computed as a function of operating current and plasma gas flow rate.

A correction to the voltage measurement was required to account for the voltage drop in the graphite stem connecting the crucible to the anode holder. All other electrical connections (cathode, crucible, anode holder, shunt and cables) had negligible voltage drops. The stem was machined from a rod of extruded graphite (grade 580, SGL Carbon Group) whose electrical resistivity (with the grain) was approximately constant over a wide temperature range (273 - 2800 K). For the estimate of the voltage drop through the stem, an electrical resistivity of 1.0×10^{-5} ohm m (293 K) and a length of 14.3 cm was assumed. This length corresponded to the portion of the stem not inserted into the crucible or base (see Figure 3.2). The inserted portions of the stem had a negligible resistance because of their short length and large contact area. Using the above assumptions, the voltage drop through the stem was estimated to be 3.93, 5.24 and 6.55 V

for currents of 150, 200 and 250 A respectively. The measured voltages reported in this section have been corrected using these values.

Typical voltage (arc + anode) profiles obtained during this study are given in Figure 3.19. Because there was a delay of approximately 1 minute between the ignition of the arc and the start of data acquisition, the voltages reported at time zero correspond to those after 1 minute of arc operation. In all cases, the voltage was initially high (> 60 V) and gradually decreased to its steady-state value through continued operation. This pattern can be explained by the decrease in the electrical resistivity of the silica anode as it was heated. The voltage attained steady-state at approximately the same time as the crucible temperature. The error in the voltage measurement was estimated to be ± 0.5 V which takes into account the error associated with the multimeter used to measure voltage and the uncertainty in the estimate of the stem voltage drop.

Figure 3.20 shows that the steady-state voltage (see Appendix 2 for data) increased with increasing plasma gas flow rate. Since the effect of current was not as clear, a statistical analysis of the data was performed using a simple linear regression:

$$V = \beta_0 + \beta_1 Q_{plasma} + \beta_2 I \tag{3.4}$$

where V is the voltage due to the arc and anode, Q_{plasma} is the plasma gas flow rate, I is the current, and β_0, β_1 and β_2 are the regression parameters whose values are given in Table 3.6. The significance of the regression parameters was verified using a statistical F-test (Himmelblau, 1980). The positive value of β_1 verifies what is already seen in Figure 3.20 with regard to plasma gas flow rate. The negative value of β_2 suggests a decrease in voltage with increasing current.

To further investigate the effect of current on voltage, experiment 117 was performed to measure the voltage due to the arc only. In this experiment, a 3.8 cm diameter graphite disk was placed 2 cm from the cathode tip to simulate the top of the silica anode. This was only an estimate of the arc voltage during actual experiments since

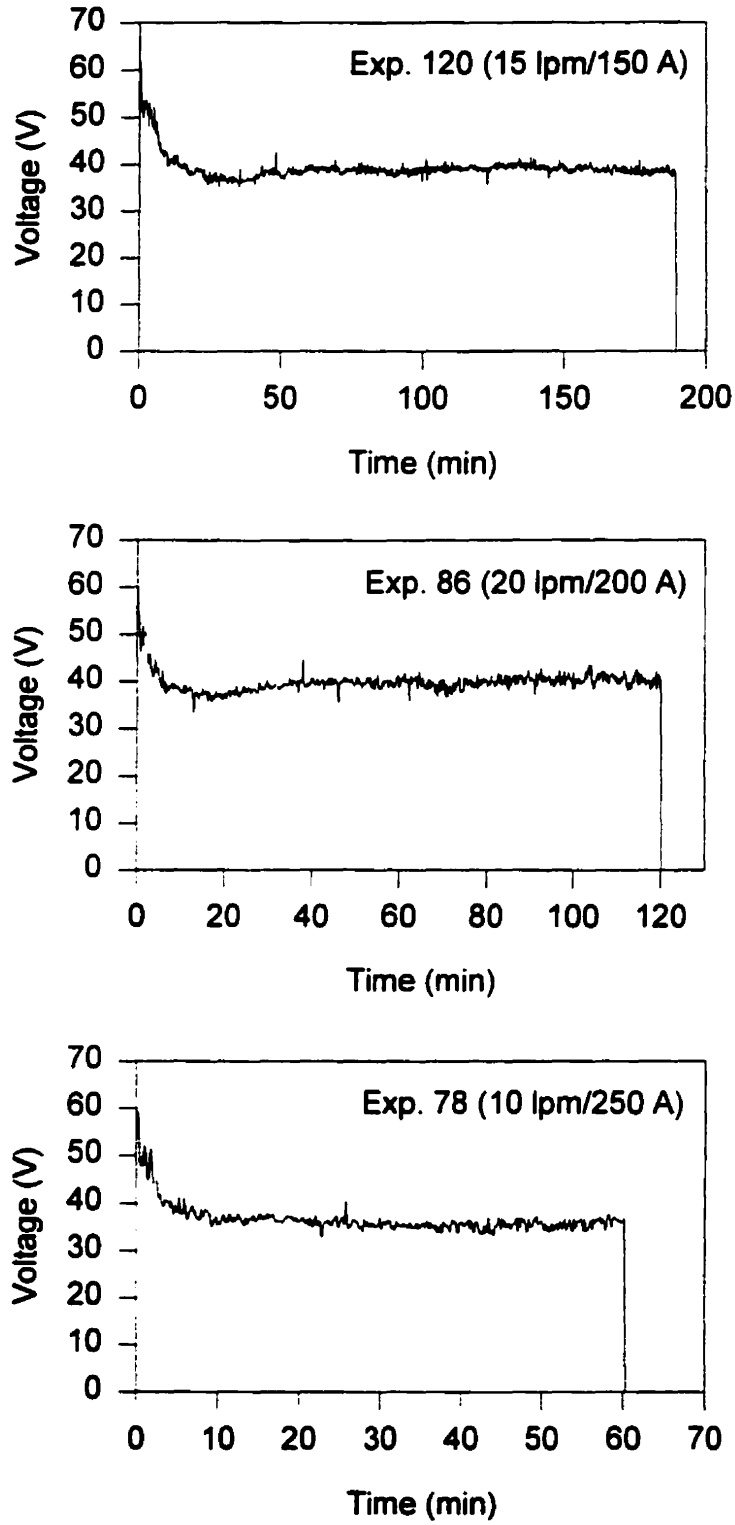

Figure 3.19 Typical voltage profiles during Ar plasma gas experiments.

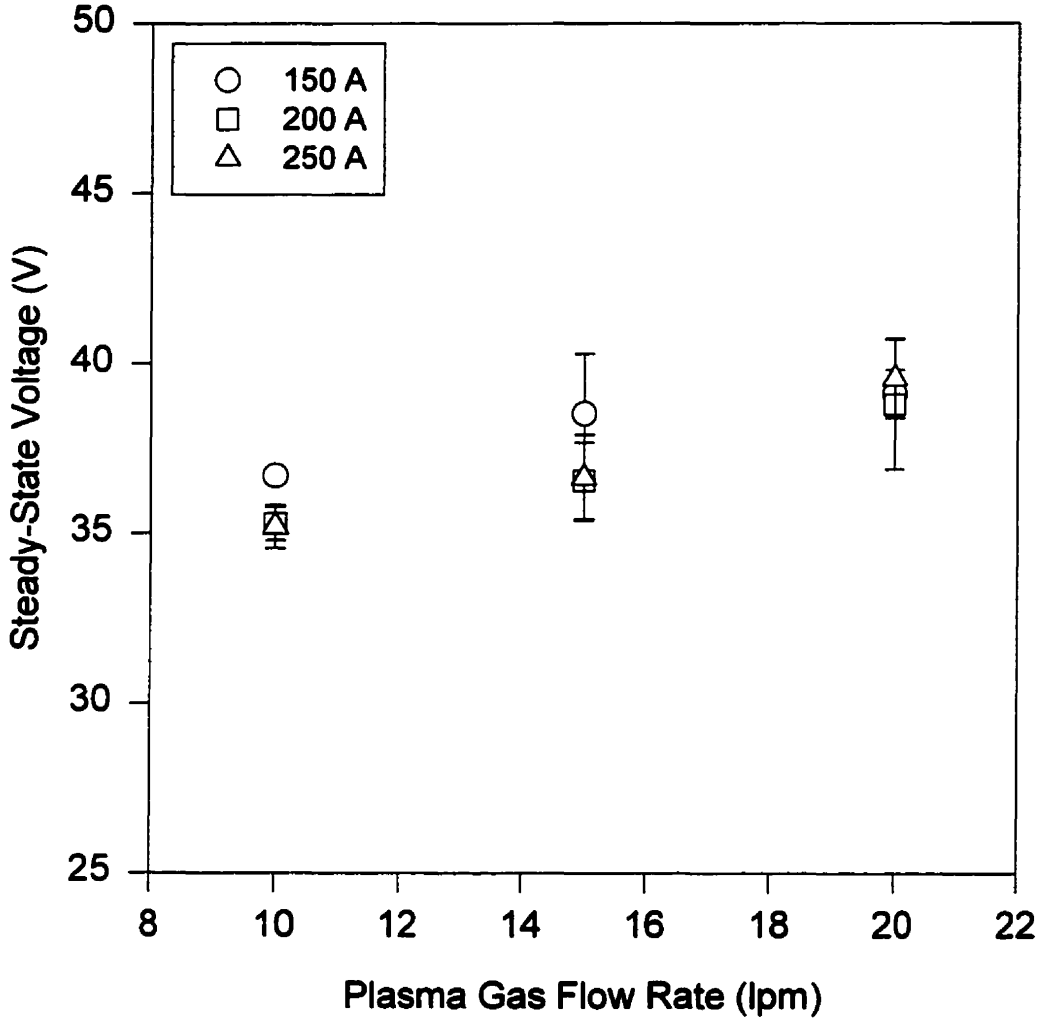

Figure 3.20 Steady-state voltage for Ar plasma gas experiments.

TABLE 3.6 Results of linear regression analysis for voltage data.

Variable	*Parameter in Equation 3.4*	*Value*	*Hypothesis Test*[1], $\beta_n = 0$
constant	β_0 [V]	34.15	hypothesis rejected
Q_{plasma}	β_1 [V/lpm]	0.356	hypothesis rejected
I	β_2 [V/A]	-1.013×10^{-2}	hypothesis rejected

1. Significance level = 0.05.

the effect of anode decomposition was not accounted for. Decomposition of silica at the anode surface results in the infiltration of Si and O species within the plasma gas. Gu (1993) estimated that for a Si vaporization rate of 3.5 mg/s at the anode surface, the voltage of a 1 cm long free burning Ar arc at 200 A would be reduced by 0.34 V. The main reason for the voltage reduction is the increased electrical conductivity of the plasma gas due to the presence of Si. This is contrary to the expected effect since metal vapor addition usually results in a local cooling of the plasma (Proulx et al., 1991) and therefore a lower electrical conductivity. The effect predicted by Gu (1993) can be explained by the relatively low emissive power of Si compared to other metals such as Fe or Al (Essoltani et al., 1994). Although the electrical conductivity of Ar/O_2 plasmas have been shown to be approximately equal to those of pure Ar up to 19 000 K, the addition of O_2 to the present plasma arc would result in an increase in its resistance due to an increase in the thermal conductivity of the gas (Murphy and Arundell, 1994). The increased heat loss would constrict the arc and therefore reduce the cross-sectional area available for electrical conduction. The infiltration of Si and O species would therefore have opposing effects and given the low decomposition rates obtained during this study, the net effect of silica decomposition on arc voltage was expected to be small.

A further discrepancy between the actual arc voltages and those measured during experiment 117 is the difference in the anode fall potential. For a high intensity Ar arc striking a water-cooled anode surface, the anode fall potential is reported to be

determined by the arc root attachment (Sanders and Pfender, 1984 and Pfender, 1997). From visual observations, the arc root on both the molten silica and graphite anode surfaces seemed diffuse (i.e. the plasma spread over the anode surface) and thus the difference in the anode fall potentials was believed to be negligible.

The arc voltages measured during experiment 117 are plotted in Figure 3.21. The effect of plasma gas flow rate and current on arc voltage was consistent with what has been observed by others (Choi and Gauvin, 1982, and Parisi, 1984). The increase in arc voltage with increasing plasma gas flow rate was due to an increase in the cooling of the arc attachment at the cathode tip. A large increase in arc voltage with increasing current was not observed suggesting the overall arc resistance decreased significantly. This was believed to be the result of an increase in the available cross-sectional area for conduction due to higher temperatures within the plasma column.

The arc voltages shown in Figure 3.21 were used to compute the silica anode voltage drop and resistance shown in Figures 3.22 and 3.23. The anode voltages estimated were significant (5.6 - 13.6 V) and the decrease with increasing current was caused by a large decrease in overall resistance (see Figure 3.23). This was the result of a decrease in the electrical resistivity of silica due to higher temperatures within the anode. The exact temperature dependence of the electrical resistivity of the present silica anode could not be determined from the experimental data because the temperature distribution within the anode was unknown. Variations in anode voltage were due to errors in the estimate of arc voltage, variations in temperature and differences in purity. As will be shown in the following section, anode voltage variations were not caused by variations in the anode height.

The fact that resistance remained approximately constant with plasma gas flow rate suggests that temperatures within the anode were not affected greatly by variations in this parameter. This effect agrees with Figure 3.13 which showed crucible temperature increasing with increasing current and remaining approximately constant with increasing plasma gas flow rate. The deviation in anode voltage at 20 lpm and 250 A was believed to be the result of an underestimation of arc voltage at these conditions due to the increased

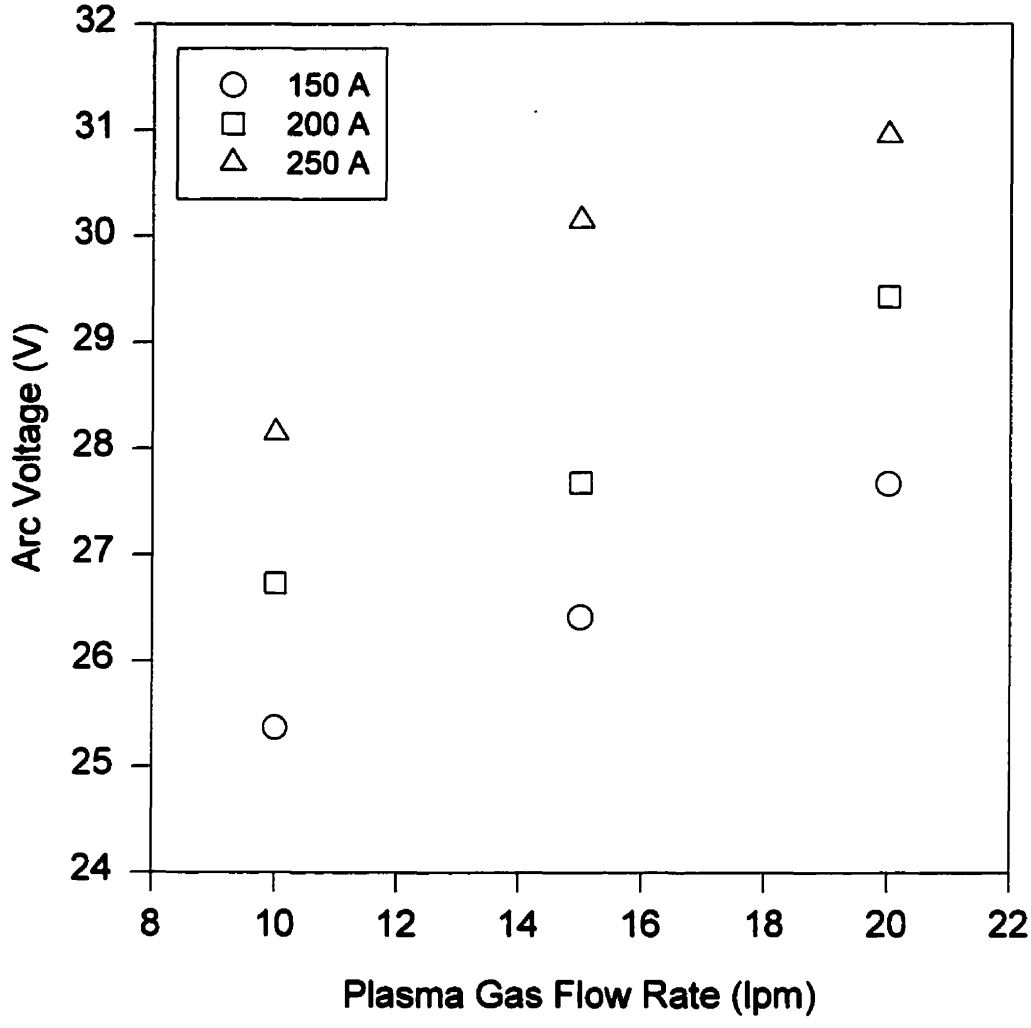

Figure 3.21 Estimate of arc voltage for Ar plasma gas experiments.

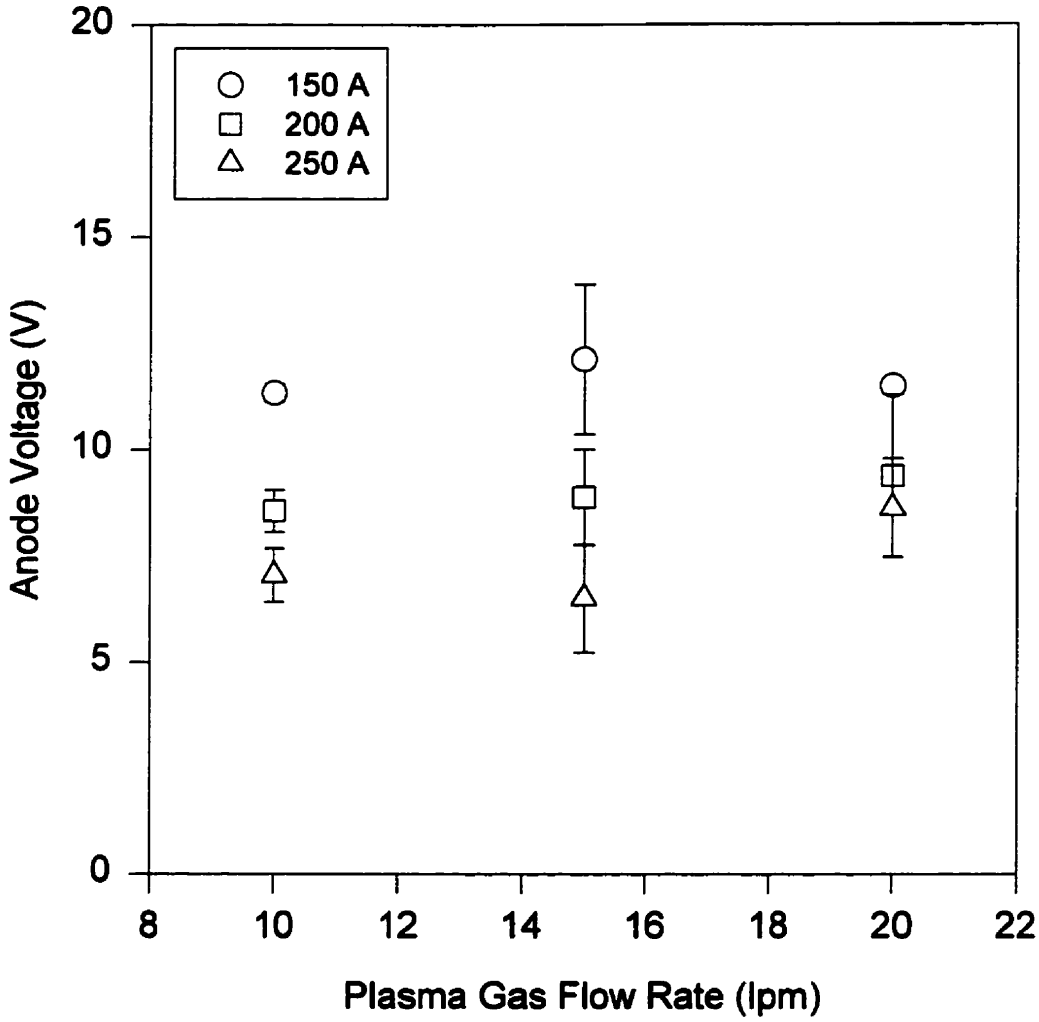

Figure 3.22 Estimate of anode voltage for Ar plasma gas experiments.

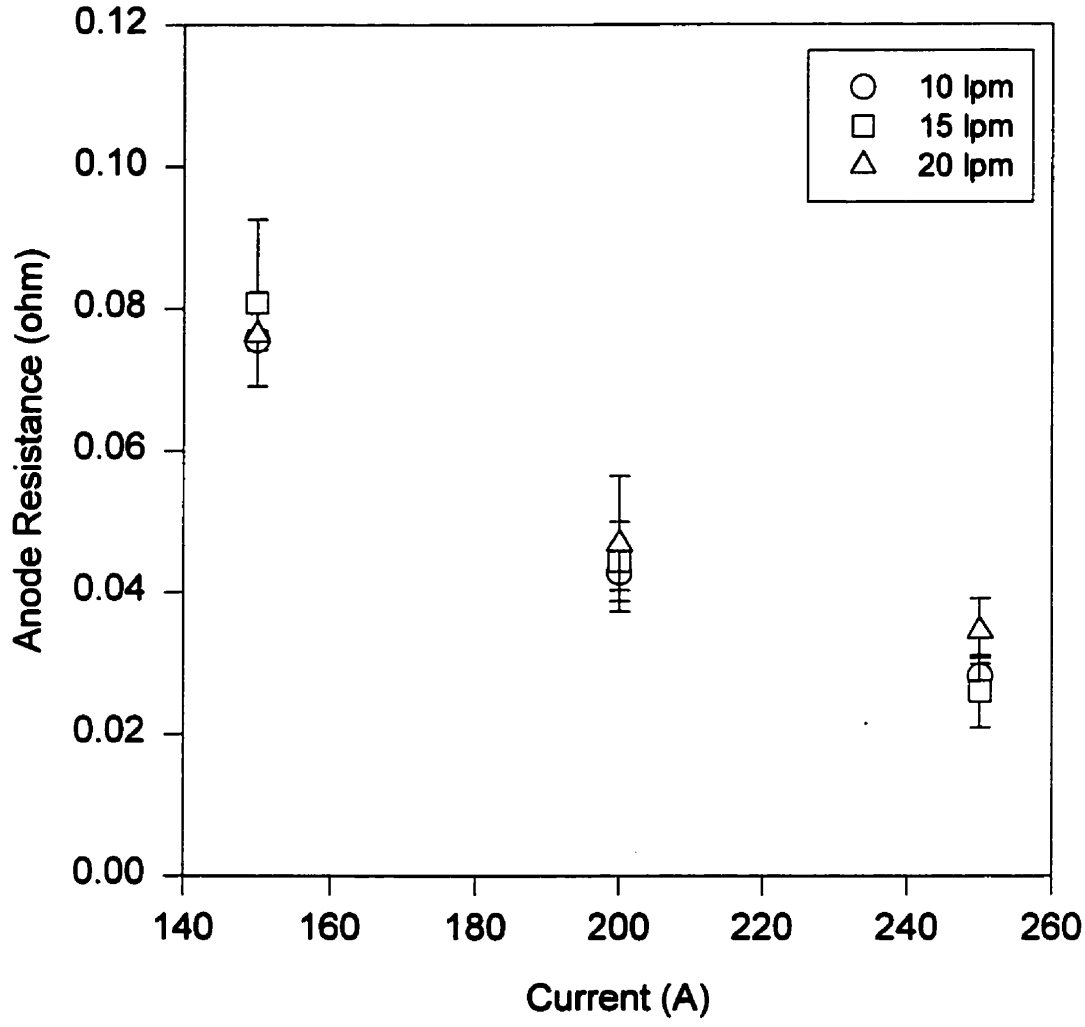

Figure 3.23 Estimate of anode resistance for Ar plasma gas experiments.

decomposition rate (see Figure 3.27). As was discussed earlier in this section, this effect seems to be linked to the addition of O_2 to the Ar plasma gas which resulted in an increase in arc resistance.

The increase in total voltage with increasing plasma gas flow rate can therefore be attributed to an increase in arc voltage since anode voltage varied little with this parameter. The small reduction in total voltage with increasing current predicted by equation 3.4 is the result of an increase in arc voltage (see Figure 3.21) being opposed by a similar decrease in anode voltage (see Figure 3.22).

3.4.1.9 Silica Mass Balance

The silica mass balance results are shown in Table 3.7. The mass of silica decomposed was determined by subtracting the mass left in the crucible and on the chamber floor from the initial mass and that fed during the experiment. The amount of silica in the crucible at the end of an experiment was approximately the same as that initially present (~ 140 g). The contribution of Na to the final anode mass was ignored. Due to the large area of the anode surface, a small variation of anode mass would have a negligible effect on its height. At an average temperature of 3000 K, a decrease of 20 g in anode mass would only result in a height decrease of 1.6 mm. This was calculated assuming a full crucible and a silica density of 1981 kg/m^3 (see Table 4.3). The voltage variations reported in the previous section were therefore probably not caused by variations in anode height. The feed rate required to maintain a constant anode mass was determined through trial and error. This was due to the fact that some particles fed into the reactor did not end up in the crucible but fell to the chamber floor. Several trials were required to determine the appropriate quartz feed rate for each condition. Feeding was inefficient at 150 A because particles had a tendency to bounce off unmelted quartz at the periphery of the crucible. The reaction of quartz particles with the chamber bottom was believed to be negligible because from Figure 3.14 we can see that the chamber wall temperature, which

TABLE 3.7 Silica mass balance results for Ar plasma gas experiments.

Exp.	*Quartz Particles [g]*		*Mass of Silica in Crucible [g]*		*Mass of Silica Decomposed [g]*	*Condensate in Reactor [g]*
	Fed	*on Floor*[1]	*Initial*	*Final*		
54	68.76	32.34	140.38	151.50	25.30	10.30
60	48.94	24.91	141.66	139.26	26.43	10.33
119	60.85	30.19	140.89	149.63	21.92	9.51
50	68.61	37.17	143.56	150.83	24.17	14.29
59	60.00	33.46	142.83	142.89	26.48	9.52
120	69.98	38.73	140.54	144.38	27.41	10.23
52	20.49	16.59	140.16	128.47	15.59	6.49
61	40.16	22.61	139.55	129.89	27.21	10.01
87	75.13	34.18	140.53	155.54	25.94	5.75
89	60.84	23.40	140.63	145.66	32.14	5.53
90	30.90	12.41	140.19	134.95	23.73	4.10
81	69.68	33.19	141.45	146.99	30.95	5.42
88	76.88	36.10	140.85	146.19	35.44	9.75
85	74.63	35.74	140.32	148.62	30.59	9.38
86	109.47	59.25	140.26	162.45	28.03	7.41
76	73.30	30.72	140.29	151.87	31.00	5.18
78	49.91	19.33	140.62	140.93	30.27	5.02
82	64.47	24.00	140.20	150.28	30.39	5.25
84	51.35	23.38	140.20	132.80	35.37	5.04
77	47.75	14.48	140.24	127.50	46.01	6.19
83	95.71	43.13	140.11	140.13	52.56	7.78
91	83.88	31.67	140.36	142.80	49.77	6.68

1. Mass of quartz particles fed which landed on the chamber floor.

approximated that of the chamber bottom, was below 1800 K for all cases (see section 2.4.3).

Also included in Table 3.7 is the mass of condensate found in the reactor at the end of an experiment. The condensate was collected on the chamber walls, crucible (only at 150 A), exit tube, torch nozzle and orifice. In general, the mass of condensate was highest at 150 A due to the lower temperatures within the reactor. Most of the reactor condensate was white in color suggesting that it was in the form of SiO_2. The condensate collected on the orifice was brown which is typical of $SiO_{(s)}$ (Tombs and Welch, 1952). The probable mechanism for SiO_2 formation on the chamber wall was $SiO_{(g)}$ condensation followed by oxidation. Above 1773 K $SiO_{(g)}$ was believed to react with the graphite chamber to produce SiC according to the following reaction (Lelièvre et al., 1988):

$$SiO_{(g)} + 2C \rightarrow SiC + CO \qquad (3.5)$$

The above reaction explains the thin green deposit observed on the chamber wall and on the outside surface of the crucible at 200 and 250 A (see Figure 3.24). This green product has been observed before and associated with SiC formation (Schei and Sandberg, 1966). The amount of $SiO_{(g)}$ lost through SiC generation on the hot graphite surfaces within the reactor was small because of the very thin product layer observed. Once an SiC layer had been formed, $SiO_{(g)}$ consumption via reaction 3.5 decreased since the graphite surface was no longer exposed. The brown coating found on the orifice was due to condensation of $SiO_{(g)}$ which was not oxidized because of the lower temperature in this region.

3.4.1.10 Crucible Mass Loss

An examination of the crucible mass loss was required to determine whether there had been significant decomposition of the silica at the anode/crucible interface. As will be shown in the following paragraphs, the decomposition of silica through reaction with the crucible was found to be negligible in all cases except at 20 lpm and 250 A. Crucible

a) Crucible before experiment.

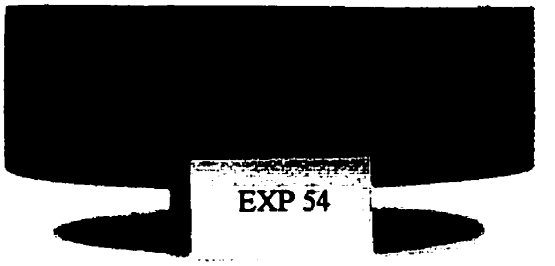

b) Exp. 54: no green deposit. (10 lpm/150 A)

c) Exp. 88: green deposit. (15 lpm/200 A)

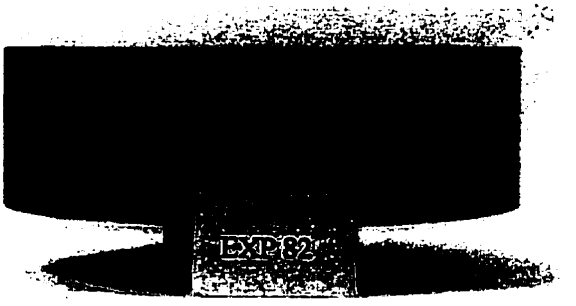

d) Exp. 82: green deposit. (15 lpm/250 A)

Figure 3.24 Side view of crucible.

consumption was mainly due to the reaction of the exposed hot graphite surface with O_2 produced at the anode surface via silica decomposition.

The crucible mass loss as a function of torch operating parameters is shown in Figure 3.25. The mass loss ranged from 0.46 - 3.30 g. No consistent trend was observed, although, experiments at 15 and 20 lpm, and 250 A produced higher crucible mass losses. There were two main mechanisms for crucible consumption. The first was reaction with the silica anode resulting in consumption via one or more of the following reactions:

$$SiO_2 + C \rightarrow SiO_{(g)} + CO \quad (3.1)$$

$$SiO_2 + 3C \rightarrow SiC + 2CO \quad (3.6)$$

$$SiO_2 + 2C \rightarrow Si_{(l)} + 2CO \quad (3.7)$$

The other was reaction with O_2 which was produced at the anode surface through silica decomposition:

$$SiO_2 \rightarrow SiO_{(g)} + \tfrac{1}{2}O_2 \quad (3.8)$$

$$C + \tfrac{1}{2}O_2 \rightarrow CO \quad (3.9)$$

Figure 3.26 shows the crucible inner surface at the end of selected experiments. Consumption of the crucible at the anode interface was not observed for experiments conducted at 150 A. This was due to the low crucible temperature since reaction between SiO_2 and C was expected to be negligible below 1800 K (see section 2.4.3). Figure 3.26b shows that consumption at the anode interface was also negligible for experiments at 200 A even though higher steady-state crucible temperatures were attained (1858 - 1930 K). The absence of significant anode bubbling was further evidence that consumption was negligible at these conditions. The occurrence of reactions 3.1, 3.6 or 3.7 would result in the formation of gaseous products ($SiO_{(g)}$ and CO) on the bottom of the crucible which would be removed at the anode surface as bubbles. The crucible mass loss for experiments conducted at 150 and 200 A was therefore attributed to O_2 consumption

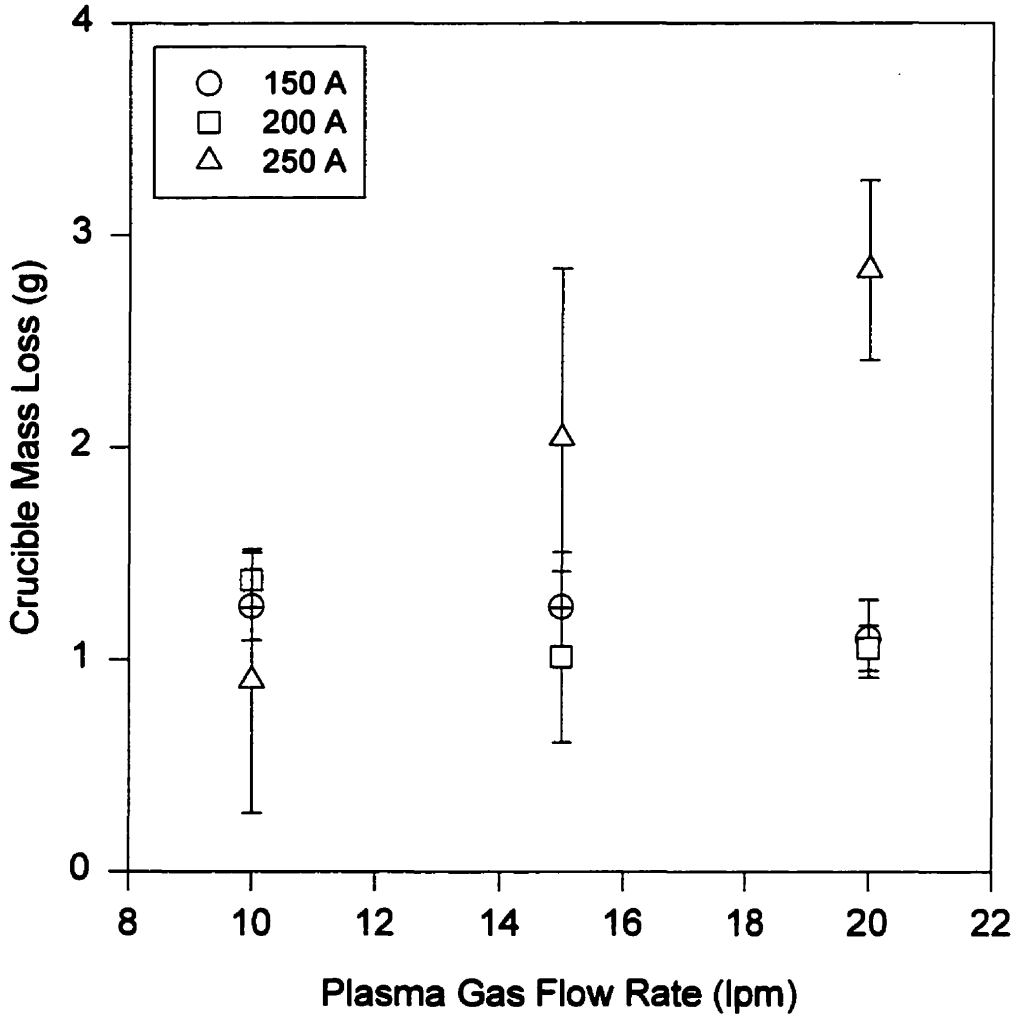

Figure 3.25 Crucible mass loss for Ar plasma gas experiments.

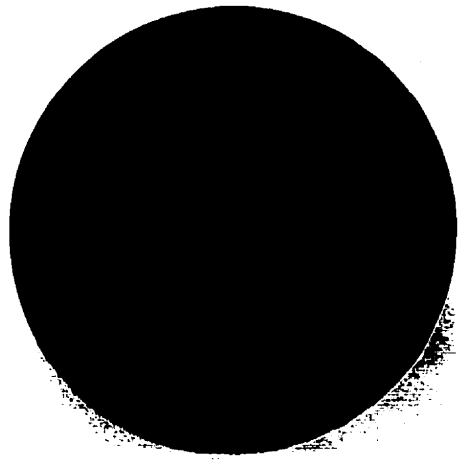

a) Crucible before experiment.

b) Exp. 88: no consumption.
(15 lpm/200 A)

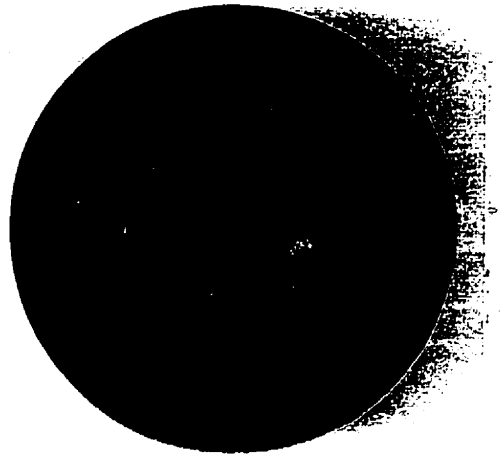

EXP 76

c) Exp. 76: slight consumption.
(10 lpm/ 250 A)

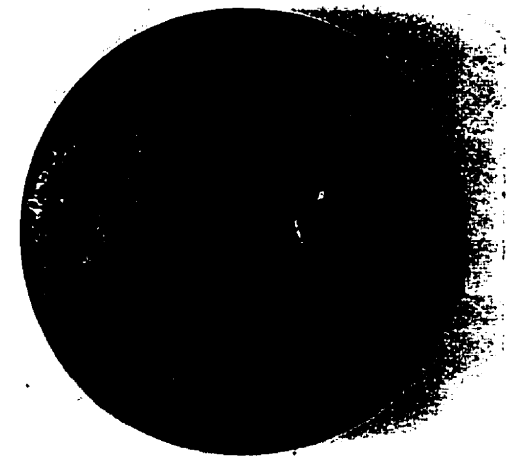

EXP 83

d) Exp. 83: considerable consumption.
(20 lpm/250 A)

Figure 3.26 Top view of crucible.

which was mainly observed at the top edge of the crucible facing the reactor exit. Oxygen concentration and temperature were highest in the gas flowing over this region of the crucible.

Figure 3.26c shows that only a minor consumption of the inner crucible surface was observed at 10 lpm and 250 A. Crucible mass loss at the anode interface was slightly increased for experiments at 15 lpm and 250 A and was worst for experiments conducted at 20 lpm and 250 A (see Figure 3.26d). The crucible surface where consumption was observed was grey in color and therefore probably the result of $Si_{(l)}$ formation via reaction 3.7. The green deposit associated with SiC was not present. Crucible consumption at 20 lpm and 250 A occurred on the upper portion of the crucible facing the reactor exit. Since this area was located furthest from the feeding point, it was slightly exposed due to the lower silica level. The exposed graphite surface was therefore more susceptible to heating by convective heat transfer and arc radiation which were greatest at the maximum plasma gas flow rate and current. This resulted in a slightly higher temperature in this region and an increase in the rate of silica decomposition at the anode/crucible interface. A portion of the $Si_{(l)}$ generated at the crucible surface likely dissolved within the anode and underwent further reaction producing $SiO_{(g)}$. This process can be described by reactions 3.7 and 3.2 with the overall result being the decomposition of silica via reaction 3.1:

$$SiO_2 + 2C \rightarrow Si_{(l)} + 2CO \qquad (3.7)$$

$$SiO_2 + Si_{(l)} \rightarrow 2SiO_{(g)} \qquad (3.2)$$

$$SiO_2 + C \rightarrow SiO_{(g)} + CO \qquad (3.1)$$

The lack of significant reaction at the anode/crucible interface also indicates that the main conduction mechanism within the anode was not electrolytic. Electrolytic conduction would require the migration of O^{2-} to the crucible surface where it would be neutralized. Due to the high temperature of the crucible, the likely result of neutralization would be CO formation. If each O^{2-} reaching the surface resulted in the formation of a

molecule of CO, the crucible consumption rate would have been approximately 0.56 g/min at 150 A. This would have resulted in a crucible consumption of 100 g after 3 hours of operation. Therefore, electrolytic conduction within the silica anode was believed to be negligible.

3.4.1.11 Silica Decomposition at the Anode Surface

Given that reaction with the crucible was negligible for most experiments, silica decomposition was believed to occur mainly at the anode surface via:

$$SiO_2 \rightarrow SiO_{(g)} + \tfrac{1}{2}O_2 \qquad (3.8)$$

The rate at which silica was decomposed was determined by momentum, heat and mass transfer effects occurring at the anode surface and within the anode itself. These effects were in turn determined by the plasma gas flow rate and current. The average silica decomposition rates are plotted in Figure 3.27. The rates were calculated as the mass decomposed divided by the duration of an experiment. Since this represents an average over an entire experiment, the actual steady-state values were slightly higher. The silica decomposition rate ranged from 0.09 - 0.88 g/min and was found to increase with increasing current and be unaffected by plasma gas flow rate. The only exception was at 250 A where an increase in the decomposition rate was observed when the plasma gas flow rate was increased from 15 to 20 lpm. This, however, was believed to be the result of an increase in the rate of silica decomposition at the crucible surface (see previous section).

The independence of the decomposition rate with plasma gas flow rate suggested that the process was not mass transfer limited. If mass transfer was the rate limiting step, then the decomposition flux at a point on the anode surface D_{SiO2}, could be expressed as:

$$D_{SiO2} = h_m \left(x_{SiO,a} - x_{SiO,\infty} \right) \qquad (3.10)$$

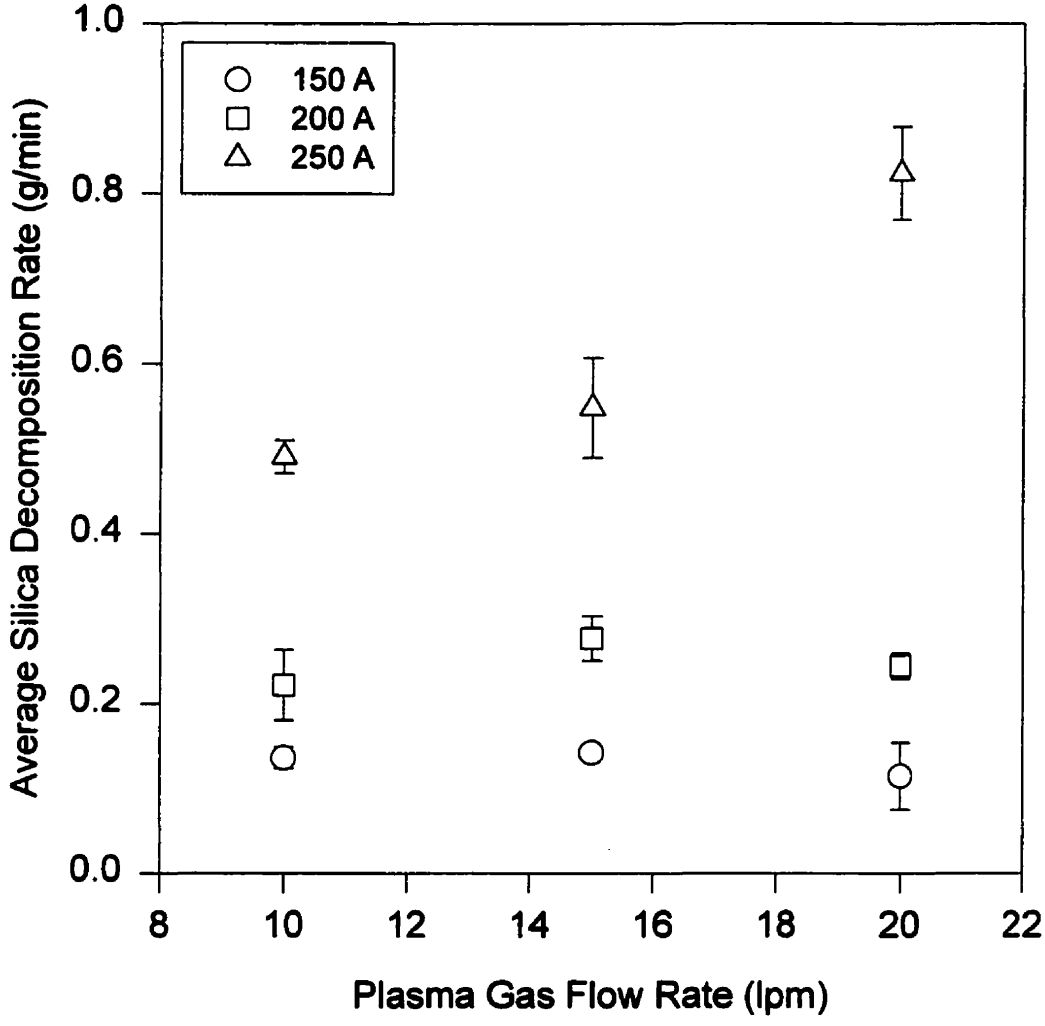

Figure 3.27 Average silica decomposition rate for Ar plasma gas experiments.

TABLE 3.8 Predicted increase in gas velocity over the center of the anode surface[1] (using Ming (1994) transferred arc model).

Increasing Ar Plasma Gas Flow Rate				*Increasing Current*			
Q_{plasma} *[lpm]*	*Current [A]*	u^2 *[m/s]*	v^3 *[m/s]*	Q_{plasma} *[lpm]*	*Current [A]*	*u [m/s]*	*v [m/s]*
10	200	32.4	15.2	15	150	21.1	9.9
15	200	43.7	20.6	15	200	43.7	20.6
20	200	55.2	26.0	15	250	62.6	29.4

1. Evaluated ~ 0.25 mm above center of anode surface. 2. Axial velocity. 3. Radial velocity.

where h_m is the mass transfer coefficient, $x_{SiO,a}$ is the mass fraction of $SiO_{(g)}$ at the anode surface and $x_{SiO,\infty}$ is some characteristic mass fraction of $SiO_{(g)}$ in the bulk gas. Since increasing the velocity of the plasma gas over the anode surface increased h_m, an increase in D_{SiO2} would have also been expected. The axial and radial components of the velocity just above (~ 0.25 mm) the center of the anode surface were estimated using a transferred arc model developed by Ming (1994). The results are shown in Table 3.8. As expected, the model predicts that increasing either plasma gas flow rate or current results in an increase in gas velocity over the anode surface and therefore greater mass transfer rates. If the increase in the decomposition rate with increasing current was due to this effect, a similar increase would have been expected with increasing plasma gas flow rate. However, we can see from Figure 3.27 that this was not the case.

Since we know that increasing current increased the heat input to the anode and that this also resulted in an increase in the decomposition rate, a heat transfer limited process was suspected. This can be understood by considering the following hypothesis. Most of the silica decomposition was believed to occur in the center of the anode where the surface had attained its boiling point. In this region, the rate of silica decomposition was determined by the surface heat balance since once the boiling point was attained, any

additional heat was removed by decomposition. The boiling point was the temperature at which the sum of the vapor pressures of the decomposition products ($SiO_{(g)}$ and O_2) equaled the pressure above the silica surface. From Table 2.5 we see that this corresponded to 3151 - 3167 K for pressures of 101.3 - 112 kPa. At the boiling point, the mass transfer of decomposition products from the anode surface was dominated by bulk flow due to the creation of a local pressure gradient. This pressure gradient was the result of a build up of decomposition vapor above the boiling liquid. The impinging gas flow onto the decomposing surface had the effect of adding an inert species (Ar) which favored a reduction in the boiling point. The exact temperature which corresponded to the boiling point was therefore slightly different from the values given above and is difficult to predict without a clearer description of the gas phase above the silica anode.

Boiling below the anode surface was believed to be negligible since little bubbling was observed. The lower temperatures below the surface resulted from heat losses to the much colder crucible (1700 - 2048 K). Bubbling was only observed to be significant at 20 lpm and 250 A; however, this was associated with the formation of $SiO_{(g)}$ and CO by reaction of the silica anode with the crucible. The decomposition of silica from the surface surrounding the arc which was below the boiling point was mass transfer limited (Choo and Szekely, 1992 and Gu, 1993). Decomposition from this region was believed to be negligible since we have seen that increasing plasma gas flow rate did not increase the decomposition rate. The likely reason for this was the increase in the concentration of decomposition products within the gas as it flowed outward from the center of the anode surface.

To verify the hypothesis of a heat transfer limited decomposition process, the anode surface heat balance was examined. This balance can be expressed as:

$$q_{surf} = q_{conv} + q_{elec} + q_{rad,in} - q_{rad,out} - q_{decomp} \tag{3.11}$$

where q_{surf} is the net heat flux to the anode surface, q_{conv} is the heat input due to convection, q_{elec} is the heat flux due to electron flow, $q_{rad,in}$ is the radiation heat input

from the arc, $q_{rad,out}$ is the radiation heat flux emitted by the anode surface and q_{decomp} is the heat flux absorbed by silica decomposition. The heat flux at the anode surface can also be expressed in terms of the axial temperature gradient within the silica bath:

$$q_{surf} = -k \frac{\partial T}{\partial z} \tag{3.12}$$

where k is the thermal conductivity of silica. For a given set of torch operating conditions, the anode surface attained a steady-state temperature profile based on the heat balance given by equations 3.11 and 3.12. The rate of silica decomposition in a region at its boiling point was determined by q_{decomp} which can be expressed as:

$$q_{decomp} = \Delta H_{decomp} D_{SiO2} \tag{3.13}$$

where ΔH_{decomp} is the heat of decomposition. If the torch operating conditions were varied such that the heat input to the boiling surface was increased and the heat loss through conduction reduced, an increase in the decomposition rate would have been expected since q_{decomp} would be increased. This is simply because the surface temperature could not increase further once the boiling point was attained. The heat loss through radiation ($q_{rad,out}$) would remain constant in a region at its boiling point because it is a function of surface temperature. The above effect was observed with increasing current since this led to an increase in q_{elec} and q_{conv}. The heat flux at the anode surface due to electron flow is proportional to the current and can be estimated by the following equation for positive anode falls (Backer and Szekely, 1987):

$$q_{elec} = j_{z,surf} \left(\frac{5 k_B}{2 e_a} (T_{e,e} - T_{e,a}) + V_{anode} + \phi_w \right) \tag{3.14}$$

where $j_{z,surf}$ is the axial current density at the arc/anode interface, k_B is the Boltzmann

constant, e_o is the elementary charge, $T_{e,e}$ is the electron temperature at the edge of the boundary layer, $T_{e,a}$ is the electron temperature at the anode surface, V_{anode} is the anode fall potential and ϕ_w is the work function of the anode material. An increase in q_{elec} and q_{conv} in regions already at the boiling point resulted in an increase in the local decomposition flux. The increased heat flux also allowed surrounding regions to attain the boiling point and reduced the conductive heat loss due to higher temperatures below the surface.

. The arc radiation term in equation 3.11 ($q_{rad,in}$) was expected to be negligible since the anode surface was transparent (see section 3.4.1.7). Radiation from the arc did increase with increasing current but this increased the heat transferred to the bulk of the anode rather than the surface since arc radiation was absorbed within the silica bath. This also contributed to an increase in the decomposition rate by reducing the temperature gradient below the boiling surface.

Increasing plasma gas flow rate increased q_{conv}; however, this did not lead to an increase in the decomposition rate. In addition to what has already been observed with regard to crucible temperature and anode resistance, this is further evidence that q_{conv} was not an important contribution to the overall anode surface heat flux. The fact that increasing plasma gas flow rate did not increase the decomposition rate suggests the high q_{conv} normally associated with free burning and transferred arcs (Pfender, 1997) was reduced by the efflux of decomposition products from the anode surface which countered the impinging plasma gas flow (Bird et al., 1960).

Another effect which must be considered is resistance heating within the anode since this may have also affected the surface heat balance. Sometimes neglected in metal anodes (Gu, 1993), the effect of resistance heating was considered here because of the higher electrical resistivity of silica. The rate of resistance heating was estimated using the anode voltages determined previously (see section 3.4.1.8). From Figure 3.28 we can see that, although significant (~ 1.75 kW), the rate of resistance heating was approximately constant for all conditions. The slight increase at 20 lpm and 250 A was believed to be the result of an error in the estimate of the arc voltage due to the higher

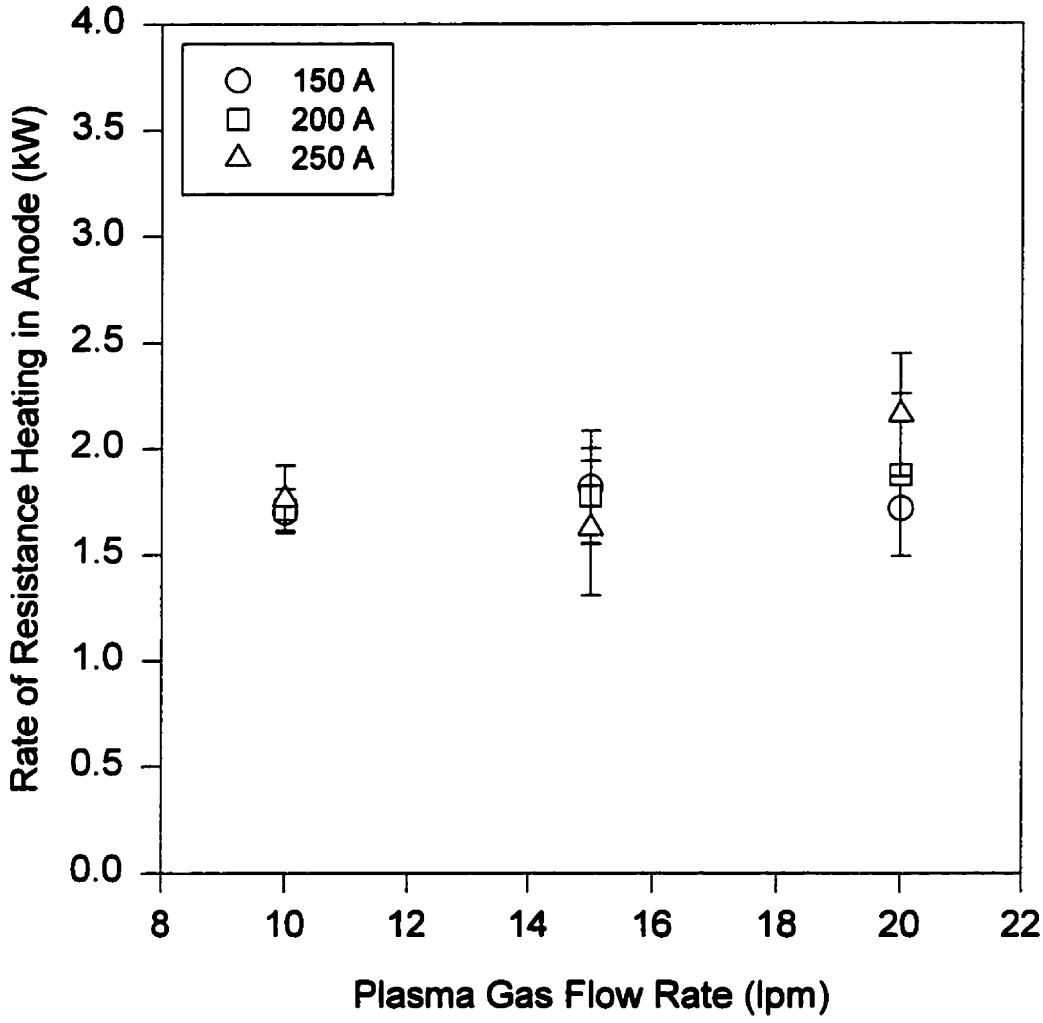

Figure 3.28 Estimate of rate of resistance heating in silica anode for Ar plasma gas experiments.

decomposition rate. The independence of the rate of resistance heating with respect to plasma gas flow rate was not surprising since we have seen from section 3.4.1.8 that this parameter did not affect anode resistance. The independence of the rate of resistance heating with respect to current can be explained by examining Figure 3.23 where we see that an increase in current was compensated by a decrease in anode resistance.

The surface heat balance was also affected by fluid flow within the anode. This fluid flow was induced by electromagnetic forces, buoyancy and shear stresses at the anode surface (gas shear and surface tension gradients). The velocities within the anode were not believed to have a major influence on the surface heat balance since they were probably small due to the high viscosity of vitreous silica (Urbain et al., 1982). This will be verified in the following chapter.

3.4.1.12 Use of CO to Monitor $SiO_{(g)}$ Concentration in Reactor Exit Gas

A direct measurement of $SiO_{(g)}$ concentration was not possible since $SiO_{(g)}$ would condense as the sampled gas was cooled for analysis. In addition to Ar, the major components in the reactor exit gas were expected to be $SiO_{(g)}$, O_2 and CO. The decomposition of silica via reaction 3.8 generated $SiO_{(g)}$ and O_2 while the presence of CO was due to the reaction of O_2 with a hot graphite surface such as the crucible, chamber wall or exit tube. The concentration of CO_2 was also monitored during preliminary experiments but found to be negligible (< 0.01 %). Some of the $SiO_{(g)}$ produced at the anode surface probably condensed as it exited the plasma chamber. The fraction of SiO exiting the reactor in a condensed state was difficult to estimate since it was a function of the gas flow, concentration and temperature distribution within the reactor. Any SiO exiting the reactor in a condensed state did so in the form of solid or liquid particles depending on their residence time in the plasma chamber. In section 5.3.5 TEM analysis of the powder products will show that condensation of $SiO_{(g)}$ was not significant when a pure Ar plasma gas was used due to the low decomposition rates obtained. The $SiO_{(g)}$ concentration in the reactor exit gas could therefore be determined from an oxygen

TABLE 3.9 Comparison of CO concentration in the reactor exit gas during blank and decomposition experiments (for a similar plasma gas flow rate).

Time [min]	*Blank Experiments (10 lpm/200 A) Average y_{CO} [mole %]*	*Decomposition Experiments Average y_{CO} [mole %]*
40	0.15	1.54 (10 lpm/250 A)
60	0.05	0.54 (10 lpm/200 A)
90	0.02	0.21 (10 lpm/150 A)

balance if both the concentrations of O_2 and CO were measured. For this to be valid, all other oxygen sources within the reactor had to be eliminated. The only additional oxygen source was H_2O and O_2 present in the air remaining in the reactor after purging.

To determine the degree to which the remaining air could perturb this measurement, two blank experiments (68 and 93) were performed using an Ar plasma gas flow rate of 10 lpm and a current of 200 A. The CO concentration profiles of these blank experiments are shown in Figure 3.29. The relative humidity and O_2 concentration in the reactor exit gas were negligible after the sampling line had been purged which usually took 10 minutes. This suggested that the H_2O and O_2 in the reactor were being converted to CO. From Table 3.9 we can see that the CO concentration due to air in the reactor was small (< 10 %) compared to the value obtained during the decomposition experiments. The air remaining in the reactor following purging was not thought to have a significant effect on the rate of silica decomposition because of its low concentration.

Typical CO concentration profiles in the reactor exit gas during silica decomposition experiments are shown in Figure 3.30. As with the blank experiments, the concentrations of H_2O and O_2 in the reactor exit gas were found to be negligible after the sampling line had been purged. Therefore, the monitoring of $SiO_{(g)}$ concentration could be done solely using the CO measurement. In addition, the concentration of $SiO_{(g)}$ and CO would be equivalent since:

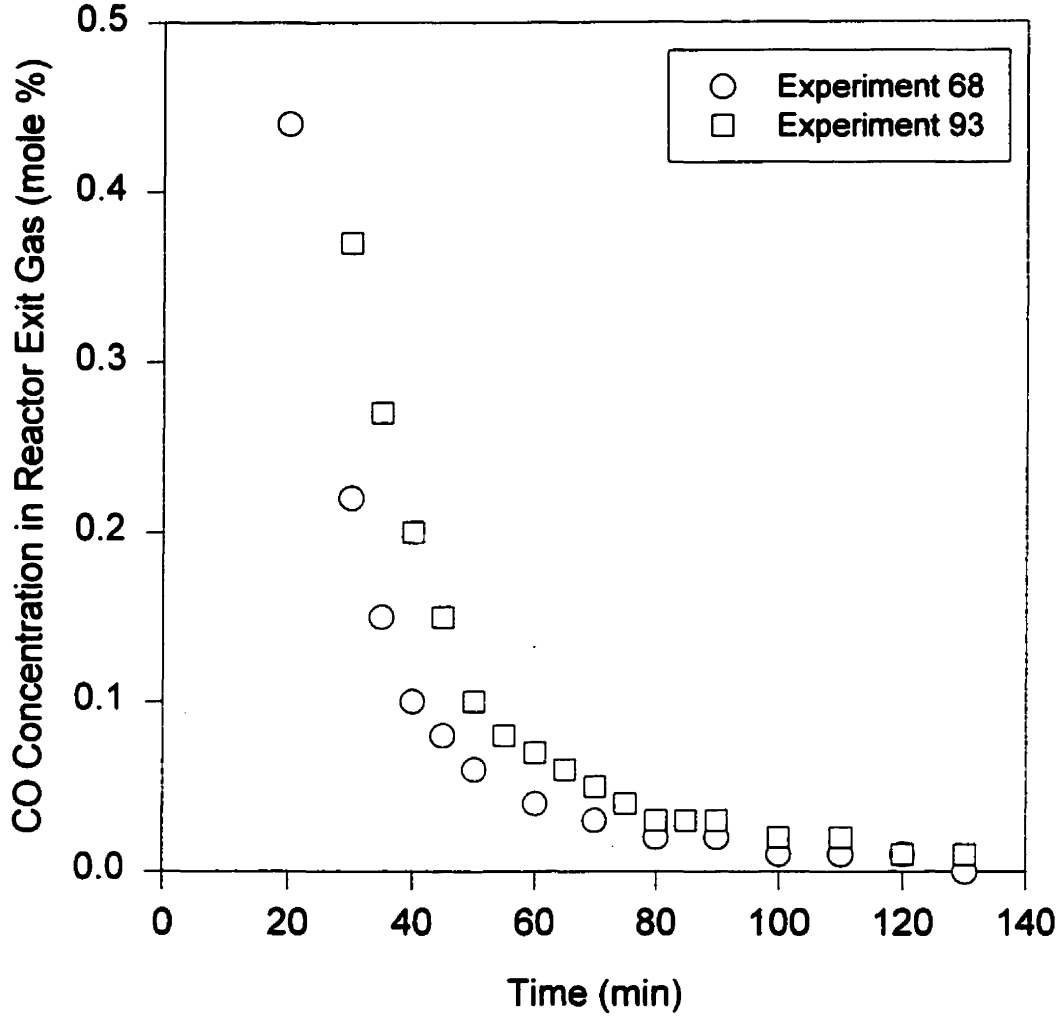

Figure 3.29 CO concentration in reactor exit gas during blank experiments 68 and 93 (10 lpm/200 A).

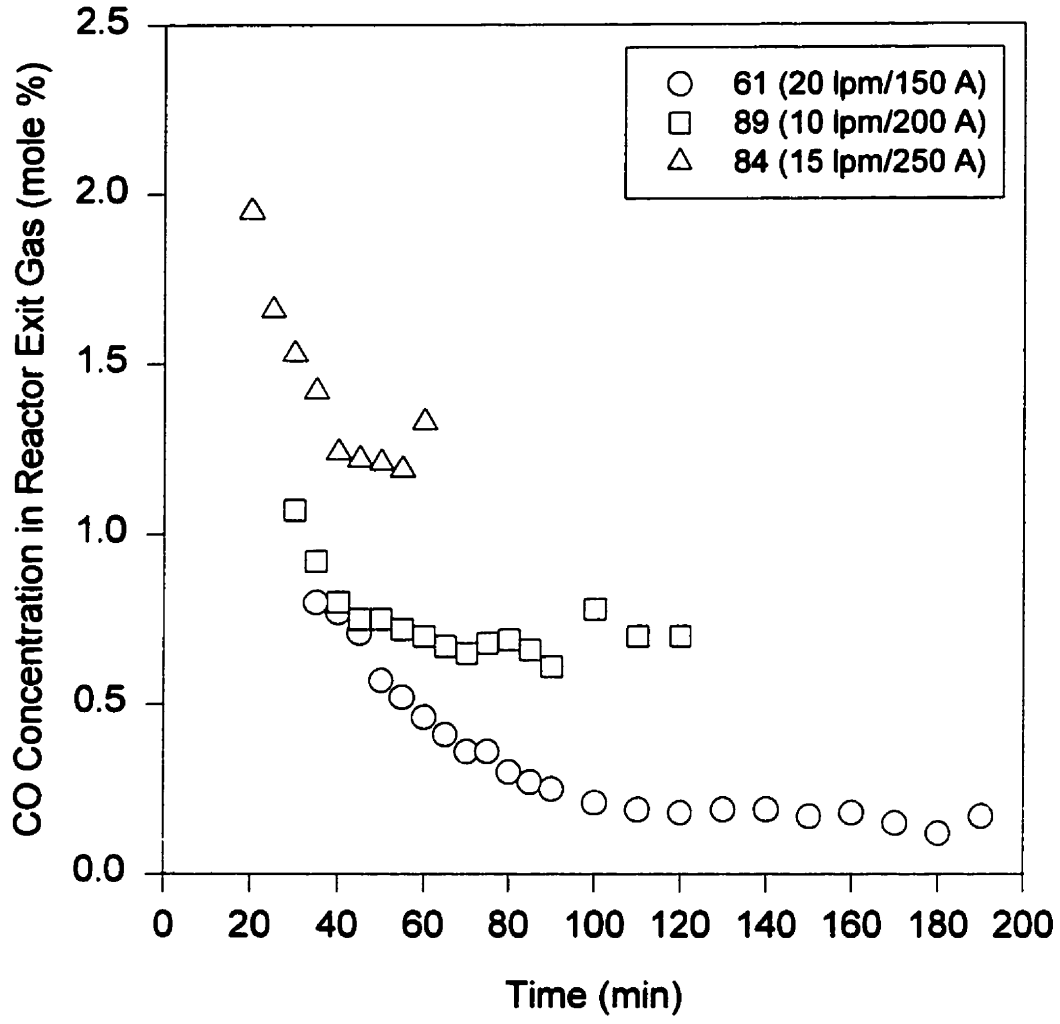

Figure 3.30 Typical CO concentration profiles in reactor exit gas during Ar plasma gas experiments.

$$y_{SiO} = \frac{F_{SiO}}{F_{Ar} + F_{SiO} + F_{CO}} \tag{3.15}$$

$$F_{SiO} = F_{CO} \tag{3.16}$$

where F_i is the molar flow rate of species i and y_{SiO} is the mole fraction of $SiO_{(g)}$ in the reactor exit gas. From Figure 3.30 we can see that the CO concentration was initially high due to the presence of air in the reactor. As the air was purged, the CO concentration attained its steady-state value which was determined by the rate of O_2 generation at the anode surface.

The steady-state CO concentrations in the reactor exit gas for the torch operating conditions examined are shown in Figure 3.31. To minimize the error associated with CO generation due to air in the reactor, the steady-state value was based on measurements made during the final stages of an experiment (see Table 3.9). At a current level of 150 A, the evaluation of the steady-state CO concentration only started after 90 minutes because of the low decomposition rate. For 200 and 250 A experiments, steady-state CO concentration was based on measurements after 60 and 40 minutes respectively. The correction required to the CO measurement due to $SiO_{(g)}$ condensation in the sampling tube was found to be negligible. From Figure 3.31 we see that the steady-state CO concentration increased with increasing current due to the increased rate of silica decomposition. When the plasma gas flow rate was increased, the CO concentration remained approximately constant at 150 A, decreased at 200 A and went through a minimum at 250 A. Since the decomposition rate did not vary with this parameter, a decrease would have been expected in all cases. The reason this was not observed at 150 A may have been due to the reduced accuracy of the CO meter at low concentrations (± 0.04 % CO). The increase in CO concentration at 20 lpm and 250 A was the result of the increased reaction at the silica/crucible interface.

To verify the use of the CO measurement to estimate y_{SiO} in the reactor exit gas, a comparison was made with the mass balance results shown in Table 3.7. The molar flow

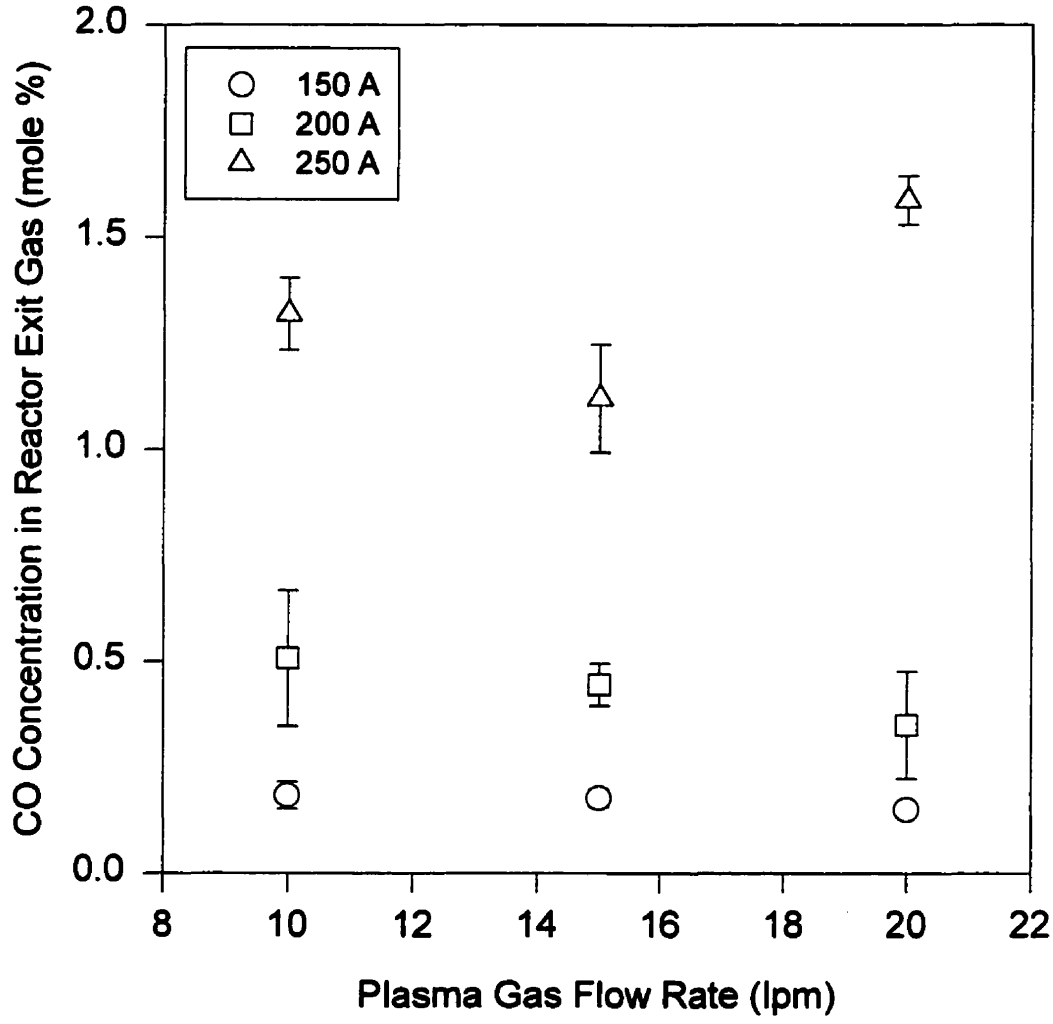

Figure 3.31 Steady-state CO concentration in reactor exit gas for Ar plasma gas experiments.

TABLE 3.10 Estimate of y_{SiO} in the reactor exit gas using mass balance results and CO concentration for Ar plasma gas experiments.

Plasma Gas Flow Rate [lpm]	***Current [A]***	***$SiO_{(g)}$ Concentration in Reactor Exit Gas [mole %]***	
		Mass Balance	$y_{SiO} = y_{CO}$
10	150	0.18	0.18
15	150	0.14	0.18
20	150	0.10	0.15
10	200	0.40	0.51
15	200	0.37	0.45
20	200	0.25	0.35
10	250	0.91	1.32
15	250	0.80	1.12
20	250	1.00	1.59

rate of $SiO_{(g)}$ exiting the reactor was estimated by subtracting from the overall mass of silica decomposed, the mass of the condensate remaining in the reactor assuming it was in the form of SiO_2. This was probably true since most of the condensate was white in color. The estimates of y_{SiO} using the mass balance results and the steady-state CO measurement are shown in Table 3.10. In general the agreement was reasonable, however, the $SiO_{(g)}$ concentration predicted by the CO measurement was consistently higher than that estimated using the mass balance results. This was mainly due to the fact that the mass balance estimate was based over the entire run whereas the CO measurement was only based on the final portion of the experiment. The instantaneous $SiO_{(g)}$ concentration in the reactor exit gas was therefore better represented by the CO concentration once the remaining air had been sufficiently purged from the reactor (see Table 3.9). An air leak was not thought to be the cause of a higher y_{CO} since the reactor was operated at 101.3 - 112 kPa. The discrepancy was greatest at 250 A because of the

short duration of these experiments (60 min compared to 120 and 180 min for 200 and 150 A respectively). The deviation was even greater at 20 lpm and 250 A because of the increased reaction at the anode/crucible interface which mainly resulted in $Si_{(l)}$ formation. From reaction 3.7 we see that this caused two moles of CO to be generated for every mole of silica decomposed instead of the one mole assumed in the mass balance calculation. If most of the silica decomposition at the crucible surface was described by reaction 3.1 then the deviation at 20 lpm and 250 A would have been expected to be similar to that observed for the lower plasma gas flow rates at this current. Of course, as can be seen from Table 3.9, some CO generation due to air in the reactor was still occurring during the final stages of an experiment and therefore also contributed to the discrepancy reported in Table 3.10.

3.4.2 Effect of Adding Hydrogen to the Plasma Gas

Most of the experiments conducted during this study used a pure Ar plasma gas. This facilitated experimentation and allowed a clearer investigation of the effect of plasma gas flow rate and current on the rate of silica decomposition. However, it is quite obvious that in any industrial application, the use of a reducing plasma gas such as H_2 would be required to improve the economics of the process (see Figure 2.11). The effect of H_2 addition to the plasma gas was therefore briefly investigated. The experiments performed are summarized in Table 3.11. Attempts to execute these experiments using the same procedure as was used for the Ar plasma gas experiments failed. When H_2 was added at the start of an experiment, transfer of the arc to a liquid anode surface was not possible. A few minutes after ignition, the quartz and NaOH particles in the center of the crucible had been decomposed and the arc struck the bottom of the crucible. It seemed that the liquid formed in the center was being decomposed too rapidly and not allowing the remainder of the quartz to melt. Because of this, a silica anode had to first be established using a pure Ar plasma gas before H_2 could be added. In addition, operation with H_2 was limited to low concentrations and short durations due to the higher

TABLE 3.11 Summary of experiments performed using an Ar/H_2 plasma gas.

Experiment	*Plasma Gas Flow Rate [lpm]*		*Current [A]*	*Time Interval [min - min]*
	Ar	*H_2*		
94	15	0	150	0 - 60
	15	0.44	150	60 - 90
	15	0	150	90 - 120
	15	0.20	150	120 - 150
	15	0	150	150 - 180
95	15	0	150	0 - 60
	15	0.20	150	60 - 90
	15	0	150	90 - 120
	15	0.44	150	120 - 150
	15	0	150	150 - 180
92	15	0	200	0 - 45
	15	0.44	200	45 - 60
	15	0	200	60 - 75
	15	0.20	200	75 - 90
	15	0	200	90 - 120

decomposition rates. Because plasma gas composition was varied during these experiments, the determination of the rate of silica decomposition by mass balance was not possible.

The results shown in Table 3.12 summarize the average conditions measured during each H_2 addition time interval. As expected, the addition of H_2 to the plasma gas increased the voltage. This was caused by a constriction of the arc resulting in a narrower, higher intensity plasma column. This effect was due to an increase in the thermal

TABLE 3.12 Summary of results for Ar/H_2 plasma gas experiments.

Exp.	*H_2 in Plasma Gas [mole %]*	*Temperature [K]*		*Voltage [V]*	*CO Concentration in Reactor Exit Gas [mole %]*
		Crucible	*Chamb. Wall*		
94	0	1770	1535	35.8	0.16
	2.8	1955	1709	50.8	1.64
	0	1846	1521	36.5	0.14
	1.3	1866	1542	46.3	0.82
	0	1817	1478	37.1	0.12
95	0	1725	1436	37.2	0.24
	1.3	1847	1540	45.3	0.84
	0	1814	1483	37.7	0.14
	2.8	1966	1638	54.3	1.76
	0	1855	1516	37.9	0.20
92	0	1898	1529	38.7	0.63
	2.8	2078	1751	52.9	2.95
	0	1994	1625	38.8	0.65
	1.3	2065	1715	47.4	1.68
	0	2020	1621	39.5	0.53

conductivity of the plasma gas (Boulos et al., 1994) which increased the rate of cooling of the arc at its fringes and reduced the cross sectional area for electrical conduction. The higher temperatures within the arc resulted in an increase in the rates of radiative and convective heat transfer to the anode. Convective heat transfer was further enhanced by the increased thermal conductivity due to the presence of H_2 in the plasma gas. However, since it was shown that convective heat transfer was reduced due to the efflux of decomposition products from the anode surface (see section 3.4.1.11), the increase in

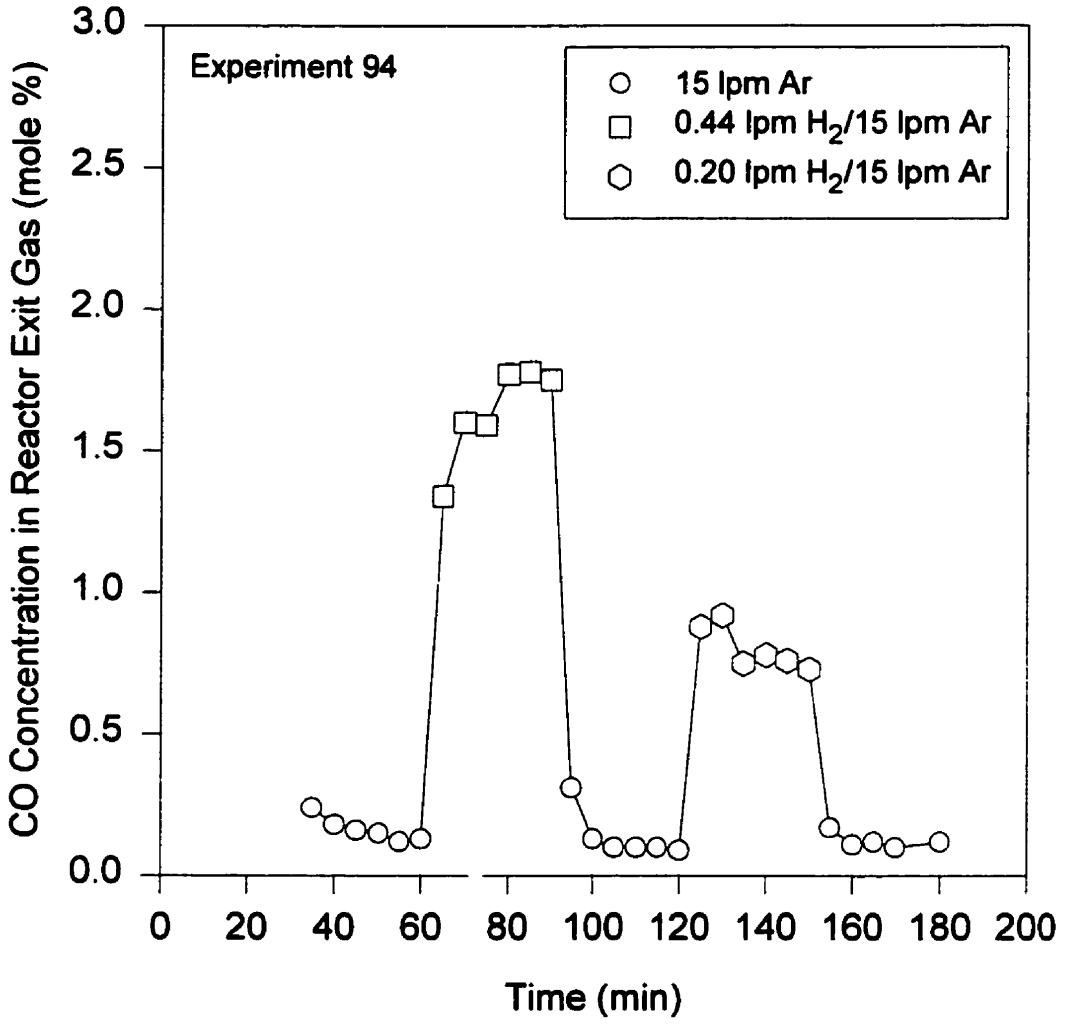

Figure 3.32 CO concentration profile in reactor exit gas for varying plasma gas composition during experiment 94.

crucible temperature upon H_2 addition (see Table 3.12) was more likely due to the increase in arc radiation. Figure 3.32 shows the profile of the CO concentration in the reactor exit gas during experiment 94. The addition of H_2 resulted in higher rates of silica decomposition at the anode surface which in turn resulted in higher concentrations of CO in the reactor exit gas.

The decomposition rate during H_2 addition was estimated using the average CO concentration in the reactor exit gas during this period. The following assumptions were made for this estimate:

1) $y_{O2} = y_{H2O} = 0$ (not detected during gas sampling).

2) $y_{SiO} = y_{CO}$.

3) Hydrogen is completely in the form of H_2 (not CH_4, C_2H_2 etc.).

4) Amount of $SiO_{(g)}$ condensing and being oxidized on surfaces within the reactor was negligible.

Using these assumptions the decomposition rate was calculated according to the following equations:

$$F_T = \frac{F_{Ar} + F_{H2}}{(1 - 2y_{CO})} \tag{3.17}$$

$$F_{SiO} = y_{CO}\ F_T = F_{SiO2} \tag{3.18}$$

where F_{SiO2} is the molar decomposition rate of silica. The estimates of the silica decomposition rates during H_2 addition are shown in Table 3.13. The accuracy of these estimates was verified by comparison with the average decomposition rates obtained by

TABLE 3.13 Estimate of silica decomposition rate for Ar/H_2 plasma gas experiments.

Exp.	*H_2 in Plasma Gas [mole %]*	*Estimated Decomposition Rate [g/min]*	*Average Decomposition Rate [g/min] Based on*	
			Estimates	*Mass Balance*
94	0	0.14[1]	0.34	0.37
	2.8	0.98		
	0	0.14		
	1.3	0.48		
	0	0.14		
95	0	0.14	0.35	0.44
	1.3	0.48		
	0	0.14		
	2.8	1.06		
	0	0.14		
92	0	0.21[2]	0.51	0.58
	2.8	1.81		
	0	0.21		
	1.3	1.00		
	0	0.21		

1. Average at 15 lpm Ar/150 A. 2. Average at 15 lpm Ar/200 A.

mass balance. The average decomposition rates based on the CO measurement were slightly lower than those from the mass balance results since some $SiO_{(g)}$ condensation and oxidation was occurring in the plasma chamber. From the results shown in Table 3.13, we can see that adding 1.3 % H_2 to the plasma gas increased the silica decomposition rate from 0.14 to 0.48 g/min at 15 lpm and 150 A and that the rate was approximately doubled (1.0 g/min) when the H_2 concentration was increased to 2.8 %.

TABLE 3.14 Comparison of specific energy requirement for silica decomposition using Ar and Ar/H_2 plasma gases.

Plasma Gas Flow Rate [lpm]	*Current [A]*	*Voltage[1] [V]*	*H_2 in Plasma Gas [mole %]*	*Decomposition Rate [g/min]*	*Specific Energy Requirement [kWh/kg]*
10	150	40.6	0	0.14	741
15	150	42.5	0	0.14	748
20	150	43.1	0	0.12	936
10	200	40.5	0	0.22	609
15	200	41.8	0	0.28	503
20	200	44.1	0	0.25	599
10	250	41.8	0	0.49	354
15	250	43.2	0	0.55	328
20	250	46.1	0	0.82	233
15.20	150	49.7	1.3	0.48	258
15.44	150	56.5	2.8	1.02	139
15.20	200	52.6	1.3	1.00	176
15.44	200	58.1	2.8	1.81	107

1. Includes voltage drop due to crucible stem (see section 3.4.1.8).

The increase in the silica decomposition rate when H_2 was added to the plasma gas was due to an increase in the heat input to the anode mainly by arc radiation and a consumption of O_2 via:

$$H_2 + \tfrac{1}{2}O_2 \rightarrow H_2O \qquad (3.19)$$

The above reaction resulted in a lowering of the boiling point which allowed

TABLE 3.15 Comparison of present transferred arc process with non-transferred process of Everest et al. (1973).

Study	*Torch System*	*Plasma Gas Flow Rate [lpm]*	*Power [kW]*	*Decomp. Rate [g/min]*	*Sp. Energy Requirement [kWh/kg]*
Everest et al. (1973)	non-transferred arc	Ar = 54 H_2 = 5.8	15.7	0.40	654
Present	transferred arc with silica anode	Ar = 15 H_2 = 0.44	11.6	1.81	107

decomposition to occur over a greater portion of the anode surface. We have seen from section 3.4.1.11 that once the anode surface attained its boiling point, decomposition was no longer mass transfer limited. The theoretical energy requirement for silica decomposition was also lowered when H_2 was added to the plasma gas (see Figure 2.11).

From Table 3.14 we can see that the specific energy requirement for silica decomposition was significantly reduced when an Ar/H_2 plasma gas was used. For the case of a pure Ar plasma gas, the efficiency of decomposition increased with increasing current and was not affected greatly by the plasma gas flow rate. As the current was increased, a greater portion of the anode surface attained the boiling point and therefore a greater portion of the heat input was being used for silica decomposition. When H_2 was added to the plasma gas, a dramatic increase in silica decomposition efficiency was observed. At approximately 15 lpm and 150 A, the addition of 2.8 % H_2 decreased the specific energy requirement from 748 to 139 kWh/kg.

Table 3.15 shows that, under similar operating conditions, the current process was able to attain a higher decomposition efficiency than the non-transferred arc system of Everest et al. (1973). Increasing the H_2 concentration in the plasma gas would probably result in an even lower specific energy requirement for the transferred arc process being

studied. Using the power rating and quartz feed rate reported by Schnell et al. (1978), a specific energy requirement of 10 kWh/kg was calculated for the non-transferred arc process used at Lonza Ltd. The reason for their high decomposition efficiency was the use of a reducing agent flow rate of 5 kg/h CH_4. The maximum H_2 flow rate used during this work was approximately 2.2 g/h H_2 which allowed an efficiency of 107 kWh/kg to be attained (see Table 3.15). The relatively high decomposition efficiency attained with such a low H_2 flow rate is promising and suggests that future work should concentrate on the use of a H_2 plasma gas.

Chapter 4 - MATHEMATICAL MODELING OF SILICA ANODE DECOMPOSITION

4.1 Introduction

A mathematical model of the silica anode in the transferred arc configuration used during this study was developed to gain a better understanding of the phenomena leading to silica decomposition. The model was to predict fluid flow, temperature and current distribution within the anode and the resulting silica decomposition rate from a knowledge of the torch operating parameters. Successful development of such a model will aid any future scale-up of the process. An existing arc model (Ming, 1994) was used to estimate the boundary conditions at the arc/anode interface.

4.2 Arc Model

The arc model used for this work was one developed by Ming (1994) in his study of high power transferred arcs. This model was used to simulate axisymmetric Ar transferred arcs at a current of 500 A and with lengths up to 20 cm. The numerical results obtained were found to be in good agreement with experimental measurements and given the similarities of the current system with that studied by Ming (1994), the model was thought to provide a good estimate of the arc/anode boundary conditions. The elliptic, laminar version of the arc model was selected since it was shown to accurately simulate short arc lengths (up to 5 cm).

Some modifications were required to account for the different torch and chamber geometry used in the current study. The modified torch and chamber geometry is shown schematically in Figure 4.1. The axial exit was replaced by a radial one located just above

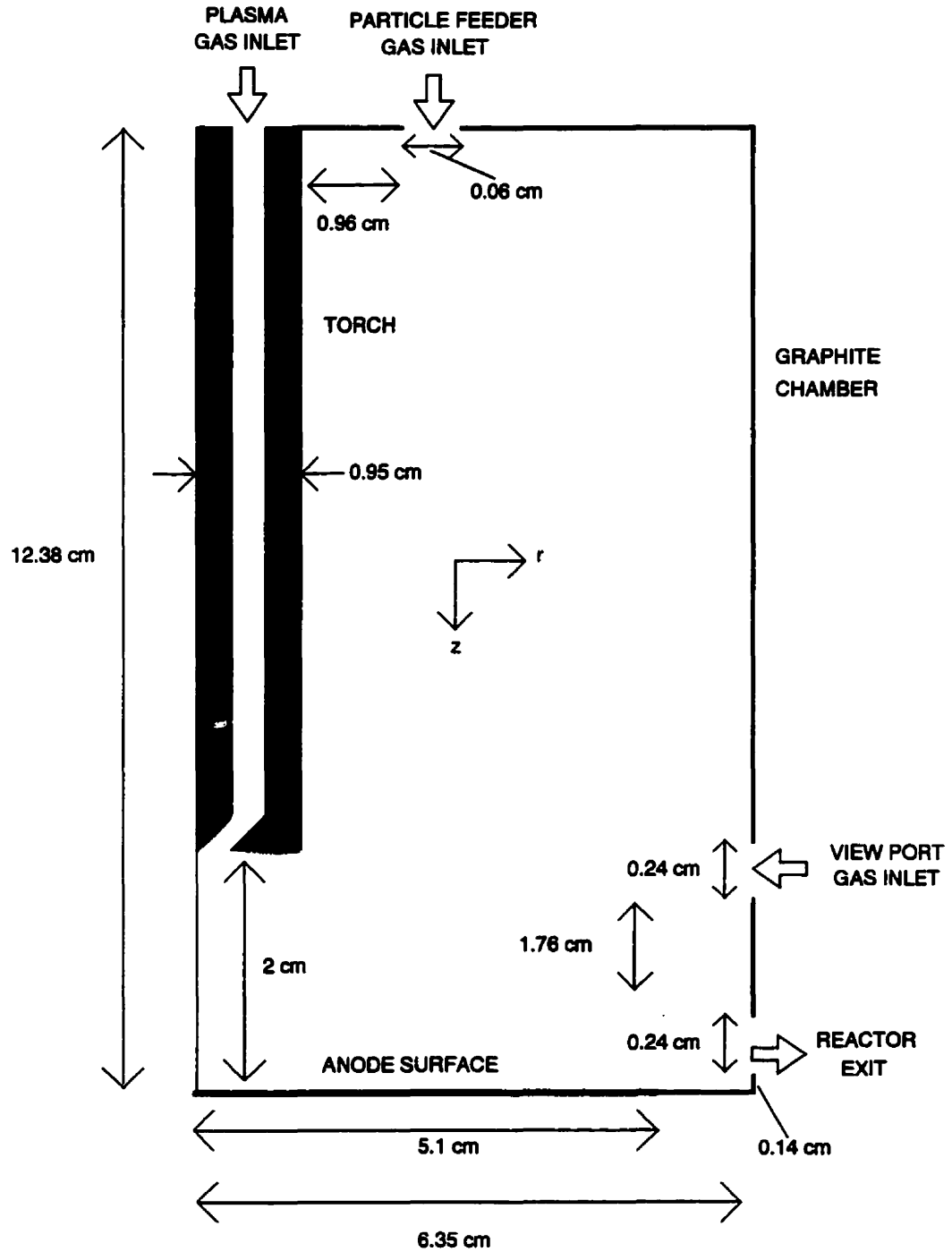

Figure 4.1 Modified torch and chamber geometry used with Ming (1994) arc model.

TABLE 4.1 Average steady-state crucible and chamber wall temperature for Ar plasma gas experiments.

Torch Operating Conditions		*Average Steady-State Temperature*	
Q_{plasma} *[lpm]*	*Current [A]*	*Crucible [K]*	*Chamber Wall [K]*
10	150	1758	1561
15	150	1758	1574
20	150	1738	1609
10	200	1892	1469
15	200	1866	1504
20	200	1889	1577
10	250	1983	1672
15	250	1978	1691
20	250	2023	1677

the top of the crucible in order to better simulate the actual chamber conditions (see Figure 3.2). In addition to the plasma gas inlet (10 - 20 lpm Ar), two more inlets were included to account for the Ar flow from the view port (3.6 lpm) and particle feeder (4.1 lpm). All feed gases were assumed to enter the system at 300 K. Due to the 2-D limitation of the arc model, all inlet and outlet gas flows were assumed to be axisymmetric. The area available for gas flow in non-axisymmetric situations was assumed to be equivalent to the actual area. For example, the area of the reactor exit slit was set equivalent to the cross sectional area of the exit tube (diameter = 3.5 cm). In general, the same boundary conditions were used with two exceptions. While Ming (1994) assumed a chamber temperature of 1000 K, the value used here was the average chamber wall temperature measured experimentally for a given set of torch operating conditions (see Table 4.1). The positions of the crucible and chamber wall temperature measurements are given in

section 3.2.3. The other notable exception was at the anode surface where the temperature would be determined by the model developed during this study. The effect of anode decomposition on arc behavior was not considered since the arc model was developed for a pure Ar plasma gas. A full description of the arc model is included in the Ph. D. thesis of Ming (1994) and is also summarized by Ming et al. (1993).

4.3 Anode Model

4.3.1 Assumptions

The anode model was based on the following assumptions some of which were derived from experimental observations of actual anode behavior:

1. The system is axisymmetric and operating at steady state.

2. The anode surface is not deformed significantly by the impinging plasma jet.

3. Fluid flow within the anode is laminar and a result of electromagnetic forces, buoyancy, surface shear stresses caused by the impinging plasma jet and surface tension gradients (Marangoni effect).

4. Silica decomposition occurs solely at the anode surface and is only significant in regions which have attained the boiling point. The rate of decomposition in these regions is determined by the surface heat balance.

5. The silica anode is in the vitreous state.

6. Arc radiation is absorbed internally by the anode since the surface is transparent.

7. Conduction is electronic.

Based on the configuration of the current transferred arc system, the anode was assumed to approach axisymmetric behavior. Deformation of the anode surface was not considered in the current model to simplify the geometry, however, some deformation was observed during experimentation. Fluid flow within the anode was assumed to be laminar because of silica's high viscosity. If the characteristic dimension of the given flow system is taken to be the maximum crucible diameter (10.2 cm), a velocity of 1 m/s would be required for a Reynolds number in the order of 10^1 at 3000 K. As will be shown in section 4.5.1, the maximum velocities within the anode were predicted to be < 1 mm/s. When reaction with the crucible was not significant, silica decomposition was believed to mainly occur in the center of the anode surface where the boiling point had been attained. In this region, the decomposition was not mass transfer limited and could be determined by the surface heat balance. Most of the silica anode was observed to be vitreous. The outer regions of the crucible where melting had not occurred were small and therefore not expected to greatly influence the conditions in the center of the anode where silica decomposition was occurring. Because the anode surface was transparent, arc radiation was assumed to be absorbed internally. Conduction was assumed electronic since electrolytic conduction was believed to be minor.

4.3.2 Governing Equations

Because of the axisymmetric assumption, the governing equations were expressed in terms of cylindrical coordinates where z and r represent the axial and radial direction respectively.

a) Continuity:

$$\nabla \cdot (\rho \bar{u}) = 0 \tag{4.1}$$

b) Momentum:

$$\nabla \cdot (\rho u \bar{u}) = \nabla \cdot (\mu \nabla u) - \frac{\partial P}{\partial z} + S_u \tag{4.2}$$

$$S_u = \frac{1}{r}\frac{\partial}{\partial r}(r\mu \frac{\partial v}{\partial z}) + \frac{\partial}{\partial z}(\mu \frac{\partial u}{\partial z}) - \frac{2}{3}\frac{\partial}{\partial z}(\mu \nabla \cdot \bar{u}) + j_r B_\theta - (\rho - \rho_o) g \tag{4.3}$$

$$\nabla \cdot (\rho v \bar{u}) = \nabla \cdot (\mu \nabla v) - \frac{\partial P}{\partial r} + S_v \tag{4.4}$$

$$S_v = \frac{1}{r}\frac{\partial}{\partial r}(r\mu \frac{\partial v}{\partial r}) + \frac{\partial}{\partial z}(\mu \frac{\partial u}{\partial r}) - \frac{2}{3}\frac{1}{r}\frac{\partial}{\partial r}(r\mu \nabla \cdot \bar{u}) + \frac{2}{3}\frac{\mu}{r}(\nabla \cdot \bar{u}) - 2\frac{\mu v}{r^2} - j_z B_\theta \tag{4.5}$$

The buoyancy force on a fluid element of density ρ_o by the displaced fluid with density ρ is accounted for by the last term in equation 4.3. The electromagnetic force is the product of the current density (j_z or j_r) and the self-induced magnetic field B_θ, which is given by Ampere's law:

$$B_\theta = \frac{\mu_o}{r}\int_0^r r\, j_z\, dr \tag{4.6}$$

where μ_o is the permeability of vacuum. The axial and radial current densities can be expressed by the electric potential gradient:

$$j_z = -\frac{1}{\rho_e}\frac{\partial \phi}{\partial z} \qquad\qquad j_r = -\frac{1}{\rho_e}\frac{\partial \phi}{\partial r} \tag{4.7}$$

where ϕ is the electric potential and ρ_e is electrical resistivity.

c) Energy:

The energy equation can be written in terms of temperature because of the constant heat capacity of silica:

$$\nabla \cdot (\rho T \bar{u}) = \nabla \cdot (\frac{k}{C_p}\nabla T) + S_T \tag{4.8}$$

$$S_T = \frac{\rho_e\,(j_z^2 + j_r^2)}{C_p} + S_{absorb} \tag{4.9}$$

Resistance heating is accounted for by the first term in equation 4.9 while the second term accounts for the volumetric heat generation within the anode due to absorption of arc radiation. An estimate of S_{absorb} will be given later.

d) Current continuity:

$$\nabla \cdot (\frac{1}{\rho_e}\nabla \phi) = 0 \tag{4.10}$$

TABLE 4.2 Boundary conditions for anode calculation domain shown in Figure 4.2.

Boundary	***Variable***			
	u	v	T	ϕ
AB	$u = 0$	$-\mu\, \partial v/\partial z = \tau_{surf}$	$-k\, \partial T/\partial z = q_{surf}$	$-1/\rho_e\, \partial\phi/\partial z = j_{z,surf}$
BC	$u = 0$	$v = 0$	$T = T_{cruc}$	ϕ = constant
CD	$u = 0$	$v = 0$	$T = T_{cruc}$	ϕ = constant
DA[1]	$\partial u/\partial r = 0$	$v = 0$	$\partial T/\partial r = 0$	$\partial\phi/\partial r = 0$

1. Axis of symmetry.

4.3.3 Boundary Conditions

The calculation domain for the anode model is shown schematically in Figure 4.2. The governing equations were only solved for the silica phase of the anode. The graphite crucible was assumed to be a solid boundary at a uniform temperature. The relevant boundary conditions are summarized in Table 4.2. Boundary DA in Figure 4.2 represents the axis of symmetry for the calculation domain. Symmetry is assumed for u, T and ϕ while v must be set to zero at this boundary. Along the solid graphite surface (BC and CD), the velocities are set to zero and the temperature is specified as the average steady-state crucible temperature measured for a given plasma gas flow rate and current (see Table 4.1). The electric potential is set to a constant value at the solid surface since there was a negligible voltage drop through the crucible body.

The top surface of the anode (AB) is where the boundary conditions become more complex. The electric potential gradient at the surface is determined by the axial current density distribution at the arc/anode interface $j_{z,surf}$, which is predicted by the arc model for a given set of torch operating conditions. The temperature gradient at the anode surface is determined by q_{surf}:

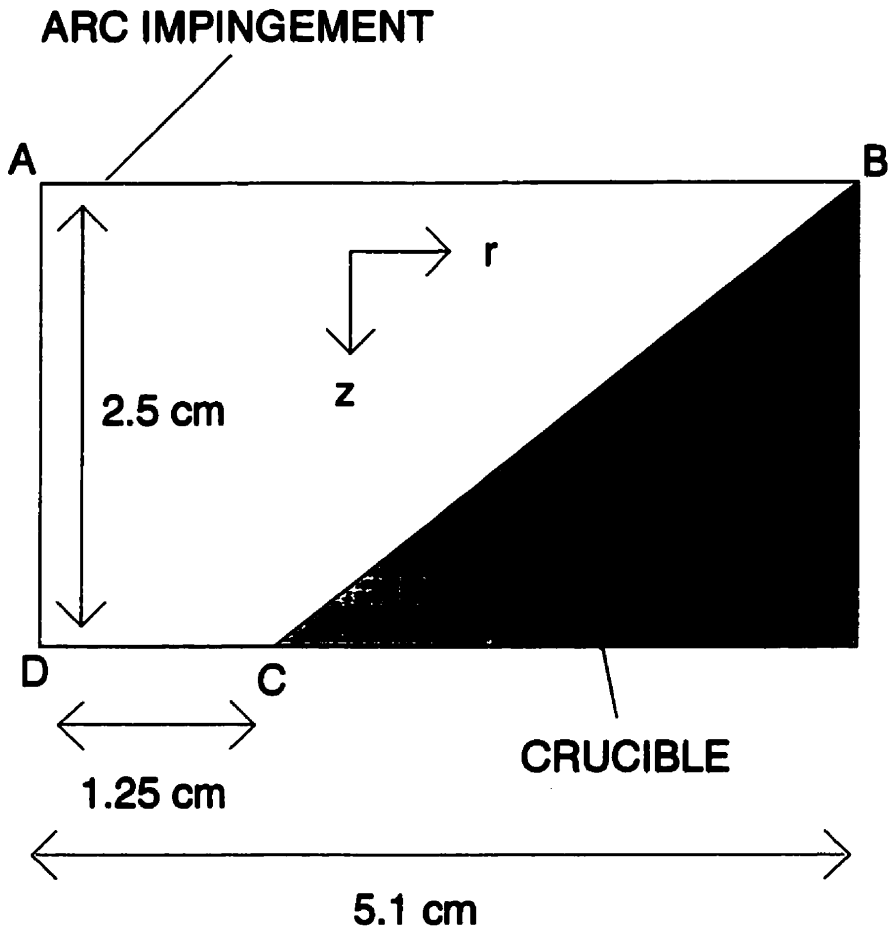

Figure 4.2 Axisymmetric calculation domain for anode model.

$$q_{surf} = q_{conv} + q_{elec} - q_{rad,out} - q_{decomp} \tag{4.11a}$$

$$q_{surf} = -k \frac{\partial T}{\partial z} \tag{4.11b}$$

where k is the thermal conductivity of silica. The heat flux to the anode surface is a result of convection (q_{conv}) and electron flow (q_{elec}). The arc radiation heat flux ($q_{rad,in}$) was not included in equation 4.11a since the surface was transparent. This heat input is assumed to be absorbed within the anode and is accounted for by S_{absorb}. The anode surface is cooled by radiation ($q_{rad,out}$) and silica decomposition (q_{decomp}).

The convective heat input was estimated using (Eckert and Pfender, 1967):

$$q_{conv} = h_T (H_e - H_a) \tag{4.12}$$

where h_T is the heat transfer coefficient and H is the gas enthalpy. The subscripts a and e refer to the anode surface and the edge of the thermal boundary layer respectively. The heat transfer coefficient in equation 4.12 is given by the following Nusselt number correlation:

$$Nu_a = 0.90\,\mathrm{Re}_a^{0.5}\,\mathrm{Pr}_a^{0.25}\left(\frac{\rho_e\,\mu_e}{\rho_a\,\mu_a}\right)^{0.43} = \frac{h_T\,C_{p,a}\,r}{k_a} \tag{4.13}$$

$$\mathrm{Re}_a = \frac{\rho_a\,v_e\,r}{\mu_a} \tag{4.14}$$

$$\mathrm{Pr}_a = \frac{C_{p,a}\,\mu_a}{k_a} \tag{4.15}$$

where v is the radial velocity, ρ is the mass density, μ is the viscosity, C_p is the heat

capacity and k is the thermal conductivity of the gas. The above correlation has been used previously by Backer and Szekely (1987) and Gu (1993) to estimate the convective heat transfer to a metal anode surface from an impinging arc. The edge of the thermal boundary layer was determined from film theory (Bird et al., 1960):

$$\delta_T = \frac{k_a}{h_T C_{P,a}} \tag{4.16}$$

where δ_T is the thermal boundary layer thickness.

The heat flux due to electron flow for positive anode fall potentials can be expressed as (Backer and Szekely, 1987):

$$q_{elec} = j_{z,surf}\left(\frac{5k_B}{2e_o}(T_{e,e} - T_{e,a}) + V_{anode} + \phi_w\right) \tag{4.17}$$

where k_B is the Boltzmann constant, e_o is the elementary charge, T_e is the electron temperature, V_{anode} is the anode fall potential and ϕ_w is the work function of the anode material. The electron temperature at the edge of the boundary layer was assumed to be equivalent to that of the gas since the plasma in this region was in LTE (Local Thermodynamic Equilibrium), while $T_{e,a}$ was set equal to the anode surface temperature. The first term in equation 4.17 accounts for the thermal energy of the electrons entering the anode (~ 2 V). The second is due to the energy acquired by the electrons as they are accelerated through the anode fall zone. The final term accounts for the potential energy difference of the electrons in the plasma and anode phases. This term can be thought of as the energy released due to the condensation of electrons which are free in the plasma phase and become associated with the anode material as they enter the surface.

The radiation heat flux to a point on the anode surface from the arc column can be estimated using the method of McKelliget and Szekely (1986):

$$q_{rad,in,j} = \int_{V_j} \frac{S_r}{4\pi r_j^2} \cos\psi \, dV_j \tag{4.18}$$

where $q_{rad,in,j}$ is the radiation flux received by a surface element from plasma volume V_j, S_r is the volumetric radiation density which accounts for the net radiation emitted by a plasma volume which is not re-absorbed, r_j is the distance from the surface element to the plasma volume and ψ is the angle that r_j makes with the normal to the surface element. By summing $q_{rad,in,j}$ over the entire plasma volume, an estimate of the net arc radiation flux to an element on the anode surface ($q_{rad,in}$) can be made. The arc model prediction of the temperature distribution within the plasma phase was required to calculate $q_{rad,in}$ since S_r is a function of temperature. The volumetric radiation density (S_r) data was available through the arc model and was calculated by Ming (1994) using the net emission coefficient method which is described by Essoltani et al. (1994). Given that the reflectivity of glass is usually small (McLellan and Shand, 1984), arc radiation was assumed to be absorbed completely and uniformly within the silica anode. The term in equation 4.9 which approximates this is expressed as:

$$S_{absorb} = \frac{q_{rad,in}}{z_{cruc} C_p} \tag{4.19}$$

where z_{cruc} is the depth of the silica anode at the radial position where $q_{rad,in}$ is evaluated. This over simplification was required because not enough was known about the absorption characteristics of the anode. Absorption was assumed complete since the bottom of the anode was opaque (see Figures 3.16 - 3.18). The radiation emitted by the silica anode surface is estimated by assuming that each surface element behaves as a small body in a large enclosure:

$$q_{rad,out} = \varepsilon \sigma (T_a^4 - T_{surr}^4) \tag{4.20}$$

where ε is the emissivity of silica (assumed constant), σ is the Stefan-Boltzmann constant, T_a is the anode surface temperature and T_{surr} is the temperature of the enclosure. In this case, T_{surr} was set equal to the average steady-state chamber wall temperature measured for a given set of torch operating conditions ($T_{surr} = T_{chamb}$).

The heat removed from the surface through decomposition is simply the product of the decomposition flux D_{SiO2}, and the heat of decomposition ΔH_{decomp}:

$$q_{decomp} = \Delta H_{decomp} D_{SiO2} \tag{4.21}$$

Because decomposition was assumed to be negligible when the surface was maintained below its boiling point, q_{decomp} was set equal to zero in these areas. If the boiling point was reached, q_{decomp} was determined by subtracting the heat flux required to bring the surface to its boiling point from the total heat flux input. The procedure for the anode surface heat balance and the determination of D_{SiO2} can be summarized as follows:

1. Assume $q_{decomp} = 0$.

2. Calculate q_{conv}, q_{elec} and $q_{rad.out}$.

3. Calculate q_{surf} using equation 4.11a.

4. Solve for T_a using equation 4.11b.

5. If $T_a < T_{boil}$ then $D_{SiO2} = 0$.

6. If $T_a > T_{boil}$ then set $T_a = T_{boil}$ and determine q_{decomp} using the following equation:

$$q_{decomp} = q_{surf} - \frac{(T_{boil} - T_{\Delta z})\,k}{\Delta z} \tag{4.22}$$

where T_{boil} is the boiling point of silica, $T_{\Delta z}$ is anode temperature just below the surface and Δz is a small axial distance below the anode surface. The decomposition flux is determined by equation 4.21 since q_{decomp} is now known. The heat of decomposition was assumed to include the heat of reaction of:

$$SiO_2 \rightarrow SiO_{(g)} + \tfrac{1}{2}O_2 \tag{4.23}$$

and the heat required to bring the silica feed (in the form of quartz) from 300 K to T_{boil}.

The radial velocity gradient at the anode surface is determined by the surface shear stress which is the result of the high velocity gas flow due to arc impingement and the surface tension gradient:

$$\tau_{surf} = \tau_{arc} + \frac{\partial T}{\partial r}\frac{\partial \gamma}{\partial T} \tag{4.24}$$

where γ is the surface tension of silica. The surface shear stress due to the arc can be estimated using the heat transfer correlation described by equations 4.13 - 4.15 and applying the Chilton-Colburn analogy (Bird et al., 1960):

$$\frac{1}{2} f = j_H = Nu_a \, Re_a^{-1} \, Pr_a^{-1/3} \tag{4.25}$$

$$\tau_{arc} = \frac{1}{2} f \, \rho_a \, v_e^2 \tag{4.26}$$

where j_H is the Chilton-Colburn j-factor for heat transfer and f is the friction factor. The

velocity boundary layer thickness was also determined from film theory (Bird et al., 1960):

$$\delta_v = \frac{\mu_a}{\frac{1}{2} f \rho_a v_e} \tag{4.27}$$

and was found to be approximately equal to δ_T. Typical profiles of the predicted thermal boundary layer thickness along the anode surface are given in Figure 4.3. Values in the arc root region (radius ~ 1 cm) ranged from 0 - 0.5 mm which is similar to that predicted by Dinulescu and Pfender (1980).

4.3.4 Solution Procedure

The governing equations were solved using an iterative, finite difference algorithm known as SIMPLER (Patankar, 1980). This algorithm has been used extensively by a variety of authors for this type of modeling work (Ming, 1994, Gu, 1993 and Hsu et al., 1983). The axisymmetric calculation grid for the arc and anode models is shown in Figure 4.4. A finer grid was used in regions where large gradients in velocity, temperature and electric potential were expected. The grid size (axial x radial) was 64 x 48 for the arc model and 31 x 35 for the anode model.

Because of a common boundary, the solution of each model required an interactive iteration procedure summarized below:

1. Provide an initial guess of the anode surface temperature profile for the arc model and execute for a given number of iterations.

2. Use the output after the final iteration to estimate q_{surf}, $j_{z,surf}$ and τ_{surf} and execute the anode model for a given number of iterations.

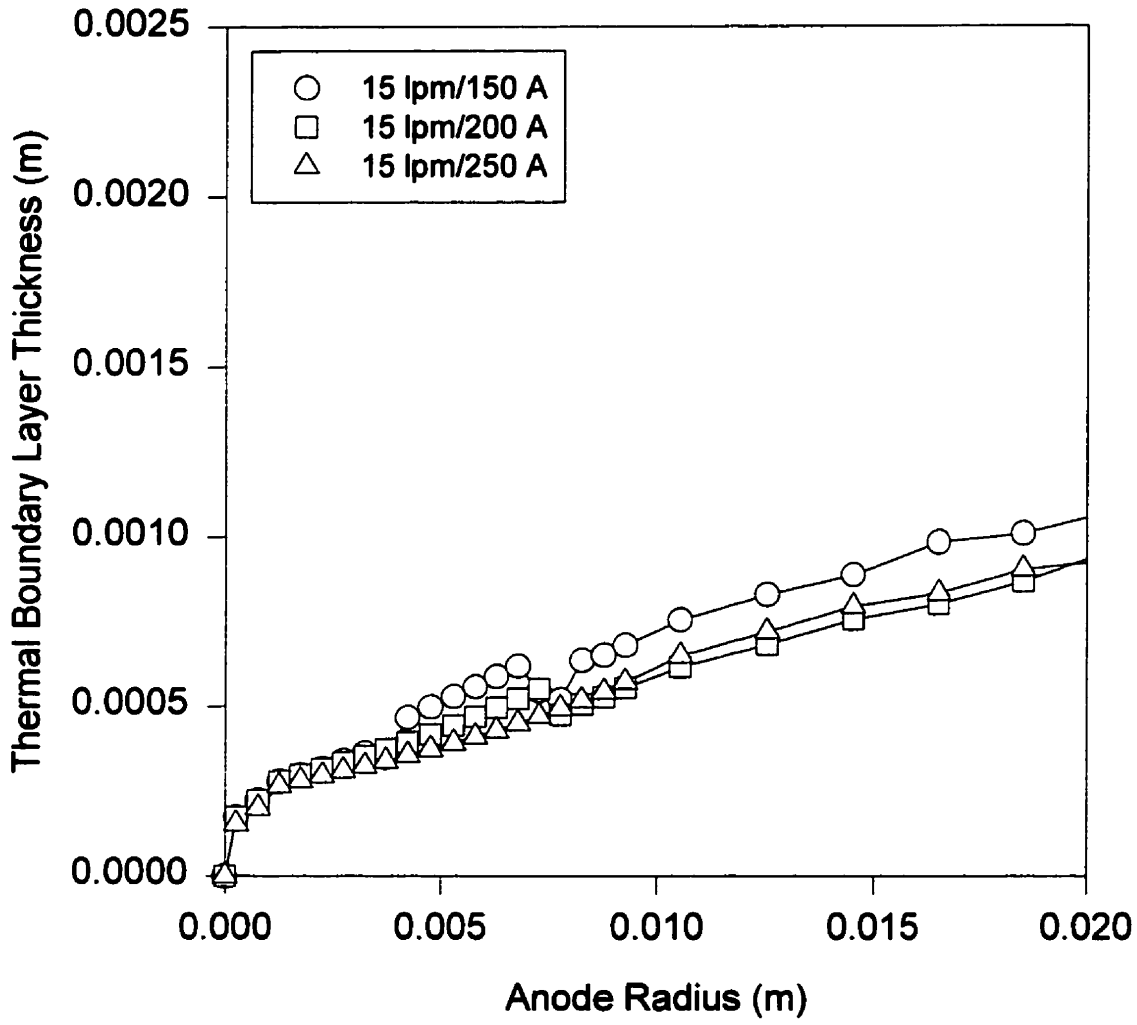

Figure 4.3 Predicted thermal boundary layer thickness along the anode surface at a plasma gas flow rate of 15 lpm.

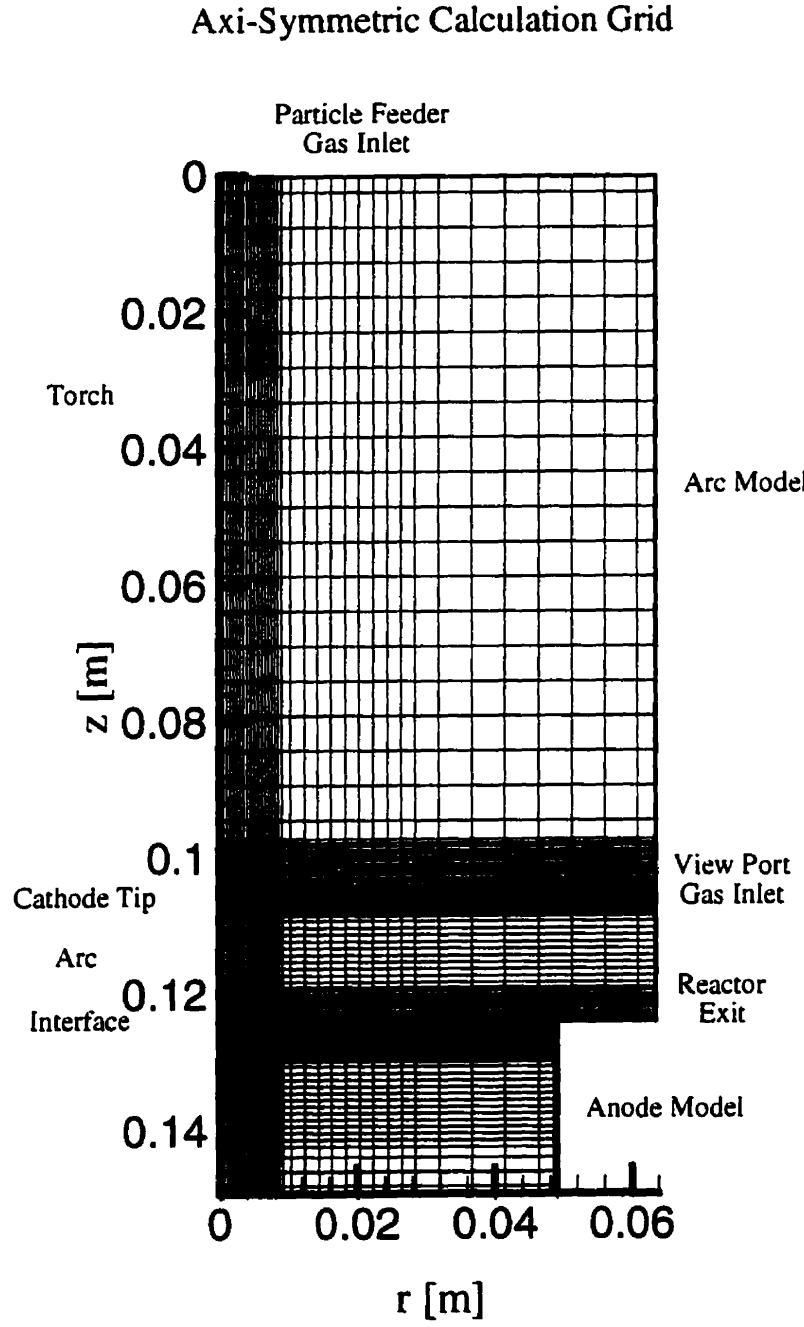

Figure 4.4 Axisymmetric calculation grid for arc and anode models.

3. Input the new anode surface temperature profile following the final iteration into the arc model and execute for a given number of iterations.

4. Repeat steps 2 and 3 until solutions to both models are converged.

The criteria for convergence was based on the method used by Njah et al. (1993) and can be summarized by the following equation:

$$\frac{\Delta\zeta_{max}}{\zeta_{max}} \times 100 < 0.001\% \tag{4.28}$$

where $\Delta\zeta_{max}$ is the maximum change for variable ζ in a given calculation domain from one iteration to the next and ζ_{max} is its maximum value. When equation 4.28 was true for all variables and the overall mass, energy and current balance was satisfied, the solution was assumed to be converged.

4.4 Silica Property Estimation

A summary of the silica properties used with the anode model can be found in Table 4.3. The sources and methods used for these estimates are briefly discussed below.

4.4.1 Density

The density of silica as a function of temperature was determined by linearly regressing the data of Bacon et al. (1960) along with the value at 2000 K given by F*A*C*T. The data and the regression line can be seen in Figure 4.5.

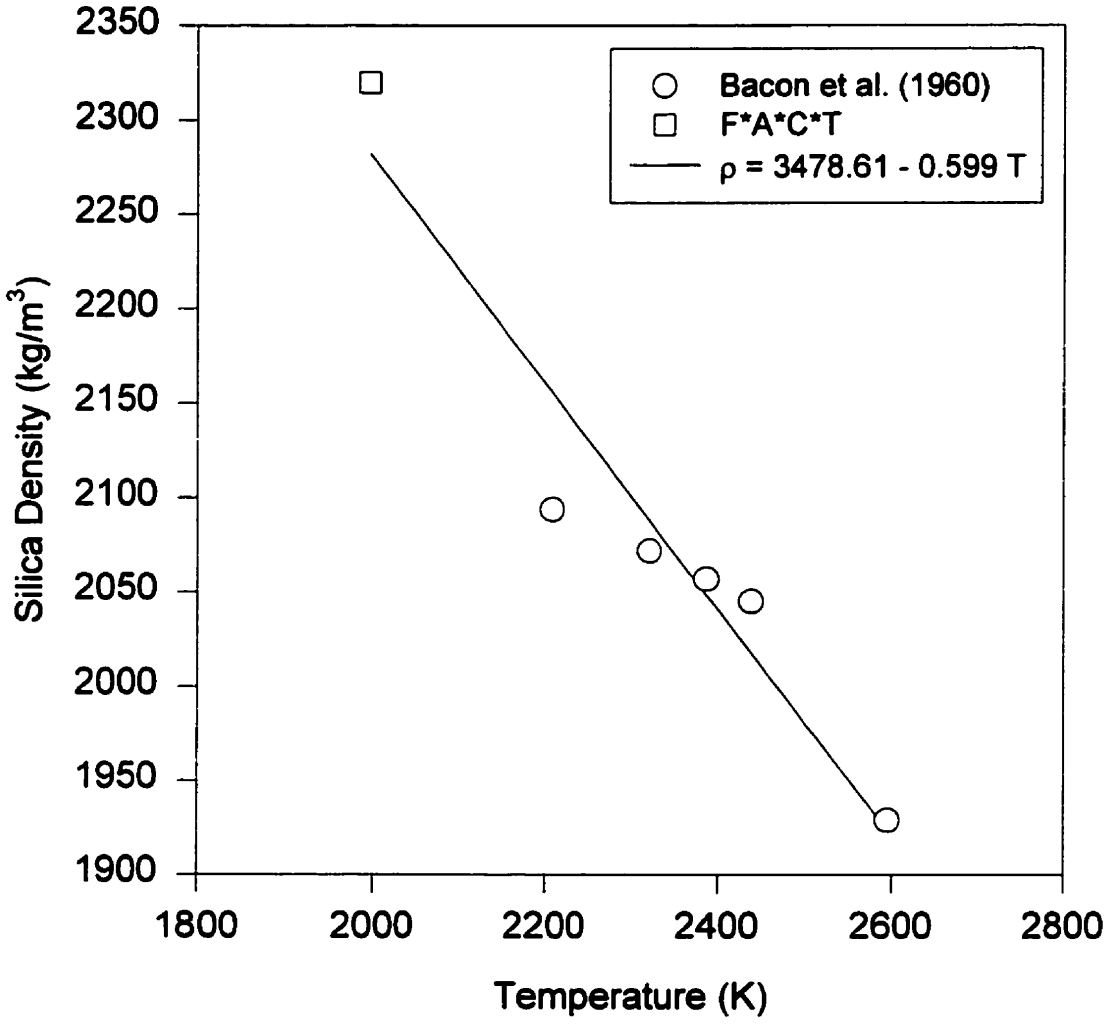

Figure 4.5 Silica density data and regression equation.

TABLE 4.3 Estimated properties of vitreous silica as a function of temperature.

Property	*Equation Used in Anode Model (T in Kelvin)*
ρ [kg/m^3]	$3478.61 - 0.599T$
μ [Pa s]	$Ae^{U/RT}$ $A = 1.02\times10^{-8}$ Pa s $U = 5.37\times10^5$ J/mol
γ [N/m]	$0.307 + 3.1\times10^{-4}(T - 2073)$
C_p [J/kg K]	1427.51
k [W/m K]	$A + BT + CT^2$ $A = 2.89$ W/m K, $B = -5.29\times10^{-3}$ W/m K^2, $C = 5.05\times10^{-6}$ W/m K^3
ρ_e [ohm m]	$Ae^{U/RT}$ $A = 3.86\times10^{-12}$ ohm m $U = 3.63\times10^5$ J/mol

4.4.2 Viscosity

The viscosity of silica has been determined experimentally by various authors (Bacon and Hasapis, 1959 and Bacon et al., 1960). Data from a more recent study (Urbain et al., 1982) were used to estimate the dependence of silica viscosity on temperature. As is the case for most liquids, the viscosity decreases exponentially with increasing temperature (see Table 4.3).

4.4.3 Surface Tension

The surface tension of silica as a function of temperature was estimated using the data reported by Kingery (1959). Unlike liquid metals, the surface tension of silica increases with temperature. At 2073 K a surface tension of 0.307 N/m was reported and the temperature dependence was estimated to be 3.1×10^{-4} N/m K. A linear extrapolation of surface tension was made from the above data (see Table 4.3).

4.4.4 Heat Capacity

According to F*A*C*T (Thompson et al., 1996), the heat capacity of vitreous silica is constant at 1427.51 J/kg K.

4.4.5 Thermal Conductivity

Heat transport through vitreous materials is the result of conduction and radiation. Because of this, an effective thermal conductivity which combines both contributions is usually defined. At low temperatures the dominant mechanism is conduction while above 673 K, the radiation effect must be accounted for (McLellan and Shand, 1984). Using the data given by Scholze (1991), the effective thermal conductivity of vitreous silica was estimated. The regression equation for the thermal conductivity is given in Table 4.3. Since the data were limited to low temperature, the thermal conductivity above 1600 K was extrapolated.

4.4.6 Electrical Resistivity

The electrical resistivity of the current silica anode was estimated using the data of Veltri (1963) and experimental observations of anode voltage. The electrical resistivity was assumed to decrease exponentially with temperature:

$$\rho_e = A\, e^{U/RT} \tag{4.29}$$

where A is a constant, U is the activation energy and R is the molar gas constant. The value of U was set to 363 kJ/mol which was estimated by Veltri (1963) in the temperature range 1658 - 2753 K. The value of A was estimated to be 3.86×10^{-9} ohm m when the data of Veltri (1963) were regressed using the above activation energy. Use of these values

resulted in the prediction of much greater anode voltages than were observed experimentally. The suspected cause of this was the reduced purity of the present silica anode (see Table 3.5) compared to that analyzed by Veltri (1963) (impurities in ppm: < 1 Fe, < 1 Cu, < 0.1 B, 2 Al). A lower electrical resistivity was also measured by Cohen (1957) whose silica sample had a total impurity content of 0.2 %, however, this data could not be used here because it was limited to 1291 - 1685 K. The reduced resistivity was obviously the result of an increase in the number of available charge carriers. This was not believed to be due to an increase in ionic conduction since Na^+ was the only significant ionic impurity and its contribution was negligible (see section 3.4.1.4). A more likely reason was donor or acceptor type semiconduction which has been associated with impurities in oxides (Hove and Riley, 1965). The reduced electrical resistivity of the present silica anode was accounted for by multiplying A by a factor of 1.0×10^{-3}. This factor was chosen because it allowed the prediction of anode voltages in the same range as those measured experimentally. A plot of the Veltri (1963) data and the electrical resistivity equation used with the anode model can be seen in Figure 4.6.

4.5 Simulation Results

4.5.1 Base Case

A base case simulation was executed to predict the silica decomposition rate for the torch operating conditions used during this study (pure Ar plasma gas only). The parameters selected as base case variables were the boiling point, anode fall potential, work function and emissivity. The values used for the base case simulation are summarized in Table 4.4. Since not enough was known about the state of the equilibrium gas above the boiling liquid surface (pressure and composition), the boiling point was assumed to be that which corresponded to the average reactor pressure during the decomposition experiments (107 kPa). From Table 2.5 we see that F*A*C*T predicts this

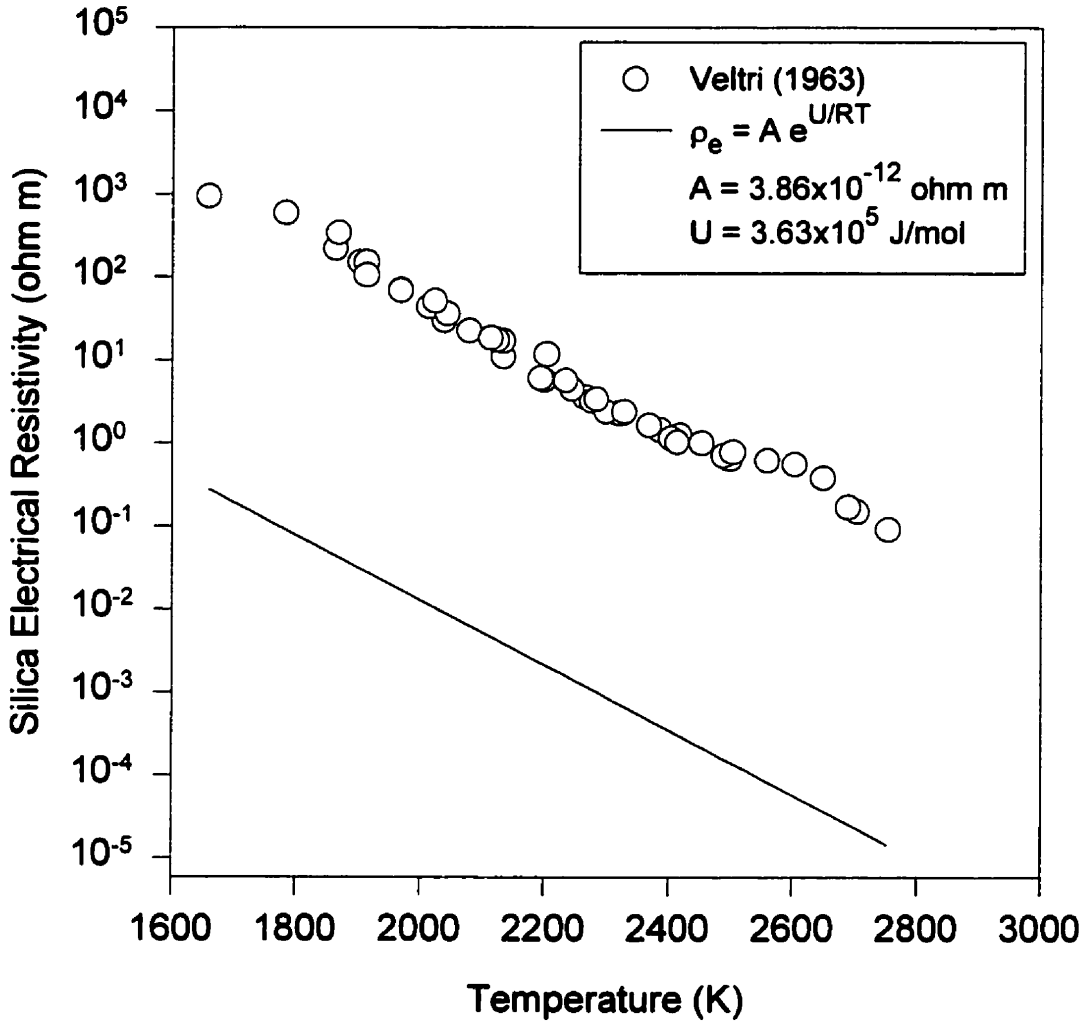

Figure 4.6 Electrical resistivity of silica according to Veltri (1963) and estimate used in anode model.

TABLE 4.4 Summary of base case conditions.

Condition	*Base Case Value*
boiling point	3159 K
anode fall potential	0 V
work function	2.0 V
emissivity	0.5

to be 3159 K. For the case of a high intensity Ar arc striking a water-cooled anode surface, the anode fall potential is expected to be positive for a constricted arc root and negative for a diffuse attachment (Sanders and Pfender, 1984 and Pfender, 1997). The magnitude of this voltage drop is estimated to be in the order of 1 V (Dinulescu and Pfender, 1980). Although the arc root at the silica anode surface seemed diffuse from visual observations, there was still some degree of uncertainty in this parameter since the present case dealt with a hot molten anode. The anode fall potential for the base case was therefore set at 0 V. We will see in the following section that this amounted to assuming a negligible positive anode fall. Data could not be found on the work function of silica. A value of 2.0 V was used for the base case simulation which was in the range of those reported for other oxides (Rivière, 1969). Data on the emissivity of vitreous silica at high temperatures (2000 - 3200 K) was also not available. The emissivity of quartz glass has been reported to decrease from 0.96 to 0.66 when temperature is increased from 533 to 811 K (Sparrow and Cess, 1978). A further decrease was expected at even higher temperatures so a constant value of 0.5 was assumed. The sensitivity of the predicted decomposition rates to variations in the base case assumptions will be examined in the following section.

Typical results from the base case simulation can be seen in Figures 4.7 - 4.12. Figure 4.7 shows the temperature distribution of the plasma gas impinging on the anode surface. Temperatures within the plasma phase just above the arc root (radius ~ 1 cm) ranged from 8000 - 14 000 K. The anode temperature distribution can be seen more

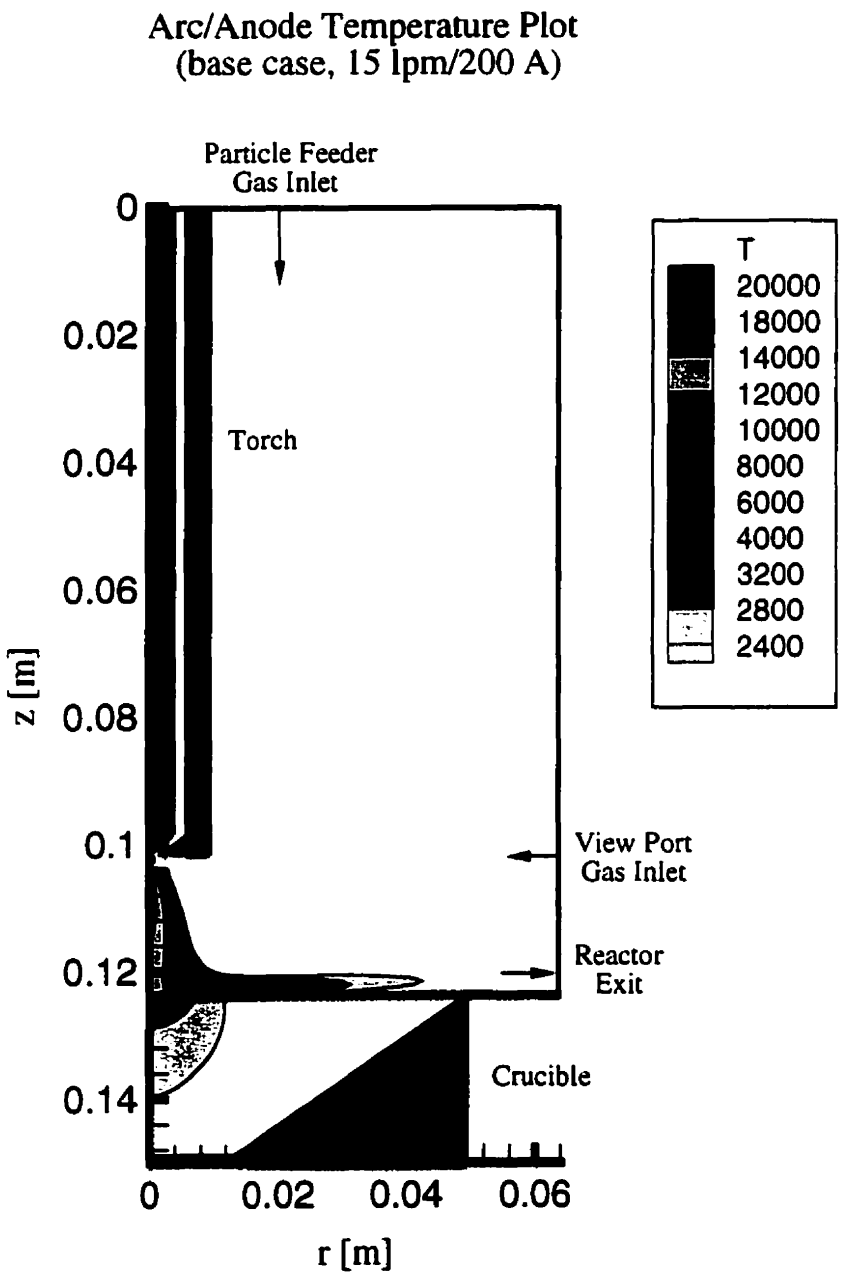

Figure 4.7 Arc/anode temperature plot at a plasma gas flow rate of 15 lpm and a current of 200 A (temperature in K).

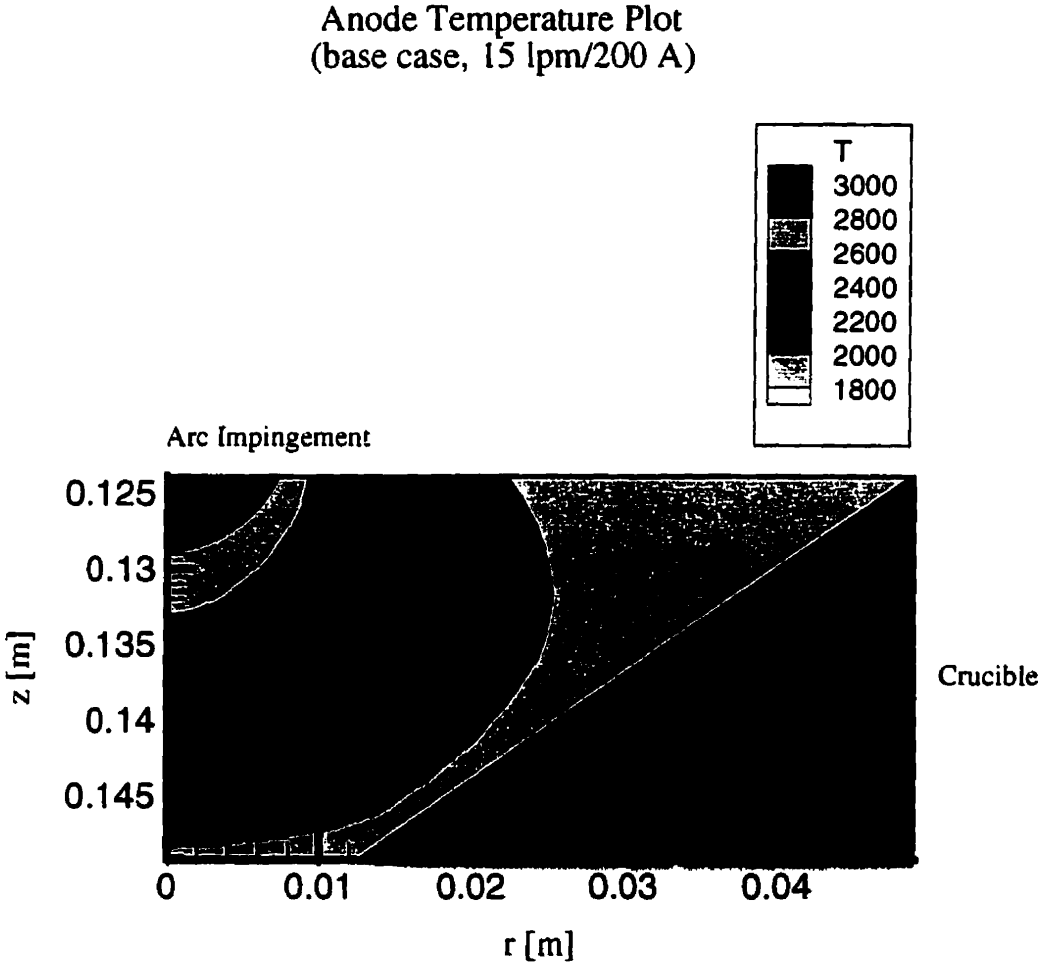

Figure 4.8 Anode temperature plot at a plasma gas flow rate of 15 lpm and a current of 200 A (temperature in K).

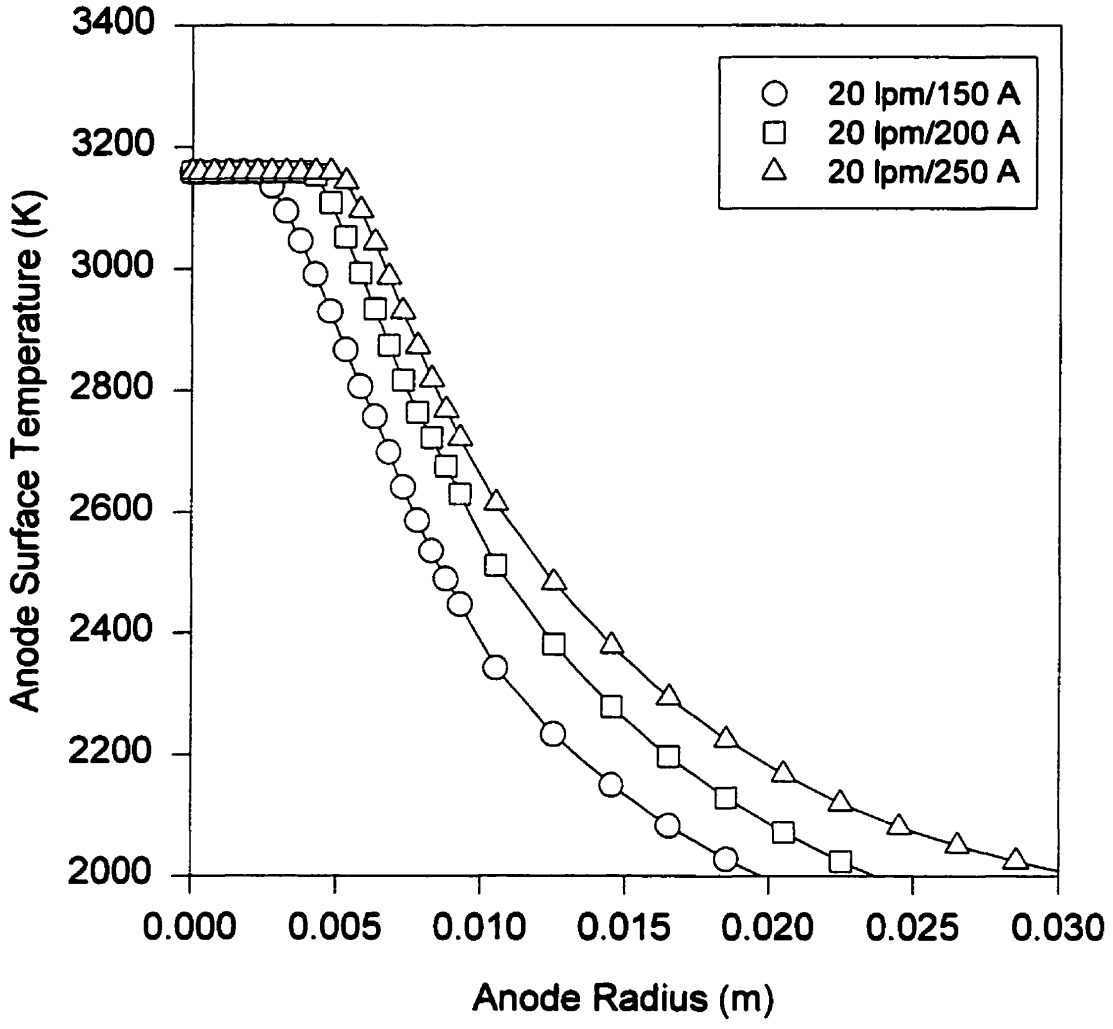

Figure 4.9 Predicted anode surface temperature profile at a plasma gas flow rate of 20 lpm.

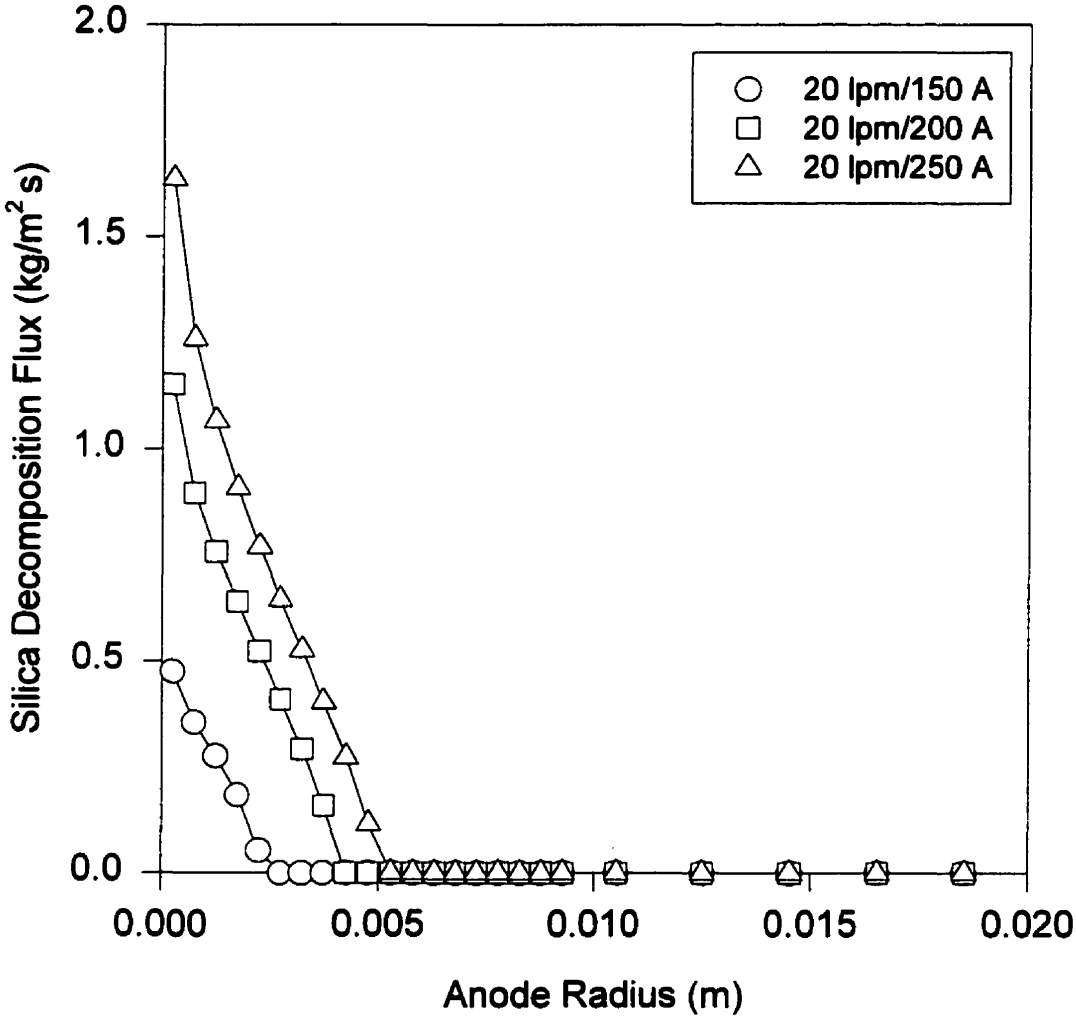

Figure 4.10 Predicted silica decomposition flux at anode surface at a plasma gas flow rate of 20 lpm.

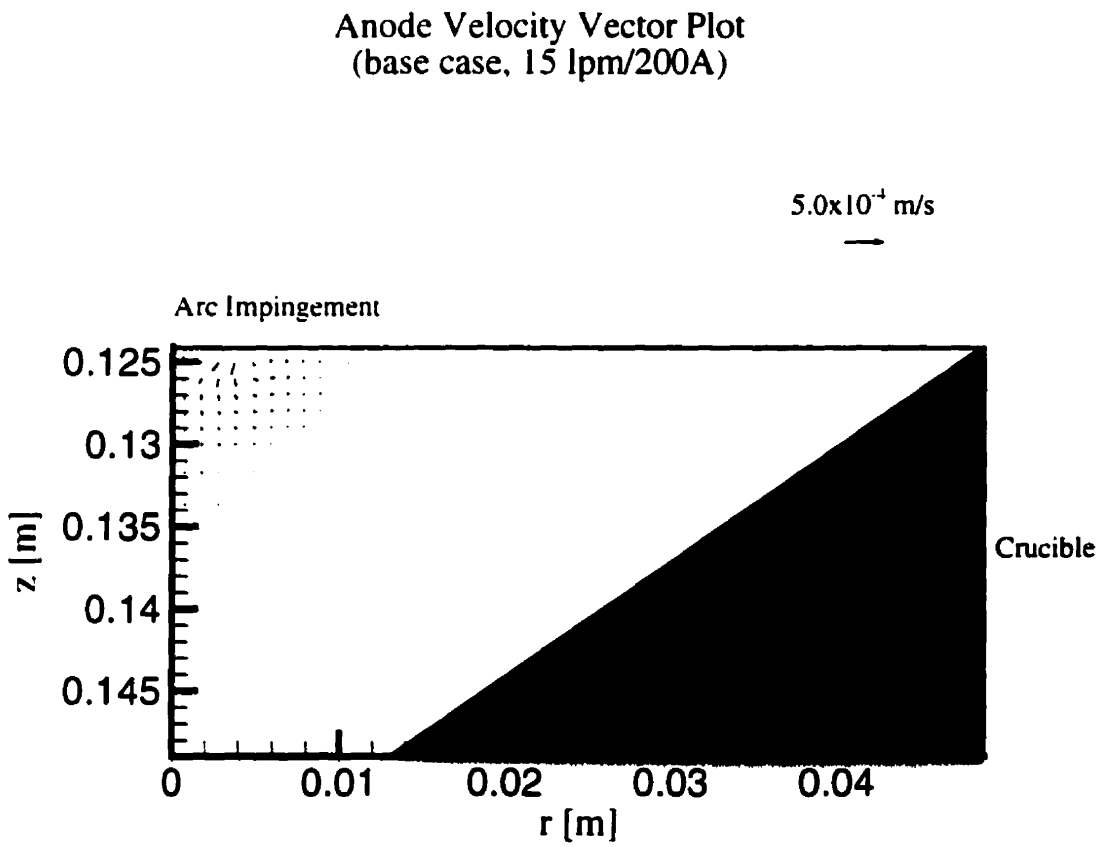

Figure 4.11 Anode velocity vector plot at a plasma gas flow rate of 15 lpm and a current of 200 A.

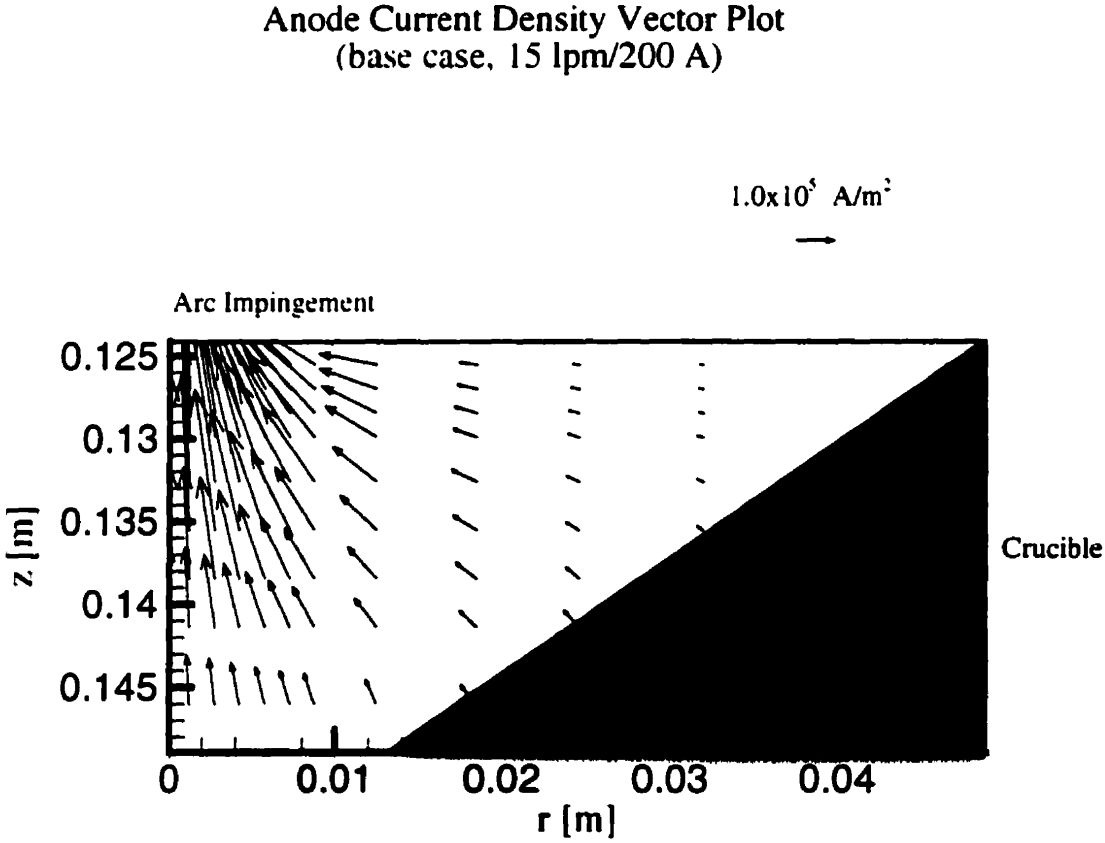

Figure 4.12 Anode current density vector plot at a plasma gas flow rate of 15 lpm and a current of 200 A.

clearly in Figure 4.8. Due to the high heat flux at the center of the anode surface, this region was predicted to attain the boiling point (3159 K). Typical surface temperature profiles are shown in Figure 4.9. Correspondingly, the decomposition flux was also predicted to be greatest at the center of the anode surface (see Figure 4.10). Boiling within the anode was not predicted to occur in the present case because temperatures were < 3159 K. This agrees with experimental observations since significant anode bubbling was only observed when reaction with the crucible was a problem (20 lpm and 250 A). In the eventual scale-up of this process, higher decomposition rates will be required which will necessarily require higher power. This may lead to internal boiling due to resistance heating effects. If this is the case, the current model would have to be modified to account for the generation of gaseous decomposition products ($SiO_{(g)}$ and O_2) within the anode and their effect on momentum and heat transfer.

Figure 4.11 shows that fluid flow within the anode was concentrated in the region just below the arc root. Although difficult to see in this figure, most of the fluid flow was predicted to be in a counterclockwise direction relative to the axis of symmetry. This was due to the high current flow in the center of the anode (see Figure 4.12) which led to strong local magnetic forces. Because of the positive temperature dependence of surface tension, the temperature gradient at the silica surface complemented the magnetic force. In the center of the anode surface, where the boiling point had been attained, no temperature gradient existed so surface tension did not influence fluid flow. In a tiny region just below the anode surface, the flow direction was reversed due to the shear stress of the impinging plasma jet. The buoyancy force also favored this clockwise flow pattern. As can be seen in Figure 4.11, velocities within the anode were very low (< 1 mm/s). This was due to the high viscosity of vitreous silica. At 3000 K, the viscosity of vitreous silica was estimated to be 22.8 Pa s compared to 9.4×10^{-4} Pa s for liquid silicon. Gu (1993) predicted the maximum velocity in a liquid silicon anode with a 200 A, 1 cm long, free burning Ar arc impinging on its surface to be 0.32 m/s. Because of this high viscosity, fluid flow within the silica anode was not thought to have a significant effect on the predicted decomposition rate. This was verified by the prediction of the same

decomposition rates when fluid flow in the anode was neglected. The current density distribution within the anode is shown in Figure 4.12. The current was predicted to flow mainly in the center of the anode where temperatures were highest. This was expected since the electrical resistivity of silica was assumed to decrease exponentially with increasing temperature.

TABLE 4.5 Comparison of model predictions for base case with experimental results.

Torch Operating Conditions		***Experimental Average***		***Base Case Prediction***	
Q_{plasma} ***[lpm]***	***Current [A]***	***Decomposition Rate [g/min]***	***Anode Voltage [V]***	***Decomposition Rate [g/min]***	***Anode Voltage [V]***
10	150	0.14	11.3	0.01	19.3
15	150	0.14	12.1	0.09	18.9
20	150	0.12	11.5	0.22	21.6
10	200	0.22	8.6	0.47	7.6
15	200	0.28	8.9	0.86	8.6
20	200	0.25	9.4	1.28	7.0
10	250	0.49	7.1	1.28	3.9
15	250	0.55	6.5	1.84	3.8
20	250	0.82	8.6	2.38	2.8

The model predictions of the silica decomposition rate and anode voltage are compared with the average experimental results in Table 4.5. The predicted anode voltage was calculated as the electric potential difference from the crucible to the anode surface below the arc root. The anode model correctly predicted the order of magnitude of the decomposition rate (0.01 - 2.38 g/min) as well as the observed increase with current. In

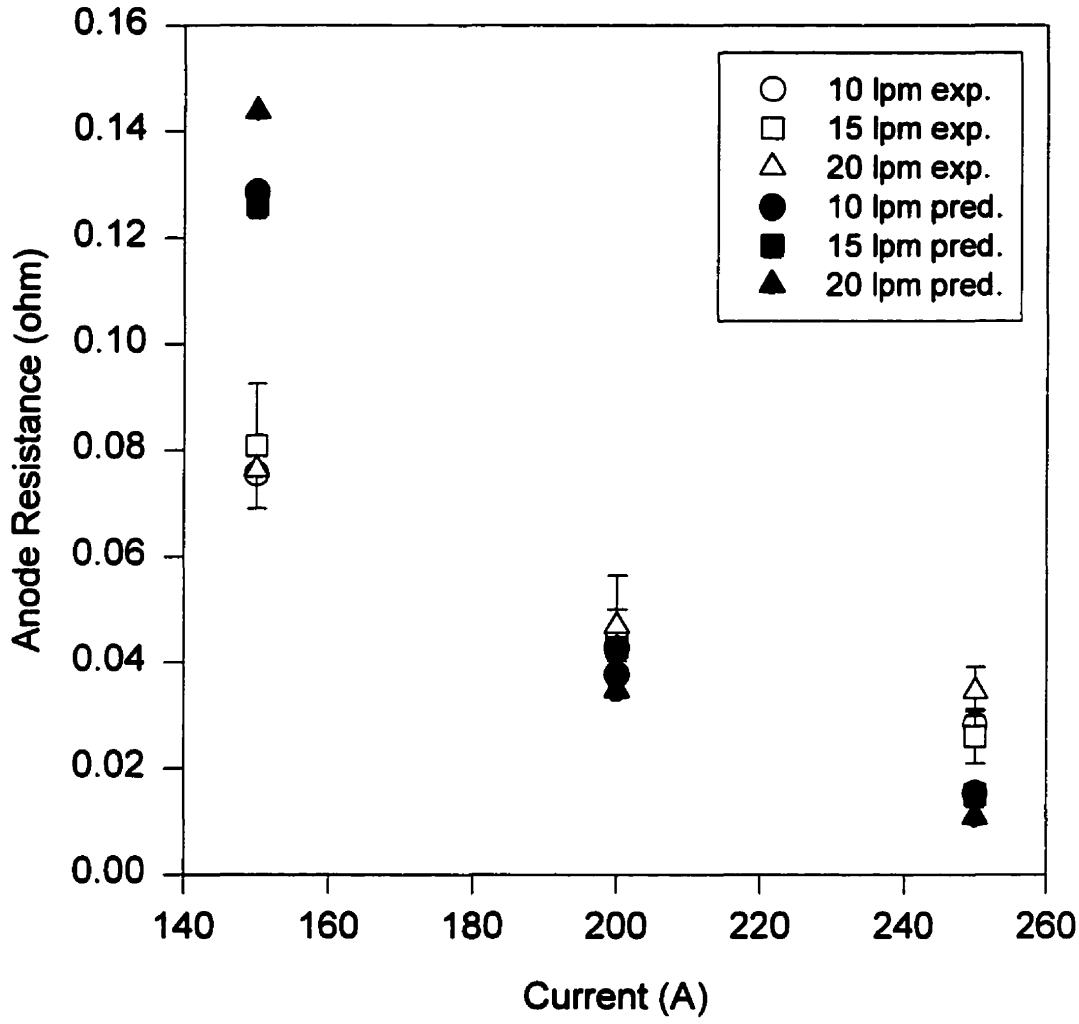

Figure 4.13 Experimental and predicted anode resistance.

general, however, the decomposition rate was overestimated and predicted to increase with increasing plasma gas flow rate. Although empirical in nature, the assumed electrical resistivity (see Table 4.3) did allow a reasonable prediction of the decrease in anode resistance with increasing current (see Figure 4.13). This is consistent with an exponential decrease in the electrical resistivity of the actual silica anode with increasing temperature.

A major reason for the discrepancy between the predicted and experimental decomposition rates was the inaccuracies of the silica properties. These inaccuracies are believed to be the result of extrapolation of existing data to higher temperatures. An example of this is thermal conductivity which had to be extrapolated beyond 1600 K. Choudhary (1997) has reported that the thermal conductivity of vitreous materials at high temperature is dominated by the radiation contribution which can be affected by minor amounts of impurities such as Fe, Cr Mn, Co, V and Cu. A better estimate of the thermal conductivity for the present silica anode is therefore required because of the wide variety of impurities in the quartz raw material (see Table 3.5). A better estimate of the electrical resistivity is also required since an empirical estimate was used with the present anode model due to a lack of data. Electrical resistivity also seems to be extremely sensitive to purity.

The overestimation of the decomposition rates for most of the conditions also suggests that the heat input to the anode is being overestimated. In the present model, this was composed of the surface heat flux due to arc impingement, arc radiation absorption (S_{absorb}) and resistance heating. A summary of these contributions for the torch operating conditions examined is given in Table 4.6. A major source of error in the heat input estimation was believed to be in the convective contribution (q_{conv}). In the actual system, increasing plasma gas flow rate had little effect on the crucible temperature, anode resistance and decomposition rate suggesting that convective heat transfer was not an important surface heat flux contribution. The predicted convective heat input to the anode surface therefore seems to be greatly overestimated (0.60 - 1.70 kW) since we see that it exceeds that associated with electron flow (0.53 - 0.92 kW). Figure 4.14 shows that the convective heat flux was predicted to be greatest in the center of the anode where it

TABLE 4.6 Predicted heat input contributions to the anode for the base case simulations.

Torch Operating Conditions		*Base Case Prediction of Anode Heat Input Contributions [kW]*			
		Surface		*Internal*	
Q_{plasma} *[lpm]*	*Current [A]*	*Convection*	*Electron Flow*	*Arc Radiation*	*Resistance*
10	150	0.60	0.53	0.55	2.89
15	150	0.68	0.53	0.59	2.84
20	150	0.76	0.53	0.61	3.24
10	200	0.94	0.73	0.85	1.51
15	200	1.18	0.73	0.90	1.72
20	200	1.41	0.73	0.93	1.39
10	250	1.19	0.92	1.16	0.96
15	250	1.45	0.92	1.23	0.95
20	250	1.70	0.92	1.26	0.69

even surpasses q_{elec}. This was likely not the case in the actual process since decomposition rates were highest in the center of the anode (see Figure 4.10). The high rate of mass transfer of decomposition products from this region would have therefore led to a significantly lower heat transfer coefficient than what was estimated (Bird et al. (1960). In order to correctly predict the convective heat flux contribution, a multi-component arc model is required which can account for mass transfer effects at the anode surface and the presence of Si and O species in the thermal boundary layer. The transport properties of the gas above the anode surface were probably very different from those of pure Ar as was assumed for the simulations.

Table 4.6 also shows that the rate of resistance heating within the anode was overestimated at 150 A (~ 3 kW) and underestimated at 250 A (~ 1 kW). Experimental observations indicated that this contribution remained constant at approximately 1.75 kW. This deviation was mainly due to the inaccuracy of the electrical resistivity estimate.

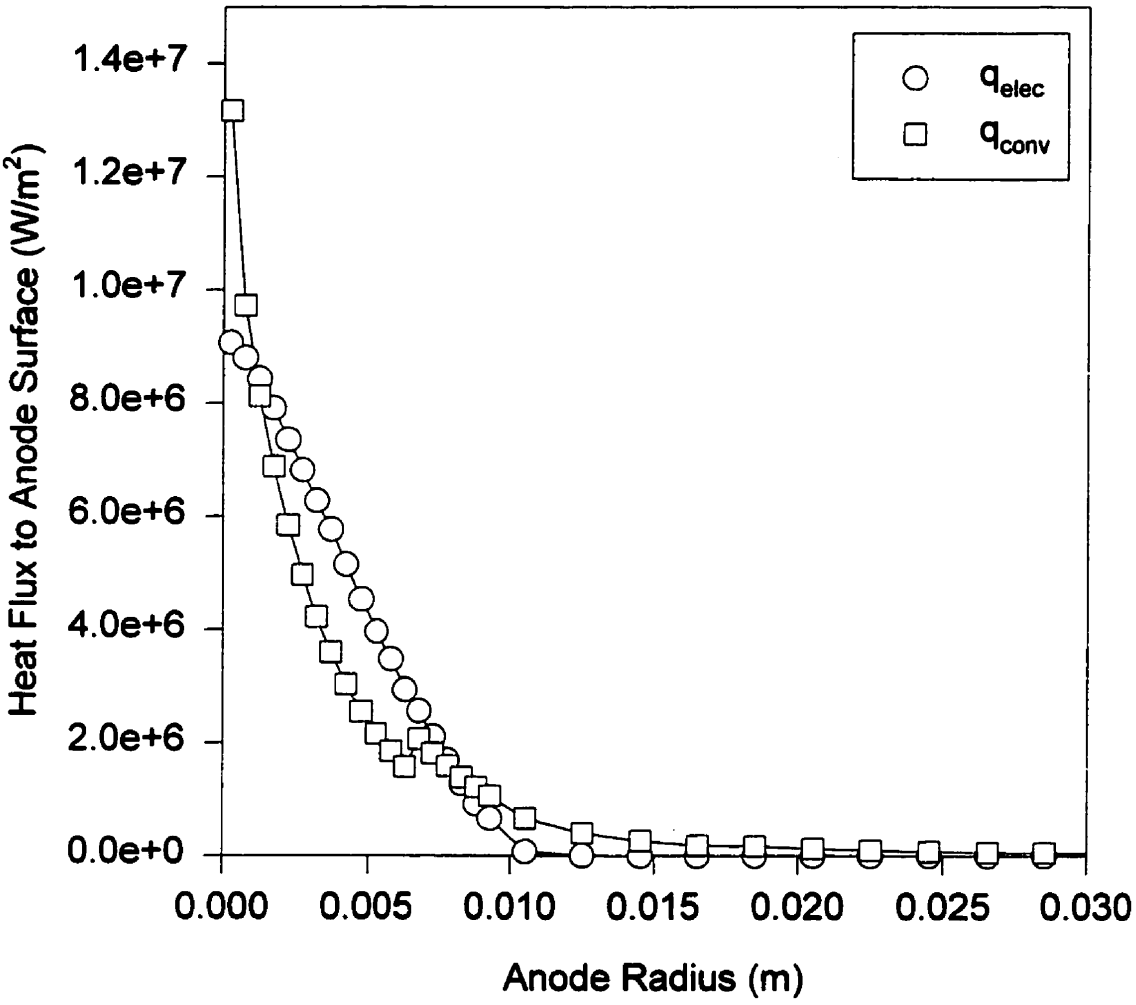

Figure 4.14 Predicted input heat flux to anode surface due to convection and electron flow at a plasma gas flow rate of 10 lpm and a current of 250 A.

The error in the estimate of internal heat generation due to arc radiation absorption was not believed to be the result of neglecting the presence of Si in the plasma phase. This is because of the low decomposition rates obtained using an Ar plasma gas and the relatively low emissive power of Si (Essoltani et al., 1994). The net heat input due to arc radiation was therefore likely correct, however, its distribution within the anode was improperly estimated since absorption was assumed to be uniform (see equation 4.19). This was obviously not the case since absorption varied along the anode depth. Absorption was likely greater at the bottom where the anode was observed to be opaque. The radiation heat loss from the anode surface was estimated to be 1.5, 2.3 and 2.5 kW for currents of 150, 200 and 250 A respectively. This heat loss was not predicted to increase with plasma gas flow rate since the chamber wall temperature remained approximately constant and the region of the anode surface where convective heat transfer was increased was already at the boiling point (i.e. the center). Since emissivity was expected to decrease with increasing temperature, the radiation heat loss from the center of the anode may have been overestimated.

4.5.2 Sensitivity of Predicted Decomposition Rate to Variations in Base Case Conditions

The sensitivity of the predicted decomposition rate was examined with respect to significant variations in the base case assumptions. A summary of the variations examined is given in Table 4.7 and the effects can be seen in Figures 4.15 - 4.18 (note that the filled symbols represent the base case predictions). The boiling point was varied from 3151 to 3167 K which corresponded to reactor pressures of 101.3 and 112 kPa (see Table 2.5). The boiling point may have also been increased as a result of a slight increase in the local pressure above the liquid surface due to the build-up of decomposition products. A factor which favored a reduction of the boiling point was the presence of species (i.e. Ar) other than $SiO_{(g)}$ and O_2 in the equilibrium gas. From Figure 4.15 we

TABLE 4.7 Summary of variations of base case conditions.

Condition	*Base Case Value*	*Variation (low - high)*
boiling point	3159 K	3151 - 3167 K
anode fall potential	0 V	-1.0 - 1.0 V
work function	2.0 V	1.5 - 2.5 V
emissivity	0.5	0.3 - 0.7

can see that a variation in the boiling point of ± 8 K had a negligible effect on the predicted silica decomposition rate.

The uncertainty in the anode fall potential was investigated by examining the effect of a variation of ± 1 V since both positive and negative falls were possible and they are usually in the order of 1 V (Dinulescu and Pfender, 1980, Sanders and Pfender, 1984 and Pfender, 1997). For negative anode falls, q_{elec} is given by (Sanders and Pfender, 1984):

$$q_{elec} = j_{z,surf}\left(3.203\frac{k_B}{e_a}(T_{e,e} - T_{e,a}) + \phi_w\right) \tag{4.30}$$

The estimate of the heat flux due to electron flow for a negative anode potential drop is slightly different than that associated with a positive drop (see equation 4.17). Firstly, V_{anode} is not included since electrons are not accelerated towards the anode surface and secondly, the increase in the thermal energy of the electrons due to thermal and ordinary diffusion is accounted for (3.203 instead of 2.5 in first term). This diffusion is believed to occur as a result of steep gradients in electron temperature and density (Pfender, 1997). Since equation 4.17 was used to estimate q_{elec} in the base case simulation, the assumption of a potential drop of 0 V was equivalent to assuming a negligible positive potential drop. Figure 4.16 shows that if the anode fall potential was negative or significantly positive

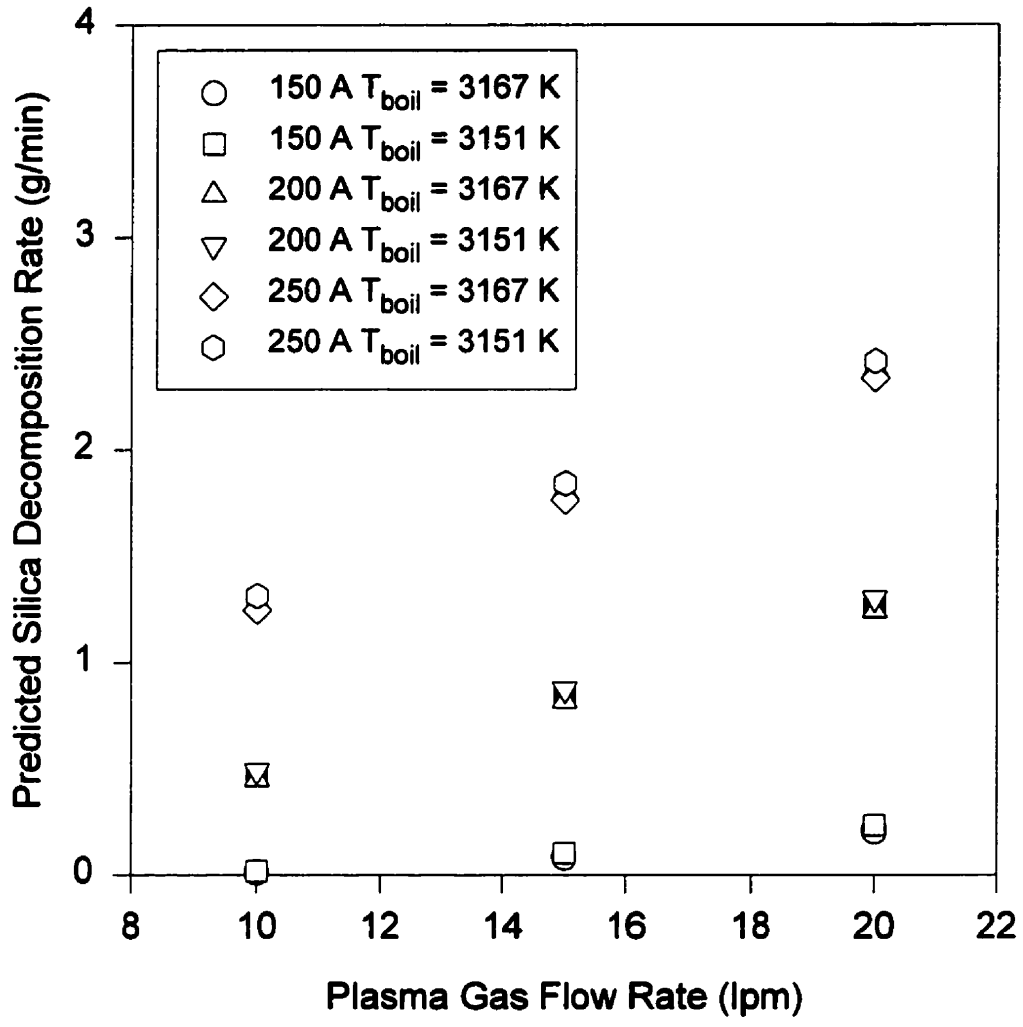

Figure 4.15 Effect of boiling point variation on predicted silica decomposition rate.

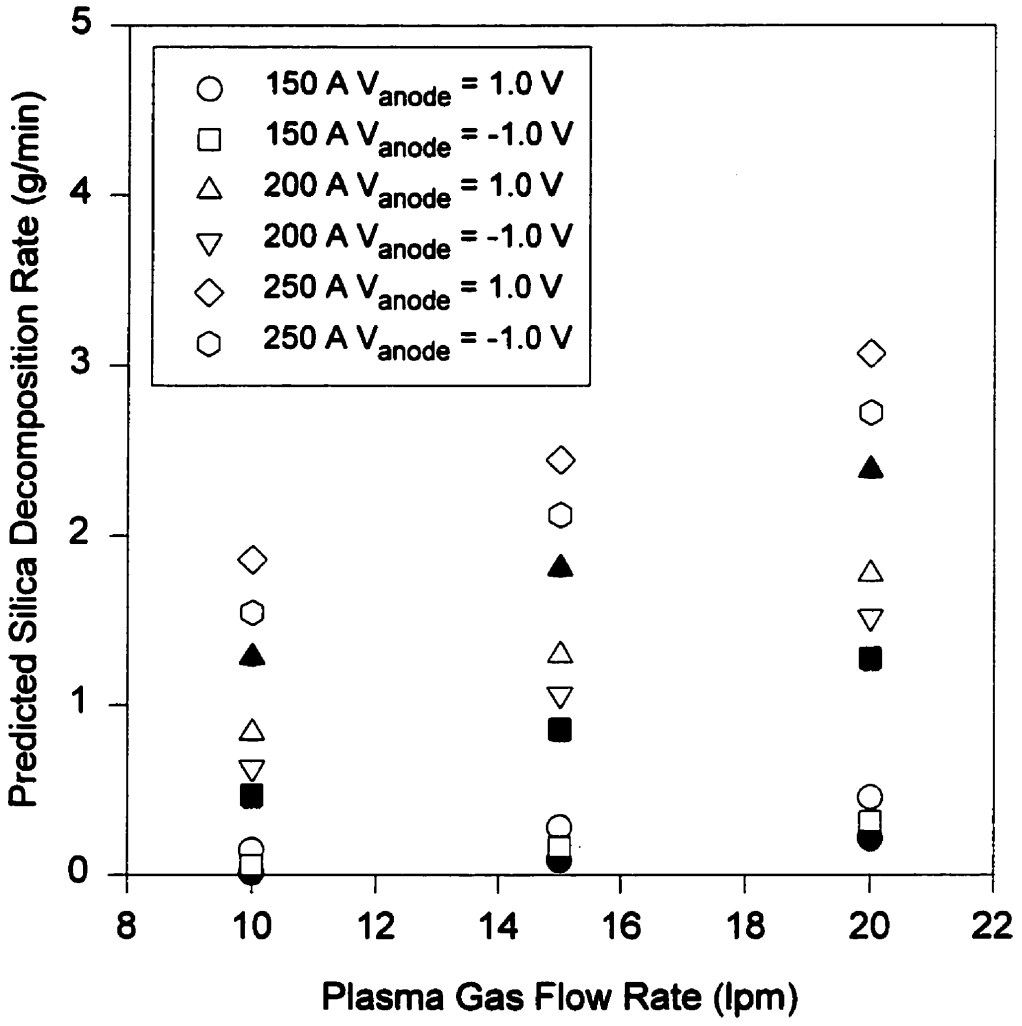

Figure 4.16 Effect of anode fall potential variation on predicted silica decomposition rate.

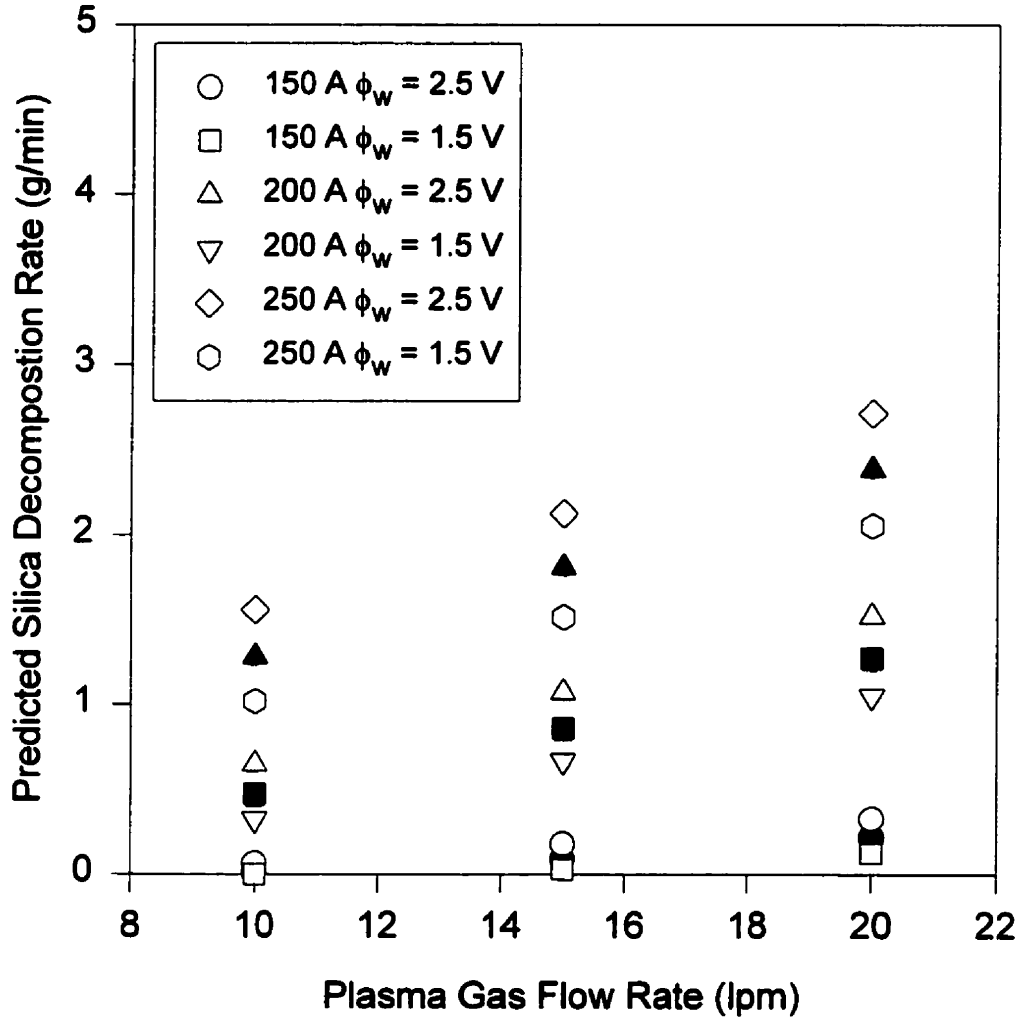

Figure 4.17 Effect of work function variation on predicted silica decomposition rate.

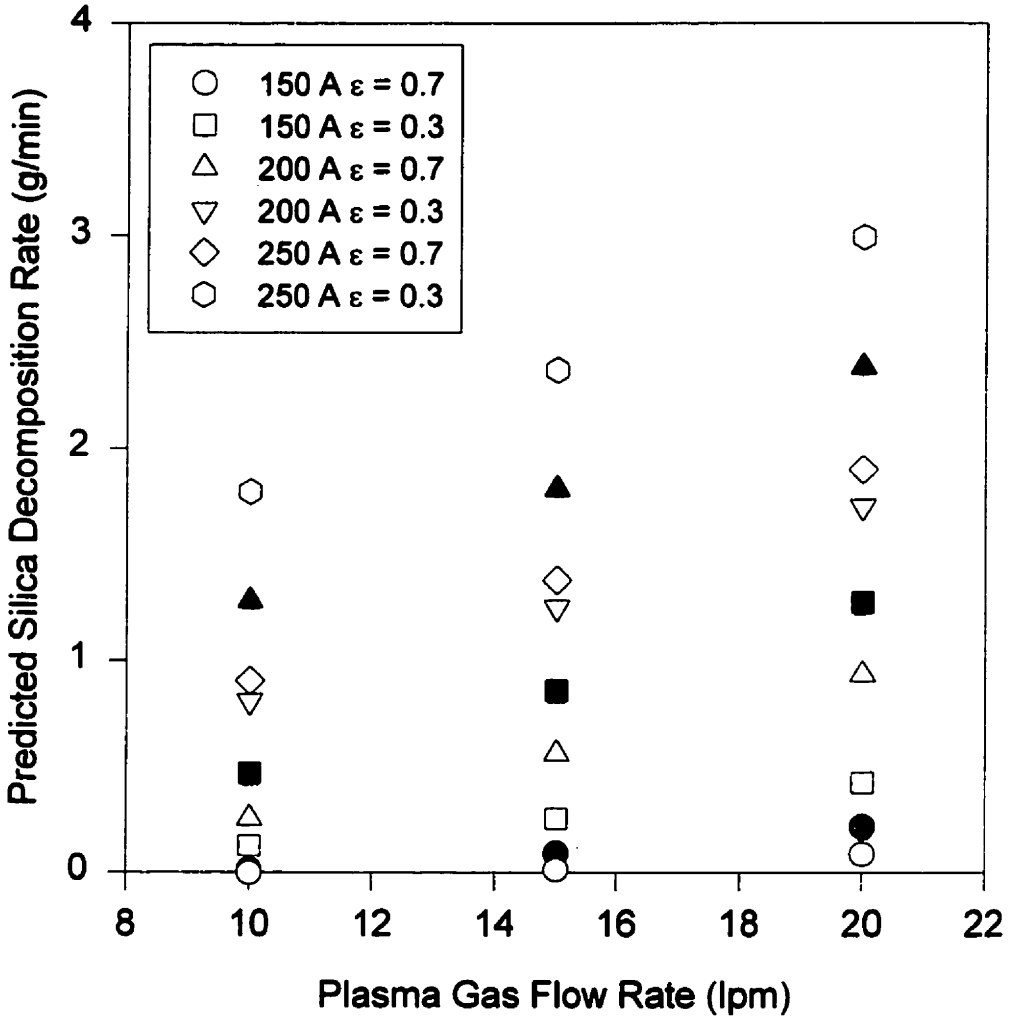

Figure 4.18 Effect of emissivity variation on predicted silica decomposition rate.

(1 V), the heat flux to the anode surface due to electron flow would be increased which would lead to the prediction of slightly higher decomposition rates.

The effect of varying the work function of silica by ± 0.5 V can also be explained by a variation in the estimate of q_{elec} (see Figure 4.17). Considering that the actual work function was likely between 1.5 - 2.5 V (Rivière, 1969), the sensitivity of the results to variations in this parameter was not considered great. Figure 4.18 shows that the predictions were most sensitive to variations in emissivity (0.3 - 0.7). This is because the radiation heat loss from the center of the anode surface was directly proportional to this parameter.

Although variations of the base case assumptions led to variations in the predicted decomposition rates, they did not reduce the discrepancy with experimental results significantly. This suggests a more fundamental problem with the anode model which is suspected to be due to an improper estimate of silica properties and convective heat transfer to the anode surface.

Chapter 5 - THE EFFECT OF OXIDATION ZONE PARAMETERS ON POWDER PROPERTIES

5.1 Introduction

An experimental investigation was undertaken during this study to examine the effect of important oxidation zone parameters on the properties of the fumed silica powder generated. A better understanding of the phenomena occurring in this region will lead to improvements in product quality and will aid any future scale-up of the current oxidation zone configuration. Shown schematically in Figure 5.1, the oxidation zone consisted of the region adjacent to the reactor exit where steam was injected radially. Injection occurred via 18 equally spaced orifices angled 20° downstream to minimize backflow. The manifold used for steam injection is shown in Figure 3.6. This type of quench system was employed because it has been shown to provide the highest cooling rates (Young and Pfender, 1985). The overall reaction occurring in the oxidation zone was believed to be the following:

$$SiO_{(g)} + H_2O_{(g)} \rightarrow SiO_2 + H_2 \qquad (5.1)$$

In addition to $SiO_{(g)}$ oxidation and aerosol formation, surface hydroxylation also occurred in the oxidation zone. The parameters which were varied were the temperature and $SiO_{(g)}$ concentration entering the oxidation zone and the steam flow rate. These parameters were selected because they have been shown to play an important role in determining the specific surface area of the powder as well as other important fumed silica properties (Addona and Munz, 1994).

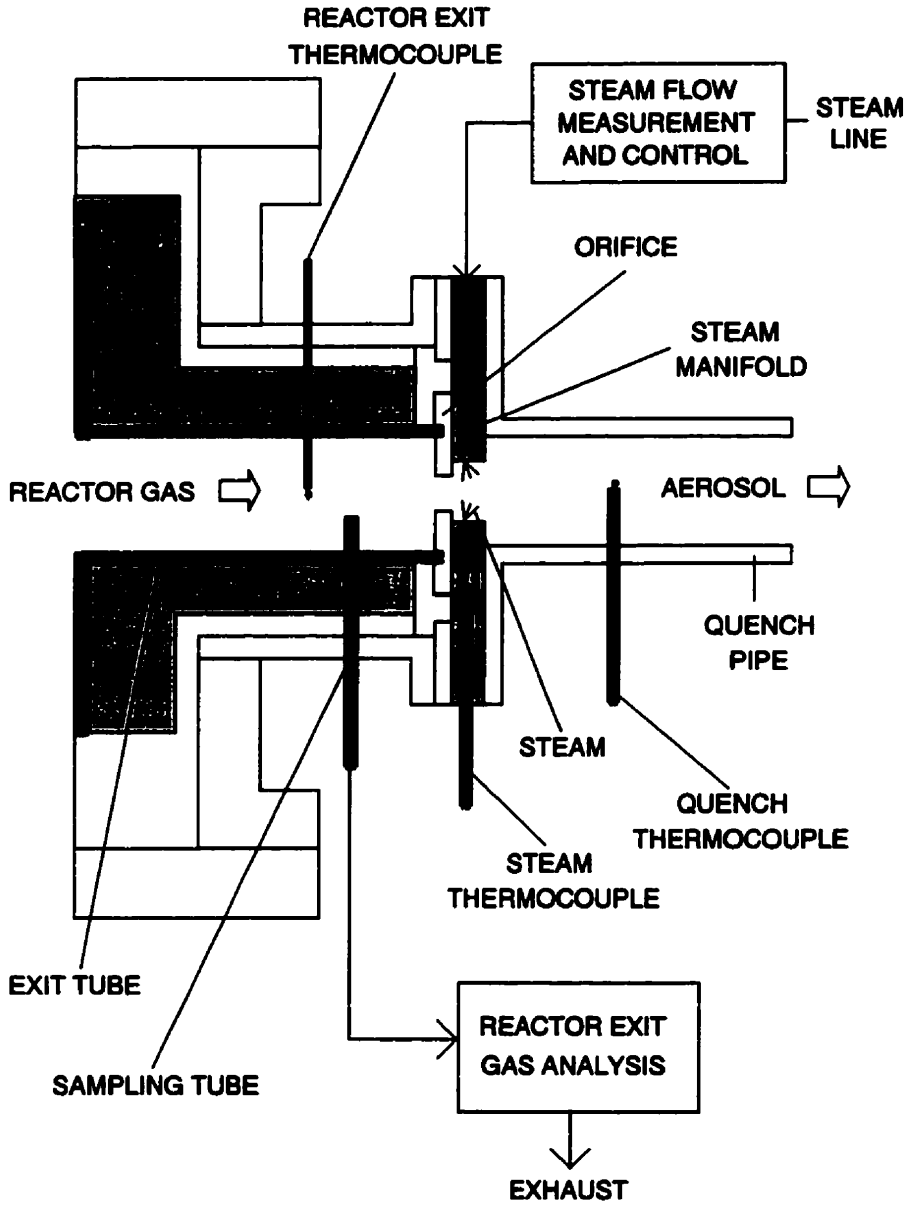

Figure 5.1 Schematic of oxidation zone configuration.

The limitations of the current oxidation zone configuration reduced the number of operating parameters which could be used to control temperature and $SiO_{(g)}$ concentration. The problem was with steam flowing back into the reactor exit when the maximum plasma gas flow rate was not used. This caused oxidation and aerosol formation to occur partially in the reactor exit. To avoid this problem, the maximum plasma gas flow rate (20 lpm) was used for all experiments. Because of this, the reactor exit gas temperature and $SiO_{(g)}$ concentration could not be controlled independently since both varied with current. The CO concentration in the reactor exit was used to monitor that of $SiO_{(g)}$ since direct measurement was not possible. The experimental apparatus used during this work was described in section 3.2.

5.2 Experimental Procedure

5.2.1 Pre-Experimental Preparation

The pre-experimental procedure used was similar to that given in section 3.3.1. Steam flow was started prior to arc ignition to purge any condensate in the line. This initial flow was sent directly to the condenser through a by-pass line. The baghouse heaters were also turned on prior to the start of an experiment to minimize steam condensation in the vessel during powder collection.

5.2.2 Arc Ignition

The same procedure was used as outlined in section 3.3.2.

5.2.3 Execution of an Experiment

1. The Ar plasma gas flow rate was set at 20 lpm and the current adjusted to its desired level. The on/off valve connecting the steam line to the manifold was opened and the by-pass to the condenser closed. An insulated quench pipe (no water-cooling) was used during these experiments.

2. Data acquisition was begun.

3. Particle feeding was started and the steam flow rate was adjusted to its desired level (46 - 71 g/min).

4. After 30 - 60 minutes of operation, powder collection was started. Gas sampling was begun approximately 10 minutes prior to the start of powder collection. If H_2 was to be added to the plasma gas, its flow was also started at this time. During powder collection, current was adjusted to maintain an approximately constant CO concentration in the reactor exit gas.

5. Prior to the termination of an experiment, particle feeding, gas sampling and powder collection were stopped and the outputs of the reactor thermocouples were connected to the data acquisition system.

6. An experiment was terminated by shutting down the rectifier bank. The flow of H_2 (if used) and steam were stopped immediately following shutdown. Argon and cooling water flows were continued until the apparatus had cooled sufficiently.

5.2.4 Post Experimental Procedure

The same post experimental procedure described in section 3.3.4 was used here with the additional task of collecting the fumed silica product from the baghouse filter.

5.3 Results and Discussion

5.3.1 General Summary of Experiments Performed

The experiments performed are summarized in Table 5.1. The plasma gas flow rate was set at 20 lpm Ar except for experiments 121 and 122 where H_2 was added to significantly increase the $SiO_{(g)}$ concentration. The oxidation zone parameters examined were the temperature and $SiO_{(g)}$ concentration of the reactor exit gas and steam flow rate. Current was used to control the reactor exit gas conditions (temperature and $SiO_{(g)}$ concentration). In reality, current was used to maintain the CO concentration in the reactor exit gas constant during powder collection. Four reactor exit gas temperature and $SiO_{(g)}$ concentration levels were examined each at three different steam flow rates (46, 57 and 71 g/min). Control of the steam flow rate was described in section 3.2.8. The steam in the manifold was superheated with a temperature ranging from 395 - 442 K (129 - 156 kPa). The reactor pressure was maintained between 101.3 - 112 kPa throughout the experiment. Powder collection was started once steady-state had been well established. Collection took place in a baghouse filter maintained at 387 - 417 K. The duration of experiments varied from 1 - 3 hours.

TABLE 5.1 Summary of experiments performed during oxidation zone study.

Exp.	*Plasma Gas Flow Rate [lpm]*		*Current [A]*	*Steam Flow Rate [g/min]*	*Duration [min]*	*Powder Collection Start Time [min]*
	Ar	*H_2*				
104	20	0	140 - 150	46	180	60
97	20	0	140 - 150	57	180	60
110	20	0	140 - 150	57	180	60
116	20	0	140 - 150	71	180	60
123	20	0	140 - 150	71	180	60
103	20	0	180 - 200	46	125	45
102	20	0	180 - 200	57	120	45
109	20	0	180 - 200	57	120	45
115	20	0	180 - 200	57	120	45
98	20	0	180 - 200	71	120	45
101	20	0	200 - 220	46	120	45
108	20	0	200 - 220	46	120	45
107	20	0	200 - 220	57	120	45
106	20	0	200 - 220	71	120	45
118	20	0	200 - 220	71	120	45
112	20	0	250	46	60	30
111	20	0	250	57	60	30
113	20	0	250	71	60	30
114	20	0	250	71	60	30
121	20	1.4	150	57	58.6	30
122	20	1.4	150	71	56.5	30

5.3.2 $SiO_{(g)}$ Concentration

The $SiO_{(g)}$ concentration in the reactor exit gas was monitored using the CO measurement. The limitations of this technique were discussed in section 3.4.1.12. The main uncertainty was whether the majority of the SiO exited the reactor in a gaseous or condensed state. The two extreme possibilities were that the SiO was completely condensed as it entered the oxidation zone or that no condensation had taken place. Ideally, the latter was desired since this allows better control of the powder formation process. If the former was true, the specific surface area of the powder would be determined prior to the oxidation zone. The steam quench in this case served only to oxidize the ultrafine $SiO_{(s \text{ or } l)}$ particles exiting the reactor. The most probable scenario was partial condensation the extent of which was small due to the low concentration of $SiO_{(g)}$ in the plasma chamber. This will be verified in section 5.3.5 through TEM analysis of the powder products. The CO concentration in the reactor exit gas during powder collection is shown in Table 5.2. For experiments 111 - 114 (20 lpm and 250 A), the CO concentration was slightly higher than that of $SiO_{(g)}$ due to the increased reaction between the silica anode and the crucible.

5.3.3 Effect on Specific Surface Area

A summary of the oxidation zone parameters and the specific surface area of the fumed silica produced is shown in Table 5.3. The reactor exit gas temperature during steady-state powder generation was assumed to be approximated by the value following shutdown. This was due to problems with arc radiation interfering with the temperature measurement (see section 3.4.1.6). The specific surface area of the experimental powders, determined using the BET technique, ranged from 104 - 257 m^2/g. Typical commercial fumed silica powders have specific surface areas ranging from 100 - 400 m^2/g. Since the reactor exit gas temperature was approximately constant for a given $SiO_{(g)}$

TABLE 5.2 CO concentration in reactor exit gas during powder collection.

Experiment	*Reactor Exit Gas CO Concentration During Powder Collection [mole %]*	
	Mean	*Std. Dev.*[1]
104	0.09	0.01
97	0.12	0.04
110	0.10	0.01
116	0.12	0.03
123	0.12	0.03
103	0.37	0.05
102	0.44	0.10
109	0.39	0.03
115	0.36	0.03
98	0.42	0.07
101	0.65	0.07
108	0.66	0.06
107	0.63	0.06
106	0.60	0.14
118	0.61	0.08
112	1.60	0.12
111	1.92	0.29
113	1.17	0.16
114	1.73	0.20
121	2.78	0.91
122	3.24	1.03

1. With respect to time.

TABLE 5.3 Oxidation zone parameters and specific surface area of powders produced.

Exp.	*Estimate of Reactor Exit Gas Conditions During Powder Collection*		*Steam Flow [g/min]*	*BET Specific Surface Area [m^2/g]*
	T^1 [K]	*y_{SiO}^2 [mole %]*		
104	1485	0.09	46	104
97	1443	0.12	57	178
110	1422	0.10	57	165
116	1414	0.12	71	176
123	1501	0.12	71	162
103	1587	0.37	46	164
102	1542	0.44	57	188
109	1685	0.39	57	228
115	1659	0.36	57	219
98	1611	0.42	71	192
101	1618	0.65	46	225
108	1656	0.66	46	224
107	1701	0.63	57	229
106	1672	0.60	71	253
118	1695	0.61	71	237
112	1784	1.60	46	257
111	1800	1.92	57	252
113	1730	1.17	71	229
114	1801	1.73	71	256
121	1747	2.78	57	139
122	1741	3.24	71	177

1. Value following shutdown. 2. Assuming $y_{SiO} = y_{CO}$.

concentration level, varying the steam flow rate allowed the quench rate in the oxidation zone to be varied. The quench rate was only important in a very small region close to the reactor exit where most of the powder formation process occurred. Determination of this local quench rate was not possible due to the steep temperature gradients within this region. The effect of increasing steam flow rate for approximately constant reactor exit gas conditions can be seen in Figures 5.2 - 5.5. At $SiO_{(g)}$ concentration levels (mole %) of 0.09 - 0.12 % and 0.36 - 0.44 %, the specific surface area of the powder increased with increasing steam flow rate initially and then remained constant. Increasing steam flow rate did not cause a significant change in specific surface area for $SiO_{(g)}$ concentrations of 0.60 - 0.66 % and 1.17 - 1.92 %.

The increase in specific surface area with increasing steam flow rate seen in Figures 5.2 and 5.3 can be explained by examining the response time of a given aerosol system to changes in supersaturation ratio (Girshick and Chiu, 1989):

$$\tau_c = \frac{1}{n_o \beta_o} \tag{5.2}$$

where τ_c the characteristic response time for aerosol dynamics, n_o is the initial monomer concentration of the condensable species and β_o is the initial collision frequency function for collisions between two monomers given by:

$$\beta_o = 4\left(\frac{3v_1}{4\pi}\right)^{1/6} \sqrt{\frac{12 k_B T}{\rho_p}} \tag{5.3}$$

where v_1 is the monomer volume, T is the temperature, k_B is the Boltzmann constant and ρ_p is the particle mass density. In the present aerosol system, $SiO_{(g)}$ and $SiO_{2(g)}$ were both potential monomers. Which monomer dominated was determined by the kinetics of gas phase oxidation. If oxidation kinetics were slow, the dominant monomer would be $SiO_{(g)}$ whereas if the opposite was true, fumed silica formation would primarily occur through

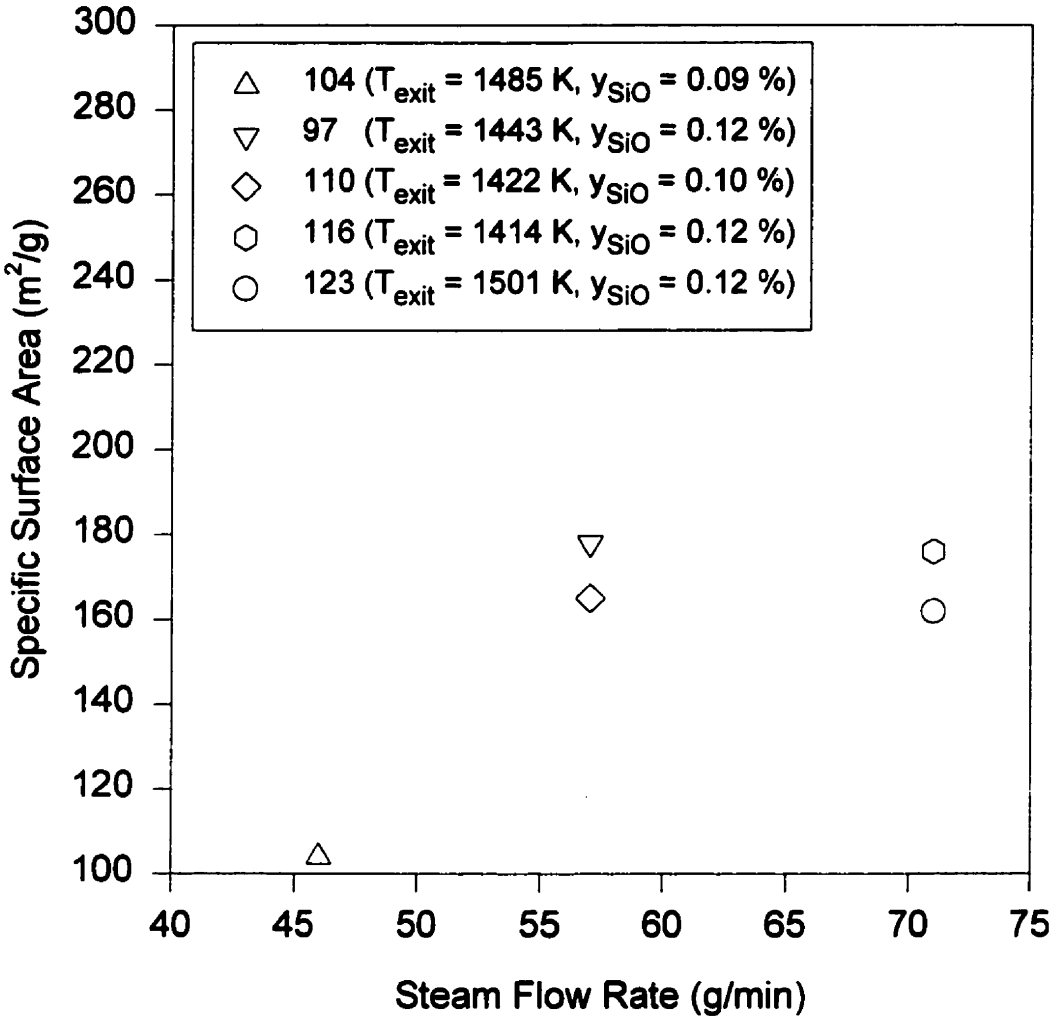

Figure 5.2 Effect of steam flow rate on specific surface area for approximately constant reactor exit gas conditions: y_{SiO} = 0.09 - 0.12 % and T_{exit} = 1414 - 1501 K.

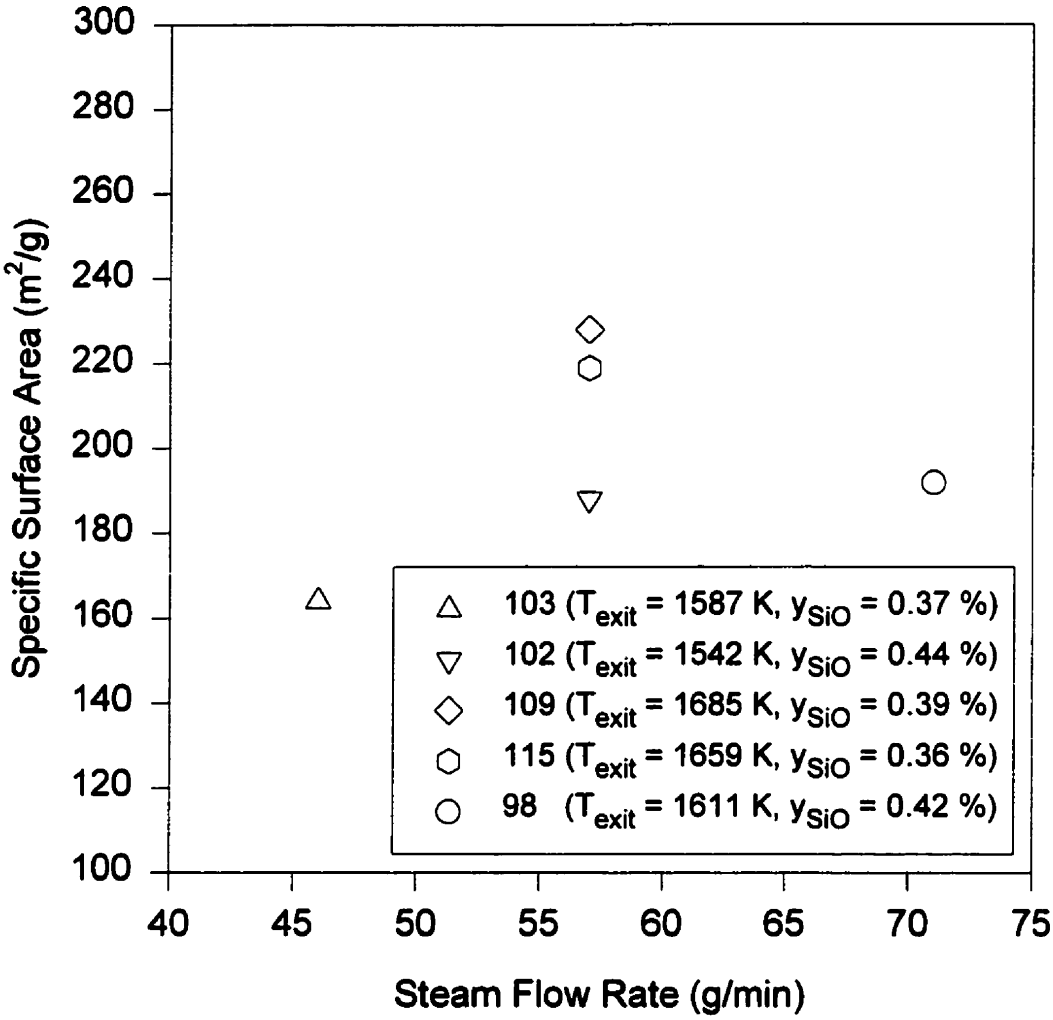

Figure 5.3 Effect of steam flow rate on specific surface area for approximately constant reactor exit gas conditions: y_{SiO} = 0.36 - 0.44 % and T_{exit} = 1542 - 1685 K.

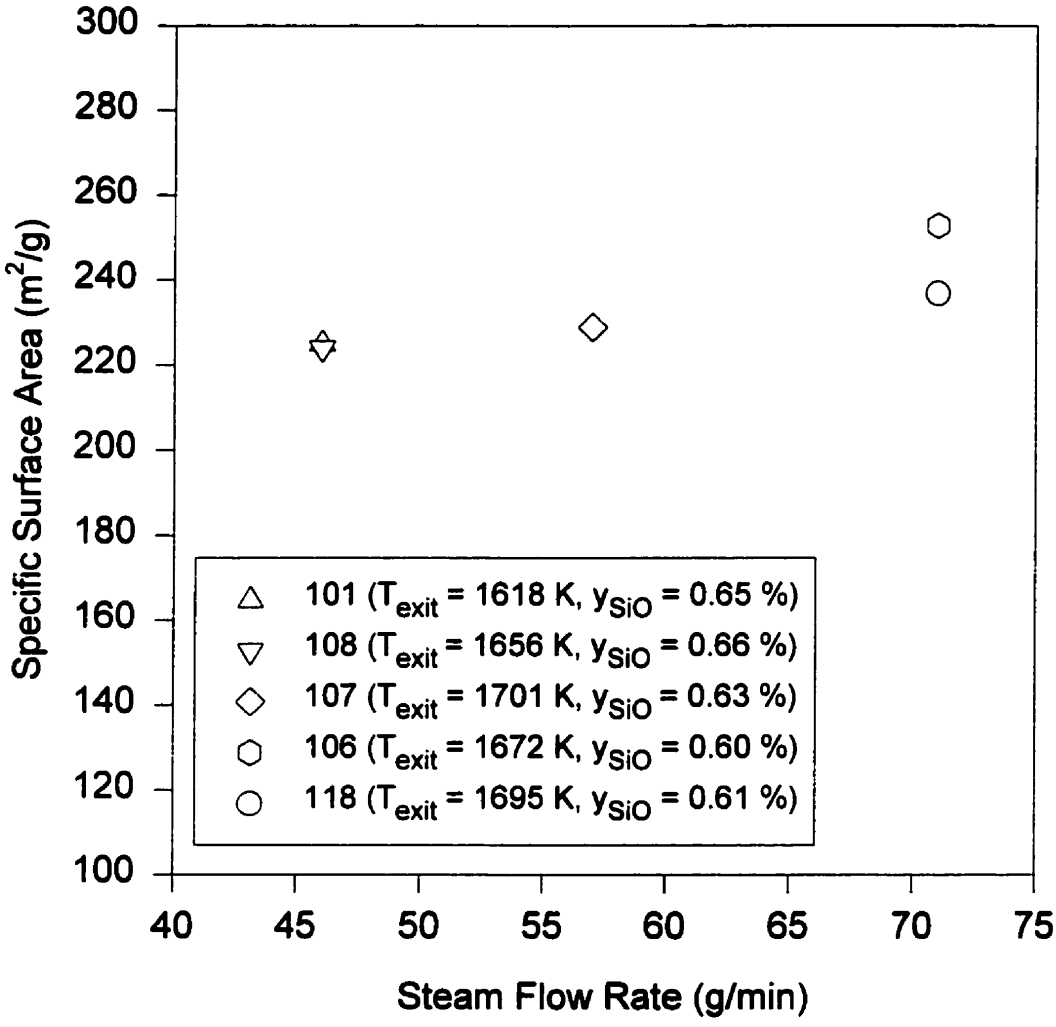

Figure 5.4 Effect of steam flow rate on specific surface area for approximately constant reactor exit gas conditions: y_{SiO} = 0.60 - 0.66 % and T_{exit} = 1618 - 1701 K.

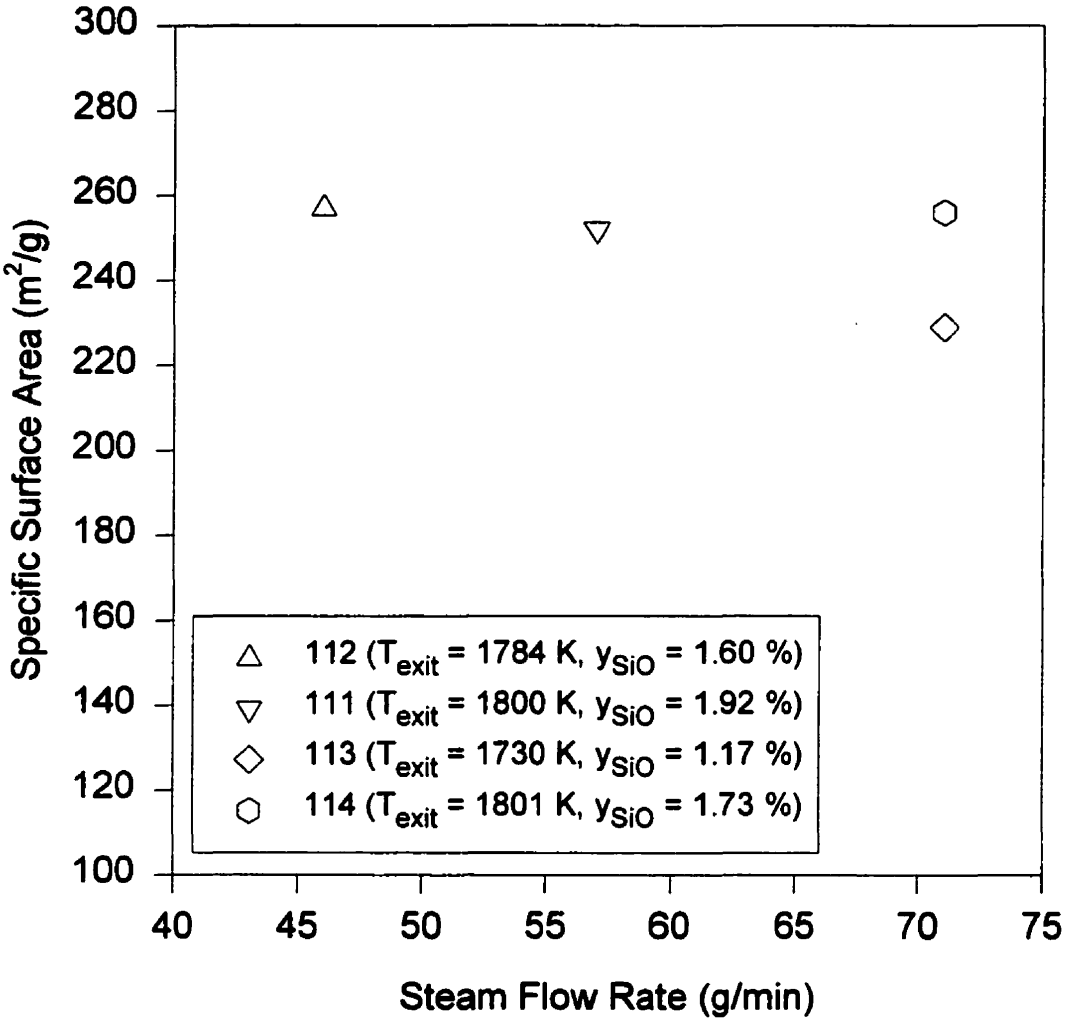

Figure 5.5 Effect of steam flow rate on specific surface area for approximately constant reactor exit gas conditions: y_{SiO} = 1.17 - 1.92 % and T_{exit} = 1730 - 1801 K.

$SiO_{2(g)}$ condensation. Fumed silica generation through $SiO_{(g)}$ condensation would be the result of the oxidation of $SiO_{(s\ or\ l)}$. Therefore, $SiO_{2(g)}$ was desired since it would ensure the complete oxidation of $SiO_{(g)}$. Both monomers probably participated in the formation of the powder either through direct nucleation, surface condensation or reaction. In either case, the initial monomer concentration could be approximated as that of $SiO_{(g)}$.

For approximately constant reactor exit gas conditions, increasing the steam flow rate resulted in a more rapid quenching of the gas entering the oxidation zone. From equations 5.2 and 5.3 we see that τ_c was not greatly affected by an increase in the quench rate ($T^{1/2}$ dependence is relatively small). Such an increase caused the monomer supersaturation ratio to shoot to higher values before nucleation occurred. Since the diameter of a stable particle is given by (Kotake and Glass, 1981):

$$d^* = \frac{4\gamma\, v_1}{k_B\, T \ln S} \tag{5.4}$$

where d^* is the critical diameter for a stable particle, S is the monomer supersaturation ratio and γ is the surface tension, the result of increasing the quench rate for a given initial monomer concentration was the formation of a large number of mostly smaller nuclei at the point of homogeneous nucleation. The fact that this effect is not seen at higher steam flow rates suggests that there is a mixing limitation within the oxidation zone. Beyond a certain steam flow rate, no improvement in the quench rate is apparent. Although the gas temperature further downstream of the reactor exit was lowered with increasing steam flow rate, only the local quench rate in the small region adjacent to the reactor exit was important in determining specific surface area. Within this region, the rate at which the gas was cooled was not significantly improved with increasing steam flow rate beyond a certain level. This limitation is more evident at higher $SiO_{(g)}$ concentrations where the specific surface area remains constant with steam flow rate (see Figures 5.4 and 5.5). The most probable reason for this was the increase in reactor exit gas temperature which occurred when $SiO_{(g)}$ concentration was increased. The hotter the gas entering the

oxidation zone, the greater was its viscosity and therefore the more difficult it was for the steam to penetrate and mix efficiently.

The effects of reactor exit gas temperature and $SiO_{(g)}$ concentration were difficult to isolate by examining Figures 5.2 - 5.5 since any increase in one parameter was accompanied by an increase in the other. In general, the specific surface area increased with increasing $SiO_{(g)}$ concentration at a constant steam flow rate. If the reactor exit gas temperature had remained constant, a decrease would have been expected. This can be seen in equation 5.2 where an increase in the initial monomer concentration results in a reduction in τ_c. Therefore, for a similar quench rate the system responds more rapidly to changes in the critical cluster size d^*. Thus, before d^* can decrease further during quenching, homogenous nucleation occurs producing a smaller number of larger diameter particles (Girshick and Chiu, 1989). The fact that the specific surface area increased with $SiO_{(g)}$ concentration was the result of an increase in the quench rate due to a higher reactor exit gas temperature. This effect also explains the higher specific surface areas reported for powders produced during experiments 109 and 115 (see Figure 5.3).

Experiments 121 and 122 examined a large increase in $SiO_{(g)}$ concentration (y_{SiO} = 2.78 - 3.24 %). Since the reactor exit gas temperature for these experiments was similar to that for experiments 111, 113 and 114 (y_{SiO} = 1.17 - 1.92 %), the effect of $SiO_{(g)}$ concentration could be isolated by comparing results for similar steam flow rates. The powders generated during experiments 121 and 122 had specific surface areas (139 - 177 m^2/g) which were significantly lower than those of experiments 111, 113 and 114 (229 - 256 m^2/g). In this case, the expected decrease of specific surface area with increasing initial monomer concentration was observed. As will be shown in section 5.3.5, the large increase in $SiO_{(g)}$ concentration also increased the degree of condensation occurring in the plasma chamber. This also contributed to the formation of lower specific surface area powders since particles formed in the plasma chamber had more opportunity to grow before they entered the oxidation zone. Particle growth in the reactor was a combination of coagulation and surface condensation.

5.3.4 Effect on Surface Hydroxyl Density

Because of a lack of sufficient powder, surface hydroxyl density could only be evaluated in a qualitative way using FTIR spectroscopy. The samples analyzed consisted of a 5 % (by weight) mixture of the powder in a finely ground KBr matrix. The percent transmittance of the samples was based on a pure KBr reference. The groups which characterize fumed silica are lattice Si-O (1500 - 1900 cm^{-1}, double peak), free surface hydroxyls (Si-OH, 3750 cm^{-1}, sharp peak), adjacent hydrogen bonded surface hydroxyls (3500 - 3700 cm^{-1}, broad peak) and adsorbed H_2O (Cabot Corp., 1983). Also present are surface Si-H groups (2100 - 2300 cm^{-1}) (Rao, 1963). The samples were dried in an oven at 373 K for 24 hours to minimize the amount of physically adsorbed H_2O which has a tendency to cover hydroxyl sites. Drying the powder at higher temperature was avoided since this may have resulted in the de-hydroxylation of the surface.

A significant difference in the FTIR spectra was not detected with varying oxidation zone parameters. The parameter most likely to cause variations in surface hydroxyl density was steam flow rate. The FTIR spectra of Cab-O-Sil® M-5 and the powder produced during experiment 116 are compared in Figure 5.6 while that of Aerosil® 200 is compared with the powder product obtained during experiment 121 in Figure 5.7. The FTIR spectra of the experimental powders was characterized by a strong broad peak at 3500 - 3700 cm^{-1} indicating the presence of a large number of hydrogen bonded surface hydroxyls and therefore a high surface hydroxyl density. The commercial powders were characterized by a strong sharp peak at 3750 cm^{-1} due to the presence of a large number of free surface hydroxyls. The surface hydroxyl density of the experimental powders was therefore believed to be greater than that of Aerosil® 200 and Cab-O-Sil® M-5. A fully hydroxylated surface is reported to have a density of 7.85 Si-OH/nm^2 while a value of 3.5 - 4.5 Si-OH/nm^2 has been estimated for Cab-O-Sil® powders (Cabot Corp., 1983). The high surface hydroxyl density of the experimental powders was believed to be due to the high $H_2O_{(g)}$ concentration in the oxidation zone. A similar steam quench

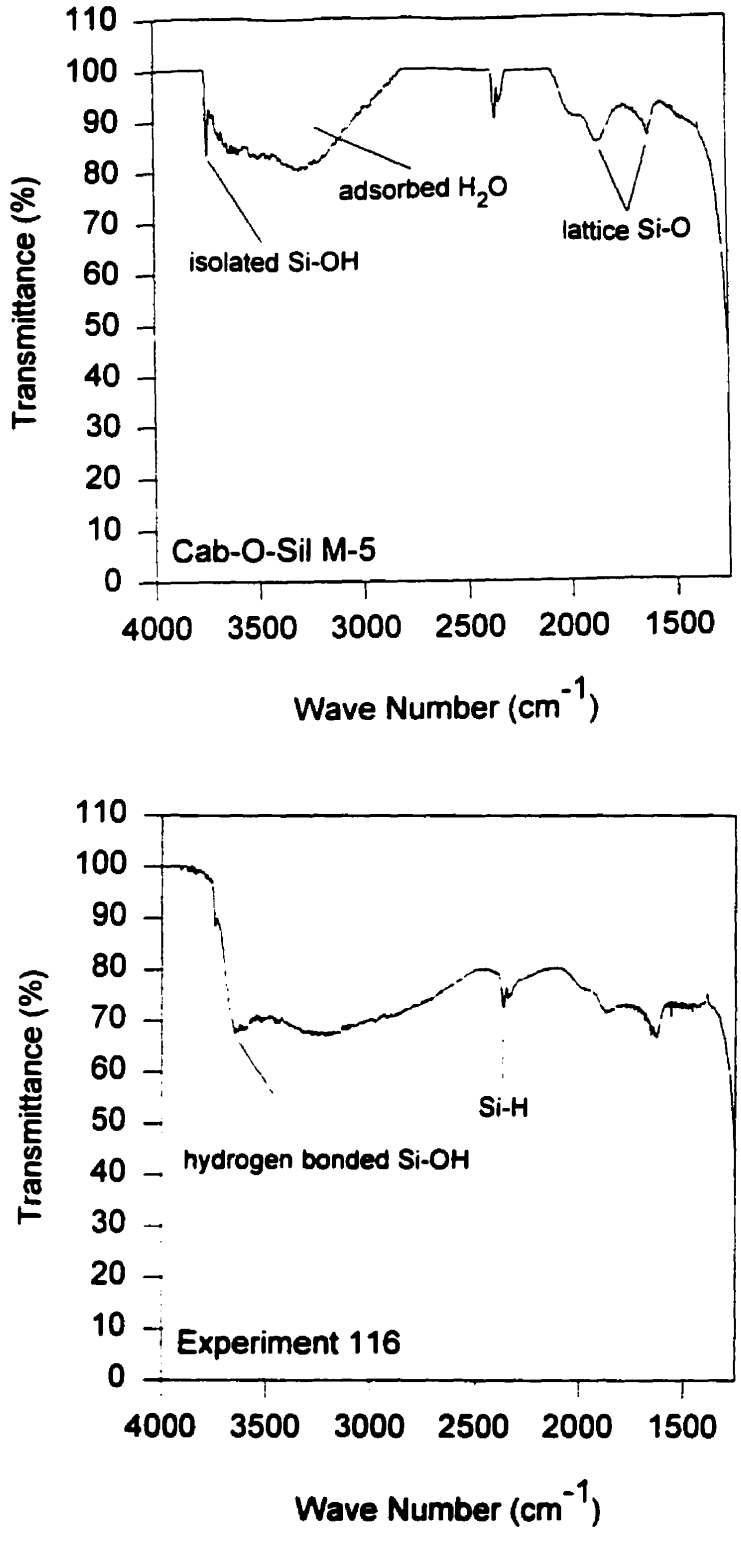

Figure 5.6 FTIR spectra of Cab-O-Sil® M-5 and experimental powder 116.

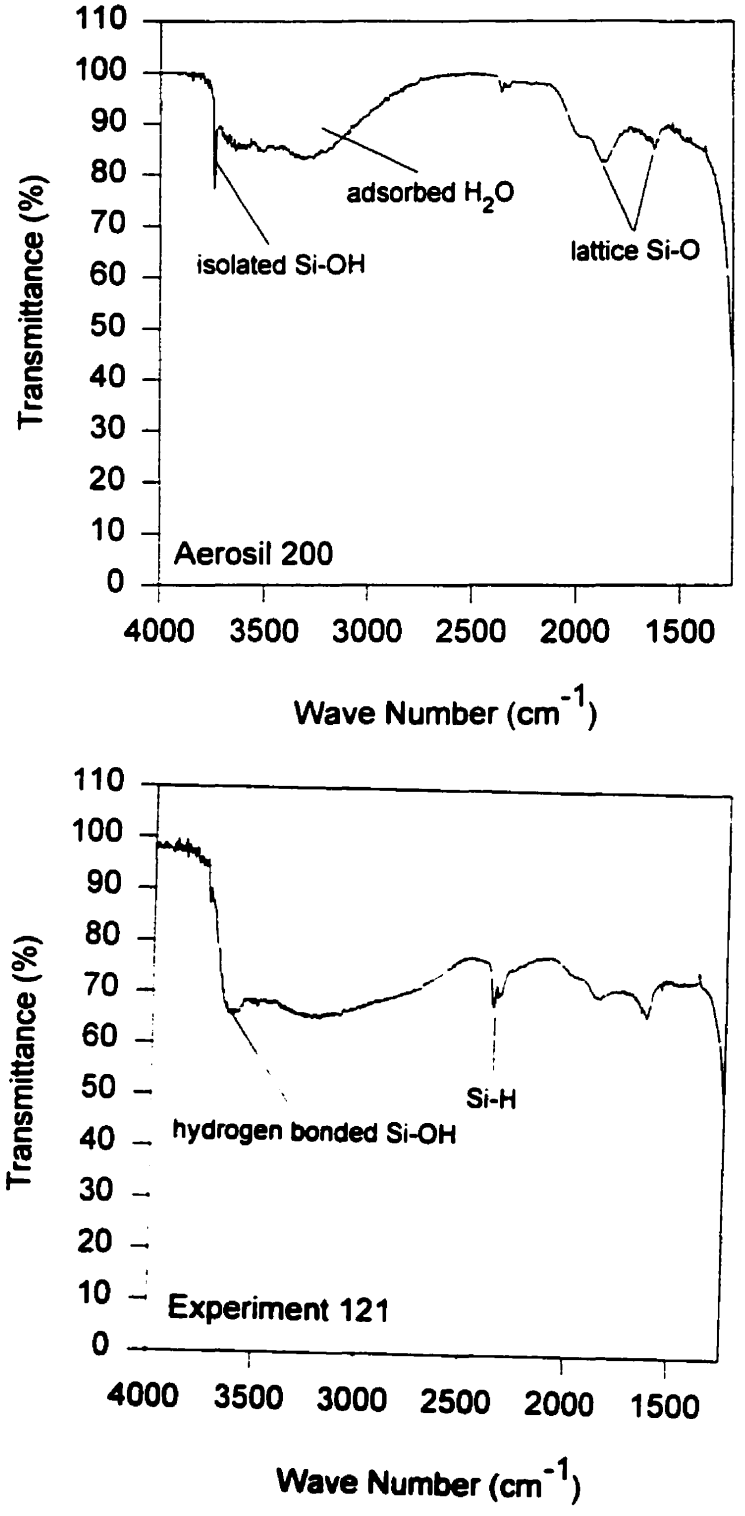

Figure 5.7 FTIR spectra of Aerosil® 200 and experimental powder 121.

system was used by Schnell et al. (1978) who reported the production of powders with a hydroxyl density of 7.5 SiOH/nm^2 (see Table 2.3).

5.3.5 Effect on Powder Morphology

The powder morphology was characterized by bulk appearance, X-ray diffraction and TEM (Transmission Electron Microscopy). The bulk appearance of the fumed silica powders produced during this study did not vary greatly with varying oxidation zone conditions. In all cases, the powders had the characteristic white, fluffy appearance of commercial fumed silica (see Figure 5.8). The white color indicated that the powders were highly oxidized (very little $SiO_{(s)}$). Like the high surface hydroxyl density, this was also the result of the high $H_2O_{(g)}$ concentration in the oxidation zone. Another important characteristic of commercial fumed silica is that it is completely amorphous. The powders produced during these experiments were also found to have negligible crystallinity. This can be seen in Figures 5.9 and 5.10 where typical X-ray diffraction patterns are plotted for the experimental powders and Aerosil® 200. The absence of sharp peaks in the X-ray pattern is evidence of the amorphous nature of the powders. This was the result of the high quench rates in the oxidation zone. The morphology of the experimental powders on a microscopic scale was examined by TEM. This work was conducted at the CM^2 Laboratory of École Polytechnique (Montreal, Quebec, Canada). The aggregate structure of the experimental powders was found to be similar to that of Aerosil® 200. Figure 5.11 shows that the powders were composed of the characteristic chain-like aggregates commonly observed in fumed silica. Important to note is the lack of individual spherical particles which Everest et al. (1973) associated with low activity fumed silica. The creation of these chain-like aggregates was the result of collision and partial fusion of molten particles in the oxidation zone.

Also verified through TEM analysis was the likely condensation of $SiO_{(g)}$ prior to entering the oxidation zone for experiments 121 and 122. Figure 5.12 shows TEM micrographs of the powder produced during experiment 122 from which we can clearly

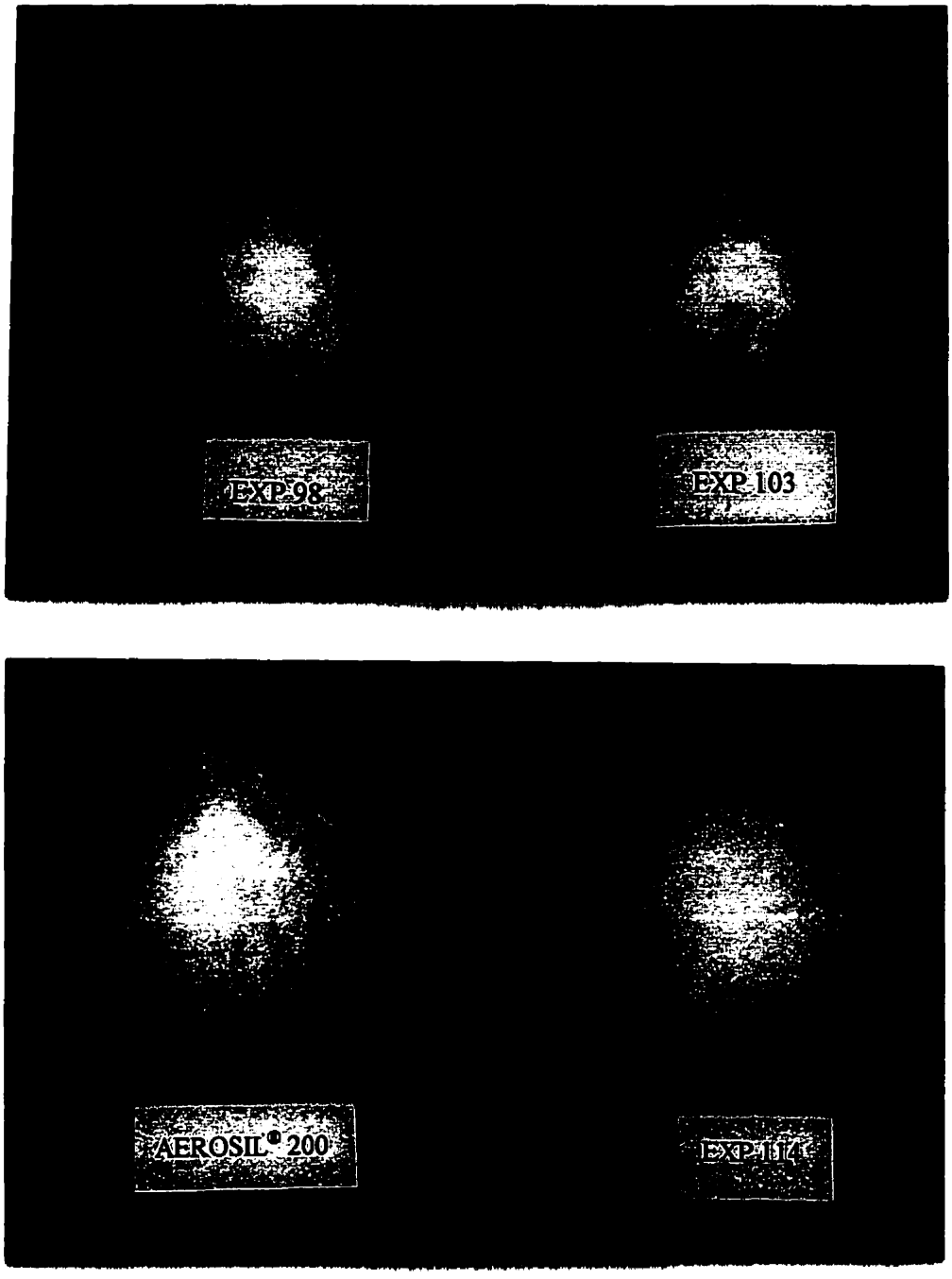

Figure 5.8 Appearance of experimental powder 98, 103 and 114 compared with Aerosil® 200.

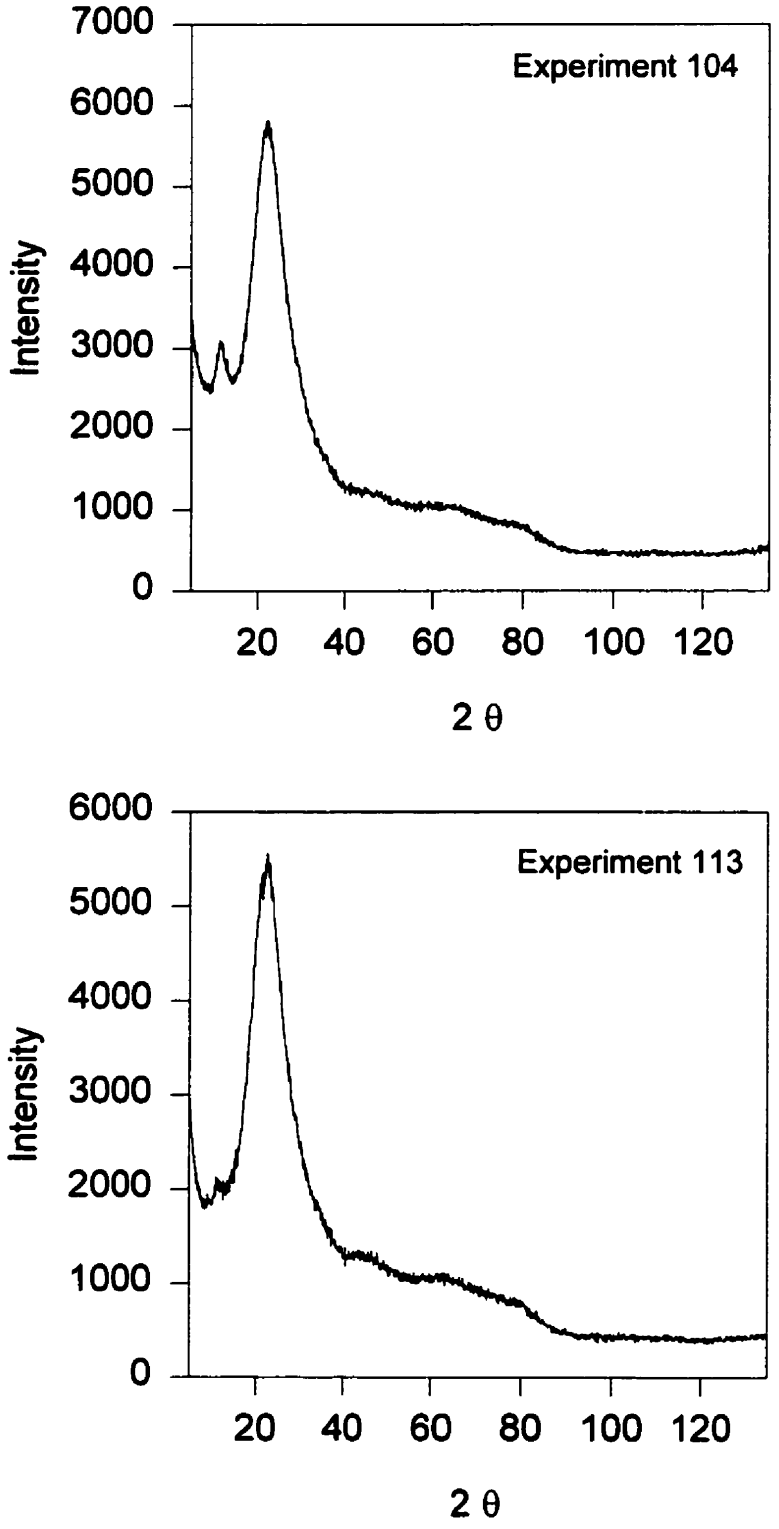

Figure 5.9 X-ray diffraction pattern of experimental powders 104 and 113.

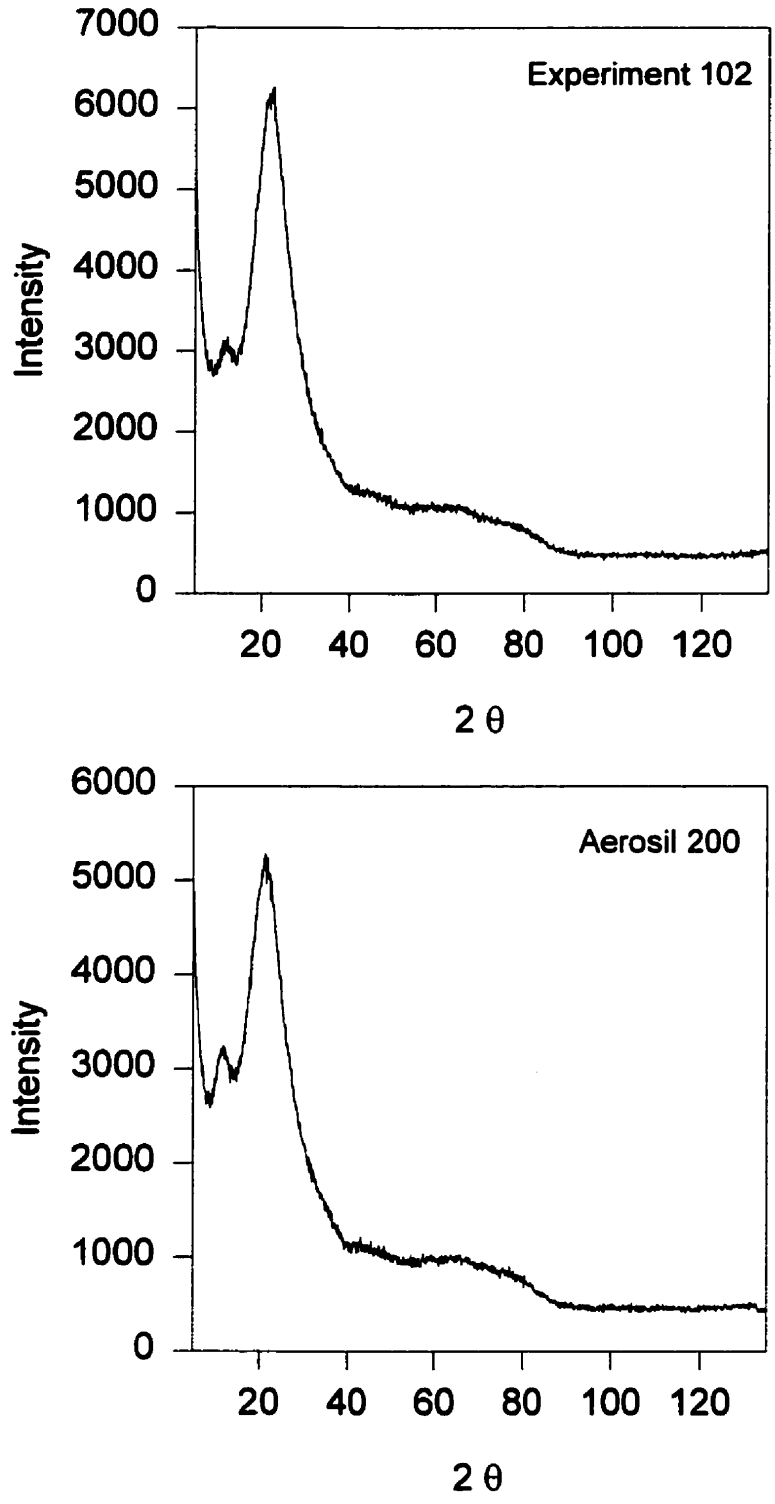

Figure 5.10 X-ray diffraction pattern of experimental powder 102 and Aerosil® 200.

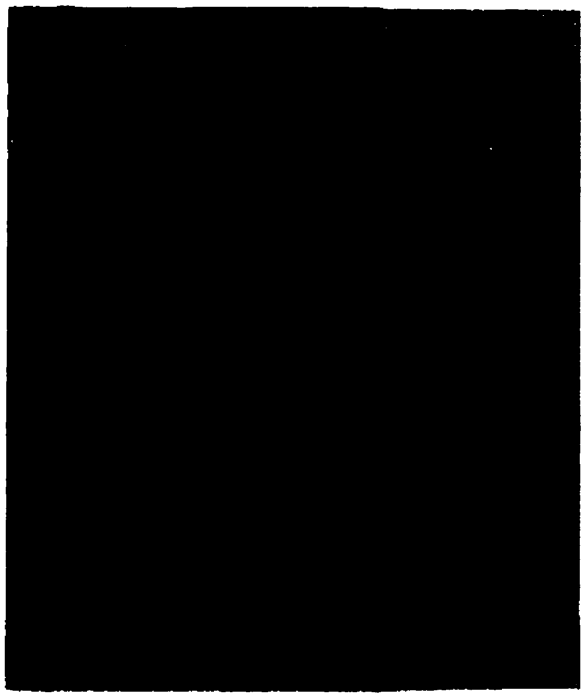

a) Exp. 101 (scale: 1.2 cm = 100 nm).

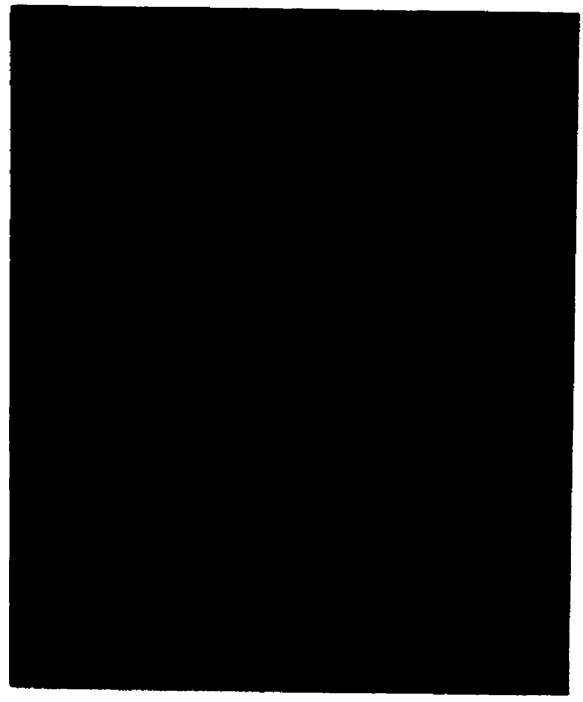

b) Exp. 109 (scale: 1.2 cm = 100 nm).

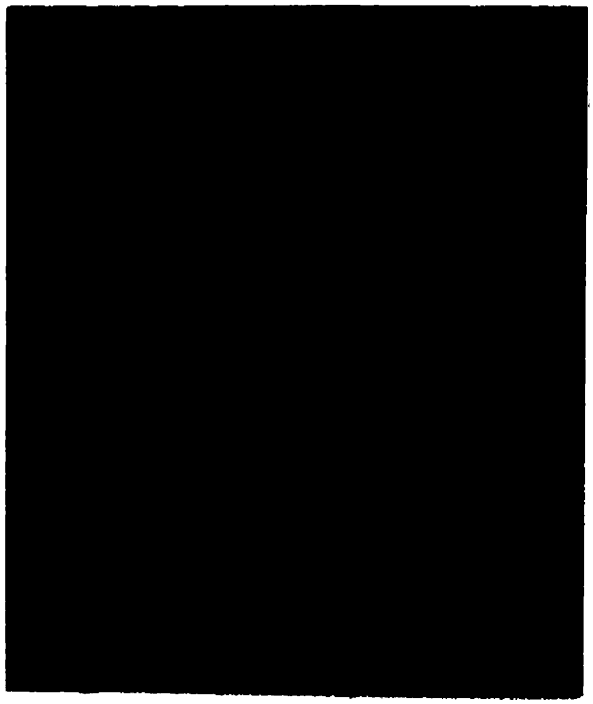

c) Exp. 114 (scale: 1.2 cm = 100 nm).

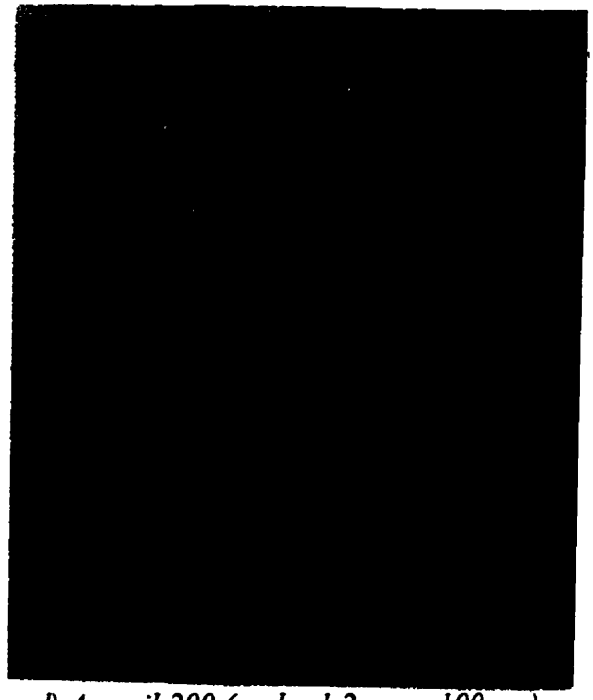

d) Aerosil 200 (scale: 1.2 cm = 100 nm).

Figure 5.11 TEM micrographs of experimental powders and Aerosil® 200.

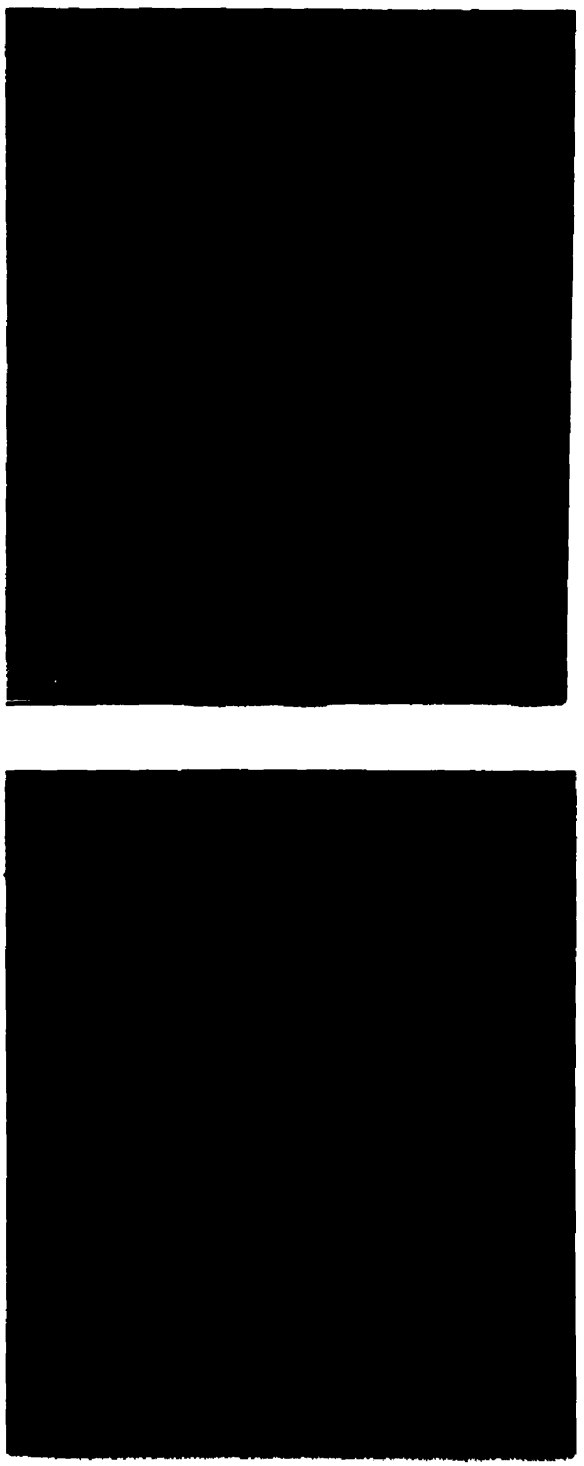

Figure 5.12 TEM micrographs of experimental powder 122 (scale: 1.2 cm = 100 nm).

see the presence of large particles (~ 100 nm). These particles were probably formed in the plasma chamber due to the high $SiO_{(g)}$ concentration. The absence of large particles at the lower $SiO_{(g)}$ concentration levels (see Figure 5.11) is evidence that condensation in the plasma chamber was not significant during experiments using a pure Ar plasma gas.

5.3.6 Test of Thickening and Thixotropic Ability

A verification of the quality of the fumed silica produced was made by simulating its application as a thickening and thixotropic agent. The thickening and thixotropic ability of the powders was determined using a rheological test based on an ASTM standard procedure for evaluating thixotropic materials (Annual Book of ASTM Standards, 1990). The test consisted of preparing a 2 % (by weight) suspension of a powder in a 1000 cp calibration oil (Dow Corning 200(R) Fluid, 1000 cst, Dow Corning Canada Inc.). According to the Cabot classification of liquids, the oil was considered a "medium to low" hydrogen bonding system (Cabot Corp., 1983). This oil was selected because the thickening and thixotropic effect of the fumed silica powder would be evident even at low concentrations. The powders were dried at 373 K for 24 hours prior to the preparation of a suspension.

The rheological properties of a suspension were measured using a Nametre® viscometer (Metuchen, New Jersey, USA) at varying spindle speeds. The suspensions were initially sheared at 5 rpm for 6 minutes which corresponded to 30 spindle revolutions. The speed was then increased to 10 rpm, again for 30 spindle revolutions. This pattern was continued until a speed of 100 rpm was attained, after which the speed was reduced back down to 5 rpm using a similar pattern. Viscosity measurements were recorded at each change in spindle speed. An example of a viscosity profile for a suspension prepared with Aerosil® 200 is shown in Figure 5.13. The thickening and thixotropic ability of the powder is obvious from this figure. The addition of Aerosil® 200 to the oil increased its viscosity approximately 9 times at a low spindle speed (5 rpm) and caused its viscosity to decrease dramatically as the shear rate was increased.

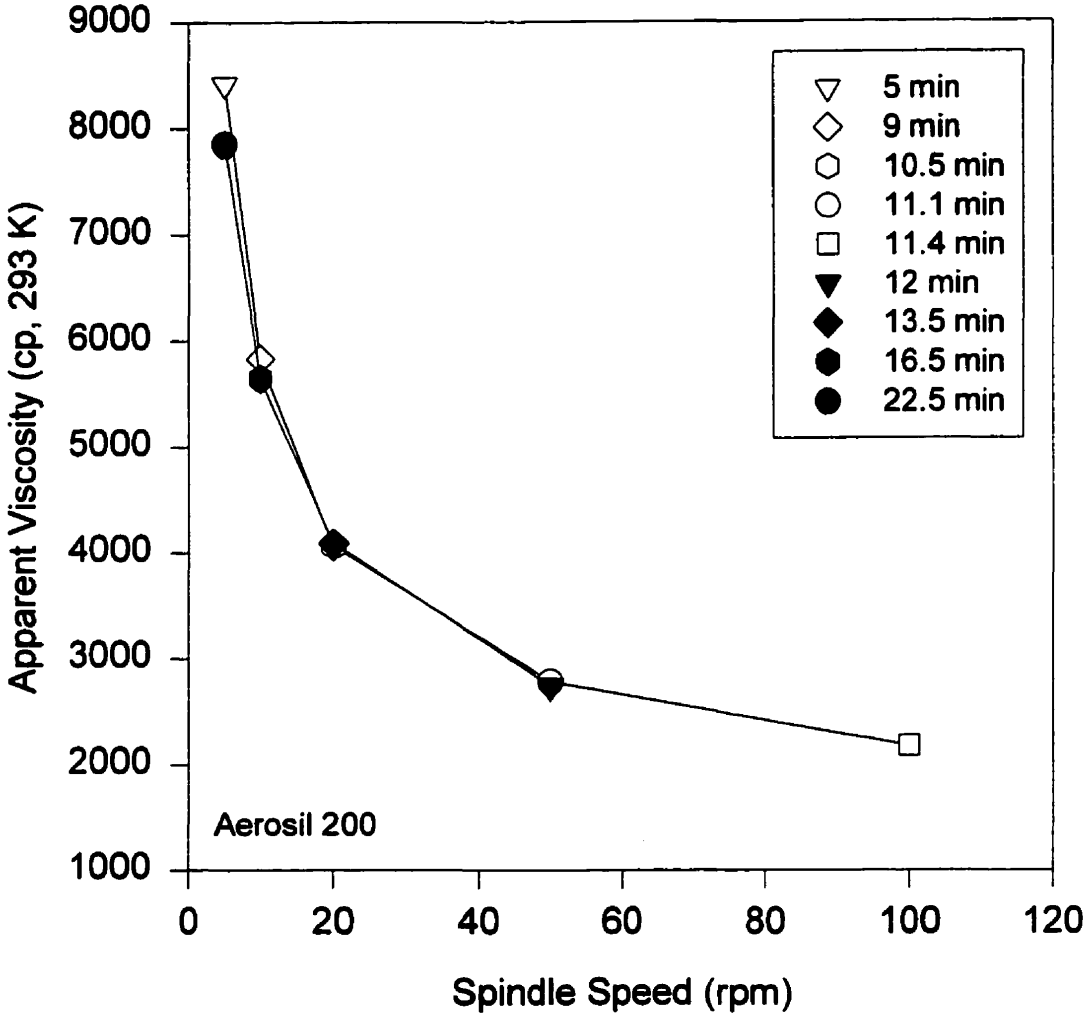

Figure 5.13 Viscosity profile during evaluation of thickening and thixotropic ability of Aerosil® 200.

Two important parameters were determined from each rheological test: 1) degree of thickening T_h, and 2) degree of shear thinning S_t. These parameters are defined below:

$$T_h = \frac{\eta_5}{\eta_{oil}} \tag{5.5}$$

$$S_t = \frac{\eta_5}{\eta_{50}} \tag{5.6}$$

where η_{rpm} is the apparent viscosity of the suspension at the specified spindle speed and η_{oil} is the viscosity of the calibration oil (1000 cp). The degree of thickening was a direct measure of the hydrogen bonding ability of the powder and therefore its effectiveness as a thickening and thixotropic agent. Recall from section 2.1.3 that fumed silica's thickening and thixotropic ability is due to the presence of surface hydroxyl groups (Si-OH) which allow hydrogen bonding networks to form between aggregates and agglomerates (see Figure 2.2). The greater the degree of network formation, the greater the effectiveness of a fumed silica powder as a thickening and thixotropic agent. The degree of shear thinning, which measures the decrease in viscosity for an increasing shear rate over a given time interval, has been shown to be dependent on T_h (Addona and Munz, 1994). This is because S_t is a measure of the number of ruptures occurring in a hydrogen bonding network. As T_h increases, the number of hydrogen bonding sites increases, therefore, as the shear rate is increased a greater number of ruptures are likely to occur.

The degree of thickening measured for a given suspension was expected to be a function of the powder properties (specific surface area, surface hydroxyl density and aggregate shape) and concentration, liquid type, temperature and degree of dispersion. In order to isolate the effect of powder properties, the powder concentration, liquid type and temperature of the suspension were kept constant. To maintain an approximately constant degree of dispersion, the same mixing technique was used in the preparation of each suspension. Initially, the suspensions were mixed with an impeller at high speed for 10

TABLE 5.4 Comparison of mixing techniques for suspension preparation.

Powder	*Degree of Thickening, T_h [η_s/η_{oil}]*					
	Manually Mixed	*Low Speed Impeller*		*High Speed Impeller*		
		3 min	*10 min*	*3 min*	*10 min*	*30 min*
Aerosil® 200	2.74	2.59	2.79	8.42	8.64	10.64
112	3.38	3.03	2.61	2.41	2.26	2.19

minutes. Using this mixing technique, the experimental powders were found to have a much lower T_h compared to Aerosil® 200. This was surprising since the powders had been determined to have equivalent, and in some cases, superior properties to Aerosil® 200 (i.e. higher specific surface areas and higher surface hydroxyl densities). Since everything else was constant, a difference in the degree of dispersion was suspected to be causing these results.

In section 2.1.3, the importance of the degree of dispersion in obtaining maximum thickening and thixotropic effectiveness was discussed. The powder should be mixed sufficiently so that an extensive fumed silica network can form within the liquid. Mixing too intensely or for too great a period results in fragmentation of the network into smaller sections which may not be able to re-combine into the optimum structure. If the experimental powders and Aerosil® 200 had similar agglomerate structures, the degree of dispersion would be equivalent for similar mixing conditions. However, we can see in Table 5.4 that increasing the intensity and time of mixing reduced the effectiveness of experimental powder 112 and increased that of Aerosil® 200. When the suspension was prepared by manually mixing the powder into the oil, the performance of experimental powder 112 improved and exceeded that of the Aerosil® 200 suspension prepared in the same way. It therefore seemed that the experimental powders were easily over dispersed.

The following hypothesis is proposed to explain the above effect. The optimum dispersion is believed to be the point at which the agglomerates which make up a fumed

silica powder are sufficiently broken down to allow the optimum hydrogen bonding network to form. Beyond a certain point, the disentanglement of the agglomerates will become infinitely slow since only those aggregates which are highly entangled remain. The optimum network is therefore believed to be composed of agglomerates consisting of highly entangled aggregates. If the agglomerate is not highly entangled as was suspected for the experimental powders, then the smallest shearing force will result in a large degree of disentanglement and the creation of very small agglomerates which may be considered over dispersed.

Determining the degree of entanglement in the agglomerates was not possible, however, SEM (Scanning Electron Microscopy) was used to examine differences between the experimental and commercial agglomerate structures. Typical agglomerate structures observed for the experimental powders are shown in Figure 5.14 while those of Aerosil® 200 and Cab-O-Sil® M-5 are shown in Figure 5.15. We can see that there is an obvious difference between the experimental and commercial agglomerates. The commercial powder agglomerates seem smoother and more densely packed. This difference in agglomerate structure was probably due to differences in the downstream processing of the fumed silica powder. In the current process, the fumed silica generated in the oxidation zone was sent directly to the baghouse filter. In the commercial flame hydrolysis process described in section 2.1.1, an agglomerator is used before powder collection. The role of this device is to generate large agglomerates which can be easily removed by a cyclone or baghouse filter. In addition to facilitating powder collection, it seems that the agglomerator also plays an important role in determining the agglomerate structure of a fumed silica powder.

A summary of the results from the rheological tests with suspensions prepared using a manual mixing technique are shown in Table 5.5. The fumed silica powders from experiments 97 and 116 were not tested due to a lack of powder. Powder from experiment 122 was tested both before and after drying with no significant difference detected. Figure 5.16 shows that the thickening ability of the powders increased with increasing specific surface area. This can be explained by an increase in the number of hydroxyl

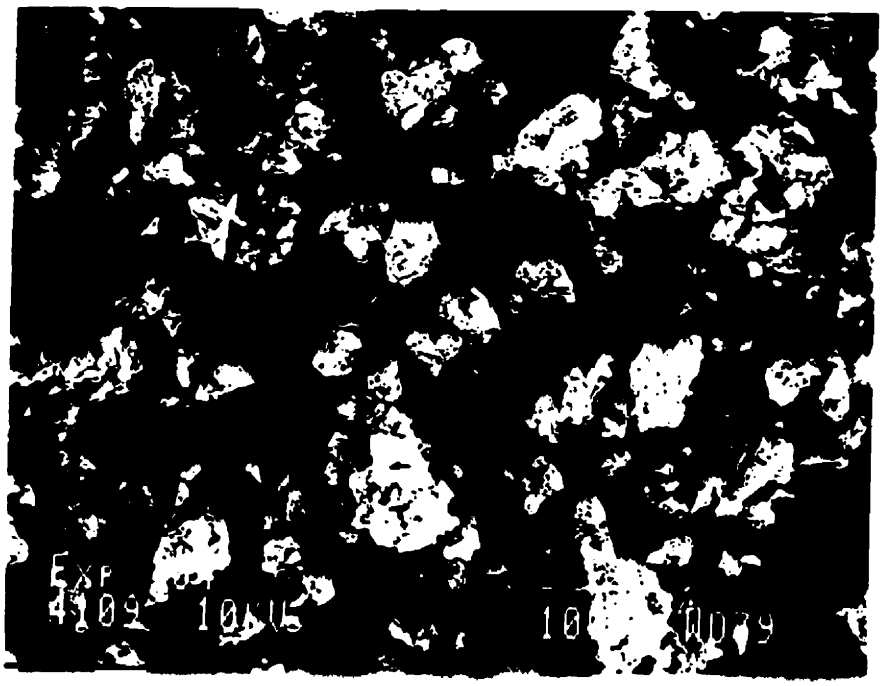

a) Experiment 104.

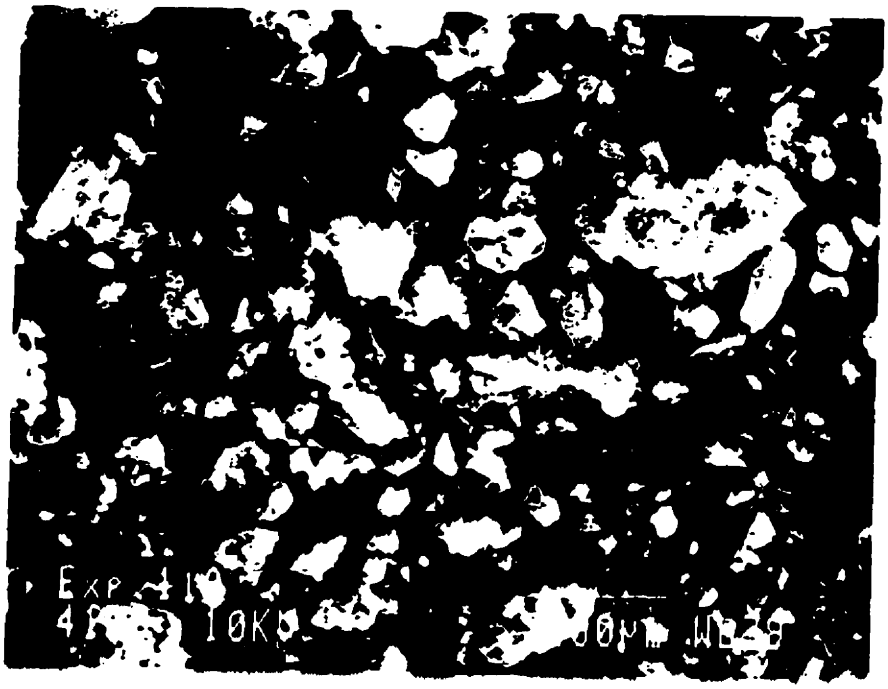

b) Experiment 112.

Figure 5.14 SEM micrographs of agglomerate structure for experimental powders.

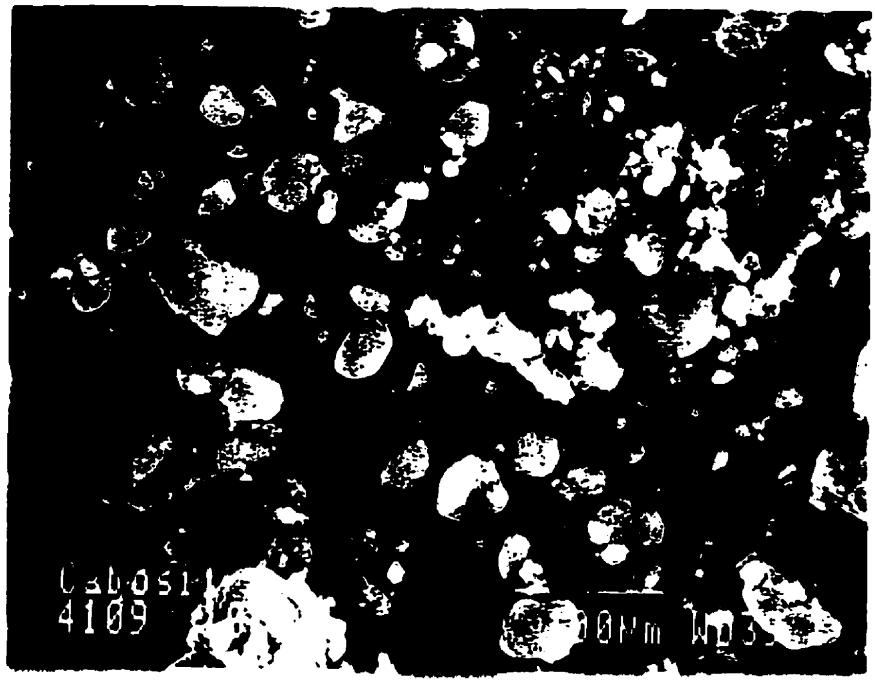

a) Cab-O-Sil® M-5.

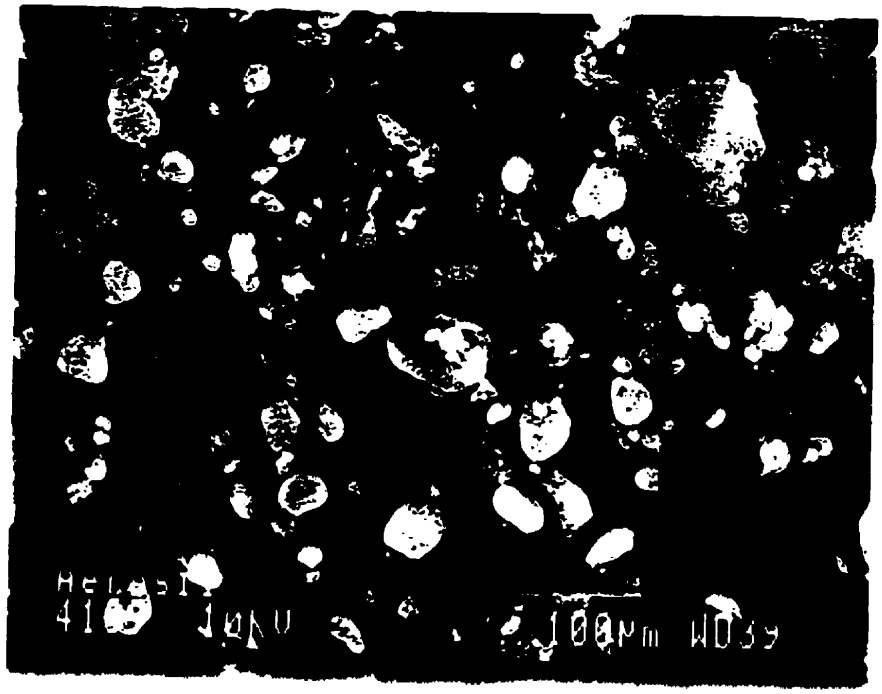

b) Aerosil® 200.

Figure 5.15 SEM micrographs of agglomerate structure for commercial powders.

TABLE 5.5 Degree of thickening and shear thinning of manually mixed suspensions.

Experimental Powder	*Degree of Thickening* $T_h = \eta_s/\eta_{oil}$	*Degree of Shear Thinning* $S_t = \eta_s/\eta_{50}$
104	1.69	1.05
110	1.85	1.11
123	1.71	1.02
103	1.66	0.98
102	2.11	1.06
109	2.04	1.05
115	1.94	1.03
98	2.13	1.09
101	2.38	1.09
108	2.39	1.12
107	2.17	1.06
106	2.11	1.06
118	2.72	1.11
112	3.38	1.22
111	2.83	1.16
113	2.06	1.05
114	2.92	1.17
121	2.24	1.07
122	2.76	1.17
122 (not dried)	2.49	1.17

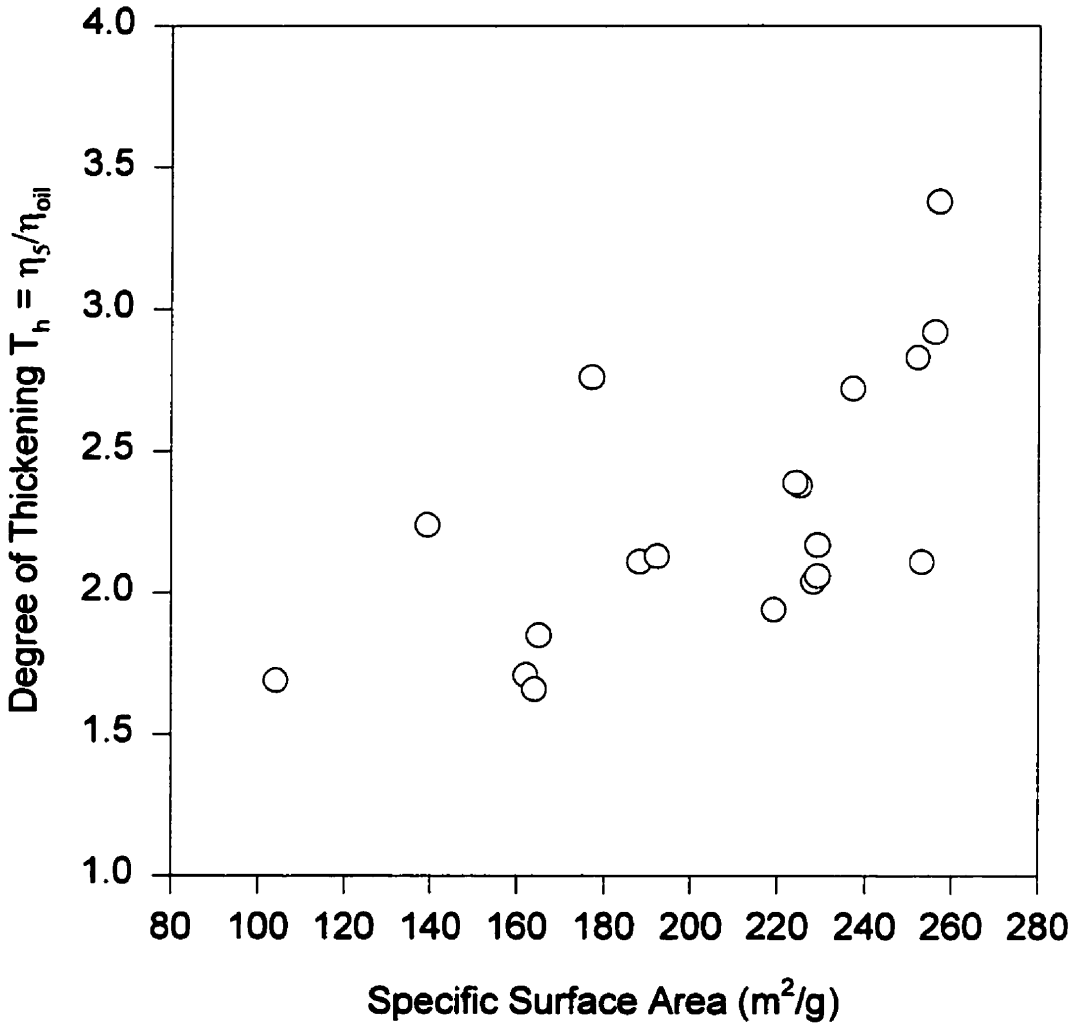

Figure 5.16 Effect of powder specific surface area on degree of thickening (assuming all other properties are equivalent).

sites which increased the degree of network formation within the liquid. In addition to experimental error, the wide scatter of the data was also due to differences in aggregate structure, surface hydroxyl density and degree of agglomeration.

5.3.7 Powder Purity

Powder purity was measured using ICP emission spectroscopy (SKW, Becancour, Quebec, Canada). The purity of selected experimental powders is summarized in Table 5.6 along with that of Aerosil® 200. The purity was found to range from 96.48 - 98.94 % SiO_2 compared to 99.95 % for Aerosil® 200. As expected, the greatest impurity in the experimental powders was due to Na. The purity could have been increased by postponing the start of powder collection until the Na had been completely purged from the reactor. This was not possible during this study since a sufficient amount of powder had to be collected for analysis during the limited experimental duration. Sodium contamination is not expected to be a problem if this process is applied industrially since operation will be for much longer periods of time. From Table 5.6 we can see that the purity of the powder produced using this process will approach that of the quartz feed (99.94 %) after Na (added as NaOH) is completely purged from the reactor.

TABLE 5.6 Composition of selected experimental powders compared to Aerosil® 200.

Oxide[1]	***Powder Composition [mass %]***								
	97	***109***	***115***	***108***	***107***	***118***	***111***	***122***	***Aerosil***
Al_2O_3	0.0229	0.0079	0.0096	0.0087	0.0093	0.2253	0.0087	0.0130	0.0036
As_2O_3	0.0012	0.0001	0.0013	---	---	---	0.0001	0.0003	0.0001
BaO_2	0.0002	---	---	0.0001	---	0.1656	---	---	---
Bi_2O_3	---[2]	0.0003	---	0.0006	0.0003	0.0006	---	---	0.0004
CaO	0.1525	0.0515	0.0620	0.0512	0.0501	0.4163	0.0313	0.0238	0.0022
CdO	0.0016	---	---	---	---	---	---	---	---
CoO	0.0001	0.0001	---	0.0001	0.0001	---	0.0001	0.0001	0.0001
Cr_2O_3	0.0009	0.0006	---	0.0007	0.0009	0.0004	0.0003	0.0007	0.0004
CuO	0.0026	0.0006	0.0046	0.0010	0.0008	0.0006	0.0004	0.0006	0.0001
Fe_2O_3	0.0422	0.0305	0.0253	0.0437	0.0603	0.0335	0.0440	0.0499	0.0084
La_2O_3	0.0002	0.0001	0.0009	---	---	0.0001	---	---	---
MgO	0.0129	0.0023	0.0113	0.0108	0.0027	0.2662	0.0015	0.0090	0.0073
MnO	0.0008	---	0.0026	---	0.0001	0.0004	---	---	0.0001
MoO_3	---	---	---	---	---	---	---	---	---
Na_2O	3.2264	2.1441	1.5555	2.0295	1.9675	2.4029	0.9739	2.1603	---
NiO	0.0024	0.0011	0.0010	0.0019	0.0019	0.0010	0.0015	0.0005	0.0006
P_2O_5	0.0025	0.0002	0.0037	0.0005	0.0014	---	---	0.0005	0.0005
Pb_3O_4	0.0006	0.0002	0.0004	---	---	0.0002	---	0.0007	---
Sb_2O_3	0.0011	---	---	---	0.0004	0.0004	---	---	---
Sc_2O_3	0.0003	---	---	---	---	---	---	---	---
SnO_2	---	0.0001	---	0.0001	---	---	0.0003	0.0001	---
SrO	0.0012	0.0004	---	0.0004	0.0004	0.0024	0.0002	0.0002	---
TiO_2	0.0010	0.0005	0.0005	0.0003	0.0005	0.0023	0.0003	0.0005	0.0013
V_2O_5	0.0005	0.0004	---	0.0002	0.0004	0.0004	0.0004	0.0002	---
ZnO	0.0103	0.0009	0.0011	0.0017	0.0015	0.0017	0.0020	0.0012	0.0012
ZrO_2	0.0004	0.0003	---	---	---	0.0018	0.0001	0.0001	---
SiO_2[3]	***96.515***	***97.758***	***98.320***	***97.849***	***97.901***	***96.478***	***98.935***	***97.738***	***99.954***
Steady -State SiO_2[4]	***99.735***	***99.895***	***99.869***	***99.872***	***99.862***	***98.874***	***99.902***	***99.892***	---

1. Impurity is assumed to be in its common oxide form. 2. Less than 0.0001 %. 3. Silica content by difference. 4. Assuming mass % Na_2O = mass % Na_2O in quartz (0.0067).

Chapter 6 - CONCLUSION

6.1 Conclusions

1. Initiating a Transferred Arc to a Silica Anode:

The high electrical resistivity of silica at low temperature makes arc transfer to a silica anode difficult. Temporarily decreasing the electrical resistivity of the silica anode by adding a conductive, volatile impurity can overcome this problem. A good candidate is Na because of its relatively low boiling point and the high mobility of Na^+. A safe and easily available source of Na is NaOH.

2. Sodium Contamination of the Silica Anode:

Sodium contamination of the anode decreased throughout an experiment due to its continued vaporization. Sodium was transported to the anode surface through the migration of Na^+ under the influence of the applied electric field and the concentration gradient. The rate of Na vaporization increased with increasing current because of higher temperatures within the anode which increased the mobility of Na^+.

3. Electric Conduction Mechanism in the Silica Anode:

The main charge carriers within the anode were free electrons and holes. The electrolysis of silica was not believed to be significant because of the low crucible mass loss.

4. Electrical Resistivity of the Silica Anode:

The decrease in anode voltage with increasing current was the result of a decrease in the electrical resistivity of the silica due to the higher temperatures within the anode. Mathematical modeling of the anode showed that if the electrical resistivity was assumed to decrease exponentially with increasing temperature, the decrease in anode resistance with increasing current was well predicted. The electrical resistivity of the present silica anode was significantly lower (~ 1000) than that measured by Veltri (1963). This was due to the increased impurity level which caused an increase in the number of available charge carriers by donor or acceptor type semiconduction.

5. Convective Heat Transfer to the Anode Surface:

Convective heat transfer was not an important contribution to the overall heat flux input to the anode surface. The convective heat transfer rate was believed to have been significantly reduced by the counter flow of decomposition products ($SiO_{(g)}$ and O_2) from the center of the anode surface.

6. Silica Anode Decomposition:

When reaction with the crucible was not significant, decomposition of the silica anode mainly occurred at the surface due to arc impingement and resulted in the formation of $SiO_{(g)}$ and O_2 via the following reaction:

$$SiO_2 \rightarrow SiO_{(g)} + \tfrac{1}{2}O_2 \qquad (6.1)$$

The decomposition of silica was a heat transfer limited process with most of the decomposition occurring below the arc root where the anode surface had attained its

boiling point. In this region, the rate of silica decomposition was determined by the anode surface heat balance.

7. Effect of Plasma Gas Flow Rate and Current on Silica Decomposition:

Increasing plasma gas flow rate did not lead to an increase in the rate of silica decomposition because convective heat transfer was a minor contribution to the overall anode surface heat input. The increase in the decomposition rate with increasing current was the result of an increased heat input to the anode due to electron flow at the surface and arc radiation which was absorbed internally since the anode surface was transparent.

8. Resistance Heating and Fluid Flow Within the Silica Anode:

Increasing current did not lead to an increase in the rate of resistance heating within the anode because the electrical resistivity of silica decreased with increasing temperature. Fluid flow within the anode was limited by the high viscosity of vitreous silica. The maximum velocities predicted within the anode were < 1 mm/s for the operating conditions studied.

9. Addition of H_2 to the Plasma Gas:

The addition of small quantities of H_2 to the plasma gas caused a significant reduction of the specific energy requirement for silica decomposition. This reduction was the result of an increase in the rate of radiative heat transfer to the anode and a consumption of O_2 via:

$$H_2 + \tfrac{1}{2}O_2 \rightarrow H_2O \qquad (6.2)$$

The above reaction resulted in a lowering of the boiling point which allowed

decomposition to occur over a greater portion of the anode surface. The theoretical energy requirement for silica decomposition was also lowered when H_2 was added to the plasma gas.

10. Modeling Silica Anode Decomposition:

The assumption of a heat transfer limited decomposition process allowed the prediction of decomposition rates which were of the same order of magnitude as those observed experimentally. The discrepancy between the predicted and experimental decomposition rates was believed to be mainly due to the inaccuracies in the estimation of silica properties and the rate of convective heat transfer to the anode surface. The inaccuracies of the property estimates was due to a lack of data at high temperature (2000 - 3200 K) and for varying purity. The rate of convective heat transfer to the anode was overestimated because the efflux of decomposition products from the anode surface was neglected. The sensitivity of the predicted decomposition rates to significant variations in boiling point, anode fall potential, work function and emissivity could not account for the discrepancy with experimental results.

11. Fumed Silica Generation in the Oxidation Zone:

Fumed silica was generated in the oxidation zone by rapidly quenching the $SiO_{(g)}$ containing reactor exit gas with steam according to the following overall reaction:

$$SiO_{(g)} + H_2O_{(g)} \rightarrow SiO_2 + H_2 \qquad (6.3)$$

In addition to $SiO_{(g)}$ oxidation and aerosol formation, surface hydroxylation also occurred in the oxidation zone. In the present aerosol system, $SiO_{(g)}$ and $SiO_{2(g)}$ were both potential monomers whose condensation led to the formation of fumed silica.

12. Effect of Oxidation Zone Parameters on Properties of Fumed Silica Product:

a) Specific Surface Area:

The increase in specific surface area with increasing steam flow rate was due to a more rapid quenching of the reactor exit gas which resulted in the formation of a large number of mostly smaller nuclei at the point of homogeneous nucleation. This effect was not seen at higher steam flow rates because of a mixing limitation within the oxidation zone. This limitation was more evident at high reactor exit gas temperature because the viscosity of the gas was increased. This mixing limitation is evidence that the quench rate was only important in a very small region close to the reactor exit where most of the powder formation process occurred. The increase in specific surface area with increasing $SiO_{(g)}$ concentration at constant steam flow rate was the result of an increase in the quench rate due to a higher reactor exit gas temperature. For an approximately constant reactor exit gas temperature, a large increase in $SiO_{(g)}$ concentration resulted in a significant lowering of the specific surface area due to a higher initial monomer concentration. This resulted in the production of a smaller number of larger diameter particles at the point of homogenous nucleation. The decrease in specific surface area was also due to an increase in the degree of $SiO_{(g)}$ condensation occurring in the plasma chamber.

b) Surface Hydroxyl Density:

Variation of the oxidation zone parameters did not have a significant effect on the surface hydroxyl density of the fumed silica product. The surface hydroxyl density approached 7.85 $SiOH/nm^2$ which corresponded to a fully hydroxylated surface. The high surface hydroxyl density was due to the high $H_2O_{(g)}$ concentration in the oxidation zone.

c) Morphology:

Powder morphology was not greatly affected by variations in the oxidation zone parameters. In all cases, the powder product had the typical white, fluffy appearance of

fumed silica. The powders were found to have negligible crystallinity due to the high quench rates in the oxidation zone. TEM analysis showed the powders to be composed of the characteristic chain-like aggregates which were the result of collision and partial fusion of molten particles in the oxidation zone.

13. Thickening and Thixotropic Ability of Fumed Silica Product:

The thickening and thixotropic ability of the fumed silica powders produced during this study was found to be much less than that of Aerosil® 200. The suspected reason was a difference in the agglomerate structure which caused the experimental powders to be easily over dispersed in the liquid being treated. Experimental powder agglomerates were believed to be composed of aggregates which were much less entangled than those found in Aerosil® 200. The difference in agglomerate structure may have been due to the use of an agglomerator between the powder formation and collection steps in the production of Aerosil® 200.

14. Purity of Fumed Silica Product:

The greatest impurity in the experimental powders was due to Na. The purity could have been increased by postponing the start of powder collection until the Na had been purged from the reactor. Sodium contamination is not expected to be a problem if this process is applied industrially since operation will be for much longer periods of time. The industrial process will therefore only suffer from Na contamination of the product during start-up which will likely occur only a few times a year. The purity of the powder produced using this process will approach that of the quartz feed (99.94 %) after Na (added as NaOH) is completely purged from the reactor.

6.2 Recommendations for Future Work

Fumed silica production using a novel thermal plasma process was demonstrated during the course of this study. Based on the promising results obtained, continued development of this process is recommended. The next step which should be considered is scale-up to the pilot plant stage. In this next stage of the process development the following work is suggested:

1. An alternative construction material for the crucible and internal plasma chamber should be examined. As we have seen from this study, graphite is consumed through reaction with silica, $SiO_{(g)}$ and O_2. A material of construction which should be examined is tungsten. Tungsten has been used to line crucibles to contain silica up to approximately 2300 K without reaction (Bockris et al., 1955).

2. The optimum H_2 concentration in the plasma gas should be determined. This study has shown that the specific energy requirement of silica decomposition is significantly reduced when H_2 is added to the plasma gas. The use of pure H_2 as the plasma gas would be ideal, however, this will lead to an increase in the amount of $SiO_{(g)}$ condensing in the plasma chamber because of the much higher decomposition rates. Adding Ar or N_2 to the reactor either by mixing it with the plasma gas or as a separate stream may be required to dilute the $SiO_{(g)}$. The use of an NH_3 plasma gas should also be looked at since this can be a H_2 source which can be easily stored on site.

3. A procedure should be established which will allow reliable continuous operation so that shutdowns are minimized. The component which will require the greatest maintenance is the torch which may need to be replaced frequently either due to consumption of the cathode or mechanical failure. A multiple torch system is suggested (two or more) in which each supplies only a fraction of the total power. Operation at

lower power will increase the life of each torch. The use of multiple torches will also allow maintenance to be done without a shutdown of the process. When maintenance is being done on one torch, power to the others is increased to maintain the same production rate. The other components which may require occasional maintenance are the crucible and plasma chamber. These components can be verified during a complete shutdown of the process. Damage to the plasma chamber is not expected to be great and so continued use after a shutdown will not be a problem. This may not be true of the crucible since once solidified, the silica will no longer be electrically conductive. If the cost of the crucible is insignificant, it should be replaced following each shutdown. If this is not the case and re-use of the crucible is required, a hole can be drilled in the center of the solidified silica so that a graphite rod for arc ignition can be inserted. The hole should be large enough to accommodate a small quantity of NaOH which can be added around the rod. Another option is to empty the crucible while the contents are still molten, however, this would require a significant increase in the complexity and cost of the plasma reactor. The cost of the silica remaining in the crucible following a shutdown will be negligible so whether it is recycled or not will not affect the process economics greatly.

4. The use of an agglomerator, such as the one described by White and Duffy (1959), between the oxidation zone and the baghouse filter should be investigated. This will determine whether difference in agglomerate structure was the reason for the lack of thickening and thixotropic ability of the experimental powders compared to Aerosil® 200.

5. The study of the effect of oxidation zone parameters on powder properties should be continued. This should include an investigation of the effect of higher $SiO_{(g)}$ concentrations which will occur when H_2 is added to the plasma gas. The effects of reactor exit gas temperature and $SiO_{(g)}$ concentration should be separated in any future study of the oxidation zone. The effect of steam flow rate on the local quench rate can be examined through mathematical modeling since an experimental investigation of this will be difficult. The mathematical modeling work can also be used to investigate different

oxidation zone configurations so that the mixing efficiency between the reactor exit gas and steam can be improved.

6. An improved estimation of silica properties at higher temperatures (2000 - 3200 K) and for varying purity is required to better simulate the phenomena occurring in the anode. The effect of purity is especially important for the thermal conductivity and electrical resistivity.

7. A multicomponent arc model which takes into account the decomposition of the silica anode should be developed. This will allow a better estimation of the heat input terms to the anode surface and therefore a better estimate of the rate of silica decomposition using the anode model developed during this study.

6.3 Contributions to Knowledge

The following contributions to knowledge have been achieved as a result of this work:

1. Silica decomposition using a transferred arc process in which silica serves as the anode has been demonstrated.

2. The effect of plasma gas flow rate and current on the rate of silica anode decomposition has been investigated.

3. A mathematical model simulating the behavior of the silica anode has been developed.

4. The effect of temperature and $SiO_{(g)}$ concentration of the reactor exit gas, and steam flow rate on the properties of fumed silica generated in a given oxidation zone configuration was examined.

REFERENCES

Addona, T., "The Effect of Quench Conditions on the Properties of Fumed Silica Produced Using an Arc Process", M. Eng. Thesis, McGill University, Department of Chemical Engineering, Montreal Canada (1993).

Addona, T. and Munz, R. J., "Thermal Plasma Production of Fumed Silica: The Effect of Quench Conditions on Thickening and Thixotropic Ability", Can. J. of Chem. Eng. **72**, 476-483 (1994).

Annual Book of ASTM Standards, 1990, "Paints, Related Coatings and Aromatics", **06.01**, ASTM, Designation D2196-86 (1990).

Backer, G. and Szekely J., "The Interaction of a DC Transferred Arc with a Melting Metal: Experimental Measurements and Mathematical Description", Metallurgical Transactions B **18B**, 93-104 (1987).

Bacon, J. F. and Hasapis, A. A., "Viscosity of Molten Silica", J. Appl. Phys. **30**, 1470-1471 (1959).

Bacon, J. F., Hasapis, A. A. and Wholley, J. W., "Viscosity and Density of Molten Silica and High Silica Content Glasses", Physics and Chemistry of Glasses **1**, 90-98 (1960).

Bakken, J. A., "High Temperature Processing and Numerical Modeling of Thermal Plasmas in Norway", Pure and Applied Chemistry **66**, 1239-1246 (1994).

Bakken, J. A., N. J. Holt, and R. Jensen, "PRESS (Plasma Reactor for Smelting at SINTEF) - Remelting of Silicon Metal Fines and Production of Ultrafine Silica", Extraction Metallurgy '89, The Institution of Mining and Metallurgy, London (1989), pp. 233-251.

Biegler, H., W. Neugebauer and H. Kempers, German Patent, DE 1180 723, 1963.

Bird, R. B., Stewart, W. E. and Lightfoot, E. N., "Transport Phenomena", John Wiley & Sons, New York (1960), pp. 26-29, 646-647, 658-668.

Bockris, J. O'M., Mackenzie, J. D. and Kitchener, J. A., "Viscous Flow in Silica and Binary Liquid Silicates", Trans. Faraday Soc. **51**, 1734-1748 (1955).

Boulos, M. I., Fauchais, P. and Pfender, E., "Thermal Plasmas - Fundamentals and Applications" Vol. 1, Plenum Press, New York (1994), pp. 240-242, 303-323, 385-448.

Cabot Corporation, "Cab-O-Sil Properties and Functions", Information Brochure, United States (1983).

Callister, W. D., "Materials Science and Engineering, An Introduction", John Wiley & Sons, New York (1991), pp. 607-652, 740.

Chang, K., "Synthese de Poudres Ultrafines de Silice en Plasma D' Arc Transfere", Thèse de Doctorat, L' Universite de Limoges, Limoges, France (1994).

Choi, H. K. and Gauvin, W. H., "Operating Characteristics and Energy Distributions in Transferred Plasma Arc Systems", Plasma Chem. Plasma Process. **2**, 361-386 (1982).

Choo, R. T. C. and Szekely, J., "Vaporization Kinetics and Surface Temperature in a Mutually Coupled Spot Gas Tungsten Arc Weld and Weld Pool", Weld. J. **71**, 77s-93s (1992).

Choudhary, M. K., "Mathematical Modeling of Flow and Heat Transfer Phenomena in Electric Glass Melting Furnaces", Proceedings of the Julian Szekely Memorial Symposium on Materials Processing, ed. H. Y. Sohn, J. W. Evans and D. Apelian, The Minerals, Metals and Materials Society, 341-364 (1997).

Cohen, J., "Electrical Conductivity of Fused Quartz", Journal of Applied Physics **28**, 795-800 (1957).

Dinulescu, H. A. and Pfender, E., "Analysis of the Anode Boundary Layer of High Intensity Arcs", J. Appl. Phys. **51**, 3149-3157 (1980).

Eckert, E. R. G. and Pfender, E., "Advances in Heat Transfer", Vol. 4, Academic Press, New York (1967), pp. 278-282.

Essoltani, A., Proulx, P., Boulos, M. I. and Gleizes, A., "Volumetric Emission of Argon Plasmas in the Presence of Fe, Si and Al", Plasma Chem. Plasma Process. **14**, 437-450 (1994).

Everest, D. A., Sayce, I. G. and Selton, B., "Preparation of Ultrafine Silica Powders By Evaporation Using a Thermal Plasma", Symposium on Electrochemical Engineering, Institution of Chemical Engineers, London, **2**, 2.108-2.121 (1973).

Ferch, H., "Amorphous Synthetic Silica Products in Powder Form. Production and Characterization", Progress in Organic Coatings **9**, 135-163 (1981).

Gans, I. and Gauvin W. H., "The Plasma Production of Ultrafine Silica Particles", Can. J. of Chem. Eng. **66**, 438-444 (1988).

Girshick, S. L. and Chiu, C-P., "Homogeneous Nucleation of Particles from the Vapor Phase in Thermal Plasma Synthesis", Plasma Chem. Plasma Process. **9**, 355-369 (1989).

Girshick, S. L., Chiu, C-P. and McMurry, P. H., "Modeling Particle Formation and Growth in a Plasma Synthesis Reactor", Plasma Chem. Plasma Process. **8**, 145-157 (1988).

Gu, L., "Transport Phenomena in Silicon Vapor Infiltrated Argon Arcs and Anodic Metal Pools", Dr. Ing. Thesis, Department of Metallurgy, The Norwegian Institute of Technology, University of Trondheim, Trondheim, Norway (1993).

Himmelblau, D. M., "Process Analysis by Statistical Methods", AlphaGraphics, Austin, Texas (1980), pp. 155.

Hove, J. E. and Riley, W. C. ed., "Modern Ceramics: Some Principles and Concepts", John Wiley & Sons, New York (1965), pp. 81-82.

Hsu, K. C., Etemadi, K. and Pfender, E., "Study of the Free-Burning High Intensity Argon Arc", J. Appl. Phys. **54**, 1293-1301 (1983).

Huczko, A. and Meubus, P., "RF Plasma Processing of Silica", Plasma Chem. Plasma Process. **9**, 371-386 (1989).

Illigen, A. and Neugebauer W., German Patent, DE 1933 291, 1969.

Incropera, F. P. and DeWitt, D. P., "Introduction to Heat Transfer", John Wiley & Sons, New York (1985), pp. 311-312, 608-609, 665-695.

Joshi, S. V., Liang, Q., Park, J.Y. and Batdorf, J. A., "Effect of Quenching Conditions on Particle Formation and Growth in Thermal Plasma Synthesis of Fine Powders", Plasma Chem. Plasma Process. **10**, 339-358 (1990).

Kingery, W. D., "Surface Tension of Some Liquid Oxides and Their Temperature Coefficients", Journal of The American Ceramic Society **42**, 6-10 (1959).

Kong, P., Huang, T. T. and Pfender, E., "Synthesis of Ultrafine Silicon Carbide Powders in Thermal Arc Plasmas", IEEE Transactions on Plasma Science **PS-14**, 357-369 (1986).

Kong, P. C. and Lau, Y. C., "Plasma Synthesis of Ceramic Powders", Pure & Appl. Chem. **62**, 1809-1816 (1990).

Kotake, S. and Glass, I. I., "Flows with Nucleation and Condensation", Prog. Aerospace Sc. **19**, 129-196 (1981).

Lelièvre, C., Pickles, C. A., Toguri, J. M. and Simpson, C., "Plasma Production of Silica Whiskers", Production and Processing of Fine Particles, Proceedings of the International Symposium, ed. A. J. Plumpton, Canadian Institute of Mining and Metallurgy, 7, 589-598 (1988).

Liu, A. T. and Kleinschmit, P., "Production of Fumed Oxides by Flame Hydrolysis", British Ceramic Proceedings, No. 38, Dec. 1986, The Institute of Ceramics, 1-10 (1986).

MacRae, D. R., "Plasma Arc Process Systems, Reactors, and Applications", Plasma Chem. Plasma Process. **9**, 85S-118S (1989).

McKelliget J. and Szekely, J., "Heat Transfer and Fluid Flow in the Welding Arc", Metallurgical Transactions A **17A**, 1139-1148 (1986).

McLellan, G. W. and Shand, E. B., "Glass Engineering Handbook", McGraw-Hill, New York (1984), pp. 2-10-2-12, 2-26-2-36.

Ming, C., "Measurements and Modeling of a High Power Transferred Arc", Thèse de Doctorat, Université de Sherbrooke, Sherbrooke, Canada (1994).

Ming, C., Proulx, P., Mostaghimi, J. and Boulos, M. I., "A Study of the Modeling of High Power Transferred Arcs", ISPC-11 Loughborough, Symposium Proceedings, **1**, 216-221 (1993).

Mishra, P. K., Mohanty, B. C. and Nayak, B. B., "Fine Silica Powder Preparation by use of a Transferred Arc Thermal Plasma Reactor", Materials Letters **23**, 153-156 (1995).

Murphy, A. B. and Arundell, C. J., "Transport Coefficients of Argon, Nitrogen, Oxygen, Argon-Nitrogen and Argon-Oxygen Plasmas", Plasma Chem. Plasma Process. **14**, 451-490 (1994).

Njah, Z., Mostaghimi, J., Faghri, M. and Boulos, M., "Study of 3-D Mixing of a Cold Jet With a Transverse Plasma Stream", Int. J. Heat Mass Transfer **36**, 3897-3907 (1993).

Parisi, P. J., "A Novel Transferred-Arc Reactor", M. Eng. Thesis, McGill University, Department of Chemical Engineering, Montreal (1984).

Patankar, S. V., "Numerical Heat Transfer and Fluid Flow", McGraw-Hill, New York (1980).

Pfender, E., "Heat Transfer in Thermal Plasmas", Proceedings of the Julian Szekely Memorial Symposium on Materials Processing, ed. H. Y. Sohn, J. W. Evans and D. Apelian, The Minerals, Metals and Materials Society, 475-508 (1997).

Proulx, P., Mostaghimi, J. and Boulos, M. I., "Radiative Energy Transfer in Induction Plasma Modeling", Int. J. Heat Mass Transfer **34**, 2571-2578 (1991).

Rao, C. N. R., "Chemical Applications of Infrared Spectroscopy", Academic Press, New York (1963), pp. 287-291.

Rivière J. C., "Work Function: Measurements and Results" in "Solid State Surface Science", Academic Press, New York (1969), pp. 274-281.

Sanders, N. A. and Pfender, E., "Measurement of Anode Falls and Anode Heat Transfer in Atmospheric Pressure High Intensity Arcs", J. Appl. Phys. **55**, 714-722 (1984).

Schei, A. and Sandberg, O., "Back Reactions During Production of Silicon Metal in a Submerged Arc Electric Furnace", Selected Topics in High Temperature Chemistry, A Collection of Papers Dedicated to Prof. Hakan Flood on his 60th Birthday, 25 Sept., 1965, ed. T. Forland, K. Grjotheim, K. Motzfeldt and S. Urnes, Unwersitelsforlaget, Oslo, Norway, 141-150 (1966).

Schick, H. L., "A Thermodynamic Analysis of the High-Temperature Vaporization Properties of Silica", Chemical Review **60**, 331-362 (1960).

Schnell, C. R., Hamblyn, S. M. L., Hengartner, K. and Wissler, M., "The Industrial Application of Plasma Technology for the Production of Fumed Silica", Powder Technology **20**, 15-20 (1978).

Scholze, H., "Glass Nature, Structure and Properties", Springer-Verlag, New York (1991), pp. 360-362.

Sparrow, E. M. and Cess, R. D., "Radiation Heat Transfer", McGraw-Hill, New York (1978), pp. 48.

Tanaka, K., Ishizaki, K., Yumoto, S., Egashira, T. and Uda, M., "Production of Ultrafine Silicon Powder by the Arc Plasma Method", Journal of Materials Science **22**, 2192-2198 (1987).

Thompson, W. T., Bale, C. W. and Pelton, A. D., F*A*C*T - Version 2.1, Thermfact Ltd., Montreal, Canada (1996).

Tombs, N. C. and Welch, A. J. E., "Thermodynamic Properties of Silicon Monoxide: An Experimental Study of the Equilibria $SiO_2 + Si = 2SiO$ and $SiO_2 + H_2 = SiO + H_2O$", Journal of the Iron and Steel Institute **172**, 69-78 (1952).

Ullmann's Encyclopedia of Industrial Chemistry, Volume A23, ed. B. Elvers, S. Hawkins, W. Russey and G. Schulz, VCH Weinheim, FRG (1993), pp. 599-642.

Urbain, G., Bottinga, Y. and Richet, P., "Viscosity of Liquid Silica, Silicates and Alumino-Silicates", Geochimica et Cosmochimica Acta **46**, 1061-1072 (1982).

Veltri, R. D., "The Electrical Resistivity of Solid and Molten Fused Silica in the Temperature Range 1000 - 2480 °C", Physics and Chemistry of Glasses **4**, 221-228 (1963).

White, L. J. and Duffy, G. J., "Vapor-Phase Production of Colloidal Silica", Ind. Eng. Chem. **51**, 232-238 (1959).

Young, R. M. and Pfender E., "Generation and Behavior of Fine Particles in Thermal Plasmas - A Review", Plasma Chem. Plasma Process. 5, 1-37 (1985).

Appendix 1

Estimation of Difference Between Actual and Thermocouple Temperature

A1.1 Crucible and Chamber Wall Temperature

The graphite crucible and chamber wall temperature were measured using type C thermocouples. The details of the thermocouple construction are given in section 3.2.3. Assuming the major heat transfer mechanisms to be conduction and radiation, a steady-state heat balance on the thermocouple junction gives:

$$E_{cond} = E_{rad} \tag{A1.1}$$

where E_{cond} is the rate of heat loss by conduction through the thermocouples wires and E_{rad} is the rate of heat input by radiation from the surrounding enclosure. The above terms can be estimated by making the following assumptions:

1. The surfaces involved are diffuse and gray.

2. The exposed thermocouple junction, composed of twisted wire and a weld bulb can be treated as an isothermal 1 cm long cylinder with an equivalent diameter of 0.5 mm.

3. The radiation exchange between the thermocouple junction and the surrounding enclosure can be estimated by assuming a two surface enclosure composed of a small convex object (thermocouple junction) in a large isothermal cavity (surrounding alumina sheath and graphite surface).

4. The thermocouple wires have properties similar to pure tungsten.

5. Heat conduction through the wires is 1-D (axial direction only).

6. Each wire has a diameter of 0.25 mm and a length of 30.5 cm.

7. The ends of the wires are maintained at 300 K.

Using relations and property data found in Incropera and DeWitt (1985), an estimate of the junction temperature for various graphite surface temperatures was made. The results are presented in Table A1.1.

TABLE A1.1 Estimate of difference between actual and thermocouple temperature for the crucible, chamber wall and reactor exit gas.

Actual Temperature [K]	***Crucible and Chamber Wall Thermocouple Temperature [K]***	***Reactor Exit Gas Thermocouple Temperature [K]***
1000	924	992
1500	1481	1495
1750	1741	1746
2000	1993	1997

A1.2 Reactor Exit Gas Temperature

A similar analysis was made for the reactor exit gas temperature which was measured using an exposed junction. The steady-state heat balance on the thermocouple junction for this case is as follows:

$$E_{cond} = E_{rad} + E_{conv} \qquad \text{(A1.2)}$$

where E_{rad} is the rate of heat input by radiation from the walls of the graphite exit tube and E_{conv} is the rate of convective heat transfer from the flowing gas. The following assumptions were made to estimate the above terms:

1. The surfaces involved are diffuse and gray.

2. The exposed thermocouple junction, composed of twisted wire and a weld bulb can be treated as an isothermal 1 cm long cylinder with an equivalent diameter of 0.5 mm.

3. The exit tube walls and junction are coated with a thin layer of silica having an emissivity of 0.5. The temperature gradient between the junction and outer silica layer is negligible.

4. The graphite exit tube acts like a large cavity which encloses the junction. Due to the heavy insulation used in the reactor exit, the wall temperature is assumed to be equivalent to that of the gas.

5. Convective heat transfer is estimated using a Nusselt number correlation for flow over a cylinder.

6. An Ar flow rate of 17.7 lpm (293 K and 101.3 kPa) is assumed in the exit tube.

7. The thermocouple wires have properties similar to pure tungsten.

8. Heat conduction through the wires is 1-D (axial direction only).

9. Each wire has a diameter of 0.25 mm and a length of 30.5 cm.

10. The ends of the wires are maintained at 300 K.

An estimate of the junction temperature for various exit gas temperatures is shown in Table A1.1. Property data for Ar were obtained from Boulos et al. (1994).

Appendix 2

Experimental Data

TABLE A2.1 Steady-state crucible, chamber wall and reactor exit gas temperature during Ar plasma gas experiments.

Experiment	*Steady-State Temperature [K]*					
	Crucible		*Chamber Wall*		*Reactor Exit Gas*	
	Mean	*Std. Dev.*[1]	*Mean*	*Std. Dev.*	*Mean*	*Std. Dev.*
54	1768	48	1590	77	1529	69
60	1750	31	1623	32	1374	18
119	1757	30	1471	26	1696	75
50	---	---	1625	29	1435	51
59	1748	26	1571	44	1451	35
120	1768	32	1525	27	1475	51
52	1700	38	1558	42	1616	47
61	1775	28	1659	32	1451	31
87	1858	50	1444	31	1558	54
89	1930	45	1488	28	1620	38
90	1887	37	1476	17	1541	46
81	1858	48	1577	33	1731	42
88	1874	51	1430	30	1713	43
85	1866	42	1567	29	1745	92
86	1911	64	1587	67	1767	89
76	1962	84	1662	59	1696	51
78	2003	80	1681	55	1666	67
82	1971	97	1696	59	1727	44
84	1984	91	1685	50	1768	35
77	2028	95	1745	63	1677	80
83	1993	84	1701	55	1903	63
91	2048	74	1585	52	1703	71

1. With respect to time.

TABLE A2.2 Crucible, chamber wall and reactor exit gas temperature before and after arc shutdown during Ar plasma gas experiments.

Experiment	*Temperature Before and After Arc Shutdown [K]*					
	Crucible		*Chamber Wall*		*Reactor Exit Gas*	
	Before	*After*	*Before*	*After*	*Before*	*After*
54	1846	1841	1673	1669	1474	1471
60	1781	1804	1617	1606	1366	1330
119	1768	1769	1480	1472	1736	1498
50	---	---	1685	1670	1527	1531
59	1794	1803	1635	1638	1451	1421
120	1793	1773	1551	1522	1587	1612
52	1736	1731	1527	1512	1599	1595
61	1794	1823	1654	1684	1509	1474
87	1900	1907	1503	1505	1642	1651
89	1968	1962	1503	1521	1605	1601
90	1921	1915	1486	1498	1629	1545
81	1901	1916	1605	1602	1685	1619
88	1921	1922	1457	1465	1774	1660
85	1901	1911	1599	1609	1860	1659
86	1970	2007	1666	1654	1729	1669
76	2020	2005	1710	1720	1748	1725
78	2056	2076	1723	1727	1748	1697
82	2027	2025	1742	1761	1768	1716
84	2041	2037	1717	1705	1827	1682
77	2100	2110	1807	1802	1774	1770
83	2070	2094	1762	1789	2041	1782
91	2130	2128	1635	1634	1800	1762

TABLE A2.3 Steady-state voltage during Ar plasma gas experiments.

Experiment	*Steady-State Voltage [V]*	
	Mean	*Std. Dev.*[1]
54	36.77	0.98
60	36.47	0.81
119	36.87	0.59
50	36.57	1.37
59	39.97	1.50
120	39.07	0.84
52	39.17	1.98
61	39.07	1.00
87	35.06	0.94
89	35.86	0.40
90	34.96	0.51
81	35.76	0.46
88	37.36	0.38
85	37.46	1.29
86	40.16	0.99
76	34.75	0.89
78	35.65	1.03
82	35.75	0.85
84	37.55	0.45
77	38.35	0.60
83	39.75	1.37
91	40.65	1.36

1. With respect to time.

TABLE A2.4 Steady-state CO concentration in the reactor exit gas during Ar plasma gas experiments.

Experiment	*Steady-State Reactor Exit Gas CO Concentration [mole %]*[1]	
	Mean	*Std. Dev.*[2]
54	0.22	0.03
60	0.17	0.03
119	0.16	0.03
50	0.20	0.02
59	0.16	0.03
120	0.17	0.03
52	0.14	0.04
61	0.16	0.02
87	0.39	0.12
89	0.69	0.05
90	0.44	0.02
81	0.48	0.03
88	0.41	0.06
85	0.26	0.03
86	0.44	0.07
76	1.26	0.17
78	1.38	0.08
82	1.03	0.13
84	1.21	0.13
77	1.52	0.08
83	1.62	0.30
91	1.62	0.32

1. Evaluated after 90, 60 and 40 minutes for currents of 150, 200 and 250 A respectively.

2. With respect to time.